

https://dspace.org/

Neoproterozoic metasediments and base metal mineralisation in an area north of the Mpande Dome in southern Zambia: an alternative lithostratigraphy classification

King, Heather Leslie

2018

https://hdl.handle.net/10539/27399

King, Heather Leslie (2018) Neoproterozoic metasediments and base metal mineralisation in an area north of the Mpande Dome in southern Zambia: an alternative lithostratigraphy classification, University of the Witwatersrand, Johannesburg, https://hdl.handle.net/10539/27399

Downloaded from a DSpace repository. https://dspace.org/

Neoproterozoic metasediments and base metal mineralisation in an area north of the Mpande Dome in southern Zambia; an alternative lithostratigraphy classification



Heather Leslie King

0315834V

A Thesis submitted to the Faculty of Science, University of the Witwatersrand, in fulfilment of the requirements for the degree of Doctor of Philosophy

August 2018

DECLARATION

I declare that this Thesis is my own, unaided work. It is being submitted for the Degree of Doctor of Philosophy at the University of the Witwatersrand, Johannesburg. It has not been submitted before for any degree or examination at any other University.



_____

(Signature of Candidate)

17 day of August 2018 in Johannesburg

EXTENDED ABSTRACT

Prospecting in 2013 to 2015 identified rift-related metasediments in the Mpande Dome area, south of Lusaka, Zambia. The metasediments were thought to be comparable to the Roan Group of the Katanga Supergroup within the Zambian Copperbelt and therefore prospective as a target for sediment-hosted, stratiform copper mineralisation. The metasediments of this area, known as Shantumbu, were last actively explored in the 1930 to 1960s'.

Shantumbu is approximately 30km south southeast of Lusaka, Zambia and lies on the northern margin of the Mpande Dome which is south of the Mwembeshi Zone. The Shantumbu area is a highly tectonised region as it is the convergence point of the Zambezi Belt, the Lufilian Arc and Irumide Belt.

Simpson *et al*. (1963), Smith (1964), and Mallick (1966), classified the metasediments as belonging to the Chunga and Cheta groups (Smith, 1964) or the Shamazio, Kafue and Cheta groups (Mallick, 1966), of the Katanga Supergroup. In 2000, Porada and Berhorst proposed correlation of the stratigraphy with the Katanga Supergroup in the Zambian Copperbelt.

For many decades, the lack of outcrop and exploration information and the effect of Pan African deformation and high-grade metamorphism, impeded prospecting. The recent exploration activities on Shantumbu, which included logging of cores, petrography, geochemical and mineralogy, highlighted a fresh examination of the metasediments and the copper mineralisation in this area were required.

This is the first detailed information in recent years on the metasediments around the Mpande Dome. The result of the research has showed the adoption of the Roan Group stratigraphy of the Katanga Supergroup, as it occurs in the Zambian Copperbelt, is proposed rather than the nomenclature for metasediments forming part of the Zambezi Supracrustal Sequence.

An alternative stratigraphic classification to the nomenclature of the Chunga and Cheta formation has been raised, indicating the metasediments north of the Mpande Dome are the southernmost limit of the Roan Group in Zambia. It therefore appears the Proterozoic rift-related terrigenous and marine sediments of the Katanga Supergroup are continuous from the Central African Copperbelt southward to the Kafue area and Shantumbu.

The metasediments at Shantumbu progress from arenites and siltstones above what is interpreted to be Kafue Rhyolite and Nazingwe metavolcanics. The metavolcanics cap the alkali granites and gneisses of the Basement. The proportion of arenites deposited diminished and

gave way to siltstone-dominated units, which in turn gave way to carbonate and lesser siltstone units. A marine transgression surface terminated the detrital units. The siliciclastic units below the transgression surface correlate to the Mindola Formation. The dolomitic carbonate and arenite units correlate with the Copperbelt Orebody Member of the Kitwe Formation, Roan Group. Carbonates, and lesser siltstone and arenite units, deposited in a near-shore marine environment overlie the Copperbelt Orebody Member, and correlated with the Kitwe Formation. The youngest succession identified on Shantumbu comprised calcitic carbonates deposited in a marine basin progressively starved of terrestrial sediments. The carbonates are correlated with the Bancroft Member of the Kirilabombwe Formation.

Petrographic examination of the drill core, together with mineralogy studies and geochemical analyses, have resulted in a contemporary account of the rift basin architecture in the Shantumbu area to be presented. New insight into the depositional environments related to rift initiation, climax and cessation, sulphide mineralisation, and oxic and anoxic conditions during deposition, were obtained.

The geochemical characteristics and mineralogy indicate the metasediments were subjected to a complex range of alteration and metasomatism. The alteration mineralogy and presence of minerals such as glaucophane, epidote, albite and sphene, indicated the area was subjected to low-temperature (250 - 400°C) and high-pressure metamorphism, that of epidote-amphibolite facies, and retrograde metamorphosed to greenschist facies.

Potassic and sodic alteration is characteristic of the detrital lower successions and the upper carbonate successions respectively. Alteration caused by diagenesis-compaction, dewatering of the terrestrial sediments, and later stage remobilisation of potassic and sodium-bearing fluids. Deformation of the area was related to the Pan African Orogeny.

Mineralisation on Shantumbu is associated with arenites capped by siltstone near the first occurrences of dolomitic carbonate in the stratigraphy. Most copper deposits in the Zambian Copperbelt are found within 200m of a marine transgression surface, within and adjacent to the Copperbelt Orebody Member. The formation of stratabound base metal sulphides in the lower detrital sequences versus the lack of base metal sulphides in the marine-dominated sequences, suggests the base metals were sourced from the Basement units and transported via basinal brines, rather than introduced from a magmatic origin.

The copper sulphides intersected in drill core at Shantumbu, and the copper oxides which crops out, are comparable to the sediment-hosted, stratiform copper deposits of the Zambian

Copperbelt, and other sediment-hosted, stratiform copper occurrences globally, such as White Pine in Michigan, the Zechstein Basin in Europe, Spar Lake in Montana, the copper occurrences in Namibia and Botswana on the Kalahari Craton, and the Mangula and Mhangura deposits in Zimbabwe.

The continuation of the metasediments from Shantumbu north through the Chongwe Copperbelt and the southerly termination of the Roan Group on the northern margin of the Mwembeshi Zone, strengthens the argument that Shantumbu is contiguous with the Roan Group of the Katanga Basin. The age of the Kafue Rhyolite and Nazingwe formations in the Mpande Dome region, have been age dated at 879 ± 19 Ma (Hanson *et al*., 1994; Selley *et al*., 2005; Johnson *et al*., 2007), which has provided further support that Shantumbu is part of the Neoproterozoic Katanga Basin system, rather than the older rift systems to the south of Zambia, such as the Zambezi Belt or the Magondi Mobile Belt.

The examination of the metasediments on Shantumbu has shown that further research would advance the understanding of the rift basin stratigraphy and related sediment-hosted, stratiform copper mineralisation. Such research topics include the investigation of the presence of metavolcanics on the northern margin of the Mpande Dome and the Kafue Rhyolite and Nazingwe Formation hosting copper sulphides, and a comparison and correlation, or otherwise, of the metasediments comprising the Chongwe Copperbelt to the Shantumbu metasediments.

ACKNOWLEDGEMENTS

My sincere gratitude is extended to Professors' Judith Kinnaird and Paul Nex for their support, assistance and patience during the research and compilation of this thesis. The School of Geosciences at the University of the Witwatersrand is gratefully thanked for use of their equipment.

The mining company which undertook the exploration at Shantumbu is appreciatively thanked for allowing the use of the exploration information and permission to publish. I would also like to thank my employers for their support during compilation of the thesis.

I owe tremendous gratitude to my husband, children and sister for supporting me, and their sacrifices during completion of the thesis.

CONTENTS

DECLARATION i
EXTENDED ABSTRACT ii
ACKNOWLEDGEMENTS v
1 INTRODUCTION 1
1.1 Introduction 1
1.2 Locality of Shantumbu 1
1.3 Geological Setting of Shantumbu 2
1.4 Motivation 5
1.5 Aims and Objectives 5
1.6 Research Methodology 6
1.7 Conclusion 7
2 STRATIGRAPHIC SETTING OF SHANTUMBU AND THE ROAN GROUP 9
2.1 Introduction 9
2.2 Literature Review 11
2.3 The Zambian Copperbelt Stratigraphy 18
2.4 Discussion 23
3 REGIONAL TECTONIC SETTING 26
3.1 Introduction 26
3.2 Neoproterozoic Rifting 26
3.3 Pan-African Orogenesis 27
3.4 Pan-African Thermo-Tectonic Events 29
3.5 Discussion 31
3.6 Conclusions 34
4 LITHOSTRATIGRAPHY OF SHANTUMBU 35
4.1 Introduction 35
4.2 Methodology 35
4.3 Hypotheses 37
4.4 Lithological Description of Shantumbu 37
4.5 Depositional Environments on Shantumbu and the Roan Group 51
4.6 Discussion 55
4.7 Conclusions 65
5 MINERALOGY AND METAMORPHISM 67
5.1 Introduction 67
5.2 Mineralogy 68
5.3 Metamorphism 108

5.4 Discussion 110
5.5 Conclusion 117
6 MINERALISATION 119
6.1 Introduction 119
6.2 Petrology and Mineralogy 119
6.3 Discussion 125
6.4 Conclusion 133
7 GEOCHEMISTRY 134
7.1 Introduction 134
7.2 Geochemical Sampling and Analytical Methodologies 135
7.3 Geochemical Results 136
7.3.1 Lithologies and Alteration 136
7.3.2 Immobile Elements 146
7.3.3 Mobile Elements 150
7.3.4 Mineralisation 160
7.4 Discussion 166
7.5 Conclusions 173
8 DISCUSSIONS, CONCLUSIONS AND RECOMMENDATIONS 175
8.1 Introduction 175
8.2 Tectonic Framework of Shantumbu 176
8.2.1 Regional Structure 177
8.2.2 Local Structure 179
8.2.3 Magmatism 181
8.3 Shantumbu Lithostratigraphy and Correlation with the Roan Group 181
8.3.1 Lithostratigraphic Correlation with the Roan Group 181
8.3.2 Metamorphism 190
8.3.3 Alteration 192
8.4 Shantumbu Copper Mineralisation in the Context of Sediment-Hosted, Stratiform Copper Deposits 194
8.4.1 Bacterial Sulphate Reduction 197
8.4.2 Basement as a Source of Copper 199
8.5 Aims and Objectives Achieved 200
8.6 Conclusions 202
8.7 Recommendations 207
REFERENCES 209
APPENDICES 222

List of Figures

Figure 1-1. Schematic sketch of the main tectonic provinces of northern Zimbabwe, Zambia, Mozambique, and southern DRC. The locations of Shantumbu, the Central African Copperbelt, Lufilian Arc, Irumide, Mozambique and Zambezi Belts. (Modified from Unrug, 1983; Porada, 1989; Kröner, 2004). 2

Figure 1-2. Simplified map of the Neoproterozoic geological setting during the breakup of Rodinia. The rift basins were closely related to the margins of the Congo Craton. The location of the Katanga Basin is shown and the proximity of Shantumbu. (Zientek *et al*., 2014, and references therein). 3

Figure 1-3. Location of Shantumbu (noted with 'x' above Mpande Dome) and the town of Kafue in relation to the Lufilian Arc, Zambezi Belt and Basement, the Mwembeshi Zone, and the Mpande Dome (M.D.). (Modified after Johnson *et al*., 2007). 3

Figure 2-1. The seven sequences and related metasediments intersected in the Shantumbu drill cores. (a) The fine-grained arkose of Sequence 1 is the oldest unit intersected in the drilling and is host to copper mineralisation. (b) Red, cream and grey arenite of Sequence 2. (c) Dolomite calc-silicate of Sequence 3. (d) Siltstone and grey carbonate of Sequence 3. (e) Iron oxide-rich calc-silicate of Sequence 4. (f) Siltstone carbonate breccia of Sequence 5. (g) Siltstone carbonate rhythmite of Sequence 5. (h) Brecciated arenite of Sequence 5. (i) Goethite-rich carbonate and arenite of Sequence 6. (j) Finely laminated grey-blue to yellow-brown carbonate of the youngest succession, Sequence 7. 10

Figure 2-2. Regional basement and sedimentary geology around Shantumbu and south of the Mwembeshi Zone (MSZ) where the relationship between the platform-shelf carbonates and the terrestrial siliciclastic sediments in relation to the Mpande Dome (MP) are illustrated. The tectonic contact of the Lusaka Dolomite Formation and the Katanga Supergroup is illustrated, together with the regional direction of thrusting and back thrusting of the Katanga Supergroup (Porada and Berhorst, 2000). The position of Shantumbu is denoted with a 'X' 17

Figure 3-1. Location of Shantumbu in relation to the Pan African orogenic regions including the Mwembeshi Zone, the Lufilian Arc and Zambezi Belt (Daly, 1988). 28

Figure 3-2. Aster false colour image of Shantumbu indicating the localities of the D_1 folds, diamond drill hole collars and major lithologies, A to C. (A) Detrital siliciclastic units. (B) Carbonate units. (C) Detrital siliciclastic units. The fringe of the Mpande Dome occurs along the southern boundary of the Shantumbu license. The image boundary equates to the Shantumbu License area. 32

Figure 3-3. Schematic plan view of the D_1 compressive tectonics immediately north of the Mpande Dome. Large-scale recumbent folding with plunge towards the north northeast characterize the Shantumbu area. Copper Hill is located at the axis of the easterly D_1 fold. The Shantumbu License is overlain for reference. 32

Figure 4-1. Section AB through the central area of Shantumbu via a schematic drill hole fence diagram referenced to the carbonate datum. Due to Pan African deformation the stratigraphy is overturned, with the older sequences at the top of the logs and the youngest at the base of the logs. 36

Figure 4-2. Section line A-B overlain on the Landsat 8 OLI false-colour composite image (September 2013) of the Shantumbu License. 36

Figure 4-3. Goethite-bearing fine-grained altered arkose of Sequence 1, Shantumbu, cross-cut by hematite-bearing veins (H08288 from PSH008 at a depth of 30m. 38

Figure 4-4. Fine-grained arenite of Sequence 1, Shantumbu. (a) Fine-grained arkose of Sequence 1 hosting malachite and chlorite (PSH008). (b) Malachite along bedding and fracture planes, hosted by fine-grained grey arkose of Sequence 1 (PSH008). (c) Outcrop of fine-grained arkose hosting malachite mineralisation At Copper Hill, Shantumbu. 38

Figure 4-5. Arkose and siltstone units of Sequence 1, Shantumbu. (a) Alternating siltstone and iron-oxide-bearing arkose layers of Sequence 1. (b) Siltstone from Sequence 1 cross-cut by a boudinaged calcite-bearing vein (H08291 from PSH007 at a depth of 100.1m). 39

Figure 4-6. Lithologies of Sequence 2, Shantumbu. (a) Sequence 2 shows rounded to sub-rounded dark grey plagioclase-quartz patches in SPA005 (at a depth from 132.35 to 136.65m). (b) Laminated arenite (SPA018 at a depth from 105.67 to 110.37m). (c) Interbedded arenite and siltstone layers (PSH008; at a depth from 89.55 to 95.55m). 40

Figure 4-7. Mottled, grey and iron oxide stained examples of the arenites of Sequence 2, Shantumbu. (a) Erosional contact between grey and pink arenites of Sequence 2 (SPA005 at a depth of c. 20m). (b) Mottled arenite debris flow (SPA005 at a depth of c. 114m). (c) Grey arkose interbedded with medium-grained goethite-rich arenite (PSH001 at a depth of 32.8 - 37.14m). 41

Figure 4-8. The sub-aqueous siltstone and carbonate lithologies of Sequence 3, Shantumbu. (a) Siltstone and grey carbonate of Sequence 3 in SPA005 (145 – 153m) overlain by grey carbonate and massive siltstone layers of Sequence 3 (PSH008 at a depth of 104 to 108m). (b) The goethite-rich arenite of Sequence 4 caps the grey carbonate of Sequence 3. 42

Figure 4-9. The upper and lower iron oxide calc-silicate layers and intervening dolomitic breccia of Sequence 4 (PSH008 at a depth of c. 108 - 118m). 43

Figure 4-10. Iron oxide-rich calc-silicate succession of Sequence 4 in SPA026B, Shantumbu. 44

Figure 4-11. The cream dolomite of facies 5a overlain by a carbonate layer containing scattered biotite clasts, Shantumbu. The succession is capped by rhythmite of facies 5b (SPA026B at depths from 101.6 to c. 109m). 45

Figure 4-12. Breccias of facies 5b, Shantumbu. (a) Brecciated siltstone and relict bedding within facies 5b in PSH007. (b) Brecciated argillite cemented by carbonate matrix of facies 5b. (c) Sulphides cross-cutting a brecciated biotite clast in facies 5b (PSH007). 46

Figure 4-13. Alternating laminations of calcite and biotite within the rhythmites of facies 5c (SPA018, sample E2181 at a depth of c. 86m), Shantumbu. 46

Figure 4-14. Biotite-dominated bands, grey carbonate, and brecciated arenite of facies 5c (SPA015 at a depth of c. 201m), Shantumbu. 47

Figure 4-15. Siltstone and dolomitic siltstone of facies 5c (SPA026A at a depth from c. 84 - 87m), Shantumbu. 47

Figure 4-16. Arenite breccias of facies 5c, Shantumbu. (a) Brecciated arenite of facies 5c (SPA018). (b) Goethite surrounding the brecciated clasts of arenite in facies 5c. 48

Figure 4-17. Goethite-rich carbonate and erosional contact between the arenite and underlying carbonate in Sequence 6 (SPA018 at a depth of c. 245m), Shantumbu. 48

Figure 4-18. Erosional contact between brecciated arenite and carbonate rhythmite in Sequence 6 (SPA018), Shantumbu. 49

Figure 4-19. Goethite-bearing brecciated feldspathic arenite of Sequence 6 (SPA018 E2184), Shantumbu. 49

Figure 4-20. Sodalite, a sodic alteration mineral, interstitial to the brecciated feldspathic clasts comprising the arenites of Sequence 6 (SPA018), Shantumbu. 50

Figure 4-21. Finely laminated grey-blue to yellow-brown carbonate of Sequence 7 (SPQ001), Shantumbu. 50

Figure 4-22. Rhombohedral carbonate (calcite) with iron oxide staining filling a vug within the grey-blue carbonate of Sequence 7 (SPQ002), Shantumbu. 51

Figure 4-23. Tectonostratigraphic evolution of the Katanga Supergroup, Zambian Copperbelt, illustrating the passive continental rift initiation, climax and rift cessation (Modified after Selley *et al*., 2005, p971). (a) rift initiation; (b) rift climax; (c) post rift and (d) thermal sag. 53

Figure 4-24. Schematic stratigraphic sequences of the Katanga Supergroup within the Lufilian Arc and Zambezi Belt. (a) The Zambian Copperbelt. (b) North of the Mpande Dome. (c) South of the Mpande Dome (Nega Section). KRF – Kafue Rhyolite Formation; NF - Nazingwe Formation; NgG – Ngoma Gneiss; MHG – Munali Hills Granite; u/C – unconformity; D/C – disconformity; T – thrust (Johnson *et al*., 2006). 54

Figure 4-25. Progressive growth of anhydrite replacing gypsum within the rhythmites of Sequences 5 and 6, Shantumbu. 61

Figure 4-26. The light earthy brown layers of Sequence 7 are quartz-feldspar (albite) calc-silicate layers interbedded with the grey to blue carbonate, SPQ001A from 158.40m to 171m, Shantumbu. 64

Figure 4-27. Outcrop of the thick succession of monotonous calcitic carbonate in Sequence 7, Shantumbu. ... 65

Figure 5-1. Fine-grained arenite with fine siltstone laminations. (a) PQ drill hole core (SPA005) and (b) outcrop of the clean, grey, fine-grained arenite and fine siltstone laminations of Sequence 1, Shantumbu. Cross-cut veining is noted in the drill hole core. 69

Figure 5-2. Feldspar alteration in Sequence 1, Shantumbu. (a) Vesicle hosting remnant K-feldspar grains (H08289 from PSH009 at a depth of 16.4m). Altered vesicular rhyolite with remnant K-feldspar within sericitised rhyolite vesicle from Sequence 1. The formation of K-feldspar is indicative of potassic metasomatism. Image is in cross polarised light. (b) Sub-rounded plagioclase grains and interstitial carbonate and goethite (H08294 from PSH001 at a depth of 36.24m). (c) Partial to complete alteration to muscovite and sericite and dissolution of the feldspars (H08289 from PSH009 at a depth of 16.4m). All images in cross polarised light. 69

Figure 5-3. Microcrystallisation of arenite at Shantumbu. (a) Quarter core sample E2199 (SPA001 at c. 35m depth) of goethite alteration of Sequence 1 arenite. (b) Microcrystalline brecciated arenite; image in cross polarised light (E2199 SPA001 at c. 35m depth). 70

Figure 5-4. Texture of the arenites of Sequence 2, Shantumbu. (a) Interlocking recrystallised plagioclase and quartz and lesser K-feldspar displaying sutured boundaries, grain bulging and distorted lattices. A quartz plagioclase vein cross-cuts across the minerals (H08303 from PSH009 at a depth of 73.57m). (b) Sericitic

matrix hosting remnant and highly altered arenite (H08297 from PSH009 at a depth of c. 79m). All images in cross polarised light. 71

Figure 5-5. Albitised breccia with elongated plagioclase grain demonstrating Carlsbad twinning, Sequence 2, Shantumbu. Sample E2180 from drill hole SPA018. 72

Figure 5-6. Dolomitic breccia of Sequences 3 and 4, Shantumbu. (a) Plagioclase and feldspar grains within a matrix of carbonate (H08307 from PSH007 at a depth of 118.35m). (b) Fragments of plagioclase cemented by interstitial dolomite (H08307 from PSH007 at a depth of 118.35m). All images in cross polarised light. 73

Figure 5-7. Brecciated siltstone from Sequence 5, Shantumbu, facies 5b composed of microcrystalline biotite, dolomite, plagioclase, K-feldspar, quartz, scapolite and calcite. 74

Figure 5-8. The mineralogy of the siltstone breccias is dominated by plagioclase, quartz, biotite, K-feldspar, and calcite, Sequence 5, Shantumbu. (a) Sulphide-bearing vein hosted by calcite and biotite-bearing brecciated siltstone – plane polarised light. Sample E2270B plane polarised light (200µm) (PSH003 at a depth of c. 180m). (b) Sulphide-bearing vein hosted by calcite and biotite-bearing brecciated siltstone-cross polarised light. Sample E2270B cross polarised light (200µm) (PSH003 at a depth of c. 180m). (c) Brecciated siltstone dominated by biotite clasts (core sample). Sample E2271C plane polarised light (200µm) (PSH003 at a depth of c. 180m). (d) and (g) Disseminated sulphides hosted by calcite and biotite-bearing brecciated siltstone - plane polarised light. (d) Sample E2270C cross polarised light (200µm) (PSH003 at a depth of c. 175m). (g) Sample E2260 cross polarised light (500µm) (PSH003). (f) Brecciated siltstone dominated by biotite clasts (core sample). Sample E2271B cross polarised light (200µm) (PSH003 at a depth of c. 175m). (e) (h) and (j) Disseminated sulphides hosted by calcite and biotite-bearing brecciated siltstone - cross polarised light. (e) Sample E2271B plane polarised light (200µm) (PSH003 at a depth of c. 180m). (h) Sample E2257 cross polarised light (500µm) (PSH003 at a depth of c. 165m). (i) and (l) Brecciated siltstone domainted by biotite clasts (core sample). (i) Sample E2271B cross polarised light (200µm) (PSH003 at a depth of c. 180m). (l) Sample E2271 (PSH003 at a depth of c. 180m). (k) Interlocking and anhedral plagioclase. Sample E2270 (PSH003 at a depth of c. 175m). (j) Sample E2270B cross polarised light (200µm) (PSH003 at a depth of c. 175m). (m) Sample E2271B (PSH003 at a depth of c. 180m). 75

Figure 5-9. Rhythmic banding of carbonate and siltstone/mudstone in Sequence 5, facies 5c, Shantumbu; quarter core sample E2181 from SPA018 at an approximate depth of 86m. 76

Figure 5-10. Mineralogy of the rhythmite bands - Sequence 5, facies c. Shantumbu (a) Garnet, calcite and aegirine phenocrysts; plane polarised light. Sample E2213A plane polarised light (200µm) (SPA015). (b) Garnet, calcite and aegirine phenocrysts; cross polarised light. Sample E2213A cross polarised light (200µm at a depth of c. 30m) (SPA015). (c) Inclusion of chlorite grains within coarse-grained aegirine; plain polarised light. E2213B plane polarised light (200µm) (SPA015 at a depth of c. 30m). (d) Inclusion of chlorite grains within coarse-grained aegirine; cross polarised light. E2213B cross polarised light (200µm) (SPA015 at a depth of c. 30m). (e) Rounded grains of amphibole and quartz within a calcite matrix; plane polarised light. E2213C plane polarised light (200µm) (SPA015 at a depth of c. 30m). (f) Rounded grains of amphibole and quartz within a calcite matrix; cross polarised light. E2213C cross polarised light (200µm) (SPA015 at a depth

of c. 30m). (g) Sulphides along the contact between the siltstone and calcite layers; the siltstone layer consists of coarse-grained and fragmented aegirine; plane polarised light. E2213D plane polarised light (200µm) (SPA015 at a depth of c. 30m). (h) Sulphides along the contact between the siltstone and calcite layers; the siltstone layer consists of coarse-grained and fragmented aegirine; cross polarised light. E2213D cross polarised light (200µm) (SPA015 at a depth of c. 30m). (i) Sutured boundaries between grains of calcite and quartz with sulphides; plane polarised light. E2213D Plane polarised light (200µm) (SPA015 at a depth of c. 30m). (j). Sutured boundaries between grains of calcite and quartz with sulphides; cross polarised light. E2213D cross polarised light (200µm) (SPA015 at a depth of c. 30m). (k) Deformed and metamorphosed rhythmite core sample from Sequence 5, facies c, denoting the fragmented siltstone layers and carbonate layers. E2213A plane polarised light (200µm) (SPA015 at a depth of c. 30m). (l) Rounded grains of albite, hornblende, and quartz within matrix of calcite. Saussuritisation (epidote) is present in the upper right corner of the plan polarised thin section photomicrograph. E2213A cross polarised light (200µm) (SPA015 at a depth of c. 30m). (m) Rounded grains of albite, hornblende, and quartz within matrix of calcite. Saussuritisation (epidote) is present in the upper right corner of the cross polarised thin section photomicrograph. E2213D plane polarised light (200µm) (SPA015 at a depth of c. 30m). (n) Rounded grains of albite and sulphides within matrix of calcite. Saussuritisation (epidote) is present in the lower left corner of the plan polarised thin section photomicrograph. E2213D cross polarised light (200µm) (SPA015 at a depth of c. 30m). (o) Rounded grains of albite and sulphides within matrix of calcite. Saussuritisation (epidote) is present in the lower left corner of the plan polarised cross section photomicrograph. facies 5c carbonate sample. 78

Figure 5-11. The well-developed schistosity imparted by the phyllosilicate mica grains interspersed by various minerals such as epidote, plagioclase and amphibole in Sequence 5, facies c, Shantumbu (a) Elongated quartz grains in the direction of the biotite and muscovite foliation; plane polarised light. Sample E2224A plane polarised light (200µm) (SPA033A at a depth of c. 85m). (b) Elongated quartz grains in the direction of the biotite and muscovite foliation; cross polarised light. Sample E2224A cross polarised light (200µm) (SPA033A at a depth of c. 85m). (c) Interstitial sulphides, granoblastic quartz and calcite to biotite and muscovite; plane polarised light. Sample E2224 plane polarised light (200µm) (SPA033A at a depth of c. 85m). (d) Interstitial sulphides, quartz and calcite to biotite and muscovite; cross polarised light. Sample E2224A cross polarised light (200µm) (SPA033A at a depth of c. 85m). (e) Polycrystalline to monocrystalline quartz grains; plane polarised light. Sample E2221A plane polarised light (200µm) (SPA033A at a depth of c. 115m). (f) Polycrystalline to monocrystalline quartz grains; cross polarised light. Sample E2221A cross polarised light (200µm) (SPA033A at a depth of c. 115m. (g) Interstitial plagioclase and amphiboles to the foliation imparted by biotite and muscovite; plane polarised light. Sample E2221B (200µm) (SPA033A at a depth of c. 115m). (h) Interstitial plagioclase and amphiboles to the foliation imparted by biotite and muscovite; cross polarised light. Sample E2221B cross polarised light (200µm) (SPA033A at a depth of c. 115m). (i) Orthomylonitic fabric dominated by quartz and calcite grains. Quartz displays pressure shadows; plane polarised light. Sample E2221B plane polarised light (200µm) (SPA033A at a depth of c. 115m). (j) Orthomylonitic fabric dominated by quartz and calcite grains. Quartz displays pressure shadows; cross

polarised light. Sample E2221B cross polarised light (200µm) (SPA033A at a depth of c. 115m). (k) and (l) Closely-spaced rhythmite bands of facies 5c; core samples. (k) Sample E2224 (SPA003A at a depth of c. 85m. (l) Sample 2221A (SPA033A at a depth of c. 115m). 81

Figure 5-12. Brecciated arenite of Sequence 5, facies c, Shantumbu. (a) Sutured boundaries of epidote grains. Quartz and goethite occur interstitial to the larger epidote grains; plane polarised light. Sample E2225 plane polarised light (SPA033A at a depth of c. 36m). (b) Sutured boundaries of epidote grains. Quartz and goethite occur interstitial to the larger epidote grains; cross polarised light. Sample E2225 cross polarised light (SPA033A at a depth of c. 36m). (c) Pervasive goethite within a sample dominated by muscovite and epidote; plane polarised light. Sample E2225 plane polarised light (SPA033A at a depth of c. 36m). (d) Pervasive goethite within a sample dominated by muscovite and epidote; cross polarised light. Sample E2225 cross polarised light (SPA033A at a depth of c. 36m). (e) Aegirine and quartz within the penetrative fabric stemming from the presence of micas; plane polarised light. Sample E2220 plane polarised light (SPA033A). (f) Aegirine and quartz within the penetrative fabric stemming from the presence of micas; cross polarised light. Sample E2226 cross polarised light (SPQ002 at a depth of c. 95m). (g) Brecciated arenite of Sequence 5, facies c; core sample. Sample E2226 (SPQ002 at a depth of c. 95m). (h) Pervasive alteration to goethite in brecciated sample from Sequence5, facies c; core sample. Sample E2226 (SPQ002 at a depth of c. 95m). All samples are at 200µm. 82

Figure 5-13. SEM data for sample E2213B (SPA015 at a depth of c. 30m) for Sequence 5, facies c, Shantumbu. (a) Thin section showing Points 1 to 5. (b) Backscattered electron image with locations of the eleven spectra; Ap – apatite, Pyr - pyrrhotite. (c) Half core sample from which the thin section was derived. (d) Mineral spectrum for apatite. (e) Mineral spectrum for pyroxene. (f) Mineral spectrum for pyrite/pyrrhotite. (g) Mineral spectrum for calcite. 85

Figure 5-14. SEM data for sample E2213B (SPA015 at a depth of c. 30m) for Sequence 5, facies c, Shantumbu. (a) Thin section showing Points 1 to 5. (b) Backscattered electron image with locations of the eight spectra; Ae – aegirine, Bio – biotite, Zr - zircon. (c) Half core sample from which the thin section was derived. (d) Mineral spectrum for pyroxene. (e) Mineral spectrum for mica/biotite. (f) Mineral spectrum for zircon. . 86

Figure 5-15. SEM data for sample E2213B (SPA015 at a depth of c. 30m) for Sequence 5, facies c, Shantumbu. (a) Thin section showing Points 1 to 5. (b) Backscattered electron image with locations of the eleven spectra; Ae – aegirine, Qtz – quartz, Pyr - pyrite. (c) Half core sample from which the thin section was derived. (d) Mineral spectrum for quartz. (e) Mineral spectrum for pyrite/pyrrhotite. (f) Mineral spectrum for pyroxene. 87

Figure 5-16. SEM data for sample E2213B (SPA015 at a depth of c. 30m) for Sequence 5, facies c, Shantumbu. (a) Thin section showing Points 1 to 5. (b) Backscattered electron image with locations of the nine spectra; Ap – apatite, Cal – calcite, Pyx - pyroxene. (c) Half core sample from which the thin section was derived. (d) Mineral spectrum for calcite. (e) Mineral spectrum for zircon. (f) Mineral spectrum for pyroxene. (g) Mineral spectrum for apatite. 88

Figure 5-17. SEM data for sample E2213B (SPA015 at a depth of c. 30m), for Sequence 5, facies c, Shantumbu. (a) Thin section showing Points 1 to 5. (b) Backscattered electron image with locations of the nine spectra

Gar – garnet, Cal – calcite, Zr - zircon, and Alb - albite. (c) Half core sample from which the thin section was derived. (d) Mineral spectrum for garnet. (e) Mineral spectrum for zircon. (f) Mineral spectrum for biotite. (g) Mineral spectrum for albite. 89

Figure 5-18. SEM data for sample E2213C (SPA015 at a depth of c. 30m), for Sequence 5, facies c, Shantumbu. (a) Thin section showing Points 1 to 4. (b) Backscattered electron image with locations of the eight spectra. (c) Half core sample from which the thin section was derived. (d) Mineral spectrum for zircon. (e) Mineral spectrum for omphacite/pyroxene/hedenbergite/augite. (f) Mineral spectrum for calcite inclusion in omphacite/pyroxene/hedenbergite/augite. (g) Mineral spectrum for iron-rich mica. OMP – omphacite.. 90

Figure 5-19. SEM data for sample E2213C (SPA015 at a depth of c. 30m), Sequence 5 facies c, Shantumbu. (a) Thin section showing Points 1 to 4. (b) Backscattered electron image with locations of the eleven spectra. (c) Half core sample from which the thin section was derived. (d) Mineral spectrum for garnet. (e) Mineral spectrum for aegirine-augite. Gar – garnet; Cal – calcite; Ae – aegirine. 91

Figure 5-20. SEM data for sample E2213D. SPA015 at a depth of c. 30m, Sequence 5 facies c, Shantumbu. (a) Backscattered electron image with locations of the eight spectra. (b) Mineral spectrum for calcite. (c) Mineral spectrum for aegirine/augite. Alb – albite; Ae – aegirine; Bio – biotite. 92

Figure 5-21. SEM data for sample E2213D (SPA015), Sequence 5 facies c, Shantumbu. (a) Backscattered electron image with locations of the five spectra. (b) Mineral spectrum for barite. (c) Mineral spectrum for aegirine/augite. Bar – barite; Ae – aegirine. 92

Figure 5-22. SEM data for sample E2213D (SPA015 at a depth of c. 30m), Sequence 5, facies c, Shantumbu. (a) Backscattered electron image with locations of the seven spectra. (b) Mineral spectrum for garnet. (c) Mineral spectrum for zircon. Ga – garnet; Ae – aegirine. 93

Figure 5-23. SEM data for sample E2213D, Sequence 5, facies c, Shantumbu. (a) Backscattered electron image with locations of the ten spectra. (b) Mineral spectrum for pyrite/pyrrhotite. (c) Mineral spectrum for ankerite. Ap – apatite; Ank – ankerite; Pyr – pyrite. 93

Figure 5-24. SEM data for sample E2213D (SPA015 at a depth of c. 30m), Sequence 5, facies c, Shantumbu. (a) Backscattered electron image with locations of the ten spectra. (b) Mineral spectrum for hornblende. (c) Mineral spectrum for aegirine-augite. Cal – calcite; Hrn – hornblende. 94

Figure 5-25. Granoblastic mosaic texture of the arenite in Sequence 6, Shantumbu, illustration of core from drill hole SPA027. 95

Figure 5-26. Pervasive goethite alteration within brecciated arenite of Sequence 6 Shantumbu, core sample (SPA018; drill core size is NQ). 95

Figure 5-27. Coarse-grained sodalite pervasive through the brecciated arenite of Sequence 6, Shantumbu core sample (SPA018; drill core size is BQ; depth at c. 312m). 96

Figure 5-28. Alteration types and minerals within arenite of Sequence 6, Shantumbu. (a) Microcrystalline quartz. Sample E2240 plane polarised light (200µm) (SPQ002 c. 270m depth). (b) Microcrystalline quartz. Sample E2240 cross polarised light (200µm) (SPQ002c. 270m depth). (c) Undulose extinction within quartz grains; plane polarised light. Sample 2212 plane polarised light (200µm) (SPA015). (d) Undulose extinction within quartz grains; cross polarised light. Sample E2212 cross polarised light (200µm) (SPA015). (e) Brecciated

arenite core sample of Sequence 6. Sample E2240 (SPQ002 at c. 270m depth). (f) Sphene within recrystallised quartz; plane polarised light. Sample E2205 plane polarised light (100µm) (SPA015. c. 90m depth). (g) Sphene within recrystallised quartz; cross polarised light. Sample E2205 cross polarised light (100µm) (SPA015c. 90m depth). (h) Altered feldspar and albite twinning; plane polarised light. Sample E2215A plane polarised light (200µm) (SPA015 at c. 160m depth). (i) Alteration products albite, orthoclase, and biotite; cross polarised light. Sample E2215A cross polarised light (200µm) (SPA015 at c. 160m depth). (j) Albitisation; cross polarised light. Sample E2205 plane polarised light (200µm) (SPA015 at c. 90m depth). (k) Albitisation; cross polarised light. Sample E2205 cross polarised light (200µm) (SPA015 at c. 90m depth). (l) Pervasive iron oxide alteration of arenite within Sequence 6; core sample. Sample 2232 (SPQ002 SPA015 at c. 245m depth). (m) Sample E2243 plane polarised light (200µm) (SPA027c. 350m depth). (n) Sample E2243 cross polarised light (200µm) (SPA027 c. 350m depth). 97

Figure 5-29. The chessboard twining of albite (upper right corner) and presence of clinopyroxene are indicative of sodic alteration within Sequence 6, Shantumbu. Thin section is cross-polarised light of Sample E2243B from SPA027 at a depth of c. 370m. 98

Figure 5-30. Alteration types and minerals within siltstones of Sequence 6, Shantumbu. (a) Foliation within rhythmite; elongated biotite grains with interstitial quartz and calcite and glaucophane. Preferred orientation of subhedral quartz and glaucophane grains in arenite layer adjacent to siltstone layer; plane polarised light. Sample E2243 plane polarised light (200µm) (SPA027 at a depth of c. 346m). (b) Foliation within rhythmite; elongated biotite grains with interstitial quartz and calcite and glaucophane. Preferred orientation of subhedral quartz and glaucophane grains in arenite layer adjacent to siltstone layer; cross polarised light. Sample E2243 cross polarised light (200µm) (SPA027 at a depth of c. 346m). (c) Clinopyroxene, feldspar, microcline, and biotite alteration minerals within siltstone; plane polarised light. Sample E2243 plane polarised light (200µm) (SPA027 at a depth of c. 346m). (d) Clinopyroxene, feldspar, microcline, and biotite alteration minerals within siltstone; cross polarised light. Sample E2243 cross polarised light (200µm) (SPA027 at a depth of c. 346m). (e) Hematite laths along grain boundaries between feldspar and quartz; plane polarised light. Sample E2207 cross polarised light (200µm) (SPA015). (f) Hematite laths along grain boundaries between feldspar and quartz; cross polarised light. Sample E2207 cross polarised light (SPA015 at a depth of c. 90m). (h) Siltstone and quartz-glaucophane lamination; core sample. Sample position for a and b indicated on sample. Sample E2243 (SPA027 at a depth of c. 346m). (g) Siltstone and quartz-glaucophane lamination; core sample. Sample E2207 (SPA015 at a depth of c. 90m). 99

Figure 5-31. Siltstone layers made up of biotite and aegirine, displaying tight folding (a and b) Sequence 7, Shantumbu. 100

Figure 5-32. Irregular annealed and sutured grain boundaries of quartz grains; Sequence 7, Shantumbu. (a), (c) and (e) Illustrations in plane polarised light. (b), (d), and (f) Illustrations in cross polarised light. (g) Blue-white carbonate of Sequence 7; core sample. Sample E2239 (SPQ002 at a depth of c. 40m). (h). White carbonate of Sequence 7; core sample. Sample E2238 (SPQ002 at a depth of c. 40m). (a) Sample E2238 plane polarised light (200µm) (SPQ002 at a depth of c. 40m). (b) Sample E2238 cross polarised light (200µm)

(SPQ002 at a depth of c. 40m). (c) Sample E2231 plane polarised light (200µm) (SPQ002 at a depth of c. 220m). (d) Sample E2231 cross polarised light (200µm) (SPQ002 at a depth of c. 220m). (e) Sample E2227A plane polarised light (200µm) (SPQ002 at a depth of c. 110m). (f) Sample E2227A cross polarised light (200µm) (SPQ002 at a depth of c. 110m). 101

Figure 5-33. Alteration processes identified in Sequence 7, Shantumbu. (a) Rounded sphene crystals, relict amphibole, strained and recrystallised calcite; plane polarised light. Sample E2227B plane polarised light (200µm) (SPQ002 at a depth of c. 110m). (b) Rounded sphene crystals, relict amphibole, strained and recrystallised calcite; plane polarised light. Sample E2227B cross polarised light (200µm) (SPQ002 at a depth of c. 110m). (c) Relict amphibole, alteration to goethite, and sulphides replacing epidote; plane polarised light. Sample E2227C plane polarised light (200µm) (SPQ002 at a depth of c. 110m). (d) Relict amphibole, alteration to goethite, and sulphides replacing epidote; cross polarised light. Sample E2227C cross polarised light (200µm) (SPQ002 at a depth of c. 110m). (e) Sphene microlets accompanied by calcite, quartz, and deformed epidote; plane polarised light. Sample E2238 plane polarised light (200µm) (SPQ002 at a depth of c. 40m). (f) Sphene microlets accompanied by calcite, quartz, and deformed epidote; cross polarised light. Sample E2238 cross polarised light (200µm) (SPQ002 at a depth of c. 40m). (g) Sub-hederal epidote grains with matrix of calcite, quartz, and plagioclase; plane polarised light. Sample E2230 plane polarised light (200µm) (SPQ002 at a depth of c. 200m). (h) Sub-hederal epidote grains with matrix of calcite, quartz, and plagioclase; cross polarised light. Sample E2230 cross polarised light (200µm) (SPQ002 at a depth of c. 200m). (i). Sericite/muscovite within a matrix of calcite, quartz, and plagioclase. Disseminated sulphides within matrix; plane polarised light. Sample E2239A plane polarised light (200µm) (SPQ002 at a depth of c. 40m). (j) Sericite/muscovite within a matrix of calcite, quartz and plagioclase. Disseminated sulphides also within a matrix; cross polarised light. Sample E2239A cross polarised light (200µm) (SPQ002 at a depth of c. 40m). (k) Sub-hederal epidote grains with a matrix of calcite, quartz, and plagioclase; plane polarised light. Sample E2239A plane polarised light (200µm) (SPQ002 at a depth of c. 40m). (l) Sub-hederal epidote grains with a matrix of calcite, quartz, and plagioclase. Albitisation present; cross polarised light. Sample E2239A cross polarised light (200µm) (SPQ002 at a depth of c. 40m). 103

Figure 5-34. Pervasive iron oxidation, Sequence 7, Shantumbu. (a) Goethite interstitial to calcite, sericite/muscovite, and quartz; plane polarised light. Sample E2231A plane polarised light (200µm) (SPQ002 at a depth of c. 220m). (b) Goethite interstitial to calcite, sericite/muscovite, and quartz; cross polarised light. Sample E2231A cross polarised light (200µm) (SPQ002 at a depth of c. 220m). (c) Goethite layer in core sample. Sample E2231 (SPQ002 at a depth of c. 220m)..... 104

Figure 5-35. Sulphide mineralisation in Sequence 7 carbonates, Shantumbu. (a) Disseminated and rounded sulphide (pyrite) within matrix of muscovite and quartz; plane polarised light. Sample E2231A plane polarised light (200µm) (SPQ002 at a depth of c. 220m). (b) Disseminated and rounded sulphide (pyrite) within matrix of muscovite and quartz; cross polarised light. Sample E2231A cross polarised light (200µm) (SPQ002 at a depth of c. 220m). (c) Disseminated and rounded sulphide (pyrite) within matrix of muscovite and quartz; plane polarised light. Sample E2227B plane polarised light (200µm) (SPQ002 at a depth of c. 110m). (d) Disseminated and rounded sulphide within matrix of muscovite and quartz; cross polarised light.

Sample E2227B cross polarised light (200µm) (SPQ002 at a depth of c. 110m). (e) Core sample of blue carbonate with disseminated sulphides. Sample E2227of drill hole (SPQ002 at a depth of c. 110m). 105

Figure 5-36. Veining within carbonates of Sequence 7 at a depth of c. 185m, Shantumbu. (a) Macroscopic calcite grains filling vein; core sample. (b) Pervasive goethite filled vein; core sample SPQ002 (c. 189.5m). 106

Figure 5-37. Layer parallel vein set at Shantumbu. (a) Layer parallel and irregular veins. (b) K-feldspar and quartz-bearing vein layer parallel with host siltstone (E2241 in SPQ002 at a depth of 344m). 106

Figure 5-38. Types of veins at Shantumbu. (a) Tension gash vein in Siltstones of Sequence 6 (SPA015 Tray 24 c. 92m). (b) Sharp vein-host rock contacts and progressive alteration away from vein. 107

Figure 5-39. Area of dolomitisation and the seepage mechanism responsible for the development of the dolomitisation observed in Sequences 1 and 2, Shantumbu (After, Kendall, 1978, p143). 111

Figure 5-40. Stability of aegirine with NaCl molar quantity, temperature, and pressure. The plot indicates with increasing pressure, the temperature at which aegirine forms is lowered (Likhoydov 1981). 114

Figure 6-1. Outcrop of fine-grained arkose hosting malachite mineralisation at Copper Hill, Shantumbu. 120

Figure 6-2. Copper-bearing sulphide veins and quartz-plagioclase-muscovite-bearing veins with accessory hematite ± malachite ± goethite, Shantumbu. (a) Rims of chalcopyrite and hematite on sulphides. (b) Chalcocite rim of a chalcopyrite grain (H08294 from PSH001 at a depth of 36.24m). (c) Vein-hosted copper-sulphides within arenite of Sequence 1 (H08300 from PSH001A at a depth of 43.42m). All images in plane polarised reflected light. 120

Figure 6-3. Vein hosted and disseminated chalcopyrite, digenite, chalcocite, covellite and pyrite of Sequence 2, Shantumbu. (a) Alteration of chalcopyrite to covellite and chalcocite (H08293 from PSH001 at a depth of 80.4m). (b) Alteration of chalcopyrite to digenite and goethite (H08293 from PSH001 at a depth of 80.4m). (c) Pyrite vein and disseminated pyrite (H08292 from PSH008 at a depth of 52m). All images in plane polarised reflected light. 120

Figure 6-4. Native copper within the calc-silicates of the marine transgression zone from sample H08304 from PSH008 at a depth of 109.20m, Sequence 3/4, Shantumbu. Image in plane polarised reflected light. 121

Figure 6-5. Anhedral to subhedral copper sulphides hosted by brecciated siltstones of facies 5b, Sequence 5, Shantumbu. (a) to (f) Disseminated chalcopyrite and pyrite within matrix of calcite and biotite. All illustrations in cross polarised light. (a) Sample E2257B plane polarised reflected light (200µm). (b) Sample E2257B plane polarised reflected light (100µm) (PSH003 at a depth of c. 165m). (c) Sample E2257BA plane polarised reflected light (100µm) (PSH003 at a depth of c. 165m). (d) Sample E2270A (200µm) (PSH003 at a depth of c. 175m). (e) Sample E2257B plane polarised reflected light (200µm) (PSH003 at a depth of c. 165m). (f) Sample E2257B plane polarised reflected light (200µm) (PSH003 at a depth of c. 165m). (g) Sample E2257 (PSH003 at a depth of c. 165m). 122

Figure 6-6. Cubic pyrite within veins whilst chalcopyrite is for the most part disseminated in the quartz and biotite host rock in Sequence 5, Shantumbu. (a) Cubic pyrite within vein hosted in calcite; plane polarised reflected light. Sample E2257A (200µm) (PSH003). (b) Cubic pyrite within vein hosted in calcite; Sample E2257A plane polarised reflected light (200µm) (PSH003 at a depth of c. 165m). (c) Sulphide bearing vein; Sample E2257A plane polarised reflected light (200µm at a depth of c. 165m) (PSH003). (d) Sulphide-bearing

vein; Sample E2257A plane polarised reflected light (200µm) (PSH003 at a depth of c. 165m). (e) Sulphide bearing vein; plane polarised reflected light. Sample E2257 plane polarised light (PSH003 at a depth of c. 165m). (f) Sulphide-bearing vein; plane polarised reflected light. Sample E2258 plane polarised reflected light (100µm) (PSH003 at a depth of c. 165m). (g) and (h) Core samples of brecciated siltstone of Sequence 5. (g) Sample E2257A (100µm) (PSH003 at a depth of c. 165m). (h) Sample E2258 (PSH003 at a depth of c. 165m)..... 123

Figure 6-7. Sulphides within Sequence 5, facies b, Shantumbu. (a) Post-brecciation veins composed of anhedral pyrite, pyrrhotite and chalcopyrite (H08292 from PSH008 at a depth of 52m). Sulphide grains (H08292 from PSH008 at a depth of 52m) both within veins and the matrix of the breccia, as shown in (b) and (c) (H08295 from PSH007 at a depth of 136.47m). All illustrations are in plane polarised reflected light. 124

Figure 6-8. Sulphides are hosted by both siltstone and carbonate layers in Sequence 6, Shantumbu; quarter core sample. (a) Large anhedral sulphides grains within carbonate (E2192 from SPA014). (b) Fine-grained sulphide within siltstone; core sample. 124

Figure 6-9. Cubic pyrite within siltstone and carbonate layers of Sequence 6, Shantumbu. Chalcopyrite (Ccp) is sub-hederal to anhedral (a to c). All images in plane polarised reflected light. (a) Sample E2215B (200µm) (SPA015 at a depth of c. 160m). (b) Sample E2268 (200µm) (SPA015 at a depth of c. 175m). (c) Sample E2268 (100µm) (SPA015 at a depth of c. 175m). 124

Figure 6-10. Lithologies of Sequence 7, Shantumbu. (a) Finely laminated grey-blue carbonate of Sequence 7 (SPQ002). (b) Hematite grains within laminations of Sequence 7. (c) Pyrite grains within the grey-blue carbonate in Sequence 7 (SPQ001). 125

Figure 6-11. Locations of several known copper and gold occurrences within the Chongwe Copperbelt, indicating the location of Shantumbu, Mpande Dome, Mulofwe Dome, Allies Mine, Tanta Wunda Chibukama, Tasaru, Chumbwe and several other known copper and gold occurrences (Modified after, Zambezi Resources, 2007)..... 130

Figure 7-1. The ICP-OES dataset for MgO (%) versus Al_2O_3 (%) shows the dolomitic carbonate dataset for Sequence 4 is offset from the calcitic carbonates of Sequence 5, Shantumbu..... 137

Figure 7-2. A scatterplot of the ICP-OES data for MnO (%) versus Al_2O_3 (%) for the dolomitic carbonate of Sequence 4 and the calcitic Sequence 5 (Pelito-Arkosic Member) carbonates, Shantumbu. The plot illustrates that the dolomites are clearly segregated from the remaining carbonates, which were deposited under oxic conditions. 138

Figure 7-3. MnO (%) versus Al_2O_3 (%) for the debris flow deposits of Sequence 2 contrasted with the arenites and arkoses from Sequence 2 (Kafue Arenite Member), Shantumbu. The behaviour of Mn is segregated from the remaining detrital units of Sequence 2. ICP-OES data is presented..... 138

Figure 7-4. MgO (%) versus Al_2O_3 (%) for the debris flows deposits of Sequence 2 contrasted with the arenites and arkoses from Sequence 2 (Kafue Arenite Member), Shantumbu. The behaviour of Mg is segregated from the remaining detrital units of Sequence 2. ICP-OES data is presented..... 139

Figure 7-5. Scatterplot illustrating the alteration of the carbonates on Shantumbu. ICP-OES. (a) K_2O (%) versus Al_2O_3 (%) of the dolomite of Sequence 4 (Copperbelt Orebody Member), contrasted with the calcitic

carbonates of Sequence 5. (b) Na_2O (%) versus Al_2O_3 (%) of the dolomite of Sequence 4, contrasted with the calcitic carbonates of Sequence 5 (Pelito-Arkosic and Chambishi members). The term 'Clean Carbonate' refers to monolithic carbonate rock without argillite interlayers. 140

Figure 7-6. Scatterplot of the ICP-OES dataset illustrating the alteration of the detrital metasediments on Shantumbu. (a) K_2O (%) versus Al_2O_3 (%) of the Sequence 2 (Kafue Arenite Member) debris flows, contrasted with the arenite and arkoses of Sequences 1, 2, 4, and 5. (b) Na_2O (%) versus Al_2O_3 (%) of the Sequence 2 debris flows deposits, contrasted with the arenite and arkoses of Sequences 1, 2, 4, and 5. 142

Figure 7-7. Scatterplot of the ICP-OES data illustrating K_2O versus Al_2O_3 per sequence, Shantumbu. (a) Scatterplot illustrating K_2O (%) versus Al_2O_3 (%) of the Sequences 1, 2, 4 and 5. (b) Scatterplot illustrating Na_2O (%) versus Al_2O_3 (%) of the Sequences 1, 2, 4 and 5. 143

Figure 7-8. Scatterplot of the ICP-OES data for K_2O versus Sc per sequence (a) Sc (ppm) versus K_2O (%) for the dolomitic carbonate of Sequence 4 contrasted with the calcitic carbonates, Shantumbu. The dolomitic carbonate points are segregated from the remaining carbonates. (b) Sc (ppm) versus K_2O (%) for the arkose and arenite units versus the debris flows of Sequence 2; Sequence 1 values are coloured separately. ... 144

Figure 7-9. Scatterplot of the ICP-OES data for Fe_2O_3 (%) versus Al_2O_3 (%) for Sequences 1, 2, 4 and 5, Shantumbu. (a) Fe_2O_3 versus Al_2O_3 for the debris flow of Sequence 2 versus the arenites of Sequences 1, 2, 4 and 5. (b) Fe_2O_3 versus Al_2O_3 for the dolomitic carbonate of Sequence 4 on Shantumbu contrasted with the remaining carbonates. The dolomitic carbonate formed a tight grouping of values in comparison to the calcitic carbonates, perhaps because of less analyses. The calcitic carbonates reflect Sequence 5. 146

Figure 7-10. Box and whisker and log probability plots for Fe (%) within the Sequences 1 to 7 on Shantumbu. The plot represents the portable XRF dataset. The dotted red outlines illustrate the grouping of similar Fe contents of Sequences 1 to 4, and a separate grouping for Sequences 5 and 6. The probability plot is cut at 90% probability for illustration purposes. 147

Figure 7-11. ICP-OES Fe_2O_3 values (%) for Sequences 1, 2 and 5 versus Al_2O_3, an immobile oxide, Shantumbu. 148

Figure 7-12. Scatterplot of the ICP-OES dataset for Ti (%) versus Al_2O_3 (%) for the detrital metasediments of Sequences 1, 2, 4 and 5, Shantumbu. 149

Figure 7-13. Box and whisker and log probability plots for Ti (%) within the Mindola, Kitwe and Kirilabombwe formations equivalents?? on Shantumbu. Portable XRF dataset presented. The dotted red outlines illustrate the onset of marine conditions and sediment starvation. The probability plot is cut at 90% probability for illustration purposes. The box and whisker plots for Sequences 1, 2, 5 and 6 show similar trends and variability of Ti. 149

Figure 7-14. Box and whisker and log probability plots for Mn (%) within the Mindola, Kitwe and Kirilabombwe formations equivalent on Shantumbu. Portable XRF dataset presented. The probability plot is cut at 90% probability for illustration purposes. The box and whisker plots demonstrate distinctive trends for the terrestrial versus marine sequences. (a) The box and whisker plots for Sequences 1 to 4 which represent sediments deposited in terrestrial to shallow water environments. (b) The box and whisker plots for Sequences 5 and 6, which were deposited under subaqueous conditions. 151

Figure 7-15. ICP-OES Sr values (ppm) for Sequences 1, 2 and 5 against Al_2O_3, an immobile oxide, Shantumbu. 152

Figure 7-16. Box and whisker and log probability plots for Sr (%) within the Mindola (Sequence 1 and 2), Kitwe (Sequences 3 to 6) and Kirilabombwe (Sequence 7) formations on Shantumbu. Portable XRF data is plotted. The probability plot is cut at 90% probability for illustration purposes. The box and whisker plots show distinctive trends for the terrestrial versus marine sequences. (a) The box and whisker plots for Sequences 1 to 2 reflect terrestrial sediments. (b) The box and whisker plots for Sequences 3 and 4 reflect marine transgression environments. (c) The box and whisker plots for Sequences 5 and 6 reflect marine depositional environments. (d) The box and whisker plots for Sequence 7 reflects a closed marine depositional environment. 152

Figure 7-17. Scatterplot of K_2O versus Al_2O_3 per sequence. ICP-OES data, Shantumbu. (a) Scatterplot illustrating K_2O (%) versus Al_2O_3 (%) of the Sequences 1, 2, 4 and 5. (b) Scatterplot illustrating Na_2O (%) versus Al_2O_3 (%) of the Sequences 1, 2, 4 and 5. 154

Figure 7-18. ICP-OES Ba values (ppm) for Sequences 1, 2 and 5 against K_2O, a mobile oxide, Shantumbu. 155

Figure 7-19. Positive correlation (48%) between K and Ba (%) for the ICP-OES dataset; all Sequences are combined into a single plot, Shantumbu. 155

Figure 7-20. Positive correlation (33%) between K and Fe (%) for the ICP-OES dataset; all Sequences are combined into a single plot, Shantumbu. 156

Figure 7-21. ICP-OES Ba values (ppm) for Sequences 1, 2 and 5 against Al_2O_3, an immobile oxide, Shantumbu. 156

Figure 7-22. Correlation plot of ICP-OES data for Rb versus K in Sequences 1 and 2, Shantumbu. 157

Figure 7-23. Correlation plot of ICP-OES data for V (ppm) in Sequences 1, 2 and 5 against Al_2O_3 (%), Shantumbu. 158

Figure 7-24. ICP-OES V values (ppm) for Sequences 1, 2 and 5 against Al_2O_3 (%), an immobile oxide, Shantumbu. 159

Figure 7-25. ICP-OES V values (ppm) for Sequences 1, 2 and 5 against Al_2O_3 (%), an immobile oxide, Shantumbu. Three outlier samples were top cut due to the bias incurred. 159

Figure 7-26. Log probability plot for the portable XRF copper readings for each Sequence individually, Shantumbu. Sequence 5 is the combination of 5a, 5b and 5c. 160

Figure 7-27. ICP-OES copper values (%) for Sequences 1, 2, and 5 against Al_2O_3, an immobile oxide, Shantumbu. 161

Figure 7-28. Box and whisker and log probability plot for copper (%) within sequences 1 to 7 on Shantumbu. Portable XRF dataset presented. The probability plot is cut at 90% probability for illustration purposes. (a) The box and whisker plots demonstrate distinctive trends with Sequences 1 and 2 being the highest grade. (b) The box and whisker plots for Sequences 6 and 7 are markedly lower than the remaining sequences. 161

Figure 7-29. ICP-OES copper values (%) for Sequences 1, 2 and 5 against Al_2O_3, an immobile oxide, Shantumbu. 162

Figure 7-30. ICP-OES dataset for Sequences 1, 2 and 5 a to c illustrating S (ppm) against Al_2O_3 (%), Shantumbu. 163

Figure 7-31. ICP-OES dataset for Sequences 1, 2 and 5 a to c illustrating S (ppm) against copper (ppm), Shantumbu. 163

Figure 7-32. Box and whisker and log probability plots for Co (%) within sequences 1 to 7. Portable XRF dataset presented. The probability plot is cut at 90% probability for illustration purposes. (a) Co displays the greatest range in C values in Sequences 3 and 4. (b) as well as in Sequence 6. 164

Figure 7-33. ICP-OES Co values (%) for Sequences 1, 2 and 5 against Al_2O_3, an immobile oxide, Shantumbu. . 165

Figure 7-34. ICP-OES Zn values (ppm) for Sequences 1, 2 and 5 against Al_2O_3, an immobile oxide, Shantumbu. The two populations are noted by the inserts. 166

Figure 8-1. Schematic cross sections of sedimentary basins, placing the Shantumbu Basin in context of the two types of basins reported by Hitzman *et al*. (2010). (A). Cross section of an intracratonic rift basin with a basal red-bed sequence and overlying siliciclastic, carbonate, and evaporite sediments. Basinal fluids in this system are trapped by confining basement and lateral sediment pinch-outs. (B). Cross section of a passive margin basin with a thin rift sequence overlain by continental siliciclastic sediments (sandstones and siltstones) that grade seaward into evaporates and then carbonates. The carbonate sediments prograde seaward and overlap deeper water carbonates. This carbonate-rich sequence is covered by deltaic to slope basin siliciclastic sediments (sandstones, siltstones, and shales). Basinal fluids in this system are able to escape from the sedimentary sequence vertically and laterally, the rift-basin at Shantumbu may be an example of this type, although further structural work would be required to verify. (Source: Hitzman *et al*., 2010, p633). 180

Figure 8-2. Lithostratigraphic column for the Roan Group in the Zambian Copperbelt with the authors interpretation of the position of Sequences 1 to 7 at Shantumbu (modified from, Selley *et al*., 2005). ... 189

Figure 8-3. The location of the Katanga Basin, Mwembeshi Zone, Zambian and the Congolese Copperbelts, with the proposed southerly extent of the Katanga Supergroup to Shantumbu, from this study (Source: Zientek *et al*., 2014). 189

Figure 8-4. Remnant organic cast, possibly of a plant or root within brecciated arenite of Sequence 6, Shantumbu. Cast composed of biotite and aegirine. The overlying strata included fine siltstone laminations and brecciated arenite pervasively altered by goethite. The arenite consists of albite, plagioclase, amphibole, calcite, quartz and goethite. Drill core is from SPA015 at a depth of c. 177m. 198

Figure 8-5. Regional basement and sedimentary geology at and around Shantumbu. The tectonic contact of the Lusaka Dolomite Formation and the Katanga Supergroup is illustrated. The continuation of the platform-shelf carbonates and the terrestrial siliciclastic sediments on either side of the Mwembeshi Zone and south to the Shantumbu /Mpande Dome (MP) area is evident, and these areas have been assigned to the Katanga Supergroup (Porada and Berhorst, 2000). Fm = Formation. 'X' denotes locality of Shantumbu. 203

LIST OF TABLES

Table 1-1. Drill holes available for lithostratigraphic interpretation of Shantumbu, southern Zambia. 7

Table 2-1. Basement and Katanga supergroups stratigraphic division of Smith (1964). 12

Table 2-2. Basement and Katanga supergroups stratigraphic division of Mallick (1966). 12

Table 2-3. Katanga Supergroup stratigraphic nomenclature of the Zambian Copperbelt. After, Clemmey (1976), Porada and Berhorst (2000), Selley *et al*. (2005), Cailteux *et al*. (2007), and Kampunzu *et al*. (2009). 20

Table 4-1. The Kafue Arenite Member at the Nkana-Mindola Mine in the Zambian Copperbelt. The primary lithologies and depositional environments are summarised (Croaker, 2011). 56

Table 4-2. Katanga Supergroup stratigraphy present at Shantumbu relating the seven sequences identified in the drill cores with the equivalent Formation and Member of the Roan Group. 66

Table 5-1. Stratigraphy of Shantumbu summarising the principal lithologies and depositional environment for each Sequence. 68

Table 7-1. V/Cr (ICP-OES) per lithology for Sequences 1, 2, 3 and 5, Shantumbu. ICP-OES analyses not undertaken for Sequence 6 and 7. 158

Table 7-2. Trace element abundances (ppm) of the upper continental crust (Hu and Gao, 2008) versus arithmetic averages (ppm) for Sequences 1, 2, 5 (a) to (c) for Cu ≥0.1% at Shantumbu. 167

Table 7-3. V/Cr ratio of the Mpande Gneiss and Granite - V/Cr ratios (Source: Katongo *et al*., 2004). 172

Table 7-4. Geochemical composition of the Munali Hills Granite – V/Cr ratios (Source: Katongo *et al*., 2004). 172

Table 7-5. V/Cr (ICP-OES) per lithology for Sequences 1, 2, 3 and 5, Shantumbu. ICP-OES analyses not undertaken for Sequence 6 and 7. 172

Table 8-1. Depositional environments on Shantumbu during the development of the Neoproterozoic rift basin. 188

Table 8-2. Comparison of the geological features of the Kupferschiefer, Shantumbu and Zambian Copperbelt sediment-hosted, stratiform copper deposits. 205

CHAPTER 1

INTRODUCTION

1.1 INTRODUCTION

Prospecting conducted from 2013 to 2015, identified rift-related metasediments on the northern flank of the Mpande Dome in southern Zambia, which resembled the metasediments of the Roan Group, of the Katanga Supergroup in the Central African Copperbelt. The metasediments are prospective for sediment-hosted, stratiform copper mineralisation.

The most complete descriptions of the lithostratigraphy for the Mpande Dome area prior to the 2013 to 2015 exploration were conducted by Simpson *et al*. (1963), Smith (1964) and Mallick (1966), which concentrated on the metasediments and metavolcanics on the southern flank of the Mpande Dome. Smith (1964) and Mallick (1966) classified the metasediments as the Chunga and Cheta groups (Smith, 1964) or the Shamazio, Kafue and Cheta groups (Mallick, 1966), of the Katanga Supergroup. Porada and Berhorst (2000) proposed a correlation of the stratigraphy with the Roan Group of the Katanga Supergroup in the Zambian Copperbelt.

For many decades, the lack of outcrop, outdated geological information and the complex deformation and metamorphism history of the area impeded prospecting, which targeted Zambian Copperbelt-style copper-cobalt mineralisation. Several questions arose during the recent exploration as to Group and Formations, and the tectonic system to assign to the Shantumbu area, highlighting that a fresh examination of the metasediments was needed.

1.2 LOCALITY OF SHANTUMBU

Shantumbu is approximately 30km south - southeast of Lusaka, Zambia, (Figure 1-1) on the northern flank of the Mpande Dome, which is a granitic gneissic basement dome surrounded by foliated and non-foliated coarse-grained gneisses (Figure 1-1). Shantumbu is situated at the junction of the Pan African Zambezi Belt, the Lufilian Arc and Irumide Belt coalesce (Figure 1-1), on the southern side of the Mwembeshi Zone. The Mwembeshi Zone, a north northeast – south southwest trending shear zone, separates the Zambezi Belt and the Lufilian Arc (Porada and Berhorst, 2000; Naydenov *et al*., 2014).

The Mpande Dome is proximal to the failed triple junction of the colinear Mid-Zambezi and Luangwa Rift zones with the Lower Zambezi Rift Zone (Mallick, 1966; Oesterlen and Blenkinsop,

1994). The Mid-Zambezi Rift is a southwest-northeast trending asymmetrical rift zone (Reimann, 1986), and the Luangwa Rift (eastern Zambia) is an extension of the East African Rift Valley system, specifically the Ruaha Rift (Oesterlen and Blenkinsop, 1994; Bailey and Woolley, 2005).

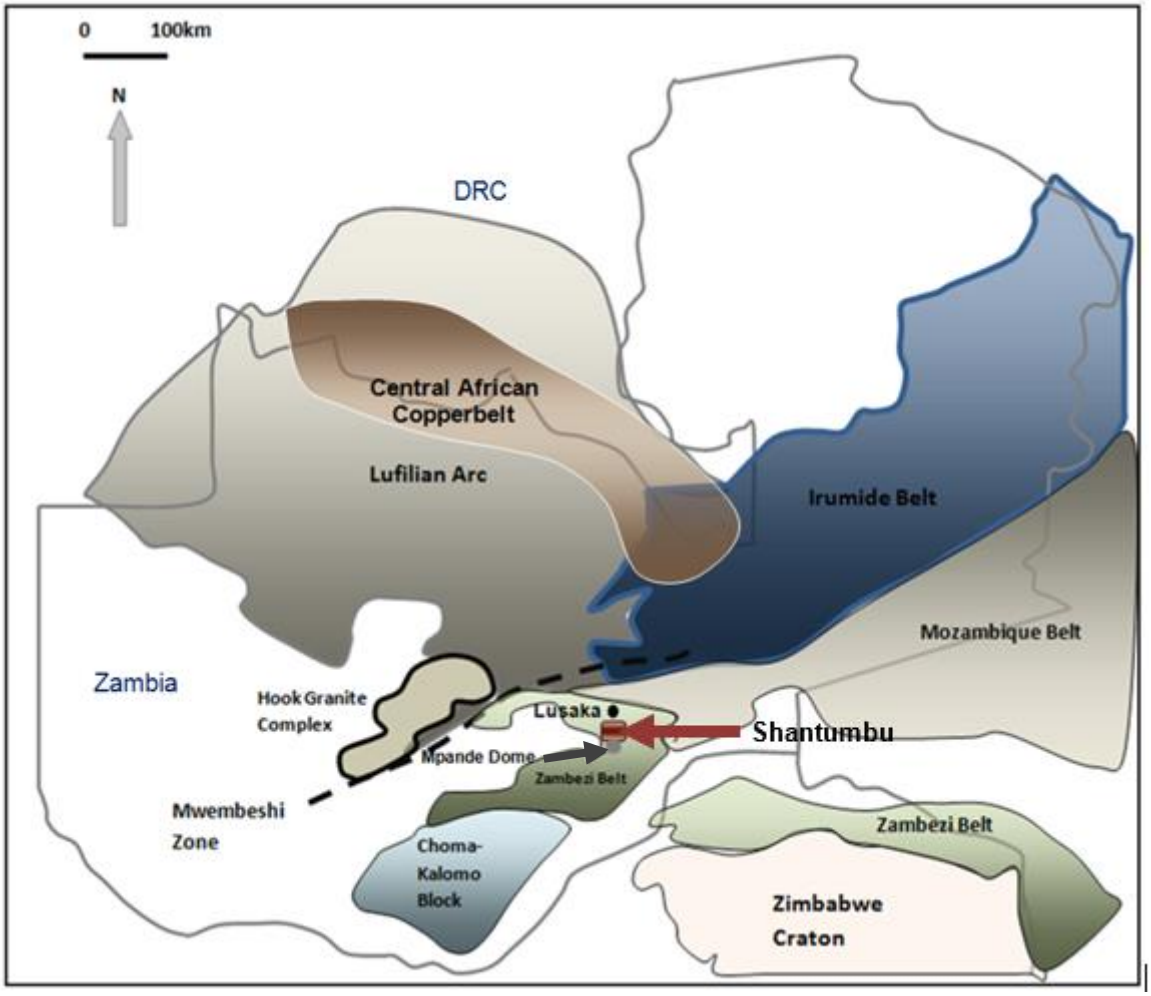

Figure 1-1. Schematic sketch of the main tectonic provinces of northern Zimbabwe, Zambia, Mozambique, and southern DRC. The locations of Shantumbu, the Central African Copperbelt, Lufilian Arc, Irumide, Mozambique and Zambezi Belts. (Modified from Unrug, 1983; Porada, 1989; Kröner, 2004).

1.3 GEOLOGICAL SETTING OF SHANTUMBU

Shantumbu flanks the world's largest sediment-hosted, stratiform copper-cobalt province, the Central African Copperbelt, which is an arcuate belt of rift basin metasediments assigned to the Katanga Supergroup (Zientek *et al.*, 2014). The Central African Copperbelt is a continuous geological feature and is often referred to in two parts, the Zambian Copperbelt in northern Zambia, and the Congolese Copperbelt in the southern part of the Democratic Republic of Congo (DRC). The Neoproterozoic rift-related sedimentary basins developed on the margin of the Congo Craton during the breakup of Rodinia (Figure 1-2 and Figure 1-3), the Katanga Supergroup basins being examples thereof and collectively referred to as the Katanga Basin System. The

Katanga Supergroup rift-related metavolcanics and metasediments were deposited during passive continental extension c. 880 Ma (Hanson *et al*., 1994; Selley *et al*., 2005; Johnson *et al*., 2007) and the Supergroup extended from the southern region of the DRC, southwards towards the Kafue Region, in southern Zambia.

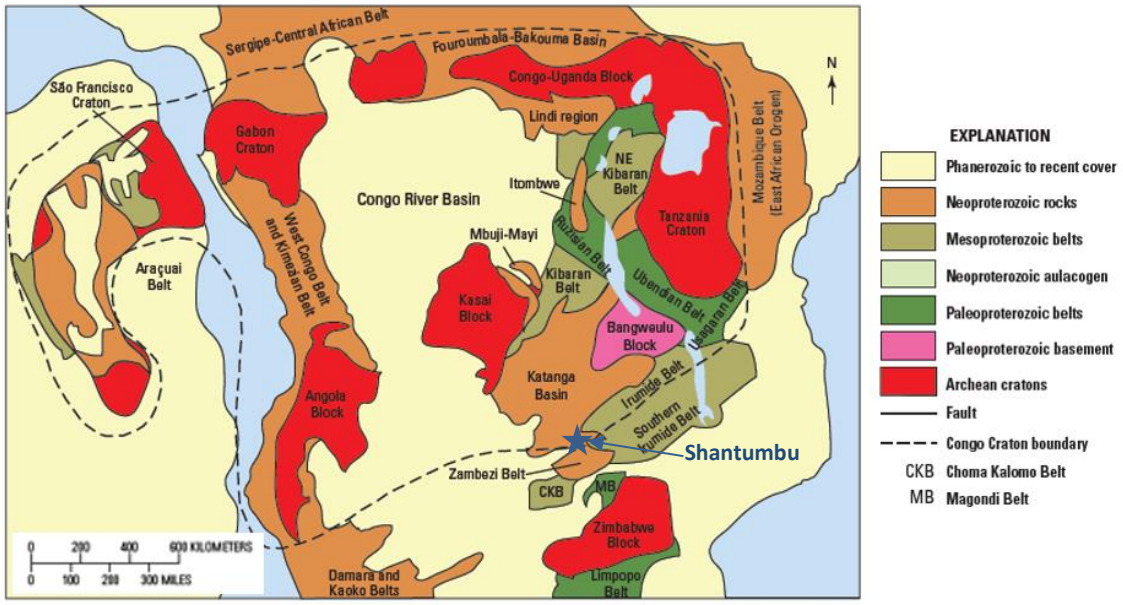

Figure 1-2. Simplified map of the Neoproterozoic geological setting during the breakup of Rodinia. The rift basins were closely related to the margins of the Congo Craton. The location of the Katanga Basin is shown and the proximity of Shantumbu. (Zientek *et al*., 2014, and references therein).

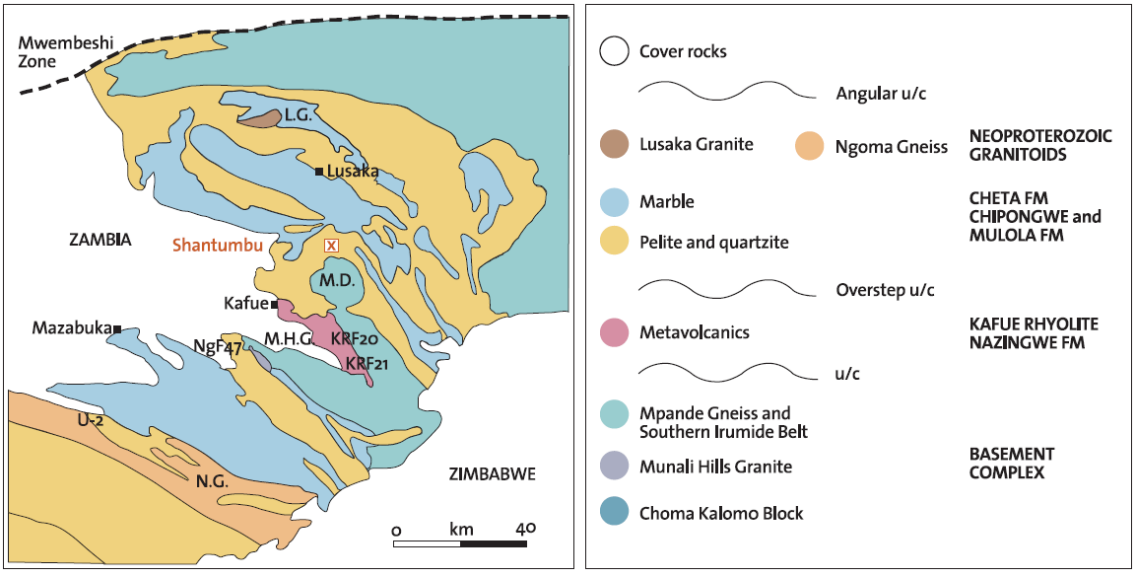

Figure 1-3. Location of Shantumbu (noted with 'x' above Mpande Dome) and the town of Kafue in relation to the Lufilian Arc, Zambezi Belt and Basement, the Mwembeshi Zone, and the Mpande Dome (M.D.). (Modified after Johnson *et al*., 2007).

The Mwembeshi Zone separates the Katanga Basin System in the north, which hosts the Central African Copperbelt, from the Zambezi Belt in the south of Zambia. There is no conclusive evidence to support the southerly side of the Mwembeshi Zone, including Shantumbu, was disconnected during the Neoproterozoic rift basin development from the rift basins within the Central African Copperbelt.

The rift sediments of the Katanga Basin are floored by basement granites and gneisses. Mpande Granite and Gneiss outcrop at Shantumbu and represent a basement anticline related to orogenic event/s prior to rift extension in the Neoproterozoic, known as the Mpande Dome. Further doming of the Mpande Dome Basement occurred during the Pan African Orogeny (Porada and Berhorst, 2000). The Mpande Gneiss has been age dated at 1,106 ± 19 Ma (Johnson *et al*., 2007) and the overlying synrift bimodal volcanic rocks, the Kafue Rhyolite and Nazingwe formations, have been age dated at 879 ± 19 Ma (Hanson *et al*., 1994; Selley *et al*., 2005; Johnson *et al*., 2007). The metasediments overlying the Kafue Rhyolite and Nazingwe formations have not been age dated.

The metasediments of Shantumbu strike west-east and oblique to the regional strike of northwest-southeast and are highly deformed and often overturned. The notable difference between the Shantumbu area and north of the Mwembeshi Zone is the higher metamorphic grade around Shantumbu, that of amphibolite grade metamorphism, compared the predominantly greenschist facies metamorphism of the areas north of the Mwembeshi Zone (De Waele *et al*., 2008).

The recent exploration at Shantumbu identified the metasediments as characteristic of rift-related lithologies similar to the metasediments of the Roan Group in the Katanga Basin System. The metasediments on Shantumbu commence with arkoses, siltstones and breccias which host iron and copper sulphides, and are superimposed onto the granitic Basement and rift-related volcanic units. The siliciclastic sediments were deposited during a period of extensional rift tectonics, with the deposition having been terminated by a marine transgression related to rift climax followed by a period of gradual subsidence and tectonic stability.

The Kafue Rhyolite and Nazingwe metavolcanics were not intersected in the drilling, presumed to be the result of the drill holes been terminated prior to intersecting the floor of Sequence 1, in the drill holes of the upright stratigraphy. The assumption is the Kafue Rhyolite and Nazingwe formations underlie Sequence 1, as relict rhyolite vesicles were noted in the Sequence 1 mineralogy examination.

1.4 MOTIVATION

The stratigraphy and copper mineralisation on Shantumbu have noticeable similarities with the Roan Group and copper-cobalt mineralisation within the Zambian Copperbelt, which prompted research into the correlation, or otherwise, of the Shantumbu metasediments with the metasediments of the Roan Group stratigraphy and the sediment-hosted, stratiform copper mineralisation of the Zambian Copperbelt. The Zambian Copperbelt, which extends for approximately 700km from the Copperbelt Province northwards to the border with the Democratic Republic of Congo (DRC), has a width of roughly 40km and hosts the world-class sedimentary-hosted copper-cobalt metallotect, which has been worked for copper since its recorded discovery in 1895 by European explorers (Fraser, 2010).

An alternative stratigraphic classification of metasedimentary rocks at Shantumbu to that assigned in the 1960s' by Smith (1964) and Mallick (1966), is investigated based on the new lithostratigraphic, geochemical, alteration, mineralisation and metamorphic information available from the recent diamond drilling completed across the Shantumbu License.

The southerly limit of the rift system responsible for the Roan Group in the Zambian Copperbelt, has not been conclusively shown in southern Zambia, that is beyond the Mwembeshi Zone. Little is known of rift basin architecture or extent of the Katanga Supergroup on the southern side of the Mwembeshi Zone, and as such, Shantumbu may represent the southerly limit of the Roan Group, of the Katanga Supergroup.

The stratigraphic subdivisions of Roan, Nguba and Kundelungu groups have been extensively applied in the Zambian Copperbelt but not used in the area south of the Mwembeshi Zone. Smith (1964) and Mallick (1966) proposed the stratigraphy for this southerly area belonged to the Chunga and Cheta groups (Smith, 1964) or the Shamazio to Cheta groups (Mallick, 1966) of the Katanga Supergroup.

The recent exploration activities indicate the application of the Zambian Copperbelt stratigraphy to the Shantumbu area required further research to determine if this southern area belongs with the Katanga Basin system, or a rift basin system further south along the margins of the Congo Craton and Kalahari Craton.

1.5 AIMS AND OBJECTIVES

The aim of the study was to examine the metasedimentary stratigraphy and copper mineralisation at Shantumbu and provide validation, or otherwise, that the area represented

the southerly extent of the Roan Group which is present in the Zambian Copperbelt. The examination of the stratigraphy and the copper mineralisation aimed to assist future exploration for copper and cobalt mineralisation south of the Mwembeshi Zone and to further the understanding as to which rifting event was responsible for the metasediments around the Mpande Dome. The objective was to present similarities and variations of the lithostratigraphy and copper mineralisation at Shantumbu to that of the Roan Group in the Zambian Copperbelt.

During the 2013 to 2015 exploration, twenty-two diamond drill holes were completed. Detailed logging, petrographic studies, mineralogy and geochemical analysis were conducted on the drill cores. Portable X-Ray Fluorescence (XRF) readings, optical microscopy, Inductively Coupled Plasma Optical Emission Spectrometry (ICP-OES) analyses of selected samples and scanning electron microprobe (SEM) analyses, together with examination of past and present literature, and earlier geological models, were undertaken.

1.6 RESEARCH METHODOLOGY

Cores from twenty-two diamond drill holes were examined and geological information was further gathered from the exploration activities carried out by the owners of the Prospecting License under the management of this author during the 2013 to 2015 exploration programme. The activities included:

- Geological field mapping – lithological and structural (2014) in selected areas;
- Remote sensing imagery processing (2014);
- Diamond core drilling (2013 and 2014) – twenty-two drill holes;
- Portable XRF analyses of core (2014);
- Quantitative Four Acid Digestion multi-element analyses (ICP-OES) completed on core samples by InterTek Genalysis (2014);
- Petrography and mineralogical studies by SGS South Africa (2014);
- Mineralogical studies by the author at the University of the Witwatersrand; and
- SEM analysis of selected samples.

The drill holes on Shantumbu were drilled at an inclination of 60° to intersect the metasediments at 90° as far as possible. Two drill holes were drilled vertically (SPA008 and SPA025). The diamond drill holes used in the study are presented in Table 1-1.

Table 1-1. Drill holes available for lithostratigraphic interpretation of Shantumbu, southern Zambia.

Shantumbu Diamond Drill Holes	
Southern Half of Shantumbu	**Northern Half of Shantumbu**
PSH001, PSH001A, PSH007, PSH008, PSH009, SPA005, SPA010, SPA011	SPQ001, SPQ002, SPA013, SPA015, SPA016, SPA018, SPA015, SPA022, SPA026B, SPA027, SPA029, SPA030, SPA033, SPA033A

Geological logging of the drill core concentrated on lithology, mineralogy and alteration features. Where possible, reference surfaces, or lithological datum/s, were identified in the drill core for stratigraphic correlation between drill holes. Geochemical data (major and minor elements) were compared to the lithological logs, to corroborate, or otherwise, the stratigraphic interpretation, identification of significant discontinuities, and depositional environments.

The mineralogical and petrographic studies concentrated on the mineralogy, textures, habits, mineral associations and alteration to understand the petrogenesis of the metasediments, the style of the copper mineralisation, and the metamorphic facies of the metasediments. Both transmitted and reflected optical microscopy was undertaken by SGS South Africa and was expanded upon by the author, with additional transmitted and reflected optical microscopy undertaken at the Geosciences Department, University of the Witwatersrand.

Geochemical analyses of selected intersections from the diamond drill core were gathered through:

- Four acid ICP-OES digestion which targeted Al, As, Bi, Sb, Ca, K, Mg, Na, Fe, Pb, Cu, Co, Ag, Sr, As, Mn, Zn, Co, Ni and Mo; and
- Portable XRF readings.

1.7 CONCLUSION

The stratigraphy, mineralogy, alteration, structure and metamorphism of the metasedimentary rocks at Shantumbu have not been researched in detail in the last 60 years, resulting in the economic potential of the metasediments at Shantumbu being poorly understood, and the area not attracting prospecting activities to any significant extent.

The information presented in this thesis challenges the stratigraphic classification assigned by Smith (1964) and Mallick (1966). An alternative stratigraphic classification is presented which indicates the southerly extent of the Zambian Copperbelt extended south of Lusaka to the Mpande Dome area. Evidence from Shantumbu is presented for sediment-hosted, stratiform

copper mineralisation. This has a significant impact on the exploration for copper and cobalt mineralisation in southern Zambia.

Chapters 2 to 7 progresses from a description of the Roan Group of the Katanga Supergroup, and the Pan African orogenesis, to the lithostratigraphy, structural setting and deformation at Shantumbu. Very limited mineralogical and petrographic studies of the metasedimentary units in the Shantumbu area had been conducted prior to this study, consequently these were examined by the inspection of hand specimens and thin sections.

Interpretations of the lithologies and mineralisation together with the conclusions and recommendations completed the research.

CHAPTER 2

STRATIGRAPHIC SETTING OF SHANTUMBU AND THE ROAN GROUP

2.1 INTRODUCTION

The metasediments and metavolcanics south of the Mwembeshi Zone, including the metasediments at Shantumbu, are assigned to the Katanga Supergroup. The metasedimentary rocks at Shantumbu were last investigated in detail between the 1930 to the 1960s'. Smith (1964) assigned the metasediments to the Chunga and Cheta groups whilst Mallick (1966) assigned the metasediments to the Shamazio, Kafue and Cheta groups.

Lithological logging of the drill cores identified seven metasedimentary sequences at Shantumbu. In the context of this study the term 'sequence' denotes an interrelated lithostratigraphic succession which stood for a specific depositional environment. Where it was possible to further subdivide a sequence into smaller units, these were termed facies.

Sequence 1 is the oldest and basal succession intersected during the drilling campaign. Only two drill holes intersected Sequence 1 and based on these two intercepts Sequence 1 progresses upwards from the iron-rich arenite, to a grey quartzose arenite which is capped by a fine-grained grey arenite and two siltstone layers with an arenite middling (Figure 2-1a). The overlying succession, Sequence 2, is a thick, massive to finely laminated dark grey arenite with subordinate siltstone beds which is overlain by mottled pink and grey arenite (Figure 2-1b).

The mottled arenite unit is also host to both siltstone and carbonate layers (Figure 2-1c and d). The siltstone has a variable carbonaceous content and alternates between black and grey colouration. The arenites give way to the laterally extensive dolomitic carbonate unit (Figure 2-1e) of Sequence 3.

Following the first appearance of dolomitic carbonate, a thick siliciclastic unit is interlayered with carbonate units and formed Sequence 4. This unit is overlain by a package of gritty to clean carbonate, carbonate and siltstone units, and carbonate-siltstone rhythmites (Figure 2-1f to h) making up Sequence 5. The siltstone units contained evaporitic characteristics.

The overlying strata to the rhythmites (Figure 2-1i) is a succession of alternating arenite-carbonate-siltstone of Sequence 6. Sequence 6 consists of cyclic successions of feldspathic arenite and subordinate carbonate and siltstone layers and bears many similarities to Sequence 5. The principal difference is the decrease in volume of carbonate layers and increase in the number of feldspathic arenite layers. An increase in volume of carbonate layers in the underlying Sequence 5 corresponds with a decrease in volume of brecciated siltstone within Sequence 6.

The youngest succession, Sequence 7 (Figure 2-1j), is dominated by a thick succession of grey-blue, finely laminated calcitic carbonate lacking the rhythmic banding of the underlying sequences. Fine siltstone laminations and thin fine-gained arenites are present, in most cases less than five centimetres in thickness.

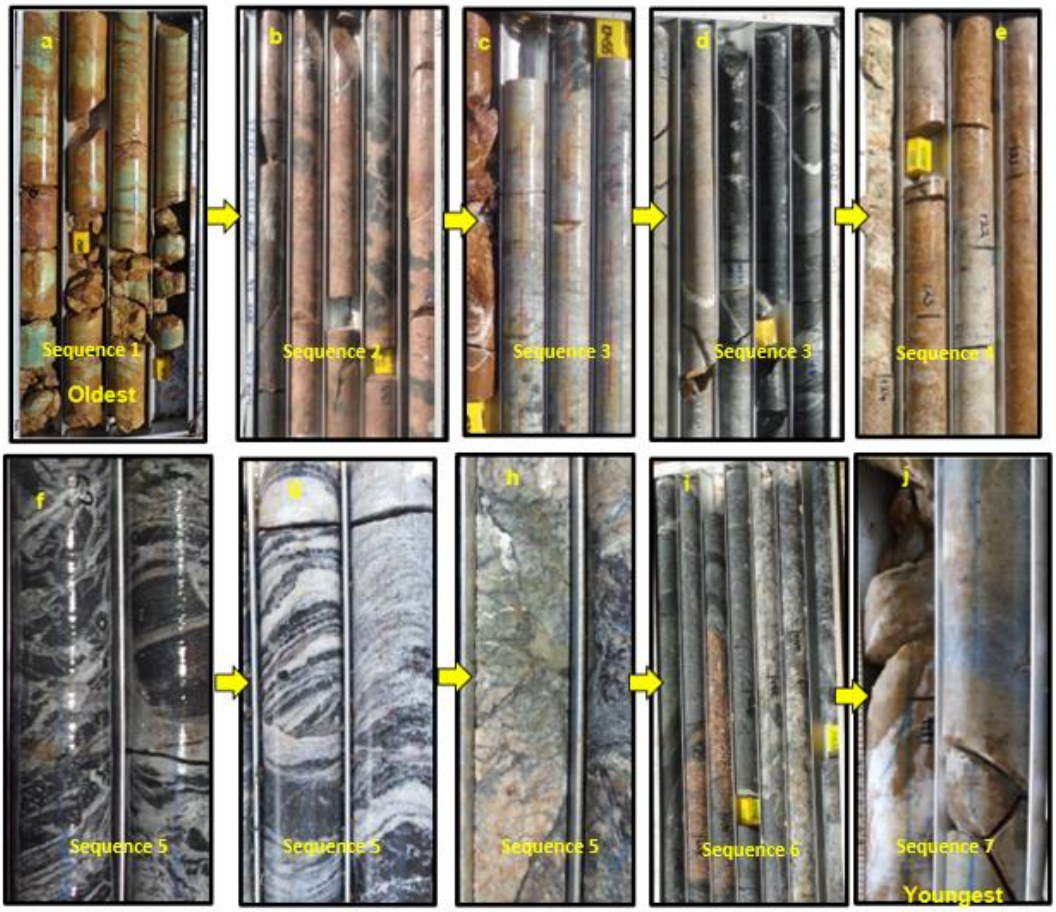

Figure 2-1. The seven sequences and related metasediments intersected in the Shantumbu drill cores. (a) The fine-grained arkose of Sequence 1 is the oldest unit intersected in the drilling and is host to copper mineralisation. (b) Red, cream and grey arenite of Sequence 2. (c) Dolomite calc-silicate of Sequence 3. (d) Siltstone and grey carbonate of Sequence 3. (e) Iron oxide-rich calc-silicate of Sequence 4. (f) Siltstone carbonate breccia of Sequence 5. (g) Siltstone carbonate rhythmite of Sequence 5. (h) Brecciated arenite of Sequence 5. (i) Goethite-rich carbonate and arenite of Sequence 6. (j) Finely laminated grey-blue to yellow-brown carbonate of the youngest succession, Sequence 7.

2.2 LITERATURE REVIEW

Smith (1964) and Mallick (1966) described the succession of metavolcanics and metasediments along the southern margin of the Mpande Dome. Both authors described the presence of underlying rhyolitic units which were overlain by altered fine-grained muscovite-bearing quartzite and quartz-muscovite schists intercalated with minor acid and mafic volcanic rocks and rhyolite (Mallick, 1966). The quartzites and schists were in turn overlain by pelitic to semi-pelitic schist and subordinate marble. The topmost succession was composed of fine- to coarse-grained banded calcitic and dolomitic marble intercalated with scapolite- and sphene-bearing schist. The succession of arkosic to carbonate units in the diamond drill core supported the metasedimentary succession documented by Smith (1964) and Mallick (1966).

Simpson *et al*. (1963) correlated the Chunga and Cheta formations to the Lower and Upper Roan Group respectively. Moore (1964) assigned the Cheta Group of Smith (1964) to a Formation termed the Kangomba Formation, Roan Group (Porada and Berhorst, 2000).

Porada and Berhorst (2000) presented a classification whereby the volcanic and sedimentary rocks of the lower clastic units of the Mulola to Chipongwe formations were grouped into the Chunga Group and assigned to the Mesoproterozoic Basement. Above the Chunga Group, the stratigraphy was assigned to the Cheta Group (Porada and Berhorst, 2000; Johnson *et al*., 2007).

Stratigraphy of Smith (1964) and Mallick (1966)

Smith (1964) (Table 2-1) assigned the Kafue Rhyolite and the Nazingwe formations to the Basement stratigraphy whilst Mallick (1966) assigned the metavolcanics to the Shamazio Group of the Katanga Supergroup (Table 2-2). Mallick (1966) assigned the stratigraphy to the Katanga System, starting at the base with the Kafue Rhyolite Formation, followed by the Mulola Formation, the Schist-Marble Formation, and the Chipongwe Semipelite Formation of the Kafue (Chunga) Group respectively. The Mampompo Limestone Formation (Cheta Group) formed the topmost stratigraphic unit.

Table 2-1. Basement and Katanga supergroups stratigraphic division of Smith (1964).

Supergroup	Group	Formation/Member
Katanga	-	Lusaka Dolomite Formation
	Cheta	Chilanga Psammite Member
		Mampompo Limestone Member
	Chunga	Chipongwe Psammite *
		Funswe Pelite *
		Mulola Formation
Basement	-	Nazingwe Formation
		Kafue Rhyolite Formation
		Mpande Gneiss

* Smith (1964) did not provide a Formation or Member term to these units

Table 2-2. Basement and Katanga supergroups stratigraphic division of Mallick (1966).

Supergroup	Group	Formation
Mpande Granites **		
Katanga	Cheta	Mampompo Limestone
	Kafue	Chipongwe Semipelitic
		Schist-Marble
		Mulola
	Shamazio	Nazingwe
		Kafue Rhyolite
Basement	Mpande Gneiss**	

** Mallick (1966) did not provide a Formation or Member term to these units

Kafue Rhyolite and Nazingwe formations

The Kafue Rhyolite Formation on the southern margin of the Mpande Dome consists of bimodal volcanics (basalt and rhyolite). To the north of the Mpande Dome, surface exposure of the Kafue Rhyolite Formation is absent and the Shantumbu drilling was not to a depth which intersected the metavolcanics.

The Kafue Rhyolite Formation was regarded by Mallick (1966) as the earliest member of the Katanga Supergroup in the Zambezi Belt and assigned the metavolcanics to the Shamazio Group. In contrast, Smith (1964) classified the two metavolcanics as part of the Basement stratigraphy.

The volcaniclastics rocks of the Kafue Rhyolite and Nazingwe formations were age dated at c. 880 Ma, which corresponds to the age of the Nchanga Granite, the youngest of the pre-Katanga intrusions in the Basement of the Zambian Copperbelt (Johnson *et al*., 2007).

The contact between the Basement and the Kafue Rhyolite Formation is not well understood due to lack of outcrop. Based on whole-rock Nd isotope signatures, that the Kafue Rhyolite and Nazingwe formations formed from assimilation and recycling of Basement Gneiss, with the

recycling having denoted the start of crustal thinning and extension (Johnson *et al*., 2007). Johnson *et al*. (2007) proposed intracrustal melting resulted from a rise in geothermal gradients concurrent with crustal thinning or juvenile mafic magmas within the lower crust leading to partial melting and crustal assimilation.

Alteration of the rhyolite varies around the southern margin of the Mpande Dome from strongly sheared leptite (feldspathic rhyolite) to isolated lenses of unaltered rhyolite. Quartzites intercalated with rhyolite are volumetrically greater higher up in the stratigraphy. Near the top of the Kafue Rhyolite Formation, Mallick (1966) noted several 30cm to 5m thick layers of semipelitic schist.

The Kafue Rhyolite Formation grades into a 500m-thick altered Nazingwe Formation. The Nazingwe Formation comprises quartz-muscovite schists and fine-grained muscovite quartzites intercalated with minor acid (now feldspar-free muscovite-rich schists) and mafic volcanic rocks and rhyolite metamorphosed to amphibolites and biotite-chlorite schists (Mallick, 1966). A 5m-thick rhyodacite tuff was noted by Johnson *et al*. (2007) within the Nazingwe Formation. No recognisable break between the rhyolite and overlying sedimentary rocks was noted by Smith (1964) or Mallick (1966).

The presence of chalcopyrite and bornite randomly distributed in the Kafue Rhyolite Formation was noted by Johnson *et al*. (2007) during age dating of the volcanic units. The copper-bearing minerals accounted for 1 - 2% of the whole rock volume (Johnson *et al*., 2007).

Kafue Group

Mallick (1966) subdivided the Kafue Group into the Mulola Formation at the base overlain by the Schist-Marble Formation (Table 2-2). The Chipongwe Semipelitic Formation capped the Kafue Group. The transition from fluvial to marine depositional environments represented the break between the Kafue Group and the overlying Cheta Group. Smith (1964) assigned the formations to the Chunga Group (Table 2-1).

The Mulola Formation

The Mulola Formation unconformably overlies the Kafue Rhyolite and Nazingwe formations. The polymictic conglomerate at the base of the Mulola Formation is overlain by kyanite-bearing biotite-rich schist and semipelitic units of the Chipongwe Formation. The Chipongwe Formation is overlain by monotonous dolomitic marble of the Cheta Formation (Smith, 1964; Mallick, 1966).

Mallick (1966) noted the basal Mulola Formation included two major quartzite and two phyllite-schists however, rapid facies variations characterised the lithostratigraphy around the Mpande Dome. The basal conglomerate is undeformed and contained rhyolite clasts, amongst other lithologies. The Mulola Formation exhibited current-bedded, foliated psammite and lenses composed of carbonates, quartz and sericite (Smith, 1964).

Johnson *et al*. (2007) proposed the rhyolite clasts implied that the Mulola Formation rested on the Kafue and Nazingwe formations as an erosional overstep contact rather than a tectonic contact. Johnson *et al*. (2007) further noted the Kafue Rhyolite Formation graded upward into a conglomerate sequence hosting amongst other lithologies granitic pebbles, indicating the Kafue Rhyolite Formation and overlying sedimentary succession formed during Neoproterozoic rifting and did not belong to the Muva Supergroup or Basement successions. The proportion of clasts present within the polymictic conglomeratic sequence progressively decreased upward grading into tuffaceous schist and then by semipelitic schist intercalated with minor volcanic horizons (Johnson *et al*., 2007).

Mallick (1996) reported that the Mulola Formation progressively overstepped the underlying formations and non-conformably overlay the Basement to the north of the town of Kafue. Mallick (1966) reported the quartzite was white and sericitic, while the Mulola Formation above the Kafue Rhyolite Formation was commonly goethite-stained and contained conglomerates. The Upper Quartzite Member was a pure quartzite.

Metamorphic grades around the Mpande Dome differed which resulted in variations within the Mulola Formation, from banded and graded siltstone-quartzite affected by low grade metamorphism, to quartz-muscovite-biotite schists which experienced higher grades of metamorphism (Mallick, 1966).

The transition from the Mulola Formation to the overlying Schist-Marble Formation was marked by the evolution from a dominantly fluviatile environment related to rift initiation to a supra- and intertidal siliciclastic-carbonate and fluvial-deltaic conditions during rift climax (Mallick, 1966).

The Schist-Marble Formation

The Schist-Marble Formation comprises pelitic to semi-pelitic schist and subordinate marble. The transition from the Schist-Marble to the Chipongwe Formation was related to the decrease in volume of the marbles and a concomitant increase in the siliciclastic units in the Chipongwe

Formation. The schist hosted brown to green magnesium biotite, kyanite, quartz, muscovite, chlorite, tremolite, hornblende and iron minerals (Smith, 1964; Mallick, 1966).

The Chipongwe Formation

The Chipongwe Formation which overlies the Schist-Marble Formation is comprised of semi-pelitic schist, subordinate pelitic schist and muscovite and biotite-bearing siltstone. White muscovite schist and thin beds of fine-grained feldspathic quartzite and graphitic mica schist form a minor part (Mallick, 1966).

Cheta Group

The Cheta Group was deposited in a platform environment during rift climax and cessation. Mallick (1966) assigned a single formation to the Cheta Group, the Mampompo Limestone Formation whilst Smith (1964) assigned the carbonates to the Mampompo Limestone and the Chilanga Psammite members to the Cheta Group.

The relationship with the Lusaka Dolomite Formation, within the classifications of both Smith (1964) and Mallick (1966), to the Cheta Group is not well described in the literature. Johnson *et al*. (2007) indicated the Lusaka Dolomite Formation formed appreciably later than the rift-related deposition of the lower portions of the Katanga Supergroup containing the Kafue and Cheta groups.

Mampompo Limestone Formation

The Mampompo Limestone Formation overlies the Chipongwe Formation and where highly variable fine- to coarse-grained banded calcitic and dolomitic marble is intercalated with scapolite- and sphene-bearing schist. The marble bands consist of impure carbonate with scapolite, albite, microcline, biotite, muscovite, pyrite, tremolite, accessory iron oxide and quartz (Mallick, 1966; Mitchell *et al*., 1998). Near the base of the formation, local pebble-bearing carbonate layers occur (Smith, 1964).

The Mampompo Limestone Formation developed in a post-rift environment dominated by platform and shelf marine conditions (Porada and Berhorst, 2000).

Gabbros and Mafic Rocks

Numerous erratically oriented isolated blocks of variably metamorphosed gabbros, together with other mafic and ultramafic blocks characterise the Cheta Group (Boni *et al*., 2011). In the

Zambezi Belt, the mafic blocks display mid-oceanic-ridge or N-MORB chemistries and isotopic signatures (De Waele *et al*., 2008, and references therein). These mafic blocks were interpreted as being emplaced as an ophiolitic mélange during deposition of the carbonate units or remnants of oceanic crust tectonically emplaced during Pan African tectonism (De Waele *et al.*, 2008).

Following rifting and deposition of platform sediments, the Lusaka Granite granitoid intrusions were emplaced into the Katanga Supergroup. The composition of the Lusaka Granite is described as metaluminous A-type with crystallisation ages dated at c. 820 Ma (Johnson *et al*., 2007). The deposition of the Katanga Supergroup in the Mpande Dome area was therefore complete by c. 820 Ma, and Johnson *et al*. (2007) indicated there was insufficient evidence to support an age younger than c. 820 Ma.

Granitic Intrusions

Various within-plate-type granitoid bodies, known as the Lusaka Granite, intruded the metasediments within the Lusaka-Kafue area (Johnson *et al*., 2007). The Lusaka Granite age of intrusion is defined at 846 ± 68 Ma (Barr *et al*., 1977). In addition, various metaluminous, monzogranitic plutons in the Munali Hills area, south of Shantumbu, intruded the metasediments and have been dated at 820 ± 7 Ma (Johnson *et al*., 2007).

Lusaka Dolomite Formation

The Lusaka Dolomite Formation was not included in the Katanga Supergroup according to Mallick (1966). Smith (1964) included the Lusaka Dolomite Formation as a standalone Formation not assigned to a Group.

The Lusaka Dolomite Formation is almost entirely composed of massive dolomite. Differentiating the Lusaka Dolomite Formation from the Mampompo Limestone Formation, marble is chiefly on the absence of garnet, scapolite, and biotite within the Lusaka Dolomite Formation. The rare occurrence of calcitic bands within the marble of the Lusaka Dolomite Formation is also characteristic (Porada and Berhorst, 2000).

The Lusaka Dolomite Formation (Figure 2-2) around Shantumbu has not been age dated, and Johnson *et al*. (2007) showed the possibility that the formation is younger than c. 820 Ma. The Lusaka Dolomite Formation was considered by Simpson *et al*. (1963) to correlate with the Lower Kundelunga Group (Porada and Berhorst, 2000).

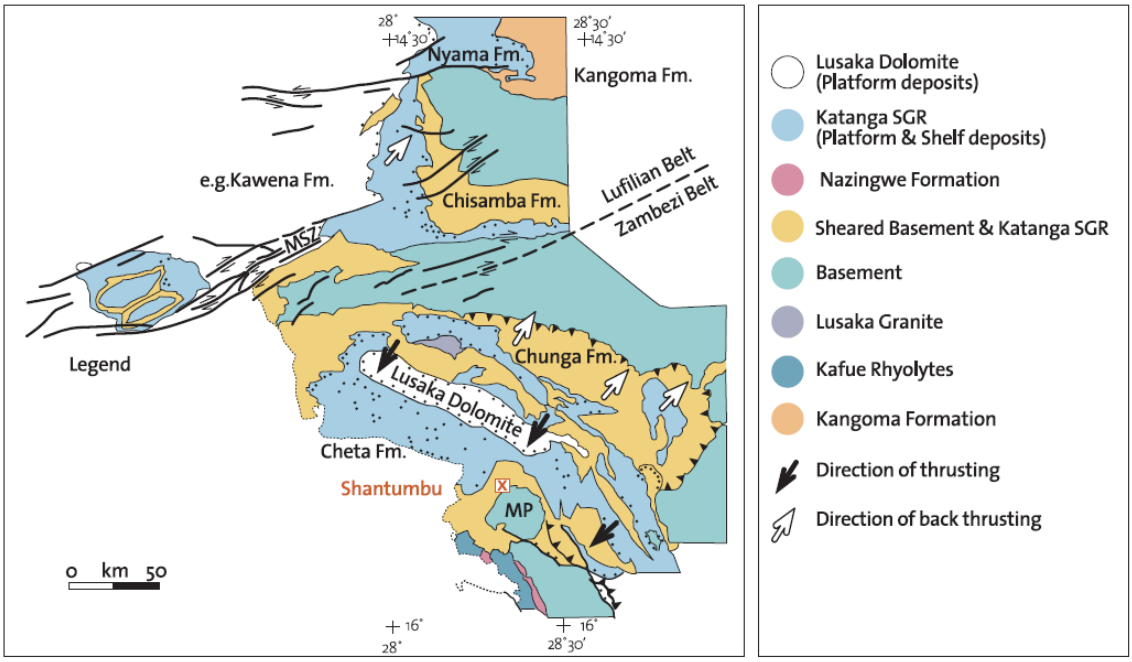

Figure 2-2. Regional basement and sedimentary geology around Shantumbu and south of the Mwembeshi Zone (MSZ) where the relationship between the platform-shelf carbonates and the terrestrial siliciclastic sediments in relation to the Mpande Dome (MP) are illustrated. The tectonic contact of the Lusaka Dolomite Formation and the Katanga Supergroup is illustrated, together with the regional direction of thrusting and back thrusting of the Katanga Supergroup (Porada and Berhorst, 2000). The position of Shantumbu is denoted with a 'X'

Johnson *et al*. (2007) concluded the Lusaka Dolomite Formation present in the Lusaka region formed appreciably later than the underlying Katanga Supergroup terrigenous sediments and that the contact between the Katanga Supergroup and the overlying Lusaka Dolomite Formation could have been a tectonic / thrust contact related to Pan African tectonism. The thrust contact at the base of the Lusaka Dolomite Formation was the highest thrust unit in the region, and the Formation is comparable to the Kabwe Platform Dolomite, which hosts the Kabwe Zn-Pb deposit, north of Lusaka. The correlation of the Lusaka Dolomite Formation to the Nyama Formation and the Nguba Group, as well as the Kirilabombwe Group (Upper Roan Group) was suggested by Barr *et al*. (1977) and Kampunzu *et al*. (2009).

The Nyama Formation is a phyllite-dolomite dominated unit with subordinate slate and mudstone at Kabwe Mine, which is approximately 110km north of Lusaka (Kamona and Friedrich, 2007). The Nyama Formation was correlated with the Nguba Group, with an age range between c. 730 Ma and 635 Ma (Kampunzu *et al*., 2009).

The Lusaka Dolomite Formation was not thrust a considerable distance northward as it rests upon platform deposits of the underlying Mampompo Limestone Formation (Porada and Berhorst, 2000) to the north of Shantumbu. Without age or isotope data for the Lusaka Dolomite

Formation, the relationship, albeit unconformable, to the Mampompo Limestone Formation of the Cheta Group is not well understood.

Basement – the Mpande Dome

The Mpande Granite and Gneisse form the basement to the metavolcanics and metasediments at Shantumbu. The Mpande Dome outcrops as a basement anticline which formed in response to orogenic event/s prior to the Neoproterozoic Rift extension. Further doming of the Mpande Dome followed during the Pan African Orogeny (Porada and Berhorst, 2000).

In the Lusaka Region, post-Katangan intrusion of the Mpande Granite was greatest in the Mpande Dome however, there is insufficient evidence to establish whether uplift of the dome was caused by intrusion of the granites or the granites initiated the doming (Mallick, 1966).

The location of the Mpande Dome is related to a single or multiple pre-Katangan orogenic events (Hanson *et al*., 1994), and is considered to have been uplifted during F_2 folding. F_3 folds were superimposed and form upright, open, and northeast-trending folds (Hanson *et al*., 1994). Deformation imparted a west-northwest trending S_1 foliation that is axial planar to macroscopic, southwest-vergent, overturned to recumbent F_1 folds with sheared limbs, which mirror larger-scale structures (Hanson *et al*., 1994). Hanson *et al*. (1994) noted there was little evidence that recumbent folding occurred south of the town of Kafue.

Between Lusaka and the Mpande Dome, the principal direction of thrust faults was to the north. Back folding and thrust faulting succeeded the initial northward thrust faulting during progressive contraction and is characterised by southward verging folds in Lusaka Dolomite Formation and underlying Cheta Group (Porada and Berhorst, 2000).

The stratigraphy north of the Mpande Dome strikes west-east, oblique to the overall regional strike of northwest southeast (Mallick, 1966) but parallel to the margins of the Mpande Dome. Mallick (1966) advocated that the Katanga Supergroup rocks were refolded on axes parallel to the margins of the Mpande Dome.

2.3 THE ZAMBIAN COPPERBELT STRATIGRAPHY

Numerous complex and deposit specific stratigraphy categorisations exist for the Neoproterozoic metasediments within the Zambian Copperbelt. Table 2-3 summarises the lithostratigraphic profile and depositional environments of the Roan Group in the Zambian Copperbelt gathered from Clemmey (1976), Porada and Berhorst (2000), Selley *et al*. (2005),

Cailteux *et al*. (2007), Kampunzu *et al*. (2009) and Croaker (2011). Table 2-3 forms the framework for comparison of the lithostratigraphy at Shantumbu to the Roan Group.

The Katanga Supergroup overlies the Muva Supergroup units, whilst the Eburnean age (c. 2,000 Ma) Lufubu schists and gneisses are overlain by sedimentary rocks of the Muva Supergroup, which were in turn intruded by the Nchanga Red Granite. The contact between the Basement and the Katanga Supergroup rocks is tectonic, where thrust faults resulted in slices of Basement rocks emplaced into the Lower Katanga Supergroup. The Katanga Supergroup sediments draped over the varying topographic surface caused by the thrusts (Daly *et al.*, 1984), and formed a one to ten kilometres thick succession. The Roan Group at the base of the Katanga Supergroup is overlain by the Mwashia/Nguba and Kundelunga groups (Selley *et al*., 2005; Johnson *et al*., 2007; Hitzman *et al*., 2012).

Roan Group

The Roan Group, of the Katanga Supergroup, is divided into a lower and an upper section, distinguished by differing palaeo-depositional environments. Present day application of stratigraphic names has shifted away from the Lower Roan Group and Upper Roan Group, to the use of a single Group name, the Roan Group. Three formations form the Roan Group; the Mindola (Mindola Clastics Formation of Selley *et al*., 2005), Kitwe and Kirilabombwe formations.

The Roan Group was deposited within half-graben sub-basins where the underlying growth-faults remained active during the deposition of the overlying Kitwe Formation often causing the merging of the initial half-graben rift basin. Master faults exerted a greater control after the deposition of the Copperbelt Orebody Member, of the Kitwe Formation (Selley *et al*., 2005). Maturity of the deposition cycles within the Kitwe Formation resulted in siltstone-mudstone sequences that sealed the underlying master fault arrays. The Mindola Formation lithologies were deposited during rift initiation and the Kitwe Formation was deposited during rift-climax. The Upper Roan Group (using the nomenclature of Selley *et al*. (2005); alternatively, the Kirilabombwe Formation) and the carbonate and siliciclastic rocks of the Mwashia Group, were deposited during the thermal sag phase following the rift climax (Selley *et al*., 2005).

Table 2-3. Katanga Supergroup stratigraphic nomenclature of the Zambian Copperbelt. After, Clemmey (1976), Porada and Berhorst (2000), Selley *et al*. (2005), Cailteux *et al*. (2007), and Kampunzu *et al*. (2009).

Authors	Supergroup	Group	Subgroup	Formation	Member
Clemmey (1976)	Katanga	Upper Roan		Bancroft	
		Lower Roan		Kitwe	Antelope Clastics
					Chambishi Dolomites
					Nchanga Quartzite
					Rokana Evaporites
					Copperbelt Orebody
				Mindola Clastic	Kafue Arenites
					Basal Quartzites
Porada and Berhorst (2000)	Katanga	Upper Kundelungu			
		Lower Kundelungu			
		Mwashia			
		Roan	Bancroft	RU 1 and RU 2	
			Kitwe	RL 3 TO 6	
			Mindola	RL 7	
Selley *et al*. (2005)	Katanga	Lower Kundelungu			
		Mwashia		Upper	
				Middle	
				Lower	
		Upper Roan		Bancroft	
		Lower Roan		Kitwe	Antelope Member
					Chambishi Member
					Nchanga Member
					Rokana Member
					Copperbelt Orebody Member
				Mindola Clastics	Kafue Arenite Member
					Basal Quartzite Member
Cailteux *et al*. (2007); Kampunzu *et al*. (2009)	Katanga	Kundelungu			
		Nguba			
		Roan	Mwashia		
			Kirilabombwe	Bancroft (RU1 and 2)	
				Kibalongo (RL 3)	
			Kitwe	Chingola (RL 4)	
				Pelito-Arkosic (RL 5)	
				Ore Shale (RL 6)	
			Mindola (RL 7)	Mutonda	
				Kafufya	
				Chimfunsi	

The lower portions of the Roan Group include sub-aerial to shallow marine clastic sequences, while the upper portion comprises platform carbonates, breccias (stratiform and discordant) and subordinate siliciclastic rocks. The transition from sub-aerial clastic rocks (rift extension) to platform carbonate rocks (post rift) is represented by the Copperbelt Orebody Member, alternatively known as the Ore Shale Unit. A stratigraphic interval of 200m to the Copperbelt Orebody Member as midpoint, hosts many of the base metal deposits in the Zambian Copperbelt (Hitzman *et al*., 2012).

Mindola Formation

The laterally and vertically variable Mindola Formation includes immature matrix supported conglomerates, breccias, subarkosic sandstones and subordinate siltstones, related to deposition in shallow alluvial fans. Deposition occurred in restricted west- to north-northwest trending isolated asymmetrical sub-basins flanked by Basement highs (Selley *et al*., 2005). The contact between the Mindola Formation arenite and conglomerate with the shale, dolomitic siltstone and siltstone of the overlying Kitwe Formation is sharp (Croaker, 2011).

Although the stratigraphy of the Chambishi Basin on the western margin of the Kafue Anticline is typical of the Zambian Copperbelt, the Mindola Formation comprises two members in the Chambishi Basin, the lowermost Basal Sandstone Member, and the overlaying Kafue Arenite Member (Croaker, 2011). The Basal Sandstone Member is a medium- to coarse-grained fining-upward sequence of arenite with subordinate sandy matrix-supported breccia intervals of variable thickness. Lenses of matrix dominated medium- to coarse-grained conglomerate underlie the arenite and breccias. The conglomerate matrix was variably replaced by anhydrite (Croaker, 2011). Granite, gneiss and quartzite clasts within the basal conglomerate at the Nkana-Mindola Deposit average between 30 to 80cm in the longest dimension (Croaker, 2011).

The Kafue Arenite Member started with a thin (<10m) conglomeratic unit overlain by a 10 - 20m thick package of medium-to coarse-grained sandstone alternating with siltstone and lesser greywacke and quartz-rich layers (Croaker, 2011).

Kitwe Formation

The Kitwe Formation is a laterally and vertically continuous package dominated by cyclical and finely-laminated dolomitic argillite, argillite, carbonaceous shale, evaporites and massive dolomite, with subordinate argillaceous sandstone (Croaker, 2011), deposited following a rift-tectonic dominated period (Selley *et al*., 2005).

The start of the Kitwe Formation is denoted by the Copperbelt Orebody Member, which is overlain by the Pelito-Arkosic Member and finally the Chambishi/Chingola Member. The Antelope Member caps the Kitwe Formation.

Deposition of the Kitwe Formation occurred within synforms floored by Mindola Formation and often ended along the sub-basin perimeters as sandstone and dolomitic facies. The Kitwe Formation incorporates cycles of upward fining clastic sediments followed by carbonate. The conglomerates progressed to sandstones and siltstone, to dolomitic siltstone, to massive carbonate (Selley *et al*., 2005).

The Copperbelt Orebody Member formed in a low energy, restricted marine depositional environment, which was subjected to periodic dry and wet cycles. The unit represented a shallow marine-peritidal depositional environment, for which four facies variations have been documented at the Nkana-Mindola Deposit. The four facies include the Northern facies composed of dolomitic argillite, argillite, fine-grained sandstone and an upper carbonaceous argillite; the Southern facies composed of black carbonaceous shale, argillite and an upper carbonaceous argillite; the Sandstone-argillite facies with an upper carbonaceous argillite, and a massive dolomite facies with upper carbonaceous argillite (Croaker, 2011).

Black carbonaceous shale indicated an organic-rich environment prevailed at the time of deposition of the Roan Group, whilst the sandstone represented input from a fluvial source into the carbonate environment, possibly along the margins of the system (Croaker, 2011). Carbonaceous-poor shale is present within the Copperbelt Orebody. The presence of shale and sandstone denoted either or both a break from replenishing waters, or the deepening of the basin conditions. Preservation of organic carbon and carbonate units with syngenetic to early diagenetic pyrite indicated anoxic conditions during deposition of the Copperbelt Orebody Member (Theron, 2013).

The Copperbelt Orebody Member is locally characterised by evaporitic textures and the upper portion of the Roan Group contains further evaporitic textures. Evaporites formed throughout deposition of the Katanga Supergroup (Hitzman *et al*., 2012). The copper-cobalt mineralisation is commonly hosted by the Copperbelt Orebody Member located below a former evaporite (Hitzman *et al*., 2012). The evaporite situated above the Copperbelt Orebody Member is known as the Rokana Evaporite unit (Pelito-Arkosic Member) and is divided into two units. Firstly, quartzites with interbedded siltstones and silicified dolomites, and secondly, dolomite and laminated to thinly bedded argillite and dolomitic argillite (Croaker, 2011). At the Chambishi

South East (SE) deposit, chicken wire anhydrite texture has been documented, indicating the depositional environment was that of sabkha-type with syn-depositional evaporite development (Croaker, 2011).

The Chambishi (or Chingola) Member started with a thick dolomite and argillite unit succession which is overlain by finely bedded siltstone-mudstone and sandstone units. The Chambishi Member developed in the peritidal environment. The succeeding Antelope Member began with a one-metre-thick dolomitic unit of shale, grit and dolomite. The Kirilabombwe Formation, alternatively known as the Bancroft Formation, in some parts of the Zambian Copperbelt, overlies the Antelope and Chambishi members.

Mwashia Group and Kirilabombwe Formation

The Mwashia Group in the Zambian Copperbelt is a shale-dominated sequence, whereas in the Congolese Copperbelt, the group is a lower dolomitic sequence of polylithic breccias with subordinate volcanic rocks and an upper clastic sequence.

The Kundelunge Group is the upper limit of the Katanga Supergroup and consists of a basal glaciogenic diamictite overlain by carbonate and clastic rocks (Selley *et al*., 2005). The diamictites were not observed at Shantumbu.

The Kundelunge Formation and Mwashia Group are dominated by carbonate strata and upward fining cycles of sandstone, siltstone, dolomite and anhydrite. The thickness of the carbonate strata is variable, hosting polylithic breccia either as single or stacked layers of less than one metre to greater than ten meters. The rounded to angular fragments are cemented by a matrix of carbonate, albite, quartz, anhydrite and chlorite (Selley *et al*., 2005).

Due to the lack of base metal mineralisation in the Kirilabombwe Formation and Mwashia Group, these successions have attracted considerably less research in comparison to the copper endowed Kitwe and Mindola formations.

2.4 DISCUSSION

The detrital and chemical metasediments at Shantumbu have several characteristics comparable to those of the Roan Group in the Zambian Copperbelt. The lack of detailed lithological and petrographic studies of the metasediments south of Lusaka and the continued use of the lithostratigraphy nomenclature assigned in the 1960s', has detracted the area from

receiving significant exploration for copper-cobalt mineralisation akin to that in the Zambian Copperbelt.

The Formation and Group terminology for the Katanga Supergroup in the Lusaka Region by Smith (1964) and Mallick (1966), have persisted to present day. The connection between the rift-related rocks south of Lusaka with the stratigraphy of the Katanga Supergroup of the Zambian Copperbelt was introduced by Simpson *et al*. (1963), Smith (1964), De Swardt and Drysdall (1964), Mallick (1966), Porada and Berhorst (2000), and Johnson *et al*. (2007).

The focus of the recent exploration activities at Shantumbu were the metasediments, which flanked the northern margin of the Mpande Dome. On the southern margin of the Dome, the Kafue Rhyolite Formation consists of bimodal volcanics with intercalated rhyolite and basalts. North of the Mpande Dome, the Kafue Rhyolite Formation has not been intersected, and overlying metasediments may or may not be in contact with the underlying Basement gneisses. The metasediments comprise terrigenous platform sequences and later marine platform sequences, overlain by sediments that were deposited in an anoxic lagoon-basin with mudflats (Porada and Berhorst, 2000).

Porada and Berhorst (2000) reported that the lower portions of the Chunga Group in the Katanga Supergroup underwent intensive shearing under greenschist- to lower amphibolite-facies conditions during a Lufilian compressional event and was partly displaced, although the distances were not documented (Porada and Berhorst, 2000). The overlying Cheta Group was thrust north-eastward onto the Basement. The Lusaka Dolomite Formation formed the highest thrust unit in the Mpande Dome area; comparable to the Kabwe Platform Dolomite to the north, except that the Lusaka Dolomite Formation was not thrust far onto the hinterland and rests upon platform or slope deposits (Porada and Berhorst, 2000).

At the base of the Cheta Group sheared carbonates abruptly overlie quartz-muscovite-biotite schists containing a few lenses of impure dolomitic limestone and layers of quartzite cut by pegmatites (Chunga Formation). Kyanite in Chunga schists indicates a primary amphibolite-facies metamorphism whilst muscovite-biotite indicates a retrograde overprint during extensive shearing (Porada and Berhorst, 2000).

Numerous isolated mafic and ultramafic bodies (metagabbros and metaherzolites), some metamorphosed to eclogites, are exposed to the south of the Lusaka Dolomite Formation in an area underlain by Cheta Formation which had undergone greenschist facies metamorphism. Eclogites within greenschist environment indicate that the mafic bodies are tectonically

displaced in thrust horizons. Kyanite-bearing eclogites may have been emplaced from deeper crustal levels (Porada and Berhorst, 2000).

The central granitic core of the Mpande Dome is surrounded by both foliated and non-foliated coarse-grained gneisses, which were reconstituted to tectonites, through shearing, crushing, sericitisation and silicification, during Pan African tectonism, and are largely indistinguishable from the overlying metasediments (Stillman and De Swardt, 1965). The Mpande Gneiss has been dated at 1,106 ± 19 Ma (Johnson *et al*., 2007) and the overlying synrift supracrustal bimodal volcanic rocks have been dated at 879 ± 19 Ma (Hanson *et al*., 1994; Selley *et al*., 2005; Johnson *et al*., 2007). The Mpande Dome experienced uplift preceding Neoproterozoic continental rifting and the onset of continental rift-related sediment deposition (Selly *et al*., 2005). The Mpande Dome underwent Pan African deformation and the gneiss acquired foliation parallel to the north easterly Lufilian trend (Mallick, 1966).

Critical to the understanding of the continental rift metasediments at Shantumbu and within the Roan Group, is an examination of the regional tectonic setting of the margin of the Congo Craton during the Neoproterozoic, which is discussed in Chapter 3.

CHAPTER 3

REGIONAL TECTONIC SETTING

3.1 INTRODUCTION

The breakup of Rodinia and the formation of Gondwana resulted in the region having undergone extensional and compressional tectonics, intensive deformation, formation of mobile belts during the Pan African orogenesis, and metamorphism, both prograde and retrograde. A notable difference between the Shantumbu area and north of the Mwembeshi Zone is the higher metamorphic grade around Shantumbu, that of amphibolite grade metamorphism, compared to the predominantly greenschist facies metamorphism of the areas north of the Mwembeshi Zone (De Waele *et al*., 2008).

Previous work by Mallick (1966), Hanson *et al*. (1994), Porada and Berhorst (2000) and Hargrove *et al*. (2003), showed that compressional deformation features dominated the current structural setting south of Lusaka.

3.2 NEOPROTEROZOIC RIFTING

The Katanga Supergroup metasediments in the Zambian Copperbelt and at Shantumbu were deposited during passive continental extension related to the breakup of Rodinia c. 880 Ma. The later collision of the Congo and Kalahari cratons occurred c. 590 to c. 512 Ma during the formation of Gondwana (Master and Wendorff, 2011).

The Katanga Supergroup sediments were deposited during a period of passive continental extension/rifting and two separate basins were envisaged to have formed north and south of a pre-existing high, the Katanga High (Porada and Berhorst, 2000). Continental rifting was accompanied by rift-related magmatism represented by the Kafue Rhyolite Formation (c. 880 Ma), Nchanga Red Granite (c. 877 Ma) and Lusaka Granite (c. 820 Ma) (Johnson *et al.*, 2007). The terrigenous clastic sediments deposited during continental rifting on the northern area of the Katanga High are referred to as the Roan Group in the Zambian Copperbelt.

The rift basins underwent subsidence at the rate at which sedimentation kept pace with the rate of subsidence, depositing siliciclastic sediments on steep depositional gradients (Porada and Berhorst, 2000). Regional scale continental rifting continued and the regional basin-bounding faults interconnected to form larger basins. The impact of the interconnected regional basin-

bounding faults increased as the climax of rifting was approached. Sedimentation during the regional rift climax stage across Central Africa was now more than the subsidence, the environment became subaerial and marine ingression occurred (Porada and Berhorst, 2000).

Increased continental rupture of Rodinia amplified rifting, concomitant deposition of sedimentary sequences and asymmetrical rapid subsidence accompanied by mafic magmatism. The Grand Conglomérat was deposited c. 750 Ma during the Sturtian-Rapitan glaciations (Porada and Berhorst, 2000). Northeast-dipping normal faults active during rifting were probably reactivated during the crustal shortening/basin closure (Hanson *et al*., 1994).

The extensional stage (c. 880 to 600 Ma; Mwashia to early Kundelunga c. 765 - 735 Ma) was followed by basin inversion and compression during the convergence of the Kalahari and Congo Cratons (c. 595 to 490 Ma) (Selley *et al.*, 2005; Master and Wendorff, 2011). Continental collision began at c. 530 Ma and resulted in high pressure-low temperature metamorphism (Selley *et al.*, 2005; Naydenov *et al*., 2015). Hargrove *et al*. (2003) noted southward directed thrust faults and transcurrent to oblique-slip ductile shear zones accommodated crustal shortening during the collision of the Congo and Kalahari cratons. In the region south of Lusaka, crustal shortening is demonstrated by southwest-vergent nappes (F_1 of D_1 structures) (Hanson *et al*., 1994).

The Mwembeshi Zone, a narrow, high strain zone formed during ductile deformation of the Proterozoic rocks, possibly indicating the boundary between the Congo and Kalahari cratons (Daly, 1988; Daly *et al*., 1989). The Mwembeshi Zone is dated younger than 530 Ma (Naydenov *et al*., 2014), and is a north northeast – south southwest trending shear zone, which separated the Lufilian Arc from the Zambezi Belt following deposition of the rift-basin sediments and volcanic units (Daly, 1988; Yemane *et al*., 2002; Selley *et al*., 2005; Miller, 2013).

The Mwembeshi Zone was thought to have been responsible for the displacement of the southern basin by approximately 200km from its original location (Porada and Berhorst, 2000). The shear zone was active during the Proterozoic to Late Permian times in Central Africa (Daly *et al*., 1989).

3.3 PAN-AFRICAN OROGENESIS

The Basement and overlying rift-basin stratigraphy at Shantumbu and in the Central African Copperbelt underwent deformation related to the Pan African Zambezi Belt and Lufilian Arc orogenesis and the consequent clockwise rotation and collision of the Congo and Kalahari cratons (c. 590 to c. 512 Ma) (Master and Wendorff, 2011) (Figure 3-1). Compressive

deformation c. 595 to 490 Ma culminated in upper greenschist-facies metamorphism (c. 530 Ma) in the Zambian Copperbelt (Selley *et al*., 2005). Collision of the Archaean Congo and Kalahari cratons caused northeast directed thrust faulting of the continental rift basin sediments. Preceding the breakup of Rodinia, the area which became the Zambezi Mobile Belt was a pre-existing zone of weakness which lent itself to extensional rifting.

The Mwembeshi Zone, which was active during the formation and closure of the continental rift basins, was reactivated in the Permian time during development of the Mid-Zambezi Rift Basin (Porada and Berhorst, 2000; Yemane *et al*., 2002).

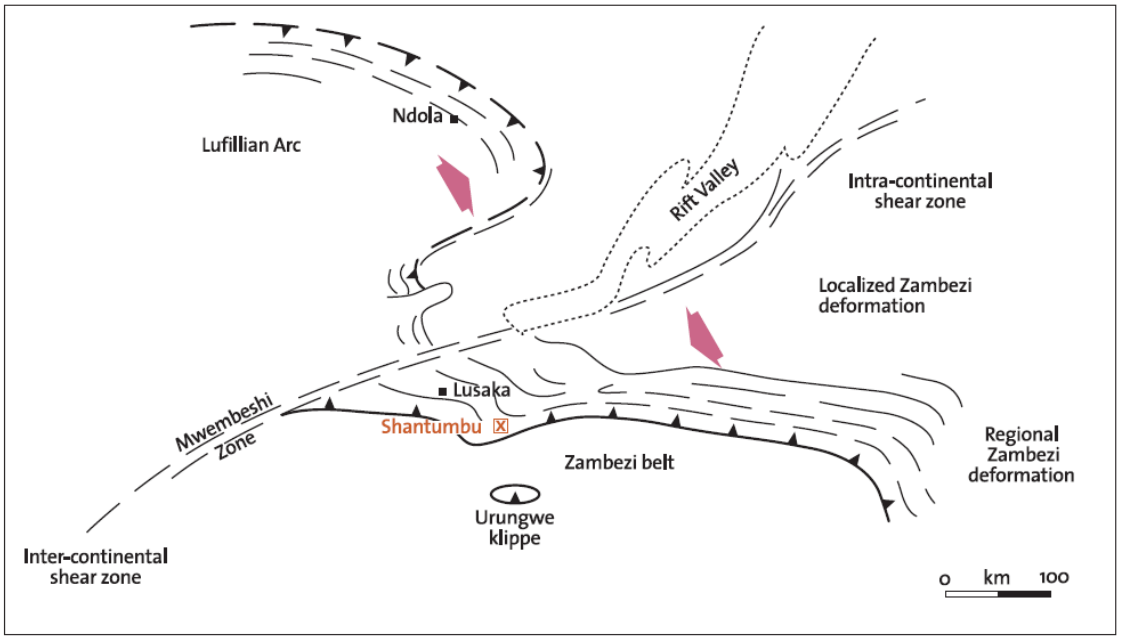

Figure 3-1. Location of Shantumbu in relation to the Pan African orogenic regions including the Mwembeshi Zone, the Lufilian Arc and Zambezi Belt (Daly, 1988).

During development of the Lufilian Arc and Zambezi Belt, the Mwembeshi Zone was primarily a sinistral shear, while during the Late Proterozoic the reactivated Mwembeshi Zone was dominantly a dextral shear, extending across southern Africa to Madagascar (Yemane *et al*., 2002). In the Palaeozoic, the Mwembeshi Zone was reactivated as a brittle-ductile to brittle fault with both sinistral and dextral strike slip directions. The overall strike of the Mwembeshi Zone is northeast-southwest with steep dips. Activation of the Mwembeshi Zone was induced by intraplate stresses arising from continental breakup and collision (Yemane *et al*., 2002).

Within the Lufilian Arc, the principal direction of the deformation was to the east-northeast, while in the Zambezi Belt the overall direction of structures was to the south and southwest (Daly, 1988). In southern Zambia, the Zambezi Belt is characterised by west-northwest to

northwest verging structures (Hanson *et al*., 1994). Two directions of transport were noted in the Zambezi Belt, an early west southwest-directed thrust faulting was succeeded by southerly directed transport (Daly, 1988).

Crustal thickening due to compressional deformation resulted in high-pressure metamorphism in the Zambezi Belt (Kröner and Stern, 2005; Reinaud *et al*., 2005). The peak metamorphic grades encountered along the Mwembeshi Zone occurred during the Late Proterozoic and attained greenschist facies (Yemane *et al*., 2002). Irregular occurrences of eclogite facies metamorphism in the Katanga Supergroup metasediments within the Zambezi Belt was due to subduction of oceanic crust and ocean basin closure during the collision of between the Congo and Kalahari cratons that occurred between c. 659 and 595 Ma (De Waele *et al.*, 2008). Peak metamorphism in the Lufilian Arc has been dated at c. 566 - 550 Ma (Kröner and Stern, 2005; Reinaud *et al*., 2005).

Limited evidence exists which suggested the Shantumbu area was a separate continental rift system to the Katanga Basin prior to the development of the Mwembeshi Zone. Rather, Shantumbu was part of the rift-tectonic system that was responsible for the Katanga Basin and development of the Central African Copperbelt.

3.4 PAN-AFRICAN THERMO-TECTONIC EVENTS

Three thermo-tectonic events between c. 1,100 Ma and 515 Ma constitute the Pan African Orogeny in the Lufilian Arc and the Zambezi Belt (Johnson and Oliver, 2004).

D_1 - Kolwezian Event

The first deformation phase, termed D_1 or the Kolwezian phase (Kampunzu and Cailteux, 1999), was a northward-directed fold and thrust event with related back-folding in the Lufilian Arc and the Zambezi Belt. The peak of the ductile D_1 deformation is age dated at c. 790 - 750 Ma and ceased completely at c. 710 Ma (Kampunzu and Cailteux, 1999). Prior to the D_1 phase, brittle deformation affected the preceding folding and thrusting (Kipata *et al*., 2013).

Within the Zambezi Belt, the D_1 event was a southwest vergence which resulted in amphibolite facies metamorphism dated at c. 535 - 517 Ma (Naydenov *et al*., 2015). West-northwest trending S_1 foliation in the Lusaka-Kafue Region is axial planar to the regional-scale southwest vergence and overturned to form recumbent F_1 folds (Hanson *et al*., 1994).

Initial thrusting related to D_1 deformation propagated northward, succeeded by back folding and thrusting during progressive contraction during Pan African orogenesis (D_2 and D_3); D_1 structures were overprinted by D_2 structures. Southward thrusting and transcurrent to oblique-slip ductile shear zones accommodated crustal shortening during the Pan African orogenesis of the Zambezi Belt (Hargrove *et al*., 2003). South to southwest (back folding) verging folding of the sedimentary rocks from Lusaka southwards to the Mpande Dome (Porada and Berhorst, 2000). The southwest folds were considered to represent F_1 structures (Hanson *et al*., 1994).

Naydenov *et al*. (2014) reported an emplacement age of c. 530 Ma for the Hook Batholith, a Pan African granitoid, north of the Mwembeshi Zone. The emplacement age of is syn-tectonic with the D_1 event of the Lufilian Orogeny.

D_2 - Monwezi Event

Brittle deformation characterised the second phase, D_2 or Monwezi, which has been dated at c. 690 - 540 Ma. Brittle deformation was accommodated along sinistral strike slip faults, such as the Mwembeshi Zone. The Mwembeshi Zone is hypothesised to have been most active during the D_2 phase. Naydenov *et al*. (2014) indicated the Mwembeshi Zone developed during the D_2 north-south shortening event.

Clockwise rotation of the Lufilian Arc commenced during the D_2 phase (Kampunzu and Cailteux, 1999) and was characterised by north south to north northeast-south southwest compression. The D_2 brittle deformation was attributed to convergence of the Congo and Kalahari cratons and the progression of strike slip faults northwards across the Pan African orogenic belts (Kampunzu and Cailteux, 1999).

The Mwembeshi Zone developed within the subsequent D_2 event as an east to northeast striking shear zone, along which the Lufilian and Zambezi belts were joined. Porada and Berhorst (2000) indicated the area south of the Mwembeshi Zone was similar to north of the Mwembeshi Zone but with more shortening and internal deformation.

South of the Mwembeshi Zone, the age of the east-west (D_1) shortening event has been constrained by Naydenov *et al*. (2014) at c. 560 - 550 Ma to 533 Ma. D_2 is constrained to after c. 533 Ma and characterised by the development of the Mwembeshi Zone in the Hook Batholith area. Naydenov *et al*. (2014) noted the lack of D_1 structures in the Hook Batholith area of the Mwembeshi Zone may have been the result of a lack of D_1 features imparted on Upper Kundelunga rocks or the D_1 features were overprinted by D_2 features.

Hanson *et al*. (1994) noted that F_2 folds were coaxial with and overprinted by overturned to recumbent F_1 folds in the Zambezi Belt. F_2 folds later experienced upright, open and northeast-trending folding to produce F_3 folds (Hanson *et al*., 1994). F_3 folding formed irregularly developed upright, open, northeast-trending folds. The up-warping of the Mpande Gneiss was proposed to have occurred during D_2 deformation at c. 530 Ma (Naydenov *et al*., 2015). At Shantumbu, F_2 folds mantle the Mpande Dome.

D_3 - Chilatembo Event

The third and final phase of the Pan African orogeny in the Lufilian Arc and Zambezi Belt, D_3 or Chilatembo Phase, was dominated by structures that are transverse to the trends in the Pan African belts and postulated to be Palaeozoic in age (Kampunzu and Cailteux, 1999). High-angle northeast-southwest faulting and open folding related to northwest-southeast compression affected the Lufilian Arc and Zambezi Belt, and resulted in the reactivation of several strike slip faults (Kipata *et al*., 2013). The D_3 period from c. 550 Ma was characterised by brittle deformation (Kipata *et al*., 2013).

3.5 DISCUSSION

A series of overturned recumbent folds along the margins of the Mpande Dome (Figure 3-2) characterises Shantumbu. The dip of the strata averages 60° although it is greater in the eastern, northeast and northern areas of Shantumbu. Similar dip and dip directions are noted from the strata in the carbonate platform area in the northern part of Shantumbu.

Based on the F_1 to F_3 compression tectonics noted by Hanson *et al*. (1994) and Porada and Berhorst (2000), the inverted stratigraphy evident in areas of Shantumbu and the ASTER false colour imagery (Figure 3-2) the tectonic evolution of the Shantumbu is considered to have formed as follows and summarised in Figure 3-3:

1. Large-scale (10km range) recumbent folding (F_1) propagating northward - D_1 event;
2. Compression tectonics in which the F_1 folds were compressed south-westward and warping around the Mpande Dome;
3. The F_2 folds experienced upright, open and northeast-trending folding and overprinted F_1; and
4. F_3 compression resulted in northeast ward plunging fold structures, demonstrated by the north-easterly plunge of the F_1 fold demonstrated in Figure 3-3.

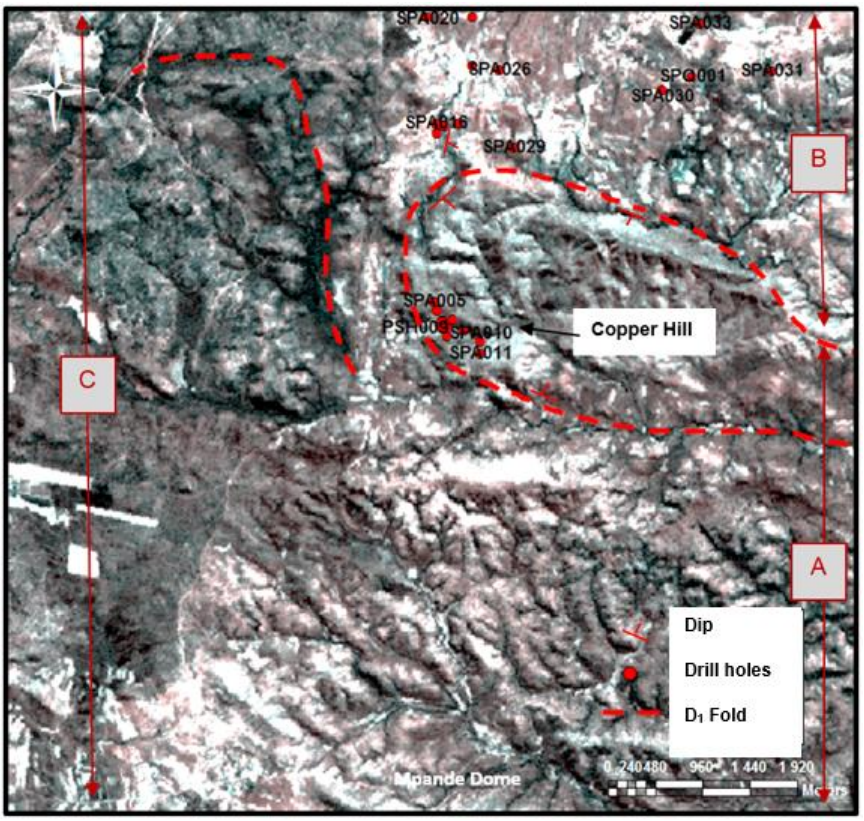

Figure 3-2. Aster false colour image of Shantumbu indicating the localities of the D_1 folds, diamond drill hole collars and major lithologies, A to C. (A) Detrital siliciclastic units. (B) Carbonate units. (C) Detrital siliciclastic units. The fringe of the Mpande Dome occurs along the southern boundary of the Shantumbu license. The image boundary equates to the Shantumbu License area.

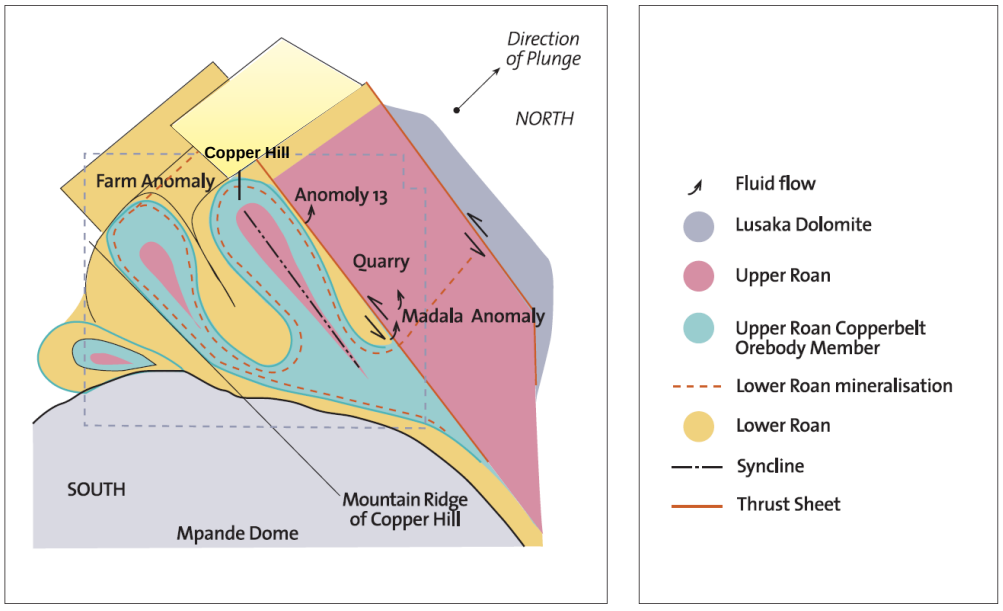

Figure 3-3. Schematic plan view of the D_1 compressive tectonics immediately north of the Mpande Dome. Large-scale recumbent folding with plunge towards the north northeast characterize the Shantumbu area. Copper Hill is located at the axis of the easterly D_1 fold. The Shantumbu License is overlain for reference.

Work by Mallick (1966), Hanson *et al*. (1994), Porada and Berhorst (2000) and Hargrove *et al*. (2003), showed that compressional deformation dominated the structural setting south of Lusaka. The structures observed on Shantumbu during the recent exploration were large-scale recumbent folding, in the order of 10km, with limbs overturned to the southwest, which confirmed that compressional deformation dominated the structural setting at Shantumbu following the deposition of the basin sediments (Hanson *et al*., 1994; Porada and Berhorst, 2000).

In the Lusaka-Shantumbu-Kafue area, regional northeast-directed thrusting involved deep crustal detachments and forward propagating faults, responsible for the location of the Lusaka Dolomite Formation and the overlying stratigraphy was thrust northeast onto Basement (Porada and Berhorst, 2000).

In southern and central Zambia, the D_1 event is considered a manifestation of the east-west collision event in the Mozambique Belt. The D_2 event represented a collision between the Congo and the Kalahari cratons and suturing of the two cratons along the Mwembeshi Zone. This resulted in an overall north-south shortening event dated at c. 530 – 520 Ma (Naydenov *et al*., 2015). Details of D_3 are not well documented in the literature. Greenschist to amphibolite facies metamorphism is considered to have accompanied the D_1 event (Naydenov *et al*., 2014). D_2 and D_3 events were accompanied by retrograde metamorphism.

Peak deformation in the Zambezi Belt is reported by Johnson and Oliver (2004) to have occurred from c. 560 to c. 515 Ma. Occurrences of eclogites south of Lusaka and within the Chongwe Copperbelt were overprinted by amphibolite facies metamorphism at c. 531 to 522 Ma (Naydenov *et al*., 2015 and references therein). The proximity of Shantumbu to the regions of eclogite facies metamorphism permits the inference of similar dates for the peak of metamorphism at Shantumbu.

Tectonic discontinuities or shear zones were not noted in the drill core for Shantumbu. The presence of extensive sodalite and pervasive goethite at the contact between the pelitic and marble sequences in the northern part of Shantumbu were noted and may be related to thermal alteration of the metasediments from an underlying intrusive, which produced a near-skarn type mineralogy. However, as detailed in next chapters, basinal brine migration and extensive sodic alternation explains the extensive development of sodalite.

3.6 CONCLUSIONS

The regional tectonic setting of Shantumbu is intrinsically related to both extensional and compressional tectonics and the resulting alteration and metamorphism of the associated rift sedimentary packages. The lithography, mineralogy and geochemistry of rift basin sediments at Shantumbu are placed in context of the regional Neoproterozoic continental extension and rift tectonics and related sedimentary succession in the succeeding chapters. The similarities and disparities between the metasediments of the rift basins north of the Mwembeshi Zone to the metasediments at Shantumbu, that is south of the Mwembeshi Zone, are described and discussed.

CHAPTER 4

LITHOSTRATIGRAPHY OF SHANTUMBU

4.1 INTRODUCTION

Debate which has spanned several decades, and is still ongoing, has deliberated the tectonic setting of the area south of Lusaka on whether the metasediments correlated with the Katanga Basin Sequence, as present in the Zambian Copperbelt, or the Basement Succession, or the Zambezi Supracrustal Sequence.

Chapter 4 examines the drill cores of the recent exploration campaign and describes the lithologies and stratigraphic arrangement of the metasediments. Consideration is given to the depositional environments responsible for the lithostratigraphy and the correlation, or otherwise, of equivalent characteristics within the Roan Group in the Zambian Copperbelt. The lithologies are discussed in terms of the sedimentary protolith and not in terms of the metamorphic equivalent.

Due to the intensive folding and deformation of the metasediments on Shantumbu, estimates of the total thicknesses of the individual sequences were not undertaken as part of this study. The lack of spatially representative data also did not allow examination of sulphide zonation within the metasediments at Shantumbu.

4.2 METHODOLOGY

The diamond drill cores were logged and sampled, and the stratigraphic, geochemical and petrographic characteristics were examined. Lithology, colour, mineralogy, structures, veining, and alteration were examined, and representative samples were marked and cut for the petrographic and geochemical studies. The samples were submitted for thin section preparation at the University of the Witwatersrand, and to an external analytical laboratory, Genalysis Laboratory Services (Intertek Minerals Group), in Perth, for geochemical analyses.

The identification of a laterally persistent horizon provided a reference datum for the subdivision of the lithostratigraphy into sequences, introduced in Chapter 2. The term ‘sequence’ denotes an interrelated lithostratigraphic succession, which represented a specific depositional environment. Where possible, a sequence was subdivided into smaller units termed facies.

The first occurrence of a dolomitic carbonate layer (Figure 4-1 and Figure 4-2) was used as the reference surface (marker horizon) in the Shantumbu Drill cores.

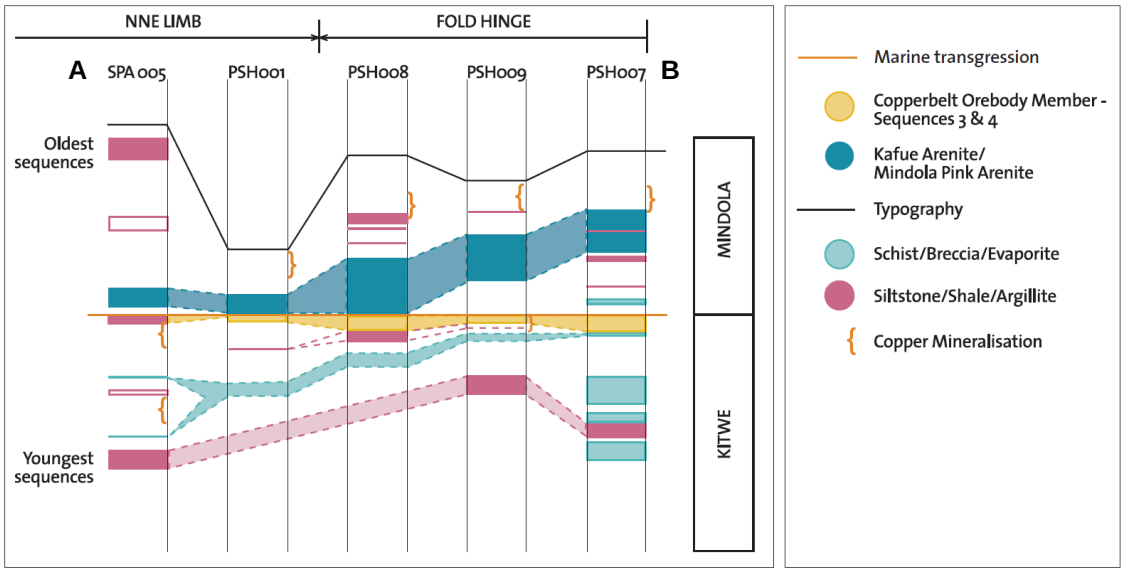

Figure 4-1. Section AB through the central area of Shantumbu via a schematic drill hole fence diagram referenced to the carbonate datum. Due to Pan African deformation the stratigraphy is overturned, with the older sequences at the top of the logs and the youngest at the base of the logs.

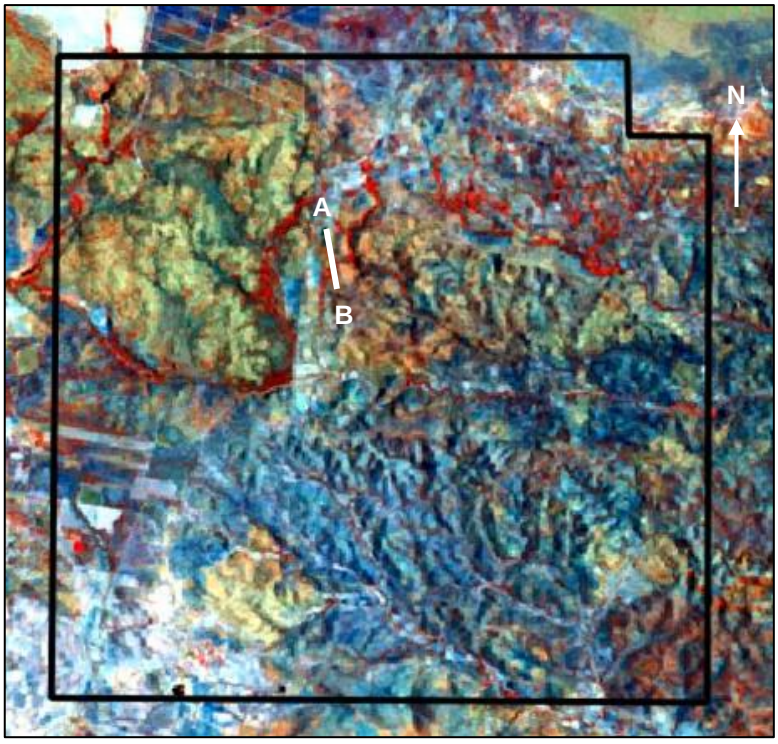

Figure 4-2. Section line A-B overlain on the Landsat 8 OLI false-colour composite image (September 2013) of the Shantumbu License.

4.3 HYPOTHESES

The limited historical information for the Shantumbu area and poor outcrop necessitated the definition of hypotheses relating to the depositional setting that was present at Shantumbu. The assumptions are later confirmed or disproved, through the interpretation of the recent exploration information. The hypotheses included:

1. Shantumbu was a basement-proximal and restricted rift basin;
2. The siliciclastic sediments were derived from the Basement lithologies;
3. Asymmetrical rift-related normal faults dipped to the north and northeast along the northern flank of the Mpande Dome;
4. The absence of thick conglomerates within the basal units of the rift sediments was assumed to indicate a subdued landscape existed at the start of rifting;
5. Rift-related igneous unit/s occur directly south of the Mpande Dome in the Kafue area but were not intersected in the Shantumbu drilling due to the limited drilling depths undertaken. On the northern margin of the Mpande Dome the metavolcanics units related to rift initiation were assumed to occur below the package of metasedimentary lithologies;
6. A moderate to high energy rift-related depositional environment characterised deposition of the older/lower siliciclastic rocks on Shantumbu; and
7. Basin subsidence, marine transgression and regression characterised rift climax and conclusion.

4.4 LITHOLOGICAL DESCRIPTION OF SHANTUMBU

Seven sequences, Sequence 1 to 7, were identified from the Shantumbu Drill cores. Sequence 1 is the oldest stratigraphic succession observed and Sequence 7 the youngest sequence recognised. The geological logs that form the basis of Chapter 4 are summarised in APPENDIX 1.

Sequence 1: Arkose Siltstone

Highly weathered Sequence 1 was intersected in two drill holes, PSH001 and PSH008, though the drilling did not penetrate the base of Sequence 1 due to the depths at which the drill holes were stopped. The adjacent drill holes did not intersect Sequence 1 due to the level of the present-day erosion surface. The drill holes which intersected Sequence 1 were collared along the hinge of a D_1 fold where Sequences 1 occurs at the present-day erosion surface due to overturned stratigraphy related to the Pan African Orogeny.

Sequence 1 progresses upwards from an iron-rich, medium-grained arkose, overlain by a grey quartzose arenite (Figure 4-3 and Figure 4-4), followed by a fine-grained grey arkose capped by two siltstone layers with an arkose middling. The fine-grained arkose middling hosts malachite and chlorite. The arkoses in contact above and below the siltstones host malachite to a lesser extent than the arkose sandwiched between two siltstone layers. The succession of arkose and siltstone is terminated by the iron-rich medium-grained arkose of the overlying Sequence 2.

Sequence 1 experienced sericitisation and alteration to goethite, primarily along bedding planes. Calcite veins cross-cut the siltstone layers (Figure 4-5).

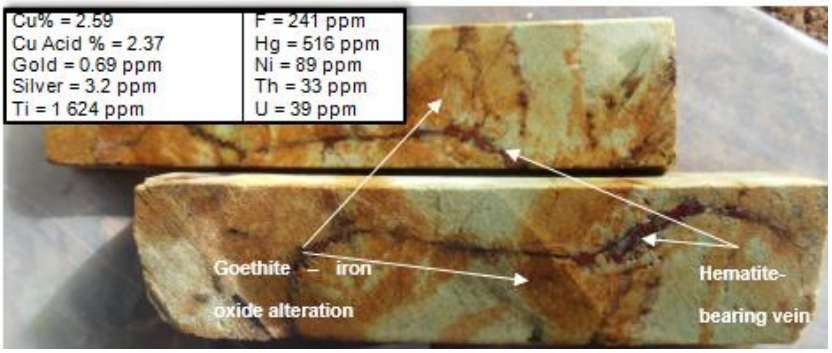

Figure 4-3. Goethite-bearing fine-grained altered arkose of Sequence 1, Shantumbu, cross-cut by hematite-bearing veins (H08288 from PSH008 at a depth of 30m).



Figure 4-4. Fine-grained arenite of Sequence 1, Shantumbu. (a) Fine-grained arkose of Sequence 1 hosting malachite and chlorite (PSH008). (b) Malachite along bedding and fracture planes, hosted by fine-grained grey arkose of Sequence 1 (PSH008). (c) Outcrop of fine-grained arkose hosting malachite mineralisation at Copper Hill, Shantumbu.



Figure 4-5. Arkose and siltstone units of Sequence 1, Shantumbu. (a) Alternating siltstone and iron-oxide-bearing arkose layers of Sequence 1. (b) Siltstone from Sequence 1 cross-cut by a boudinaged calcite-bearing vein (H08291 from PSH007 at a depth of 100.1m).

Only two drill holes intersected Sequence 1; together with this and the highly altered arkose and siltstone, fining-upward changes, or otherwise, and bedding were not identified in Sequence 1.

Sequence 2: Feldspathic Arkose

Sequence 2 is a laterally persistent unit consisting of an altered mottled to bedded unit of pink, red, brown, cream and dark grey massive arenite, and subordinate siltstone layers (Figure 4-6 and Figure 4-7). The contact between the arenite and siltstone is non-erosional. Laterally continuous, medium- to coarse-grained bedded pink arkose with numerous thinner interbedded dark grey arkose layers occur.

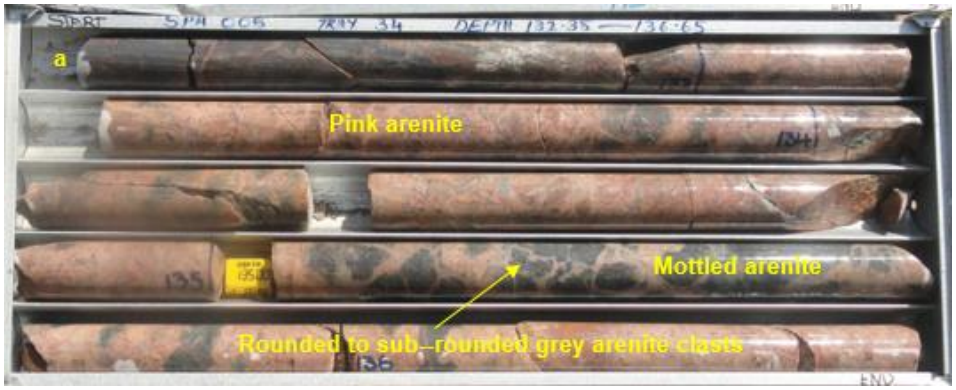

Continued next page

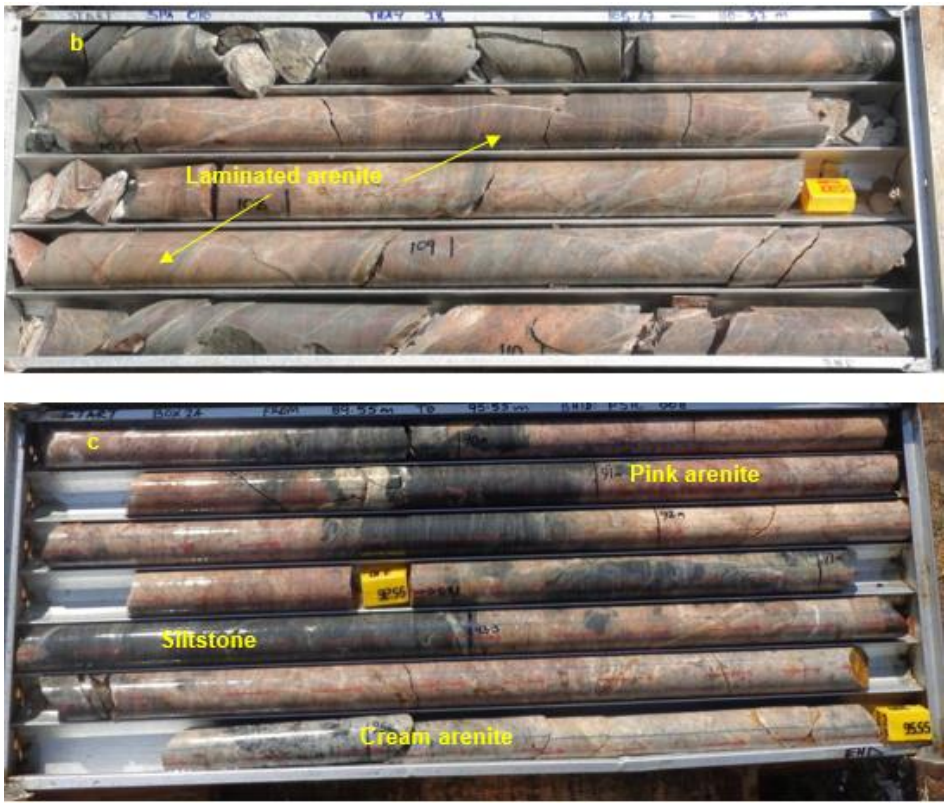

Figure 4-6. Lithologies of Sequence 2, Shantumbu. (a) Sequence 2 shows rounded to sub-rounded dark grey plagioclase-quartz patches in SPA005 (at a depth from 132.35 to 136.65m). (b) Laminated arenite (SPA018 at a depth from 105.67 to 110.37m). (c) Interbedded arenite and siltstone layers (PSH008; at a depth from 89.55 to 95.55m).

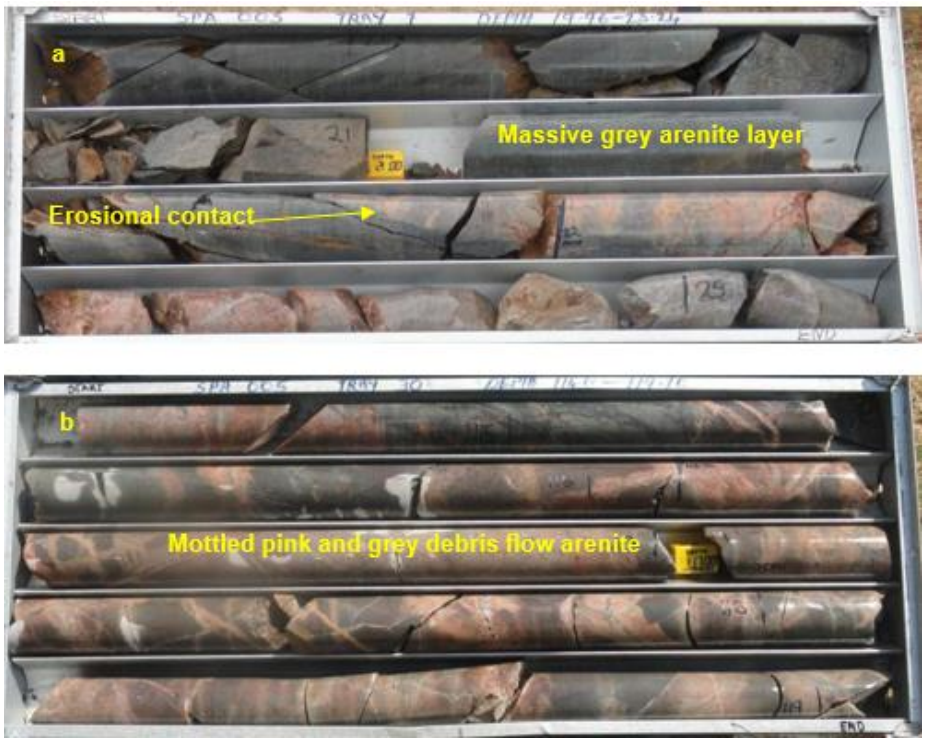

Continued next page



Figure 4-7. Mottled, grey and iron oxide stained examples of the arenites of Sequence 2, Shantumbu. (a) Erosional contact between grey and pink arenites of Sequence 2 (SPA005 at a depth of c. 20m). (b) Mottled arenite debris flow (SPA005 at a depth of c. 114m). (c) Grey arkose interbedded with medium-grained goethite-rich arenite (PSH001 at a depth of 32.8 - 37.14m).

The mottled arenite consists of patches of pink and grey arenite caused by variable alteration and recrystallisation. Plagioclase, hematite and goethite impart the pink colouration to the arenite. Fine-grained hematite is scattered throughout the matrix of the arenite and has in places altered to goethite. Patches of iron oxide staining and recrystallised plagioclase, together with irregular alteration and recrystallisation of the plagioclase and quartz are characteristics of the Sequence 2 mottled arenites. Malachite was noted at the base of Sequence 2.

Sequence 2 has variable thickness; in PSH001 the sequence is thin compared to the intersections in drill holes PSH007, PSH008 and PSH009. Drill holes SPA005 and SPA010 contain the thickest succession of Sequence 2 and it is dominated by the grey arkose units. Sequence 2 demonstrates characteristics of a debris flow origin.

Sequence 2 is overlain by a laterally extensive thick grey carbonate layer, with or without an associated siltstone layer, or a 5 - 10m siltstone unit, which denotes the start of Sequence 3. The contact is non-erosional (Figure 4-7a).

Sequence 3: Siltstone and Grey Carbonate

Sequence 3 is the first recognizable sub-aqueous sequence above the terrestrial sediments of Sequences 1 and 2 (Figure 4-8) and consists of a 5 - 10m thick siltstone overlain by a finely laminated grey carbonate, composed of dolomite, plagioclase and quartz. The carbon content of the siltstone across drill holes is variable, based on the colour variation of the siltstone from grey to black. The top and bottom contacts of the Sequence 3 are sharp and the lithologies above or below the contact are enriched with goethite. Sequence 3 is the first discernible dolomite layer within the stratigraphy.



Figure 4-8. The sub-aqueous siltstone and carbonate lithologies of Sequence 3, Shantumbu. (a) Siltstone and grey carbonate of Sequence 3 in SPA005 (145 – 153m) overlain by grey carbonate and massive siltstone layers of Sequence 3 (PSH008 at a depth of 104 to 108m). (b) The goethite-rich arenite of Sequence 4 caps the grey carbonate of Sequence 3.

Sequence 4: Calc-silicate

The calcareous arkose and dolomitic carbonates of Sequence 4 formed during a flood or marine transgression event. The calcareous arkose pervasively altered to iron oxide minerals. The layer is cross-cut by numerous plagioclase and calcite veins.

In PSH001, PSH007, PSH008 and PSH009, the iron oxide-rich calc-silicate is overlain by a fine-grained dolomitic breccia and capped by a second iron oxide-bearing calc-silicate (Figure 4-9). The dolomite breccia consists of plagioclase and quartz cemented by interstitial dolomite, pyrite, hematite and goethite. The dolomitic breccia (Figure 4-9) is crosscut by numerous dolomitic veins. Two generations of dolomite were noted, an early and a late stage dolomitisation.



Figure 4-9. The upper and lower iron oxide calc-silicate layers and intervening dolomitic breccia of Sequence 4 (PSH008 at a depth of c. 108 - 118m).

Three iron oxide-rich calc-silicate layers alternate with grey carbonate and argillaceous carbonate in drill hole PSH008. In PSH009, the iron oxide-rich calc-silicate layers are present, however, the intervening carbonate layer is accompanied by brecciated siltstone and arkose. The iron oxide-rich calc-silicate in SPA005 hosts three grey carbonates underlain by a thick Sequence 2. The iron oxide-rich calc-silicate layers are overlain by arkosic units rather than carbonate layers in SPA005. Where the dolomitic breccia formed the intervening bed between the two layers of iron oxide-rich calc-silicate beds, copper mineralisation is noted in Sequence 1 (Figure 4-9). Where the intervening layer to the two layers of iron oxide-rich calc-silicate includes arkose, copper mineralisation is not evident in the underlying detrital units.

SPA026B and SPA029 are in the northern region of Shantumbu and Sequence 4 was intersected in SPA026B (Figure 4-10) underlain by Sequence 2 with a very thin (c. 0.5m) grey carbonate of Sequence 3. In SPA029, the iron-oxide calc-silicate layer is thin in comparison to typical thicknesses encountered in Sequence 4.



Figure 4-10. Iron oxide-rich calc-silicate succession of Sequence 4 in SPA026B, Shantumbu.

Sequence 5: Carbonate-Siltstone-Arkose

Three distinct facies makeup Sequence 5. Facies 5a is volumetrically the least of the three facies, facies a, b and c. Sequence 5 commenced with facies 5a, a gritty to clean cream carbonate with siltstone content progressively increasing upwards. Facies 5b is recognised by an increase in carbonate content. Facies 5c developed where the carbonate content dominates over the siltstone part. The centimetre-scale intercalations of siltstone and carbonate of facies 5c were termed rhythmite. The siltstones of facies 5b experienced variable brecciation and in Sequence 5, the increase in number of carbonate layers corresponded with a decrease in the number of brecciated siltstone layers. The rhythmite sequence is capped either by Sequence 6, an arenite-dominated carbonate sequence, or by the blue-grey calcitic carbonates of Sequence 7.

Facies 5a: Scattered Granule-bearing Carbonate

A single intersection of facies 5a was intersected during the drilling campaign. Facies 5a is underlain by the progression from Sequence 2 to 4 discussed above, however at the level of Sequence 5 the lithological succession was dissimilar to the other Sequence 5 intersections.

To distinguish this unique intersection from the remaining Sequence 5 intersections, the scatted granule-bearing carbonate was termed facies 5a. Where facies 5a was intersected, both facies 5b and 5c were thinly developed.

The thin cream dolomitic carbonate of facies 5a is overlain by a matrix-supported carbonate with scattered biotite clasts and capped by carbonate-biotite-rhythmites (Figure 4-11). The biotite-dominated clasts in facies 5a measure up to one centimetre in diameter and form less than 5% of the unit. The biotite clasts are orientated parallel with the faint laminations discernible in the carbonate host rock.

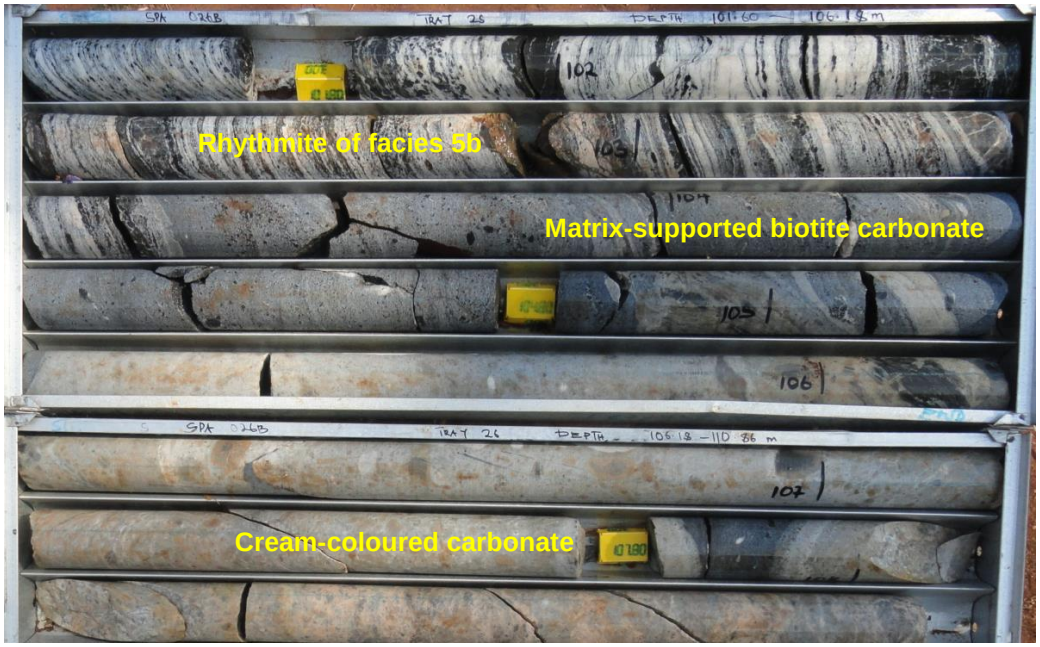

Figure 4-11. The cream dolomite of facies 5a overlain by a carbonate layer containing scattered biotite clasts, Shantumbu. The succession is capped by rhythmite of facies 5b (SPA026B at depths from 101.6 to c. 109m).

Facies 5b: Carbonate-Siltstone-Arkose Breccia

Facies 5b is a light grey medium- to coarse-grained carbonate alternating with brecciated siltstone and intercalated carbonate-siltstone-arkose layers. Occasionally, the carbonate layers have altered to a maroon-brown colour. A distinguishing feature of facies 5b is the layer-cake morphology of beds and the brecciation of the siltstone, termed rhythmite. Brecciation is restricted to the siltstones and does not extend into the adjacent lithologies.

The composition of the breccia is identical to the rhythmite sequence. The brecciated clasts are dominated by biotite and the light grey to green matrix includes angular to sub-rounded quartz and scapolite grains cemented by dolomite, calcite and late-phase pyrite, chalcopyrite and

pyrrhotite (Figure 4-12). Alteration of the breccia clast rims was not found. Angular clasts progress to smaller clasts towards the contacts of the breccia unit, having imparted a speckled appearance to the breccia. Veins have cross-cut the clasts parallel to the preferred clast orientation however, fracturing has largely destroyed the original textures.

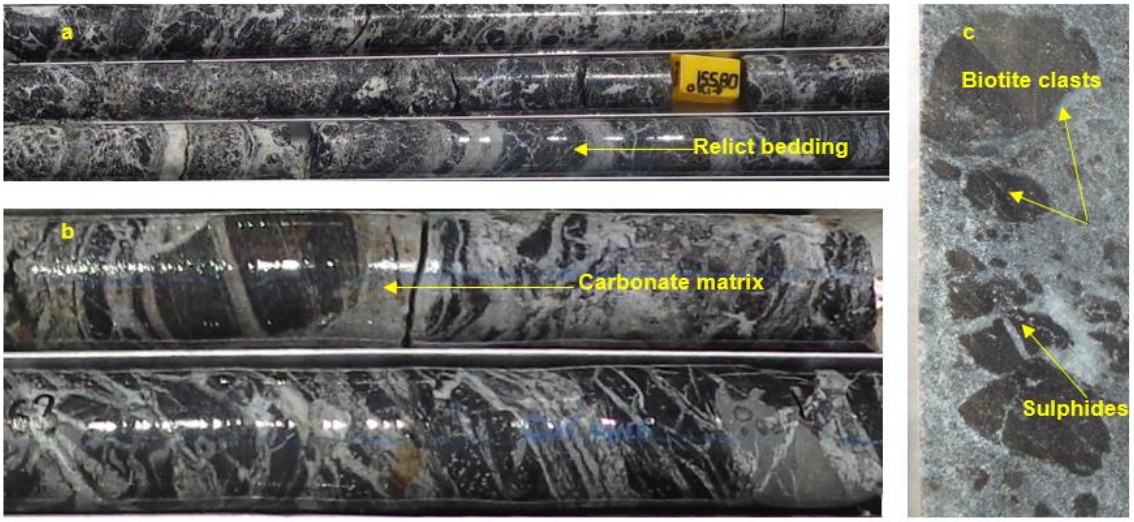

Figure 4-12. Breccias of facies 5b, Shantumbu. (a) Brecciated siltstone and relict bedding within facies 5b in PSH007. (b) Brecciated argillite cemented by carbonate matrix of facies 5b. (c) Sulphides cross-cutting a brecciated biotite clast in facies 5b (PSH007).

Facies 5c: Carbonate-Pelite and Arenite Rhythmite

Facies 5c comprises cycles of white and grey carbonate, siltstone and arenite. A cycle consists of carbonate and biotite laminae overlain by dolomitic siltstone (biotite spotted carbonate rock), which is in turn overlain by brecciated arenite (Figure 4-13 and Figure 4-14) and capped by shale/siltstone.

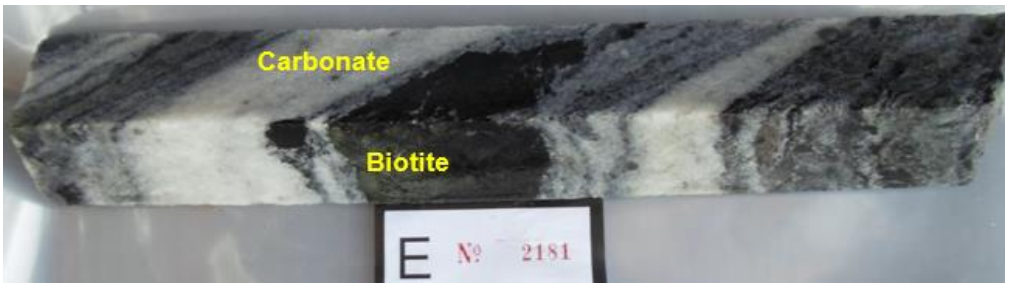

Figure 4-13. Alternating laminations of calcite and biotite within the rhythmites of facies 5c (SPA018, sample E2181 at a depth of c. 86m), Shantumbu.

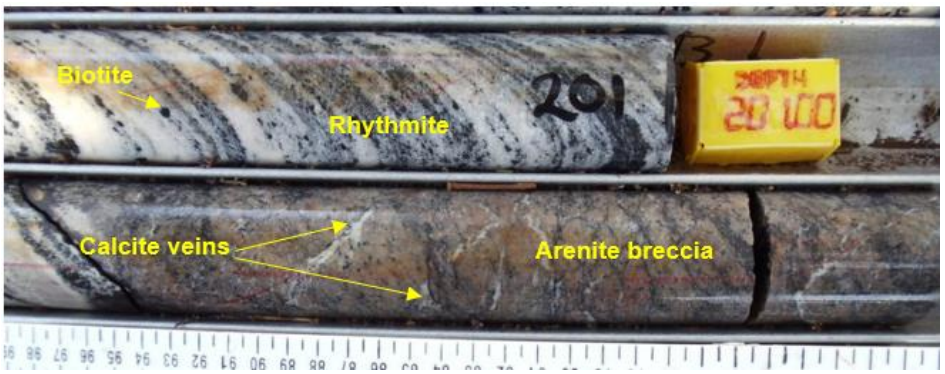

Figure 4-14. Biotite-dominated bands, grey carbonate, and brecciated arenite of facies 5c (SPA015 at a depth of c. 201m), Shantumbu.

The interbedded carbonate-rich and pelitic sediments vary from lenses of white-grey carbonate intercalated with sub-millimetre to ten centimetres biotite-dominated dark to black lenses and bands (Figure 4-15). Abundant fine-grained biotite is disseminated throughout the massive grey carbonate. The carbonate bands and lenses are intercalated with thin laminations of calcareous siltstone and arenite and brecciated feldspathic calcareous arenite. Metamorphosed calcareous mudstone or siltstone up to a metre thick are dominated by biotite.

The arenites have undergone uneven carbonatisation and reaction between the silicate and carbonate minerals, as demonstrated by both clinopyroxene and epidote surrounded by calcite. The brecciated arenites are dominated by plagioclase and K-feldspar and contain abundant hematite and goethite (Figure 4-16). The matrix consists of biotite, hematite and dolomite.

The white/clean carbonate is made up of 50 - 100% calcite, 20 - 50% biotite and 10 - 20% plagioclase with negligible pyrite, hematite, chlorite, chalcopyrite, zircon, rutile and apatite. The plagioclase grains are sub-angular within a matrix dominated by anhedral to subhedral calcite.

Plastic deformation textures (flow and dissolution) within the carbonate layers of the rhythmites were identified in Sequences 5 and 6.

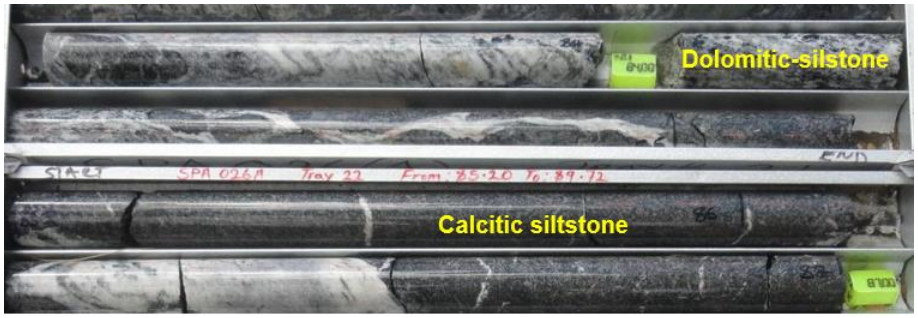

Figure 4-15. Siltstone and dolomitic siltstone of facies 5c (SPA026A at a depth from c. 84 - 87m), Shantumbu.

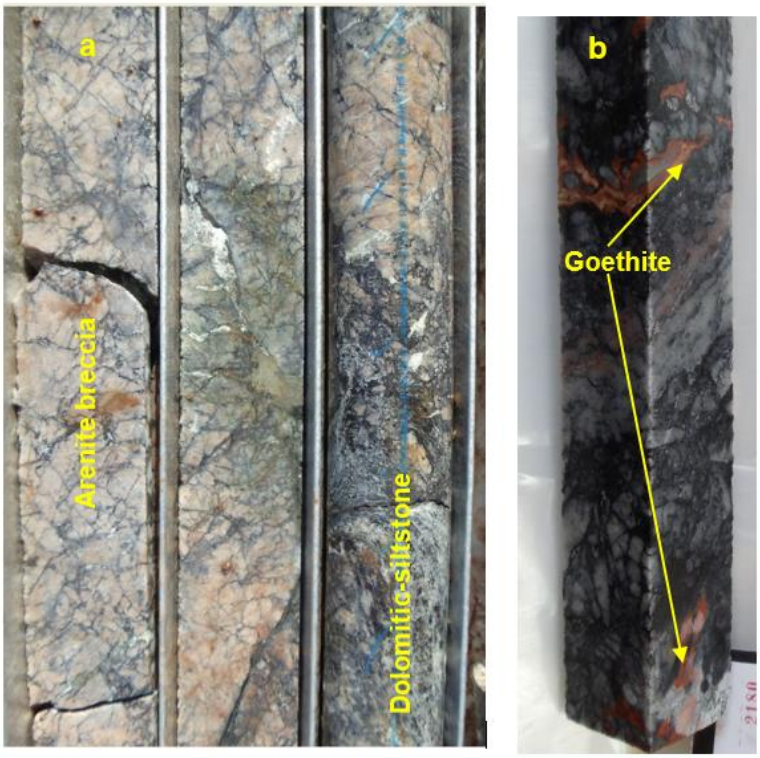

Figure 4-16. Arenite breccias of facies 5c, Shantumbu. (a) Brecciated arenite of facies 5c (SPA018). (b) Goethite surrounding the brecciated clasts of arenite in facies 5c.

Sequence 6 – Shale, Siltstone, Arenite and Carbonate

Sequence 6 is a cyclic succession of feldspathic arenite, subordinate carbonate and siltstone layers and is lithologically comparable to Sequence 5. The primary difference is the decrease in volume of carbonate layers and the increase in feldspathic arenite layers. The contacts between the siltstone/shale layers and the arenites are erosional (Figure 4-17 to Figure 4-19). .

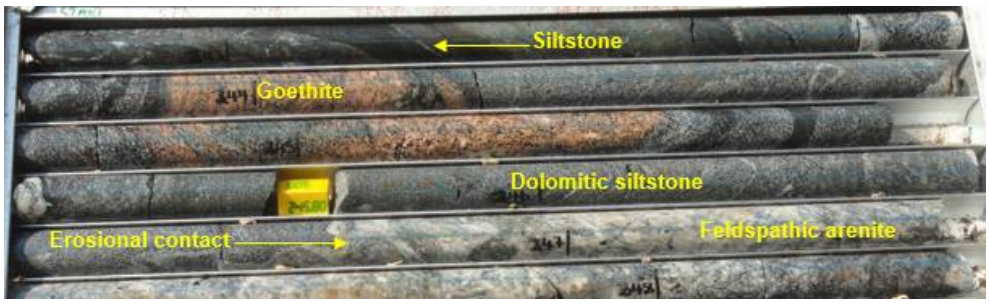

Figure 4-17. Goethite-rich carbonate and erosional contact between the arenite and underlying carbonate in Sequence 6 (SPA018 at a depth of c. 245m), Shantumbu.

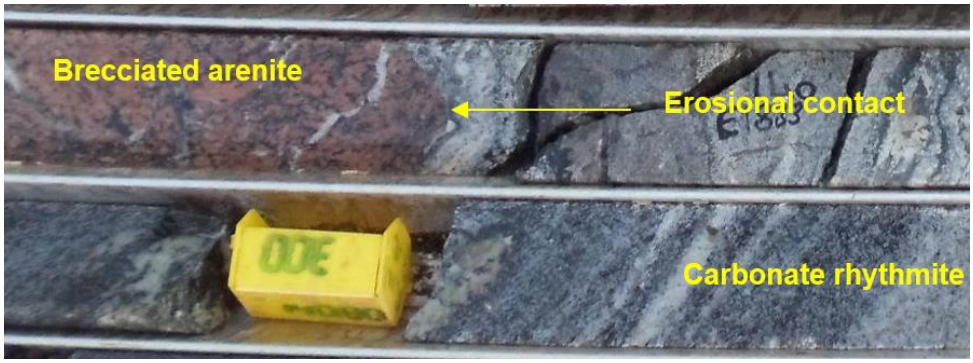

Figure 4-18. Erosional contact between brecciated arenite and carbonate rhythmite in Sequence 6 (SPA018), Shantumbu.

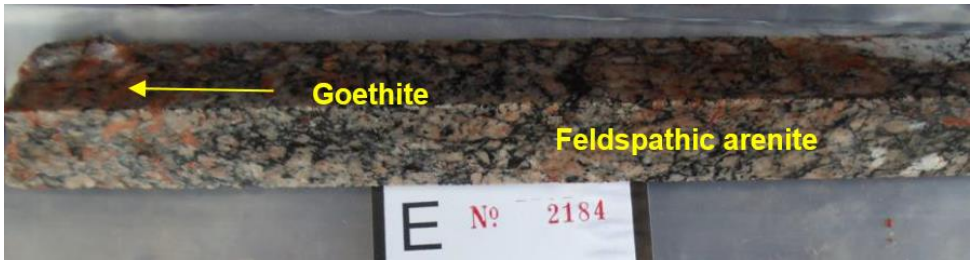

Figure 4-19. Goethite-bearing brecciated feldspathic arenite of Sequence 6 (SPA018 E2184), Shantumbu.

The arenite layers host extensive goethite development following the patchy replacement of magnetite, pyrite and pyrrhotite. Coarse-grained pyrite is visible both within and adjacent to the biotite-dominated bands. Minor amounts of marcasite, a low-temperature mineral, were noted during mineralogical investigations.

Biotite and microcrystalline goethite grains and lesser calcite and apatite (Figure 4-19 above) dominate the matrix of the arenite and the interstitial spaces were filled by biotite, goethite, sodalite (Figure 4-20), dolomite, epidote and hematite.

The calc-silicate layers and lenses underwent carbonate alteration noted by the replacement of silicate minerals by carbonate minerals, the recrystallisation of fine-grained calcite and iron oxides and sericitisation of feldspar grains in the cement of the bands and layers.

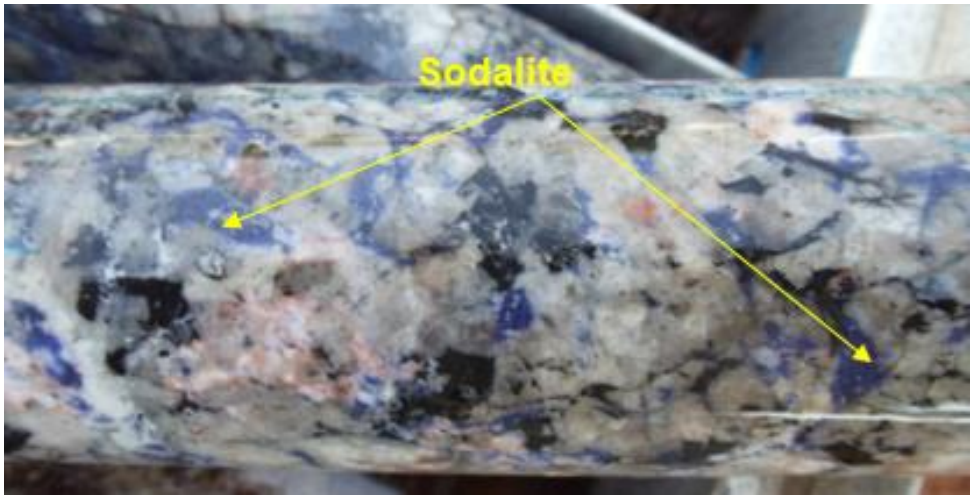

Figure 4-20. Sodalite, a sodic alteration mineral, interstitial to the brecciated feldspathic clasts comprising the arenites of Sequence 6 (SPA018), Shantumbu.

Sequence 7 – Grey Arenaceous Carbonate

Sequence 7 was intersected in SPQ001, SPQ001A and SPQ002, in the north-eastern area of Shantumbu. The succession is dominated by a significant thickness of several metres of grey-blue, finely laminated calcitic carbonate. The fine laminations within the massive carbonate layers consist of calcite, ankerite, magnesite, anhydrite, quartz, phlogopite, chlorite, goethite and pyrite. Oxidation occurred along the bedding planes.

Sequence 7 lacks the prominent rhythmic banding of the underlying Sequences 5 and 6, however, fine siltstone laminations are present, which are less than five centimetres in thickness. A significant part of the carbonate assumes a light earthy yellow brown colour (Figure 4-21) due to the presence of fine biotite grains. Within the earthy yellow-brown rock, anhedral quartz grains were observed within calcite grains and the dominant mineral was calcite with subordinate (5 - 10% weight) quartz.

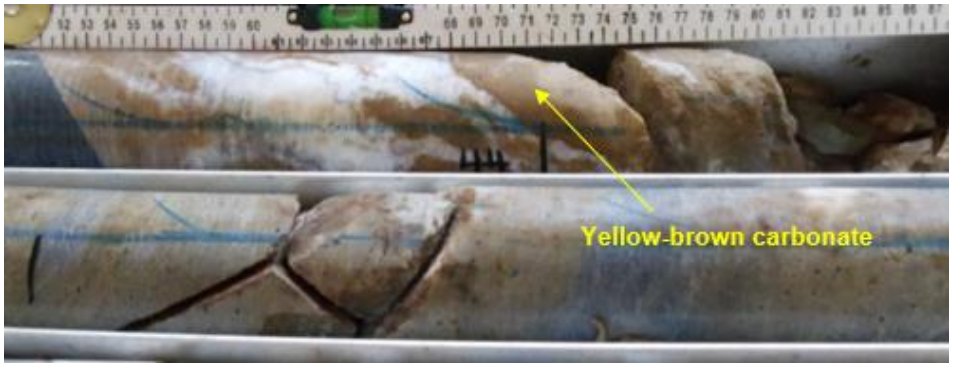

Figure 4-21. Finely laminated grey-blue to yellow-brown carbonate of Sequence 7 (SPQ001), Shantumbu.

Sequence 7 is not extensively cross-cut by veins, and where veins were noted, coarse-grained rhombohedral carbonate with iron oxide staining filled the vugs and cavities (Figure 4-22).



Figure 4-22. Rhombohedral carbonate (calcite) with iron oxide staining filling a vug within the grey-blue carbonate of Sequence 7 (SPQ002), Shantumbu.

4.5 DEPOSITIONAL ENVIRONMENTS ON SHANTUMBU AND THE ROAN GROUP

Shantumbu, Southern Zambia

The lithological characteristics of Sequences 1 and 2 indicate deposition occurred within an alluvial fan environment during extensional rift imitation. Rift climax and waning resulted in a marine incursion (Sequences 3 and 4) and a halt to the deposition of the detrital Sequences 1 and 2.

The siltstone and dolomitic carbonate of Sequence 3 were deposited during increased subsidence which resulted in the transition to sub-aqueous conditions. The dolomitic breccia of Sequence 3 is presumed to have formed from a calc-silicate unit deposited during shallow water conditions and which underwent dissolution when subjected to alteration and dissolution of evaporitic cements. The depositional environment of Sequence 3 evolved into a shallow water conditions which were responsible for deposition of the dolomitic carbonate and siliciclastic of Sequence 4. Shallow subtidal through to tidal flat environments which were subjected to cycles of subaerial exposure related to a fall in sea level, produced Sequence 5.

Sequence 5 was dominated by chemical precipitation in a sub-aqueous/marine environment, with the subordinate input of detrital material from up-platform areas. The repetitive and thick sequence of interbedded carbonate-rich with pelitic lenses and bands is interpreted to record slow subsidence in a marine environment.

The carbonate-siltstone rhythmites of Sequence 5 were progressively overlain by siliciclastic sediments deposited within the shallow marine setting of Sequence 6. The youngest lithologies

intersected in the drill cores was related to the gradual subsidence and stability of the rift environment which formed the carbonates of Sequence 7 within a shelf/platform environment.

Roan Group, Katanga Basin, Zambian Copperbelt

Both the Roan Group sediments of the Katanga Basin system and the rift-related sediments at Shantumbu (Figure 4-24) were deposited during the passive continental Neoproterozoic Rift imitation, rift climax, and rift conclusion. The sediments from both areas were deposited within similar rift basin depositional environments.

The basal unit of the Roan Group, the Mindola Formation, was deposited during rift initiation, whilst the Kitwe Formation formed during rift-climax and conclusion. The Upper Roan Group (using the nomenclature of Selley *et al*., 2005) alternatively termed the Kirilabombwe Formation) (Table 2-3 above) and Mwashia Group were deposited during the thermal sag phase following rift climax (Figure 4-23a).

The lower portion of the Roan Group consists of sub-aerial to shallow sub-aqueous clastic sequences, whereas the upper portion of the Roan Group comprises platform carbonates, breccias (stratiform and discordant) and subordinate siliciclastic rocks. The transition from sub-aerial rift extension (Figure 4-23a and b) conditions to post rift (Figure 4-23c) deposition of platform carbonate rocks is represented by the Copperbelt Orebody Member (Figure 4-24c), alternatively known as the Ore Shale Unit in the Zambian Copperbelt. The Copperbelt Orebody Member marked the onset of a marine transgression (Hitzman *et al*., 2012).

Evolution of the rift tectonics in the Katanga Basin gave rise to the intrusion of mafic sills and flows, and the latter stages of rifting resulted in a glaciogenic period, responsible for the deposition of the Grand Conglomérat glaciogenic unit of the basal unit of the Nguba Group. The Kundelungu Group, which overlies the Nguba Group, started with the deposition of the Petit Conglomérat unit (Hitzman *et al*., 2012). The glaciogenic period did not appear to have formed in the Shantumbu area.

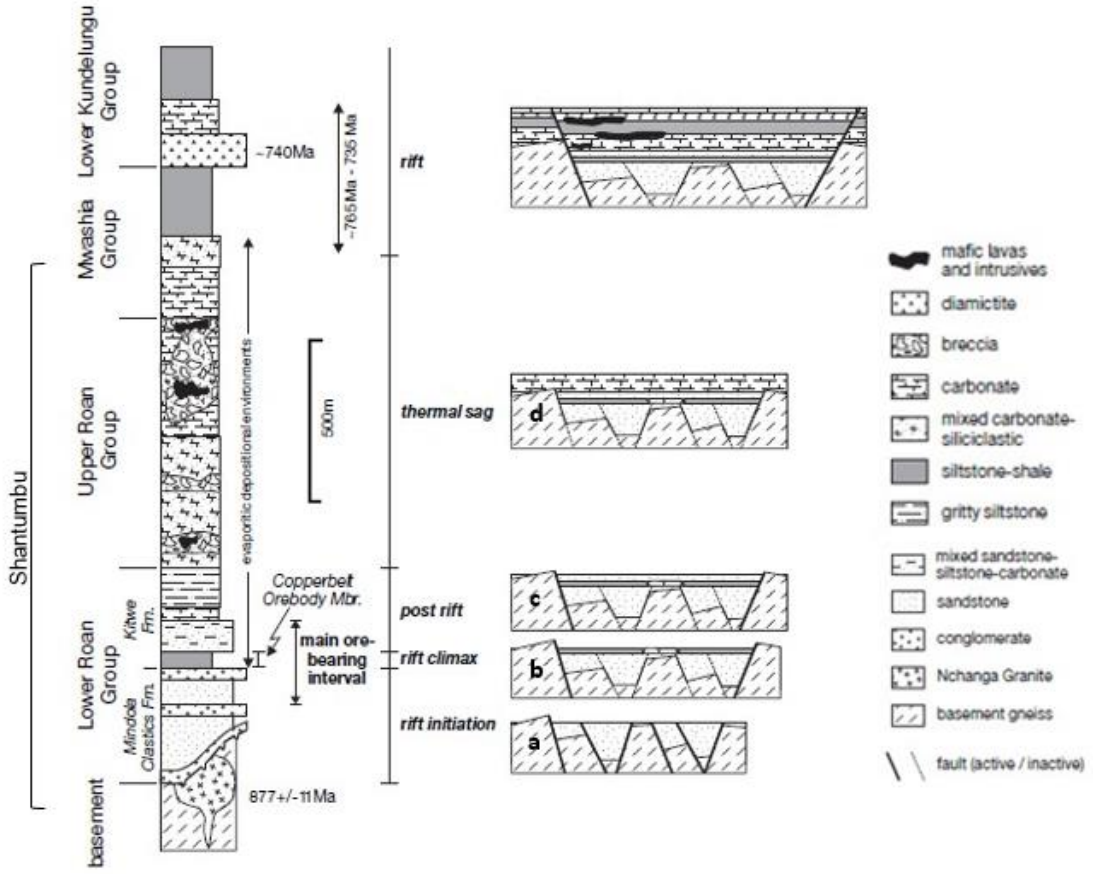

Figure 4-23. Tectonostratigraphic evolution of the Katanga Supergroup, Zambian Copperbelt, illustrating the passive continental rift initiation, climax and rift cessation (Modified after Selley *et al*., 2005, p971). (a) rift initiation; (b) rift climax; (c) post rift and (d) thermal sag.

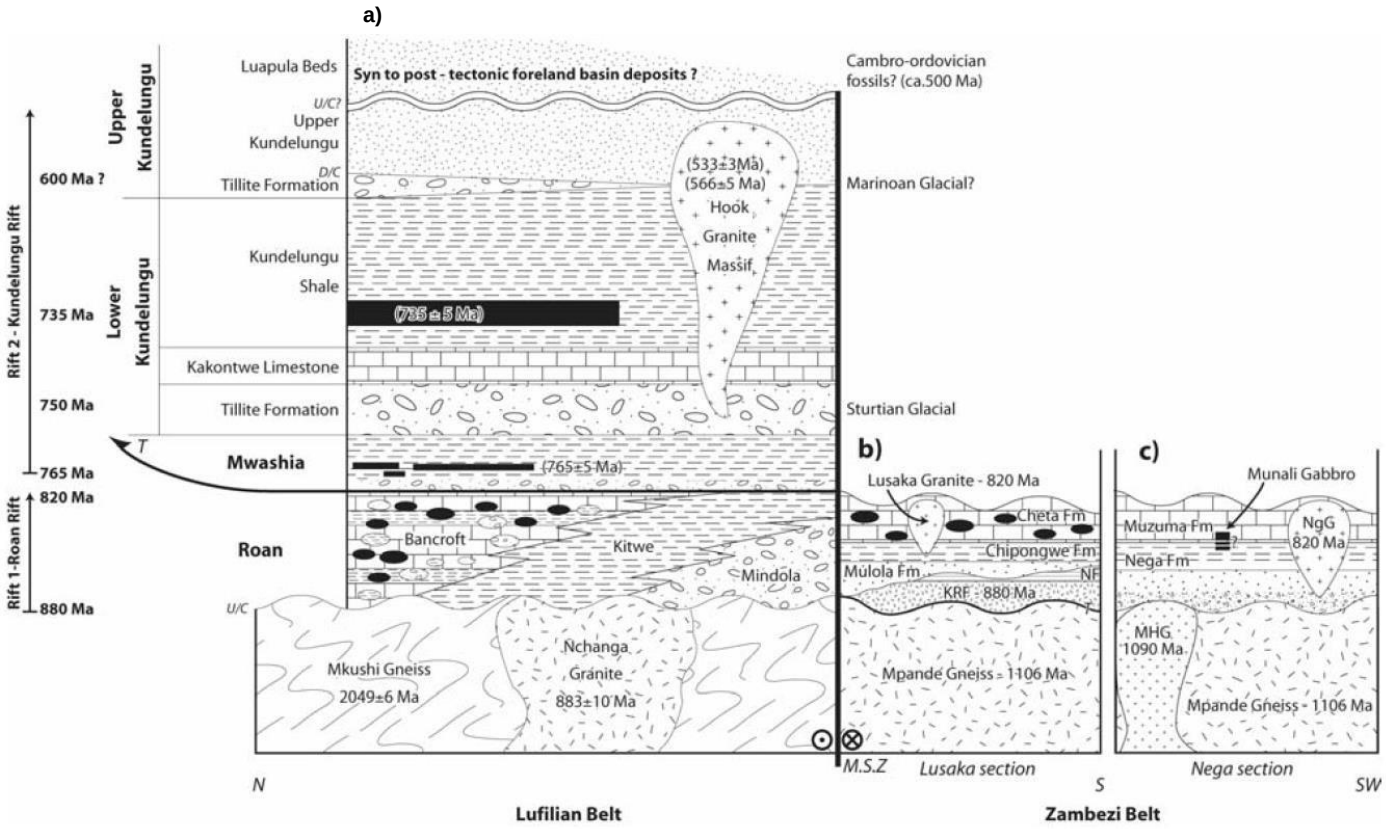

Figure 4-24. Schematic stratigraphic sequences of the Katanga Supergroup within the Lufilian Arc and Zambezi Belt. (a) The Zambian Copperbelt. (b) North of the Mpande Dome. (c) South of the Mpande Dome (Nega Section). KRF – Kafue Rhyolite Formation; NF - Nazingwe Formation; NgG – Ngoma Gneiss; MHG – Munali Hills Granite; u/C – unconformity; D/C – disconformity; T – thrust (Johnson *et al*., 2006).

4.6 DISCUSSION

Sequence 1

The arenites of Sequence 1 were deposited in a moderately high-energy environment whilst the siltstones which dominate the top of the Sequence were deposited in a lower energy system. The moderate- to high-energy environment of Sequence 2 superseded the sub-aerial alluvial fan environment of Sequence 1. Sequence 2 is interpreted to have deposited during sub-aerial mass-flow conditions within wide distributor channels or within a floodplain environment.

Similarly, the Basal Sandstone Member of the Mindola Formation, Roan Group, was deposited within a fluvial, alluvial fan, to fan-delta environment, which was of limited extent (Selley *et al*., 2005), and pinched out against the Basement rocks (Croaker, 2011).

Immature, coarse-grained grey, pink and white arkose with distinct lateral and vertical variations and fining-upward sequences with minor conglomeratic units are characteristic of the Mindola Formation of the Roan Group (Croaker, 2011). Mineralisation is occasionally hosted in the Mindola Formation, usually within the arkose units which are capped or bounded by siltstone. A similar style of mineralisation was noted in Sequence 1 within the arkose units capped by siltstone.

The laterally and vertically variable Sequence 1 correlates with the Basal Sandstone Member of the Mindola Formation of the Roan Group in the Zambian Copperbelt.

Sequence 2

The medium- to coarse-grained arkose and the subordinate siltstones of Sequence 2 were deposited via debris flows within a sheet-flood environment under peritidal to supratidal and rift-controlled conditions. The sheet flood sediments were deposited in either wide-distributor channels and/or as debris flows, where the mass movement of detrital material resulted in the mottled composition of Sequence 2.

The siltstone laminations were deposited via suspension fallout following the debris flows. The mass-flow (moderate- to high-energy) processes did not produce well-defined stratification, imbrications and sorting that is typical of an alluvial fan environment. In contrast, alluvial fan deposits which formed in channel-dominated conditions would display sorting, stratification, and imbrications (Horton and Schmitt, 1996). Turbidity current deposits develop due to suspension fallout during the waning phase of currents or distal to the turbidity zone. Both forms

of suspension fallout rarely create well-developed beds (Horton and Schmitt, 1996), as noted in Sequence 2.

The Kafue Arenite Member (Table 2-3 above) of the Zambian Copperbelt commenced with the deposition of a thin conglomeratic unit which was overlain by a thick package of medium-to coarse-grained sandstone alternating with siltstone and lesser greywacke and quartz-rich layers. The cyclicity of lithologies had an overall fining-upward nature (Croaker, 2011). The pink to grey medium-grained feldspathic and micaceous arenite of the Kafue Arenite Member is the upper unit of the Mindola Formation in the Zambian Copperbelt. Thin siltstone, and lesser sandy layers are volumetrically less than in the arenites. The Kafue Arenite Member was deposited during rift initiation within an alluvial fan environment dominated by debris flows and lesser channel flow.

The pink to grey arkosic mass flow units and subordinate siltstone beds of Shantumbu are interpreted as equivalent to the Kafue Arenite Member of the Zambian Copperbelt.

Table 4-1. The Kafue Arenite Member at the Nkana-Mindola Mine in the Zambian Copperbelt. The primary lithologies and depositional environments are summarised (Croaker, 2011).

Member	Dominant Lithologies	Lithologies	Depositional Environment
Kafue Arenite Member	Conglomerate	Basal conglomerate hosts clasts of schist, quartzite, argillite, and granite.	Debris flows within alluvial fan. Thin conglomerates represented pseudoplastic debris flow and stream channel flow. Alluvial fan to sheet flood environment.
	Sandstone and siltstone	Quartz, K-feldspar, micaceous matrix of sericite, muscovite, and quartz. Calcite, dolomite, and anhydrite increase in upper portions.	Braided stream environment with alternating high and lower energy conditions.
	Conglomerate	Basal conglomerate hosts clasts of schist, quartzite, argillite, and granite.	Debris flows within alluvial fan. Thin conglomerates represented pseudoplastic debris flow and stream channel flow. Alluvial fan to sheet flood environment.

Sequence 3

Sequence 3 formed in a shallow low-energy subtidal/shallow aqueous environment with restricted input of clastic material. The Kafue Arenite Member in the Zambian Copperbelt is conformably overlain by the Kitwe Formation. East of the Kafue Anticline in the Zambian Copperbelt, a one to two-meter-thick dolomitic layer denotes the start of the Kitwe Formation.

Elsewhere, the Kafue Arenite Member is overlain by a finely laminated dolomitic siltstone, the Copperbelt Orebody Member (Selley *et al*., 2005; Bull *et al*., 2011).

Sequence 3 is interpreted to be the equivalent of the basal part of the Copperbelt Orebody Member, specifically the footwall to the Dolomitic Facies at the Nkana-Mindola Deposit and along the eastern flank of the Kafue Anticline.

Sequence 4

The laterally extensive grey and black carbonaceous siltstones and alternating dolomitic and calcitic carbonates/breccias of Sequence 4, were interpreted to have been deposited within supratidal to subtidal, to shallow water conditions which experienced varying input of siliciclastic sediments. The grey carbonate within the Zambian Copperbelt stratigraphy is characteristic of the base of the Copperbelt Orebody Member (Bull *et al*., 2011). Interaction between shallow emergent and sub-aqueous conditions resulted in the vertically and laterally variable carbonate, arkose and siltstone of Sequence 4. Sequence 4 related to a period of increased sediment input into a sub-aqueous/marine environment, caused by either or both an increase in tectonic activity or storm activity.

Sequence 4 varied from three iron oxide-rich calc-silicate layers which alternated with grey carbonate and argillaceous carbonate, to iron oxide-rich calc-silicate layers that were accompanied by brecciated siltstone and arkose rather than an intervening carbonate. The brecciation is interpreted to relate to the dissolution of the evaporitic minerals within the siltstone and arkose. The progression from carbonate to siltstone to arkose is interpreted as an upward coarsening cycle which followed an extended period of deposition of sub-aerial sediments. The protolith is interpreted as having been deposited as an organic-rich siliciclastic unit during an emergence cycle.

Dissolution of the evaporite cements and/or nodules within the calcareous arenite unit of Sequence 4 may have resulted in the brecciation of the unit during an emerging cycle. The dolomitic breccia is crosscut by numerous dolomitic veins. The two dolomite generations indicated at least two alteration stages, an early and a late stage dolomitisation, occurred. The early dolomitisation and related change in degree of porosity guided the basinal brines through the over- and underlying siliciclastic layers altering the layers to calc-silicate layers with pervasive goethite.

Extensive development of goethite characterised both Sequences 3 and 4 and represented the oxidisation product of syngenetic and diagenetic pyrite formed by bacterial sulphate reduction

(Berner, 1984). The increase in detrital material deposited in Sequences 3 and 4 increased the nutrients available to support bacterial sulphate reduction thereby causing the precipitation of pyrite which was later oxidised to goethite. The sedimentary pyrite formation was controlled by the presence of decomposable organic matter, dissolved sulphate and reactive iron (Berner, 1984).

The siliciclastic unit of Sequence 4 underwent carbonatisation followed by oxidation/hydration. The carbonates recrystallised to fine-grained calcite whilst iron oxidation (goethite) accompanied the sericitisation of feldspar. The calcite is likely to have precipitated during deposition in a lacustrine/marine environment by way of descending seawater and ascending connate water from compaction of the underlying units. Pyrite is an interstitial mineral within the dolomite and within dolomitic veins which cross-cut Sequence 4.

The Copperbelt Orebody Member in the Roan Group of the Zambian Copperbelt consists siliciclastic turbidites and debris-flows, grey and black carbonaceous siltstones and dolomitic and calcitic carbonates. The Copperbelt Orebody Member began with a finely laminated dolomitic siltstone with lesser argillaceous arenite and massive to laminated dolomite, and the variability from arenite to siltstone to carbonate represented episodic emerging and submergence conditions (Selley *et al*., 2005).

At the Nkana-Mindola Deposit, four facies represent the Copperbelt Orebody Member (Croaker, 2011): (1) The Northern Facies is a dolomitic argillite (Nkana Metamorphic terminology kept), argillite, fine-grained arenite and grey, carbonate rich and an upper carbonaceous argillite; (2) The Southern Facies is a black carbonaceous shale, carbonate organic-rich shale and argillite, and an upper carbonaceous argillite; (3) The Arenite-Argillite Facies is characterised by sandstone and argillite with an upper carbonaceous argillite; and (4) The fourth facies is a massive dolomite layer with an upper carbonaceous argillite (Croaker, 2011). The Dolomitic Facies, which formed at the Chambishi SE and Mwambashi B deposits, is interpreted as having formed in a restricted subtidal environment with isolated stromatolitic biotherm structures (Croaker, 2011). East of the Kafue Anticline, a thin dolomitic bed denoted the start of the Copperbelt Orebody Member rather than the thick siltstone/shale layer.

The four facies of the Copperbelt Orebody Member (Table 2-3 above) are capped by carbonaceous- and pyritic-rich, grey interbedded siltstone and shale with high carbonate content. The shale and siltstones grade upward into fine- to medium-grained sandstone interbedded with siltstone and shale (Croaker, 2011). The sandstone-argillite and the dolomitic facies, which had a limited lateral extent, have historically been linked to barren gaps of base

metal mineralisation, although Broughton (2002) established the barren gaps at Konkola North Deposit were not lithologically controlled.

Alternating dry and wet cycles characterised the depositional environment of the Kitwe Formation in the Zambian Copperbelt. The evaporitic carbonate units represented cycles of low water levels, while the siltstone layers were deposited in wet cycles or high-water levels during replenishment of the marine basin. Organic carbon was typically deposited and preserved during the wet cycles. Syngenetic pyrite precipitated as disseminated, fine- to medium-crystalline clusters of subhedral grains (Machel, 2001), and was preserved in this anoxic environment. Bacterial sulphate reduction, which was responsible for the precipitation of syngenetic pyrite, formed from H_2S activity during bacterial sulphate reduction of the organic and calcareous content, scavenged iron and precipitated iron sulphide (Machel, 2001). The dry cycles were conducive for dolomitisation and carbonatisation of the evaporitic units (Theron, 2013).

Sequence 3 and Sequence 4 are considered Facies similar to the Dolomitic Facies of the Copperbelt Orebody Member (Table 2-3) at the Nkana-Mindola Deposit and along the eastern flank of the Kafue Anticline.

Sequence 5

Sequence 5 consists of three facies, facies 5a, 5b and 5c. The facies formed under environmental conditions which were dominated by water-level changes and fluctuating sediment supply. Facies 5a comprised upward fining cycle of laminated carbonate and biotite lenses, calcareous siltstone and mudstone lenses and is considered atypical of Sequence 5. Facies 5a is highly thinned in one of the drill hole cores and may have been influenced by an underlying topographic high which minimised the effect of distal turbidite currents, or sedimentation occurred within a restricted depositional environment; the quantity of information available for facies 5a is insufficient to strengthen at this stage.

The alternating siltstone-arkose-carbonate layers and brecciated siltstone of facies 5b formed in a shallow subtidal through to tidal flat environment, which underwent cycles of emergence and subaerial exposure during falling water/sea level. The arkose represented peritidal cycles overlain by subtidal cycles during shallow platform transgression or high water stands. Alternatively, the siliciclastic material washed onto the shallow marine platform during tectonic or climatic events.

Brecciation was restricted to the siltstones, the result of a physical or chemical change within the siltstone, but not all siltstone layers have undergone brecciation. The brecciated zones are

interpreted as formerly rhythmites which underwent surface exposure and collapse. Dissolution of the more soluble content, such as high-Mg-calcite, aragonite (Elrick, 1996) and evaporite minerals occurred. Dissolution of the evaporite content resulted in the collapse of the unit. Within the Roan Group in the Zambian Copperbelt, stratabound monolithic and less frequent polymictic breccias have developed. According to Bull *et al*. (2011) an evaporitic origin is preferred over a syntectonic derivation for the breccias of the Roan Group.

The siltstone formed as a low-energy suspension fallout deposit within a shallow marine setting, or distal turbidites or subaerially exposed tidal flat through to shallow subtidal depositional environments. Inflow of basinal brines, due to compaction, chemical gradients from arid periods and tectonic activity, resulted in dissolution of the evaporite (halite, gypsum and anhydrite) minerals and a supply of sulphate necessary for bacterial sulphate reduction. Fermentation of the organic matter may have produced methane (CH_4) through the release of CO_2 during bacterial sulphate reduction.

The brecciation of the siltstone may have been caused by hydrothermal fluid fracturing however, the adjacent arenite layers would also have undergone alteration and brecciation along the contacts with siltstone/shale layers, although this was not observed in the drill cores. If the brecciation was related to hydrothermal fluid fracturing, the breccia clasts would have undergone alteration and the breccia clasts would have undergone alteration along the rims, as well as rounding. Alteration of the breccia clasts was rarely noted in Sequence 5. Veins crosscut both the breccias, and the hanging wall and footwall units, indicating that later remobilisation and reprecipitation occurred.

The biotite clasts within the rhythmites of Sequence 5 represented altered rip-up clasts from storm events which indicated deposition occurred below the storm-wave base. The biotite grains may also have resulted from the alteration of pebbles, which were deposited in the nearshore to platform area, within the sub-tidal zone below the storm wave line. The clasts are orientated parallel with the faint laminations discernible in the carbonate host rock.

High-sedimentation rates in the inland environments would favour deposition of suspension-fallout in the shelf and tidal environment whilst periods of low sediment supply in the supratidal environment facilitated the deposition of carbonate layers in the shelf/lagoon environment.

The rhythmic cycles of subtidal detrital sediments intercalated with subtidal carbonate layers of facies 5c were formed from the distal or turbidity currents within a platform depositional environment. The relief of the depositional area is interpreted as having been shallow and

reflecting a platform to basin transition zone where the influence of tides and storms provided sediment input without disruption of the layering. The detrital sediments were washed down the platform slope during distal storm or high-tide activities within input of wind borne grains.

The protolith of the calcite carbonate bands was that of impure limestone whilst the calc-silicate (arenite) layers were calcareous sandstones and the biotite-dominated bands were calcareous shale, siltstone and mudstone. Within facies 5c, the dolomite bands formed a minor component derived from dolostone protoliths. Munyanyiwa and Hanson (1988), based on the carbonate dominated Muzuma Calc-Silicate Formation south of Munali Hills and the Mapanza Carbonate Formation, showed the formation of dolomite during deposition of calcareous units only rarely produced dolomite and where dolomite did form, it was under restricted conditions. Munyanyiwa and Hanson (1988) investigated the geochemistry of marbles and calc-silicate units in the Zambezi Belt and interpreted that dolomite played little to no part in the formation of the calcite carbonate bands and intercalated calcareous shales and arenaceous units.

Metamorphism attenuated the compositional banding of the rhythmites, which were of sedimentary origin. The rhythmic banding is not interpreted to have been formed by metamorphic segregation as the lenses and bands formed as a result of the depositional processes in nearshore and platform areas of the basin.

Within the rhythmites progressive conversion of gypsum and carbonate units to anhydrite resulted in wavy contacts between the siltstone and carbonate units (Figure 4-25). Alternatively, rehydration of the anhydrite to gypsum may also have resulted in this texture.

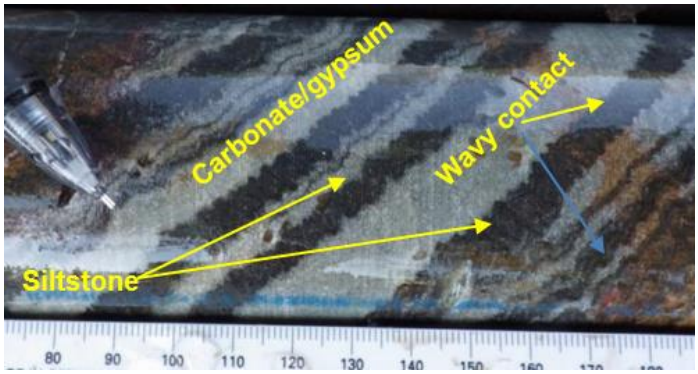

Figure 4-25. Progressive growth of anhydrite replacing gypsum within the rhythmites of Sequences 5 and 6, Shantumbu.

Facies 5a is formally correlated as the basal facies of the Chambishi Member of the Kitwe Formation. The alternating siltstone-arkose-carbonate layers of facies 5b correlates with the

alternating siltstone, arkose and carbonate layers comprising the Pelito-Arkosic Member, whilst the brecciated siltstone correlate to the Rokana Evaporite facies.

The Pelito-Arkosic Member (Table 2-3 above) in the Zambian Copperbelt is a mixed siltstone/shale, arkose and carbonate unit, with carbonate and evaporite cements where the siltstone coarsened upward to arkose, and developed into a thick silicified dolomitic bed which was capped by a laminated dolomitic siltstone/shale (Croaker, 2011). The chief distinguishing feature of the Pelito-Arkosic Member was the presence of evaporite, now represented by breccias. A shallow marine environment with periodic subaerial exposure is the interpreted depositional environment for the Pelito-Arkosic Member.

At Mufulira, Hitzmann *et al*. (2012) indicated the arenites from the lower portions of the Roan Group had variable amounts of disseminated carbonaceous matter within both primary and secondary porosity. The carbonaceous zones transgress bedding and formed from the introduction of mobile hydrocarbons infiltration into arenite reservoirs. Remobilisation of the hydrocarbon content may have caused the fracturing and brecciation (Hitzmann *et al*., 2012).

The Chambishi Member (Table 2-3 above) is underlain by the Pelito-Arkosic Member and overlain by the Antelope Member. The Chambishi Member is the first thick gritty siltstone above the Pelito-Arkosic Member, Kitwe Formation in the Zambian Copperbelt. The Chambishi Member is a basal zone of alternating carbonate and argillite laminates grading into a thicker succession of white calcitic beds with subordinate siltstone and fine-grained sandstone beds (Croaker, 2011). The overlying member, the Antelope Member of the Kitwe Formation, consists of a one-metre-thick carbonate bed comprised of shale and grit followed by carbonate.

The Chambishi Member formed during stable tectonic conditions and represented a platform succession of alternating detrital sedimentation and carbonate precipitation. The Chambishi Member using the old stratigraphic terminology is the upper unit of the Lower Roan Group. Selley *et al*. (2005) summarised this Group as a laterally extensive, meter-scale, upward fining cycles of sandstone, siltstone, dolomite, algal dolomite and local anhydrite with a preserved thickness in the Zambian Copperbelt between <30m to 8,700m. Facies 5a and 5c are formally correlated with the Chambishi Member of the Kitwe Formation.

Sequence 6

Sequence 5 and 6 were deposited within a marine setting during the waning stages of rifting as denoted by the presence of rhythmites and cyclical calc-silicate and carbonate successions, which are stratigraphy higher than the Copperbelt Orebody Member. Sequence 6 formed in a

shallow/marginal restricted marine setting with an influx of siliciclastic material, in an inner shelf lagoon area.

The alternating arenite-carbonate-siltstone succession signified deposition occurred in an environment characterised by fluctuations in sediment supply and sea-level. The contacts between the siltstone/shale layers and the arenites were erosional, due to the fluctuating energy levels and low-energy conditions. The low-energy conditions as indicated by the finer-grain sizes of the arenites and rhythmic layers of the carbonates and siltstones persisted below the storm - wave base, lagoon or tidal flat environment. The change to a calc-silicate dominated succession with lesser carbonates on Shantumbu has a striking similarity to the Antelope Member of the Roan Group.

The interbedded shales, argillite, and fine-grained sandstone of the Antelope (Clastic) Member reflected the relatively abrupt change from the preceding carbonate-dominated stratigraphy to calc-silicate lithologies (Woodhead, 2013). Woodhead (2013) interpreted the Antelope Member as having been deposited in a marginal marine environment, which was subjected to a fall in sea level, and Croaker (2011) interpreted the depositional environment was that of shallow/marginal marine to near-shore environment. The increased volume of calc-silicate units represented cyclical sedimentation during periodic influx of fluvial and aeolian sediments (Woodhead, 2013).

Sequence 7

Sequence 7 at Shantumbu formed in a marine platform/shelf setting and consists of massive blue-grey carbonate with minor intercalations of calc-silicate layers. The massive and monolithic chemical succession and the minor fine- to medium-grained sandstone are considered characteristic of the transition zone between the nearshore and deeper water regions of a basin (Horton and Schmitt, 1996). The succession of monotonous calcitic carbonate experienced prolonged periods of detrital sediment starvation and the infrequently developed calc-silicate layers of Sequence 7 (Figure 4-26) indicated deposition occurred in a platform to deep water environment which was too distal from the palaeo-shoreline to receive significant clastic input.

In the Zambian Copperbelt the carbonate succession above the Kitwe Formation is dominated by dolomite, in contrast to the calcite of Sequence 7. The dominance of calcite over dolomite at Shantumbu is ascribed to the scarcity of calc-silicate layers and the high degree of deformation and alteration the Shantumbu area was subjected to.



Figure 4-26. The light earthy brown layers of Sequence 7 are quartz-feldspar (albite) calc-silicate layers interbedded with the grey to blue carbonate, SPQ001A from 158.40m to 171m, Shantumbu.

A significant part of Sequence 7 at Shantumbu has a light earthy brown colour from the alteration of the ferrous content. Alternatively, iron-rich fluid migrated through the carbonate sequence along preferential layers and partially replaced the calcite component.

The biotite-quartz-feldspar (albite) calc-silicate layers interbedded with the grey to blue carbonate imparted a light earthy brown colouration to Sequence 7 (Figure 4-26 and Figure 4-27). The iron was sourced from alteration of microcrystalline diagenetic pyrite, which formed a subordinate component of the grey-blue calcitic carbonate layers. In addition, the yellow-brown colouration is often associated with fine laminations of biotite. The biotite originated from the alteration of calcareous siltstone, shale and mudstone laminations deposited from suspension fallout. A characteristic of the nearshore environment is the alternating carbonate units with stratified and massive detrital clastic and matrix-supported conglomeratic lenses related to episodic deposition of sediments from high energy events, such as wind, storms and tectonic activity (Horton and Schmitt, 1996).



Figure 4-27. Outcrop of the thick succession of monotonous calcitic carbonate in Sequence 7, Shantumbu.

Woodhead (2013) interpreted the Bancroft Dolomite Formation (Table 2-3 above) as an evaporitic carbonate succession which formed in a restricted, shallow carbonate ramp or shelf area, which was characterised by gradual subsidence and flooding of a low-relief platform. Croaker (2011) described the Bancroft Member as grey arenaceous dolomite, light-grey massive dolomite, grey slightly carbonaceous dolomite and dark carbonaceous dolomite, and grey to pink argillaceous dolomite.

Sequence 7 is formally correlated to the Bancroft Member of the Kirilabombwe Formation, Roan Group.

4.7 CONCLUSIONS

The petrographic inspection of the cores from the twenty-two diamond drill holes has provided new insight into the depositional environments related to the Neoproterozoic Rifting, rift climax and cessation and the related sulphide mineralisation at Shantumbu.

Chapter 4 examined the seven lithostratigraphic sequences identified in the diamond drill core, from which it was noted that the depositional environments and evolution of rift-related sediments at Shantumbu have numerous similarities with the lithostratigraphy and depositional environments within the Roan Group of the Zambian Copperbelt.

From the lithostratigraphy identified in the drill cores at Shantumbu, both the lower and upper successions of the Roan Group stratigraphy have been identified. Linking modern stratigraphic nomenclature of the Roan Group to lithostratigraphy present on Shantumbu has been achieved, albeit that Shantumbu is found at the triple junction between the Zambezi and Irumide Belts, and the Lufilian Arc, and later experienced higher-grade metamorphism than in the Zambian

Copperbelt. The correlation between the stratigraphy at Shantumbu and the Roan Group stratigraphy of the Katanga Supergroup, within the Zambian Copperbelt is summarised in Table 4-2.

Table 4-2. Katanga Supergroup stratigraphy present at Shantumbu relating the seven sequences identified in the drill cores with the equivalent Formation and Member of the Roan Group.

Supergroup	Group	Formation	Member	Sequence, Shantumbu
Katanga	Roan	Kirilabombwe	Bancroft	7
		Kitwe	Antelope	6
			Chambishi	5
			Pelito-Arkosic	5
			Copperbelt Orebody	3 and 4
		Mindola	Kafue Arenite	2
			Basal Sandstone	1

Given the correlation between the Roan Group and Sequences 1 to 7 of Shantumbu, petrographic and geochemical analyses in Chapter 5 presents detail of the alteration and metamorphism experienced at Shantumbu. The relationship between the lithostratigraphy and sulphide mineralisation on Shantumbu is further explored through mineralogy studies of Chapter 6.

CHAPTER 5

MINERALOGY AND METAMORPHISM

5.1 INTRODUCTION

Very little is known about the mineralogy of the metasedimentary units present around the Mpande Dome prior to this study. Hence, examination of the mineralogy and petrology of the Shantumbu metasediments was undertaken by the inspection of both hand specimens and thin sections, and a total of 128 thin sections were examined using transmitted and reflected optical microscopy.

A total of three thin sections from Sequence 5c were prepared for Scanning Electron Microscopy (SEM) analyses where a total of 116 sites of interest were measured. SEM analyses assisted in the identification of the mineral phases present, providing both descriptive and semi-quantitative data on the alteration events within the carbonate lithologies. Specimens were analysed using the FEI Quanta 200 SEM with EDS which is located at the University of the Witwatersrand.

The examination of the mineralogy of the metasediments on Shantumbu will facilitate an understanding of the post-depositional events, which occurred in the Shantumbu Region and provide a platform for the examination of the copper sulphide mineralisation intersected in the metasediments. Table 5-1 recapitulates the petrography and depositional environments of the Sequences of the metasediments on Shantumbu, to assist in the understanding of the mineralogical and metamorphic examination.

Table 5-1. Stratigraphy of Shantumbu summarising the principal lithologies and depositional environment for each Sequence.

Stratigraphy	Principal Lithologies	Depositional Environments
Sequence 1	Arkose and siltstone.	Alluvial fan arenites and siltstones.
Sequence 2	Feldspathic arkose and subordinate siltstone.	Debris flow and suspension fallout.
Sequences 3 and 4	Siltstone and grey calcitic and dolomitic carbonate, arenites, and calc-silicates.	Cycles of alternating arid (low water levels) and wet (high water levels) conditions.
Sequence 5	Carbonate-siltstone-arkose.	Inter- to subtidal aprons to the supratidal reef areas.
Sequence 6	Shale, siltstone, arenite, and carbonate.	Shallow/marginal marine to near-shore.
Sequence 7	Grey arenaceous carbonate.	Marine platform depositional environment.

5.2 MINERALOGY

Sequence 1

The arenite of Sequence 1 is chiefly composed of quartz, plagioclase and muscovite/sericite (20-50%) whilst K-feldspar accounts for 5 - 10% of the mineral assemblage (Figure 5-1). Interstitial minerals include calcite, ferroan dolomite (ankerite), chlorite, tourmaline, rutile, zircon, hematite, goethite and malachite. Alteration minerals within the arenite include plagioclase, K-feldspar, muscovite, sericite, dolomite, calcite, chlorite, goethite, covellite, chalcocite and secondary albite. Muscovite is present as both primary grains and the product of alteration. Sericitisation, saussuritisation and potassic alteration dominate the alteration suite with only minor albitisation and carbonatisation.

The massive grey, pink-red and cream arenite of Sequence 1 (Figure 5-1) have varied degrees of brecciation and veining. Fine-grained brecciation is often associated with the veins. The massive grey, pink-red and cream arenite (Figure 5-1) underwent varying degrees of brecciation and veining. The siltstone layers are also cross-cut by extensive veining.



Figure 5-1. Fine-grained arenite with fine siltstone laminations. (a) PQ drill hole core (SPA005) and (b) outcrop of the clean, grey, fine-grained arenite and fine siltstone laminations of Sequence 1, Shantumbu. Cross-cut veining is noted in the drill hole core.

The average grain size of plagioclase and K-feldspar within the arenite ranges from c. 200µm up to 5mm. Quartz grains are microcrystalline and average from 200 to 800µm in size, however, quartz grains up to 6mm were found. The size of the muscovite grains varies between 300µm to 1.5mm. Hematite is both coarse-grained (up to c. 5mm) and microcrystalline.

Quartz and plagioclase have recrystallised to a microcrystalline mass of interlocking plagioclase and quartz grains with sutured boundaries. The alteration of the silicate phases in Sequence 1 varies from partial to complete, with the complete dissolution of the feldspars noted (Figure 5-2).

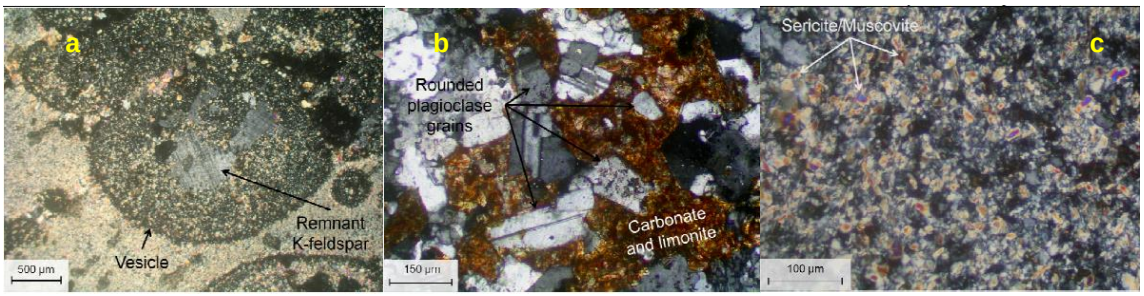

Figure 5-2. Feldspar alteration in Sequence 1, Shantumbu. (a) Vesicle hosting remnant K-feldspar grains (H08289 from PSH009 at a depth of 16.4m). Altered vesicular rhyolite with remnant K-feldspar within sericitised rhyolite vesicle from Sequence 1. The formation of K-feldspar is indicative of potassic metasomatism. Image is in cross polarised light. (b) Sub-rounded plagioclase grains and interstitial carbonate and goethite (H08294 from PSH001 at a depth of 36.24m). (c) Partial to complete alteration to muscovite and sericite and dissolution of the feldspars (H08289 from PSH009 at a depth of 16.4m). All images in cross polarised light.

Microcrystalline brecciation of arenites was noted (Figure 5-3), and the breccia cement consisting of dolomite/ankerite with minor muscovite. The red colour of the arenites was caused by iron oxide (goethite), which occurred within and around ankerite grains. The brecciated clasts are composed of interlocking quartz and plagioclase, which range in shapes from anhedral to subhedral.

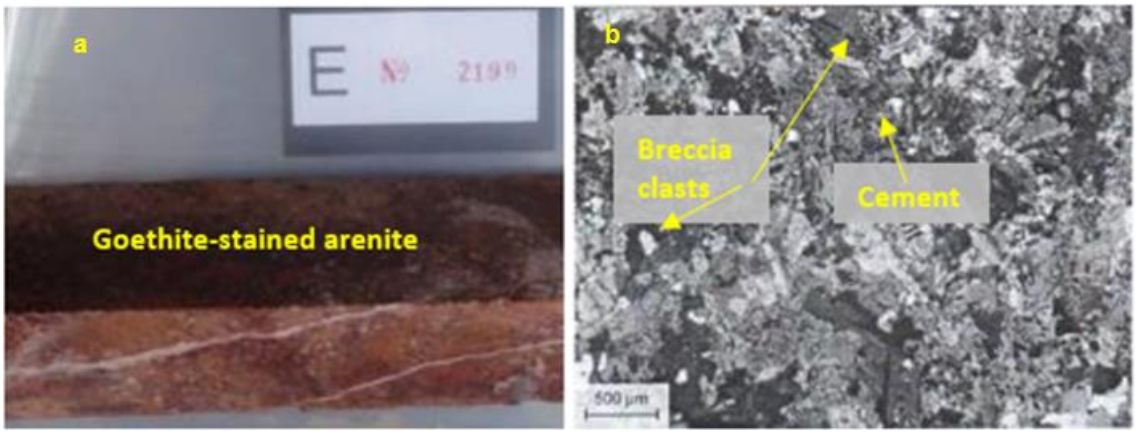

Figure 5-3. Microcrystallisation of arenite at Shantumbu. (a) Quarter core sample E2199 (SPA001 at c. 35m depth) of goethite alteration of Sequence 1 arenite. (b) Microcrystalline brecciated arenite; image in cross polarised light (E2199 SPA001 at c. 35m depth).

Fine-grained muscovite, biotite, quartz, plagioclase, K-feldspar and hematite make up the siltstone units of Sequence 1. Alteration of magnetite occurred to hematite. Deformation of the siltstone was displayed by a preferred orientation of the muscovite and biotite grains; the foliation appears to postdate the sericitisation of the siltstone. Crenulation cleavage together with the foliation indicate more than one deformation phase occurred. Hematite and sulphides cross-cut the foliation and are late-phases; they do not display deformational features. Quartz and lesser calcite veins cross-cut the siltstone.

Both macroscopic and microscopic veins cross-cut the arenite and siltstone and two vein types were noted; the one set of veins were copper-bearing sulphide veins and the second vein set consisted of quartz-plagioclase-muscovite-bearing veins with accessory hematite ± malachite ± goethite ± chlorite. The copper-sulphide/malachite-bearing veins are restricted to the arenite, whilst iron-oxide veins cross-cut both the siltstone and arenite units. A third but less common vein set was noted and consisted of dolomitic veins which contained subhedral to euhedral dolomite grains which had been variably altered to ferroan dolomite/ankerite and goethite.

Sequence 2

The mottled pink and grey feldspathic arenite, the medium- to coarse-grained pink arenite and the thin interbedded dark grey arenites of Sequence 2 are texturally massive and composed of recrystallised interlocking plagioclase and quartz, which display sutured boundaries, grain bulging and distorted lattices (Figure 5-4). These low temperature features are discussed further under the metamorphism section.

The secondary minerals present include muscovite/sericite, albite, scapolite, chlorite, biotite, malachite, hematite, goethite, dolomite and calcite. Goethite is mostly restricted to the interstitial spaces between plagioclase grains. Rutile constitutes an accessory mineral.

The plagioclase and K-feldspar grains vary in size from 400µm to 5mm, whereas the quartz grains are microcrystalline, averaging c. 400µm in diameter and up to 3mm. Muscovite grains as large as 800µm were observed.

Extensive albitisation, sericitisation, carbonatisation, silicification and oxidation/hydration affected the protolith mineralogy. Most of the albite content appears to be secondary. The order of alteration appears to be carbonatisation, sericitisation, albitisation, silicification and lastly oxidation.

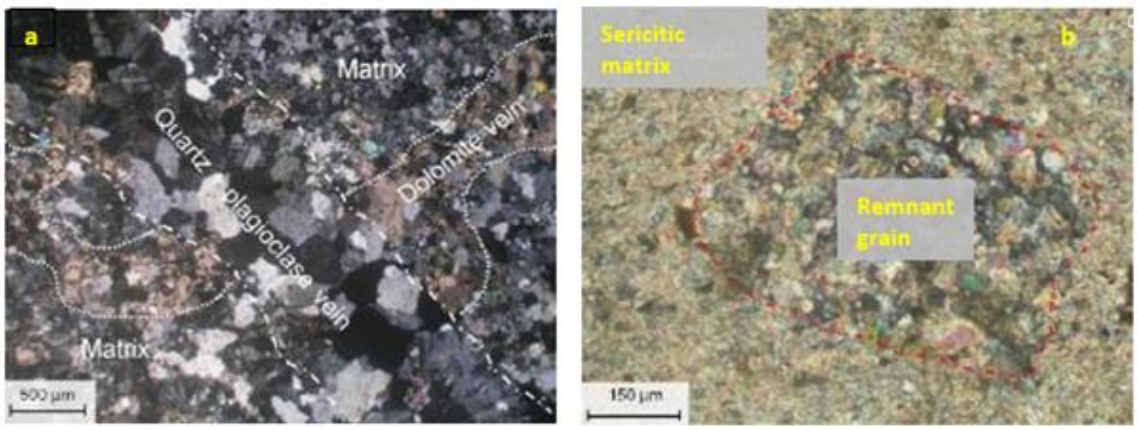

Figure 5-4. Texture of the arenites of Sequence 2, Shantumbu. (a) Interlocking recrystallised plagioclase and quartz and lesser K-feldspar displaying sutured boundaries, grain bulging and distorted lattices. A quartz plagioclase vein cross-cuts across the minerals (H08303 from PSH009 at a depth of 73.57m). (b) Sericitic matrix hosting remnant and highly altered arenite (H08297 from PSH009 at a depth of c. 79m). All images in cross polarised light.

The mottled appearance of the arenites resulted from inconsistent alteration across Sequence 2. Areas of irregularly altered plagioclase and quartz with little to no interstitial biotite and muscovite are mixed with recrystallised interlocking quartz, plagioclase, interstitial biotite and muscovite. Unaltered plagioclase and quartz grains are coarser grained than the altered grains. In the altered areas plagioclase displays Carlsbad twinning and sericitisation (Figure 5-5). The products of feldspar alteration are silica and potassium, the sources of authigenic quartz and silicification, and potassic alteration (El Desouky *et al*., 2008). The quartz grains often display undulose extinction. The scapolite noted was either a protolith mineral or an alteration product of calcareous minerals within the mudstones/siltstones, which were associated evaporitic

deposits. Chlorite pseudomorphically replaced biotite, although this is not a common feature. Anhedral hematite grains are disseminated throughout the unit.

Multiple generations of quartz and dolomite veins cross-cut the arenite. The quartz veins are dominated by coarse-grained quartz and plagioclase. Veining caused a salvage of alteration of the enclosing host rock. The minerals constituting the veins in addition to quartz and dolomite included goethite, calcite, hematite, muscovite and biotite. The veins sets host both copper sulphides (<1 - 5%) and copper oxides such as malachite (1 - 5%).

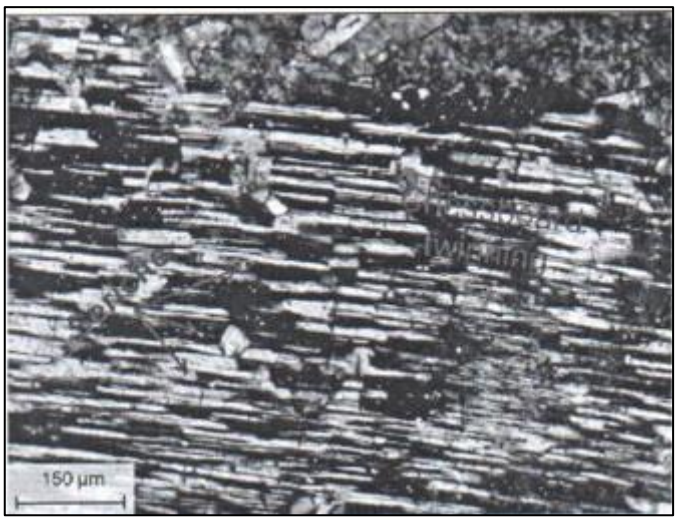

Figure 5-5. Albitised breccia with elongated plagioclase grain demonstrating Carlsbad twinning, Sequence 2, Shantumbu. Sample E2180 from drill hole SPA018.

Sequences 3 and 4

The breccias in Sequences 3 and 4 comprise fine-grained plagioclase, dolomite, quartz and muscovite/sericite. In areas where plagioclase and quartz dominate over dolomite the carbonate assumed a mottled texture. When present, goethite imparted a pink-orange colouration to the carbonate. Laths of silty material, which renders a crude illustration of the remnant bedding were noted in the carbonates. The carbonate is extensively cross-cut by dolomitic veins.

Veins with widths of less than 1cm have cut the carbonate host and contain large hematite laths and microcrystalline goethite. Subhedral inclusions of microcrystalline pyrite were observed within the hematite laths. Coarse-grained plagioclase is characteristic of the vein sets and large anhedral to subhedral dolomite and quartz grains make up the bulk of the matrix of the arenite, together with lesser microcrystalline muscovite and fine-grained plagioclase.

The average carbonate grain size is microcrystalline up to 8.5mm in diameter, while the plagioclase and K-feldspar grain sizes vary up to 4mm and the quartz grains vary up to 2. Muscovite grain size tends to be finer grained with diameter up to 850µm present. Hematite is either coarse-grained (up to c. 1cm) or microcrystalline. Pyrite grains vary between c. 120µm and 420µm.

The calcareous arenite of Sequence 4 consists of secondary plagioclase, muscovite, iron oxides (goethite) and calcite. The dolomitic breccia (Figure 5-6) of Sequence 4 is bounded by extensively altered calcareous arenite in which the plagioclase, quartz and muscovite/sericite, iron oxides and dolomite (Figure 5-6) are secondary minerals. The arenite is entirely altered displaying anhedral, interlocking secondary plagioclase (chess-board twinning) and muscovite grains with interstitial calcite, microcrystalline goethite. The iron-rich carbonate of Sequence 4 was subjected to albitisation, carbonatisation and oxidation/hydration, and cross-cut by numerous plagioclase and dolomite veins. Although the dolomitisation is extensive and pervasive it appears to have been superseded by potassic, sericitic and sodic alteration. The silicification event was succeeded by oxidation/hydration.

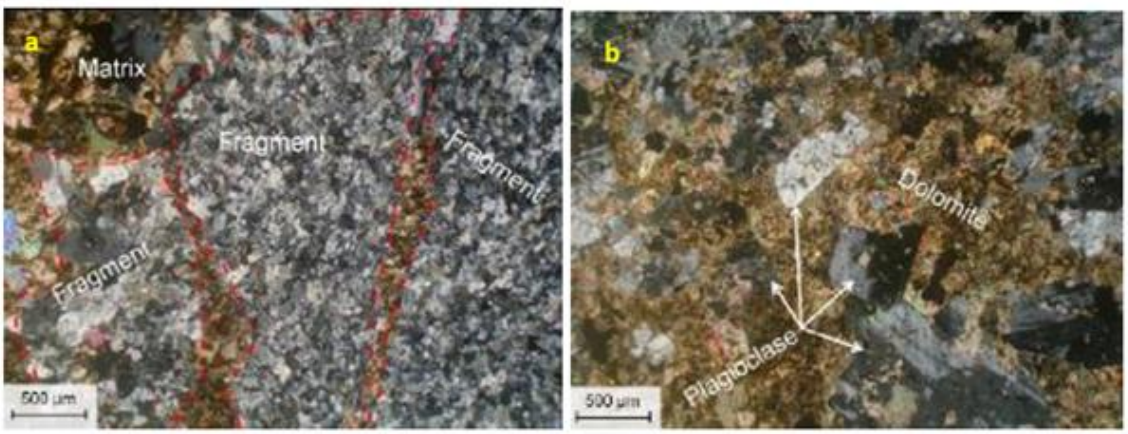

Figure 5-6. Dolomitic breccia of Sequences 3 and 4, Shantumbu. (a) Plagioclase and feldspar grains within a matrix of carbonate (H08307 from PSH007 at a depth of 118.35m). (b) Fragments of plagioclase cemented by interstitial dolomite (H08307 from PSH007 at a depth of 118.35m). All images in cross polarised light.

Muscovite occurs as both anhedral to subhedral fine grains and microcrystalline grains, where the microcrystalline grains were the product of sericitisation of plagioclase. Plagioclase grains ranged from fine-grained to very coarse and formed interlocking grains with muscovite. Carlsbad twinning showed the plagioclase was secondary. Hematite has variably altered to goethite and goethite also represented the oxidation product of magnetite and pyrite. Numerous plagioclase

and calcite veins cross-cut the carbonate of Sequence 4. The veins have the same mineral assemblage as the host arenite and dolomite.

Sequence 5

Calcite and dolomite and lesser fractured biotite clasts constitute the bulk of the mineral assemblage of facies 5a. The brecciated siltstone of facies 5b is composed of microcrystalline biotite, dolomite, plagioclase, K-feldspar, quartz, scapolite and calcite. Facies 5b exhibits layer-cake morphology of the brecciated siltstone/shale units (Figure 5-7). Biotite occurs throughout the samples with the largest grains occurring along vein boundaries (Figure 5-8 a to i). Quartz and calcite veins cross-cut the siltstone (Figure 5-8 g and h). Texturally, facies 5b occurs as either finely laminated to massive siltstone or brecciated siltstone with the breccia clasts which caused the moderately developed foliation and cleavage. Isoclinal to ptygmatic folds are common within the banded carbonate and more competent siltstone layers.

The rhythmic fabric resulted from the planar directionality of compositional distinctive lamellae. The lamella formed continuous to semi-continuous layers and in facies 5c consisted of carbonate-rich and pelite-rich lamellae. The carbonate layers vary from white to grey carbonate which were intercalated with thin, millimetre to ten centimetres, aegirine- and biotite-dominated dark green to black lenses. Overall, the millimetre to centimetre planar fabric reflects grain-size and mineralogical variations were enhanced during metamorphism, where the compositional segregation, which had resulted in a strong planar protolith fabric altered to a more diffuse compositional banding, particularly in the very thin lamellae.

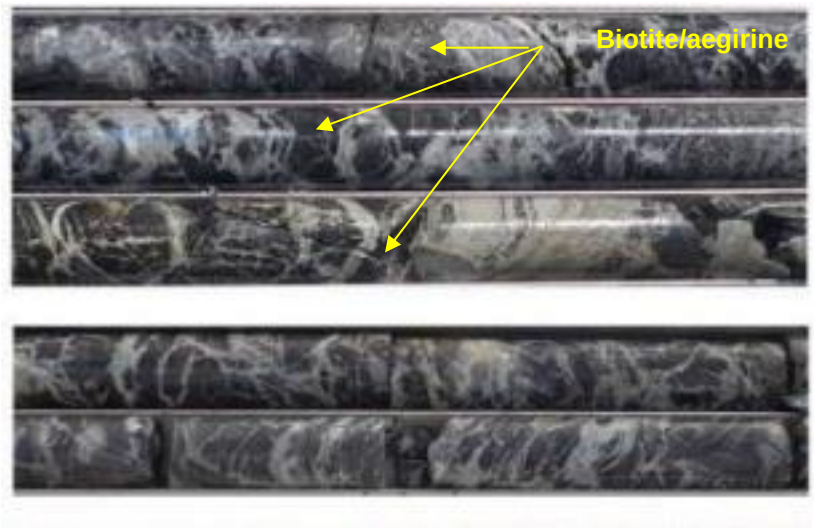

Figure 5-7. Brecciated siltstone from Sequence 5, Shantumbu, facies 5b composed of microcrystalline biotite, dolomite, plagioclase, K-feldspar, quartz, scapolite and calcite.

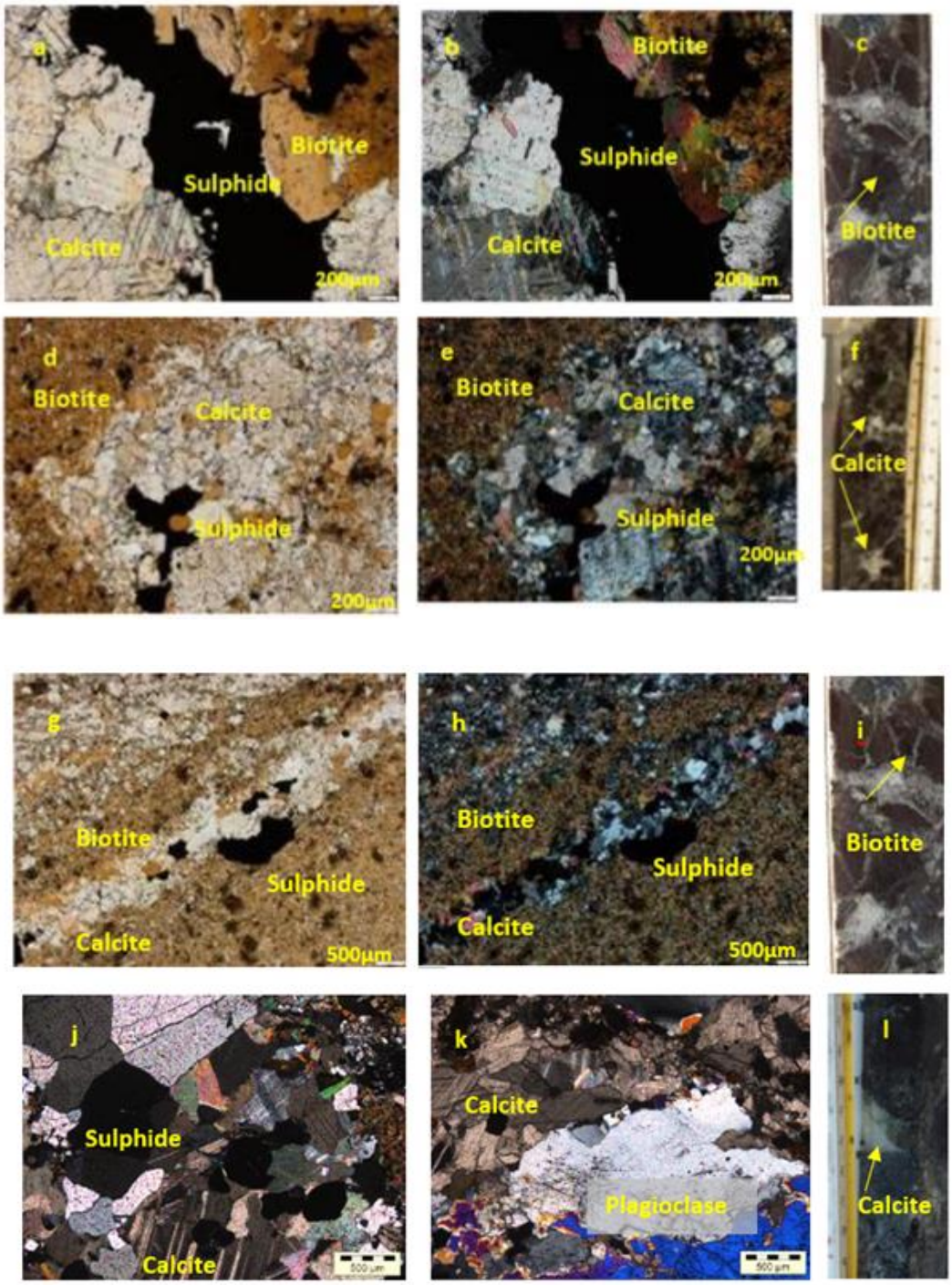

Figure 5-8. The mineralogy of the siltstone breccias is dominated by plagioclase, quartz, biotite, K-feldspar, and calcite, Sequence 5, Shantumbu. (a) Sulphide-bearing vein hosted by calcite and biotite-bearing brecciated siltstone – plane polarised light. Sample E2270B plane polarised light (200µm) (PSH003 at a depth of c. 180m). (b) Sulphide-bearing vein hosted by calcite and biotite-bearing brecciated siltstone-cross polarised light. Sample E2270B cross polarised light (200µm) (PSH003 at a depth of c. 180m). (c) Brecciated siltstone dominated by biotite clasts (core sample). Sample E2271C plane polarised light (200µm) (PSH003 at a depth of c. 180m). (d) and (g) Disseminated sulphides hosted by calcite and biotite-bearing brecciated siltstone - plane polarised light. (d) Sample E2270C cross polarised light (200µm) (PSH003 at a depth of c. 175m). (g) Sample E2260 cross polarised light (500µm) (PSH003). (f) Brecciated siltstone dominated by biotite clasts (core sample). Sample E2271B cross polarised light (200µm) (PSH003 at a depth of c. 175m). (e) (h) and (j) Disseminated sulphides hosted by calcite and biotite-bearing

brecciated siltstone - cross polarised light. (e) Sample E2271B plane polarised light (200µm) (PSH003 at a depth of c. 180m). (h) Sample E2257 cross polarised light (500µm) (PSH003 at a depth of c. 165m). (i) and (l) Brecciated siltstone domainted by biotite clasts (core sample). (i) Sample E2271B cross polarised light (200µm) (PSH003 at a depth of c. 180m). (l) Sample E2271 (PSH003 at a depth of c. 180m). (k) Interlocking and anhedral plagioclase. Sample E2270 (PSH003 at a depth of c. 175m). (j) Sample E2270B cross polarised light (200µm) (PSH003 at a depth of c. 175m). (m) Sample E2271B (PSH003 at a depth of c. 180m).

Quartz and calcite veins cross-cut the siltstone. The calcite veins are often boudinaged. The quartz grains vary from rounded to anhedral, and from fine- to coarse-grained. Coarse euhedral to subhedral pyrite grains are hosted within quartz veins. Magnetite is most abundant in proximity to calcite veins and as anhedral to subhedral grains within the veins. The magnetite grains have altered to hematite with remnant cores of magnetite enclosed by the hematite. Within the siltstone, hematite is present as euhedral grains.

The rhythmic banding of carbonate and siltstone/mudstone of facies 5c is well developed (Figure 5-9). A lesser number of arenite layers developed within facies 5c.

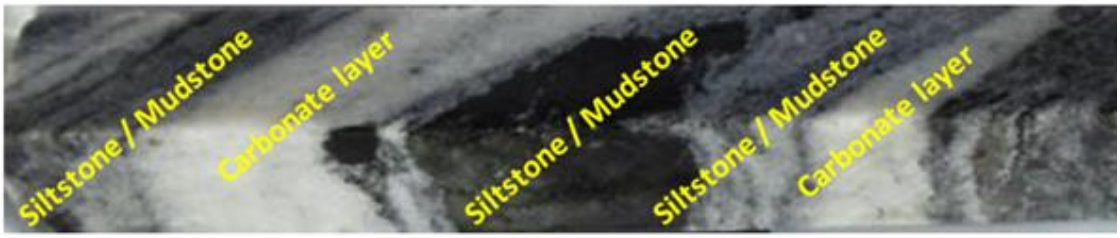

Figure 5-9. Rhythmic banding of carbonate and siltstone/mudstone in Sequence 5, facies 5c, Shantumbu; quarter core sample E2181 from SPA018 at an approximate depth of 86m.

The carbonate and siltstone bands consist of calcite, green and tan brown aegirine (Figure 5-10), quartz, hornblende, plagioclase (albite), K-feldspar and biotite, with accessory epidote, apatite, sphene, zircon, garnet (Figure 5-10a to d), sericite, hematite and sulphides (Figure 5-10). The calcite grains recrystallised demonstrated by the annealed and sutured grain boundaries. Both normal and undulose extinction are characteristic of the quartz grains. Feldspar (albite) grains have irregular grain boundaries. Epidote occurs as fine- to large-grained subhedral grains while sphene is anhedral, fine-grained and fragmented.

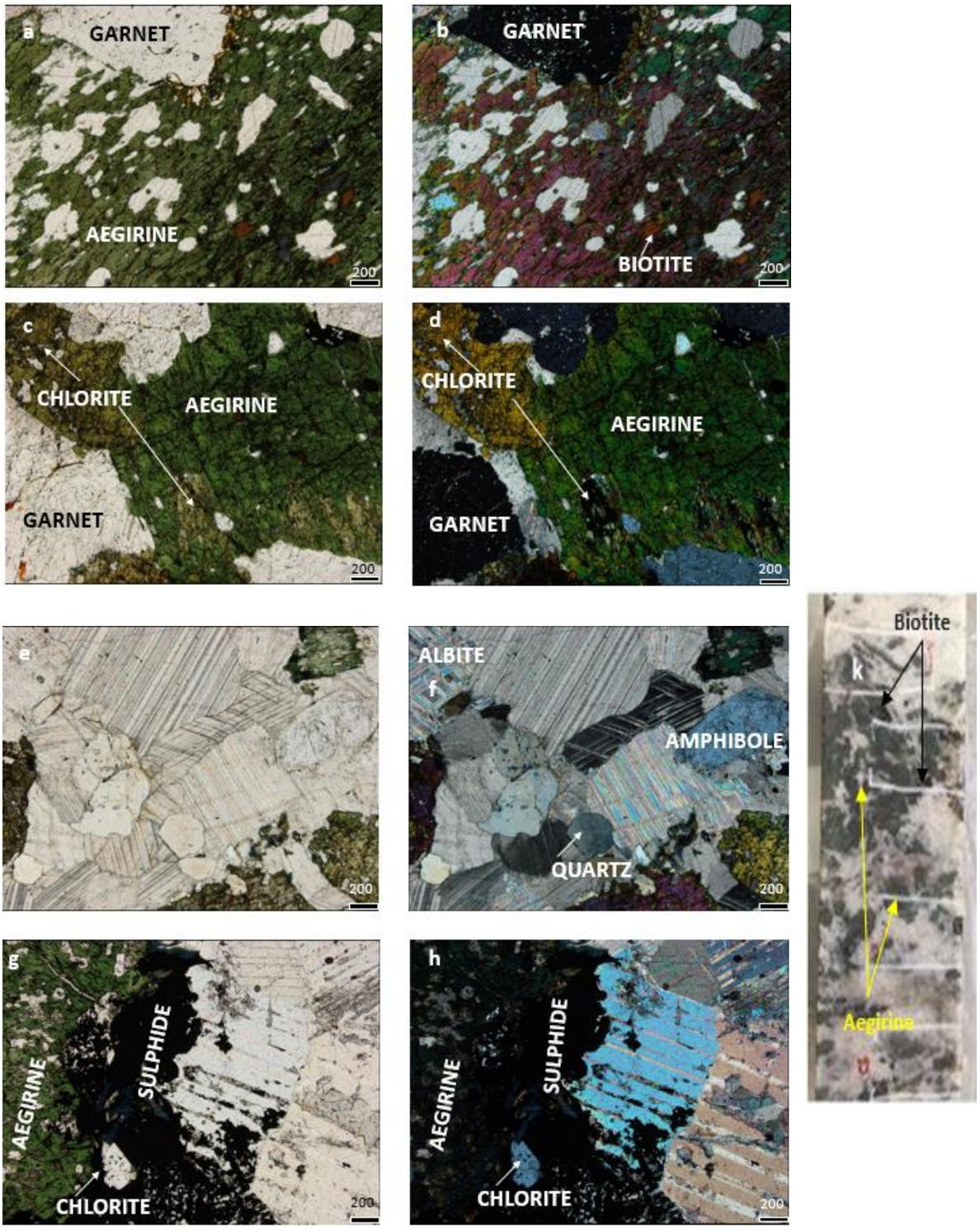

Continued next page

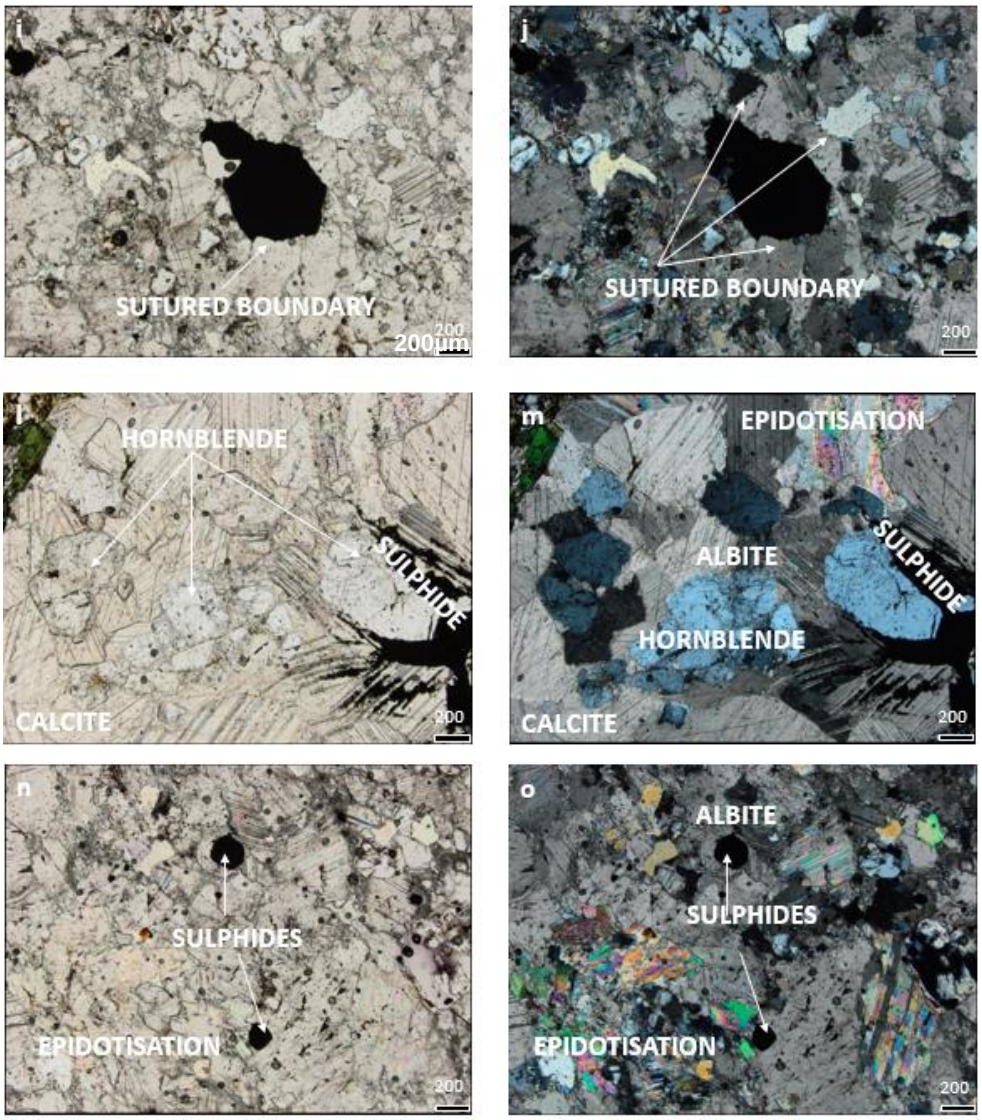

Figure 5-10. Mineralogy of the rhythmite bands - Sequence 5, facies c. Shantumbu (a) Garnet, calcite and aegirine phenocrysts; plane polarised light. Sample E2213A plane polarised light (200µm) (SPA015). (b) Garnet, calcite and aegirine phenocrysts; cross polarised light. Sample E2213A cross polarised light (200µm at a depth of c. 30m) (SPA015). (c) Inclusion of chlorite grains within coarse-grained aegirine; plain polarised light. E2213B plane polarised light (200µm) (SPA015 at a depth of c. 30m). (d) Inclusion of chlorite grains within coarse-grained aegirine; cross polarised light. E2213B cross polarised light (200µm) (SPA015 at a depth of c. 30m). (e) Rounded grains of amphibole and quartz within a calcite matrix; plane polarised light. E2213C plane polarised light (200µm) (SPA015 at a depth of c. 30m). (f) Rounded grains of amphibole and quartz within a calcite matrix; cross polarised light. E2213C cross polarised light (200µm) (SPA015 at a depth of c. 30m). (g) Sulphides along the contact between the siltstone and calcite layers; the siltstone layer consists of coarse-grained and fragmented aegirine; plane polarised light. E2213D plane polarised light (200µm) (SPA015 at a depth of c. 30m). (h) Sulphides along the contact between the siltstone and calcite layers; the siltstone layer consists of coarse-grained and fragmented aegirine; cross polarised light. E2213D cross polarised light (200µm) (SPA015 at a depth of c. 30m). (i) Sutured boundaries between grains of calcite and quartz with sulphides; plane polarised light. E2213D Plane polarised light (200µm) (SPA015 at a depth of c. 30m). (j). Sutured boundaries between grains of calcite and quartz with sulphides; cross polarised light. E2213D cross polarised light (200µm) (SPA015 at a depth of c. 30m). (k) Deformed and metamorphosed rhythmite core sample from Sequence 5, facies c, denoting the fragmented siltstone layers and carbonate layers. E2213A plane polarised light (200µm) (SPA015 at a depth of c. 30m). (l) Rounded grains of albite, hornblende, and quartz within matrix of calcite. Saussuritisation (epidote) is present in the upper right corner of the plan polarised thin section

photomicrograph. E2213A cross polarised light (200µm) (SPA015 at a depth of c. 30m). (m) Rounded grains of albite, hornblende, and quartz within matrix of calcite. Saussuritisation (epidote) is present in the upper right corner of the cross polarised thin section photomicrograph. E2213D plane polarised light (200µm) (SPA015 at a depth of c. 30m). (n) Rounded grains of albite and sulphides within matrix of calcite. Saussuritisation (epidote) is present in the lower left corner of the plan polarised thin section photomicrograph. E2213D cross polarised light (200µm) (SPA015 at a depth of c. 30m). (o) Rounded grains of albite and sulphides within matrix of calcite. Saussuritisation (epidote) is present in the lower left corner of the plan polarised cross section photomicrograph. facies 5c carbonate sample.

The silicates minerals underwent albitisation and epidotisation/saussuritisation and calcite partially replaced silicate minerals. Epidote replaced plagioclase and occurred associated with aegirine and biotite.

The aegirine (Na, Fe^{3+}, Fe^{3}+ Si_2O_6) grains are coarse-grained and fragmented, hosting grains of biotite, garnet and zircon. The coarse-grained aegirine is bright green, elongated and fragmented forming distinctive layering within the carbonates of Sequence 5. The tan-coloured aegirine grains are finer-grained and the elongated crystal shape is ill-developed. Alteration of the aegirine to iron oxides was noted in several thin sections. Zircon grains noted were elongated parallel with the fabric of the clinopyroxene. Quartz, a minor phase, is restricted to the interstitial spaces with anhedral fragmented and coarse-grained pyrrhotite/pyrite and sodic clinopyroxene grains. Biotite was partially altered to chlorite along grain boundaries. Remnants of interlocking, massive plagioclase grains as well as quartz grains occur in association with biotite.

Within the rhythmic carbonate-siltstone layers, biotite grains up to 1.7cm were observed. Plagioclase and subordinate K-feldspar, epidote and clinopyroxene grains measured up to 5mm in diameter, whilst quartz was microcrystalline up to 1mm. Dolomite and calcite grains measuring up to 4.8mm were noted. Muscovite grains ranged in size up to 900µm. Hematite varies from microcrystalline to 1mm. Amphibole grains averaged c. 500µm and apatite grains measuring 200 - 600µm were noted. Zircon and epidote grains both measured c. 250µm. Scapolite grains measured up to 1.5mm.

Figure 5-10 (a to o) illustrate aegirine, calcite, biotite and feldspar forming the carbonate layers of the rhythmic 5c facies. Aegirine is widespread throughout non-brecciated shale units, but absent from the brecciated units. Calcite veins cross-cut the siltstone host mineral assemblage (Figure 5-10).

The siltstone bands within the regularly and closely-spaced rhythmite of facies 5c have a well-developed schistosity with phyllosilicate mica grains intergranular to the non-micaceous grains (Figure 5-11). Biotite, muscovite/sericite, pyroxene, calcite and quartz and accessory amphibole

formed the bulk of the siltstone bands' mineralogy. The quartz, amphibole and pyroxene grains are typically anhedral and triple junctions are displayed by the calcite grains. The equigranular quartz grains often displayed halos/pressure shadows. All minerals are elongated in a preferred direction.

The siltstone banding in micrographs of Figure 5-11, consists of granoblastic calcite and quartz with accessory mica flakes. The micas are strongly foliated. Relict and fragmented amphibole grains form interstitial to quartz. Polycrystalline to monocrystalline quartz grains are present, together with undulose extinction and pressure shadows. Calcite grains are inequigranular and anhedral and elongated according to the foliation, displaying an orthomylonitic fabric. Quartz grains display pressure shadows and are fine-grained, and the larger quartz grains display domains related to strain.

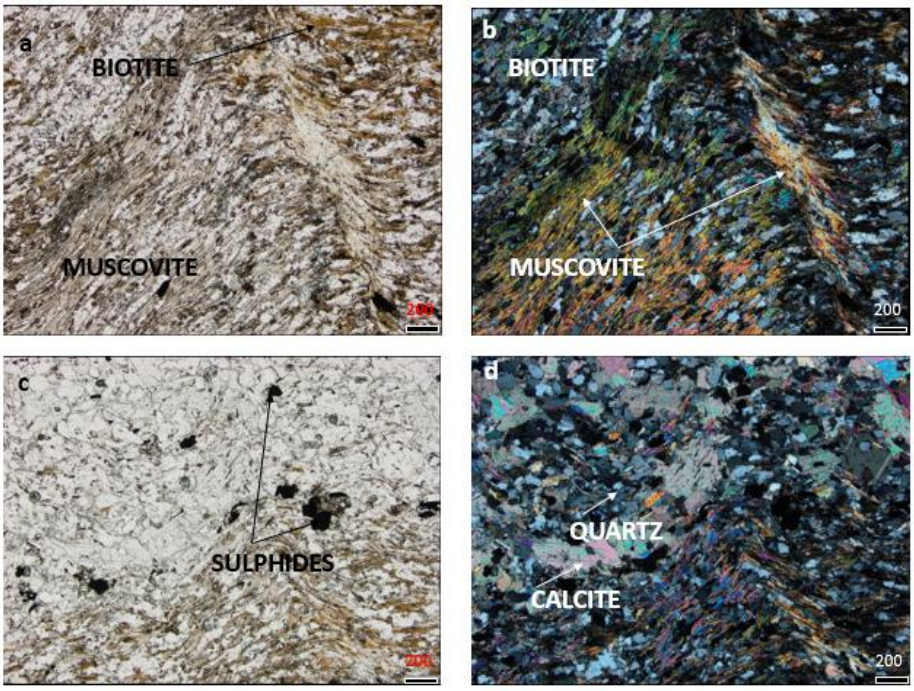

Continued next page

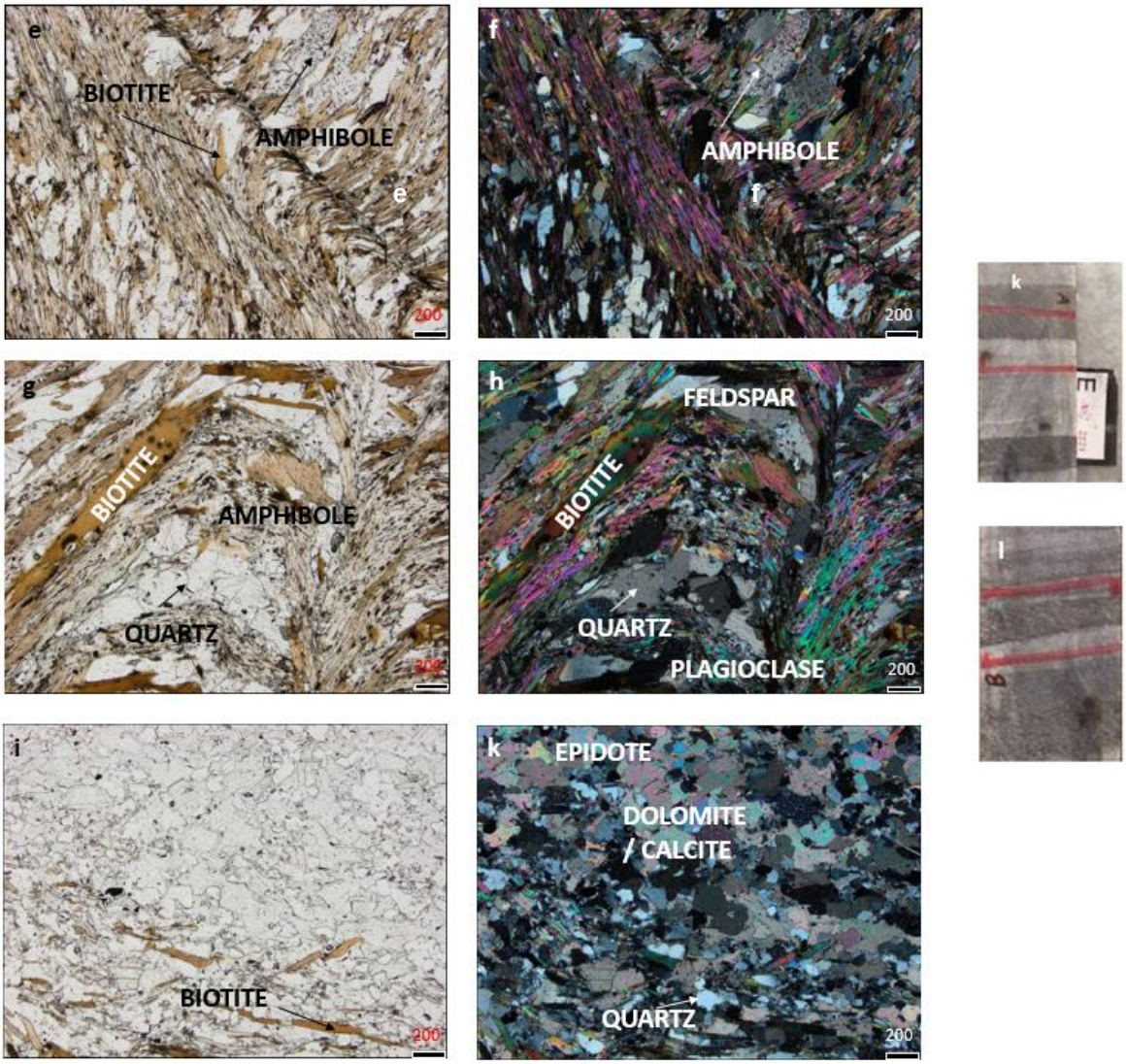

Figure 5-11. The well-developed schistosity imparted by the phyllosilicate mica grains interspersed by various minerals such as epidote, plagioclase and amphibole in Sequence 5, facies c, Shantumbu (a) Elongated quartz grains in the direction of the biotite and muscovite foliation; plane polarised light. Sample E2224A plane polarised light (200µm) (SPA033A at a depth of c. 85m). (b) Elongated quartz grains in the direction of the biotite and muscovite foliation; cross polarised light. Sample E2224A cross polarised light (200µm) (SPA033A at a depth of c. 85m). (c) Interstitial sulphides, granoblastic quartz and calcite to biotite and muscovite; plane polarised light. Sample E2224 plane polarised light (200µm) (SPA033A at a depth of c. 85m). (d) Interstitial sulphides, quartz and calcite to biotite and muscovite; cross polarised light. Sample E2224A cross polarised light (200µm) (SPA033A at a depth of c. 85m). (e) Polycrystalline to monocrystalline quartz grains; plane polarised light. Sample E2221A plane polarised light (200µm) (SPA033A at a depth of c. 115m). (f) Polycrystalline to monocrystalline quartz grains; cross polarised light. Sample E2221A cross polarised light (200µm) (SPA033A at a depth of c. 115m. (g) Interstitial plagioclase and amphiboles to the foliation imparted by biotite and muscovite; plane polarised light. Sample E2221B (200µm) (SPA033A at a depth of c. 115m). (h) Interstitial plagioclase and amphiboles to the foliation imparted by biotite and muscovite; cross polarised light. Sample E2221B cross polarised light (200µm) (SPA033A at a depth of c. 115m). (i) Orthomylonitic fabric dominated by quartz and calcite grains. Quartz displays pressure shadows; plane polarised light. Sample E2221B plane polarised light (200µm) (SPA033A at a depth of c. 115m). (j) Orthomylonitic fabric dominated by quartz and calcite grains. Quartz displays pressure shadows; cross polarised light. Sample E2221B cross polarised light (200µm) (SPA033A at a depth of c. 115m). (k) and (l) Closely-spaced rhythmite bands of facies 5c; core samples. (k) Sample E2224 (SPA003A at a depth of c. 85m. (l) Sample 2221A (SPA033A at a depth of c. 115m).

The brecciated arenites of facies 5c consist of plagioclase, clinopyroxene, epidote, quartz, biotite, dolomite, calcite, and amphibole. Muscovite, sericite, goethite and hematite constitutes the minor minerals present (Figure 5-12). Columbite, a sodic mineral, together with secondary albite, indicated that the lithologies were subjected to sodic alteration. Plagioclase grains with Carlsbad twinning and sutured boundaries were cemented by biotite, calcite, muscovite, hematite, chlorite and goethite.

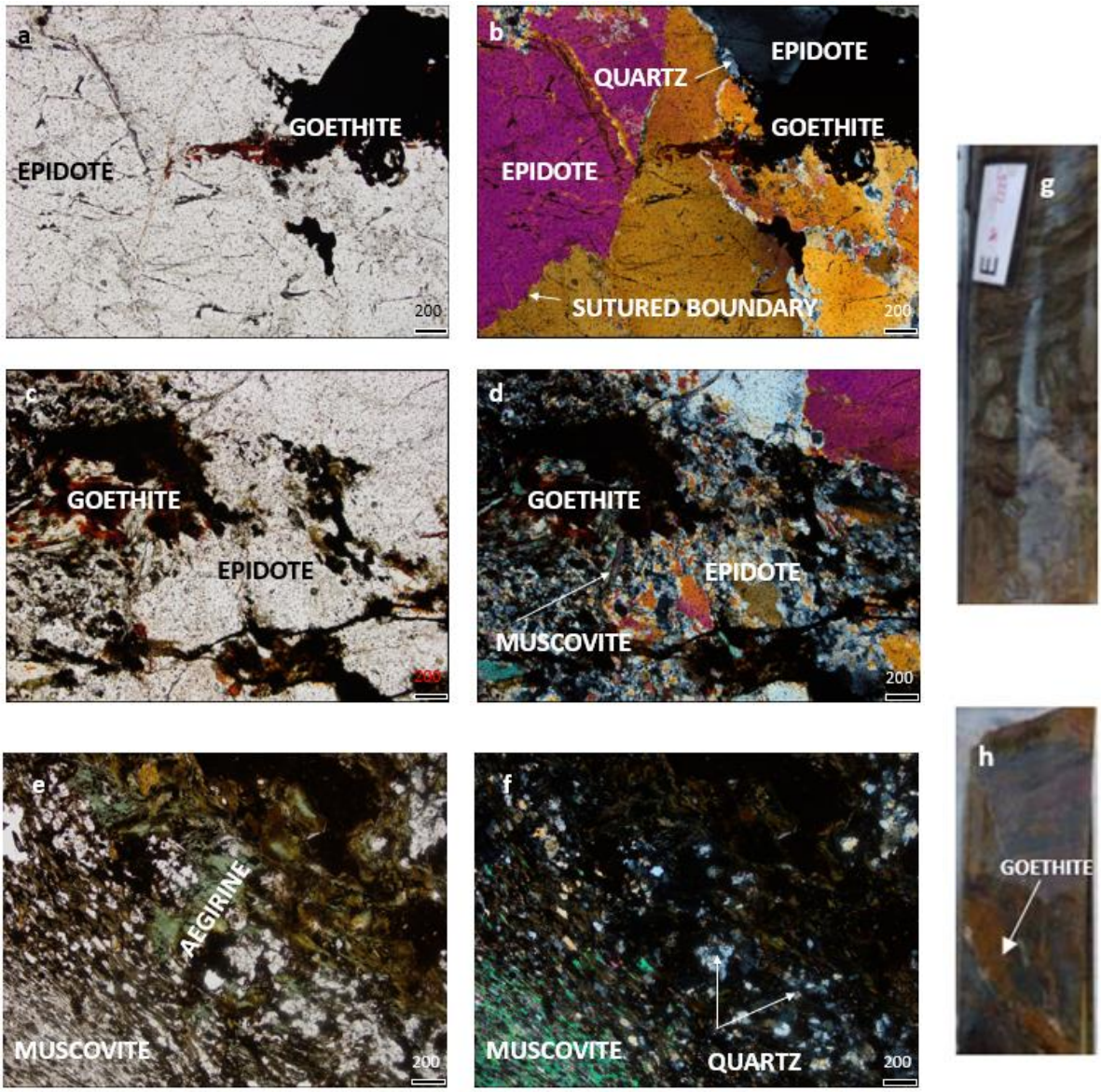

Figure 5-12. Brecciated arenite of Sequence 5, facies c, Shantumbu. (a) Sutured boundaries of epidote grains. Quartz and goethite occur interstitial to the larger epidote grains; plane polarised light. Sample E2225 plane polarised light (SPA033A at a depth of c. 36m). (b) Sutured boundaries of epidote grains. Quartz and goethite occur interstitial to the larger epidote grains; cross polarised light. Sample E2225 cross polarised light (SPA033A at a depth of c. 36m). (c) Pervasive goethite within a sample dominated by muscovite and epidote; plane polarised light. Sample E2225 plane polarised light (SPA033A at a depth of c. 36m). (d) Pervasive goethite within a sample dominated by muscovite and epidote; cross polarised light. Sample E2225 cross polarised light (SPA033A at a depth of c. 36m). (e) Aegirine and quartz within the

penetrative fabric stemming from the presence of micas; plane polarised light. Sample E2220 plane polarised light (SPA033A). (f) Aegirine and quartz within the penetrative fabric stemming from the presence of micas; cross polarised light. Sample E2226 cross polarised light (SPQ002 at a depth of c. 95m). (g) Brecciated arenite of Sequence 5, facies c; core sample. Sample E2226 (SPQ002 at a depth of c. 95m). (h) Pervasive alteration to goethite in brecciated sample from Sequence5, facies c; core sample. Sample E2226 (SPQ002 at a depth of c. 95m). All samples are at 200μm.

Plagioclase, typically albite, has variably altered to sericite and experienced weak carbonatisation noted from the occurrence of microcrystalline dolomite grains within the plagioclase grains. Alteration of plagioclase to epidote (saussuritisation) is extensive. Anhedral hematite grains occur in close association with biotite grains within the matrix. Quartz grains have sutured and bulging grain boundaries.

Dolomite and calcite veins cross-cut the arenite and host anhedral pyrite and hematite grains. Sulphides are restricted to veins crosscutting the brecciated arenite. Chalcopyrite occurred as fine anhedral inclusions within anhedral pyrite grains, indicating that at least two episodes of sulphide growth had occurred, these being the initial precipitation of diagenetic sulphides and secondly, replacement. Chalcopyrite also occurs as large anhedral grains (up to c. 7mm in diameter) within fractures. Anhedral marcasite and magnetite are present to a lesser extent and restricted to the veins.

Several generations of veins were noted in Sequence 5; some veins are entirely composed of pyrite, while others of quartz. Overall, two main vein sets were noted in facies 5b, the veins which either predated the brecciation as they terminated at clast boundaries or post-dated the brecciation.

Scanning Electron Microprobe of Facies 5c

A total of three thin sections (E2213B, E2213C and E2213D) from facies 5c were prepared for SEM analyses and a total of 116 sites of interest were measured. The SEM analyses were undertaken to confirm, or otherwise, the presence of aegirine and glaucophane which were identified in thin section microscopy work. The mineral phases present, together with descriptive and semi-quantitative data provided insight into the sodic alteration of the carbonate above the Copperbelt Orebody Member.

Mineral species noted in E2213B Points of Interest 1 to 5 (Figure 5-13 to Figure 5-17) include calcite, quartz, apatite, albite, pyroxene (aegirine-augite), biotite, accessory zircon and garnet (titanite/grossular/andradite). Pyrrhotite/pyrite were the only sulphides present. Interstitial

elongated sphene, garnet and zircon are hosted together with biotite within the sodic clinopyroxene grains.

The SEM graphs for the clinopyroxene suggest a combination of the end-members aegirine-augite, noted by the presence of Na together with Mg and Ca. Both brown and green clinopyroxene were noted, with replacement between aegirine and augite or sodic clinopyroxene and sodic amphiboles, within the plane polarised light thin section micrographs for E2213. As noted during microscopy work, the tan-coloured aegirine grains are finer-grained than the green version and the elongated crystal shape was ill-developed.

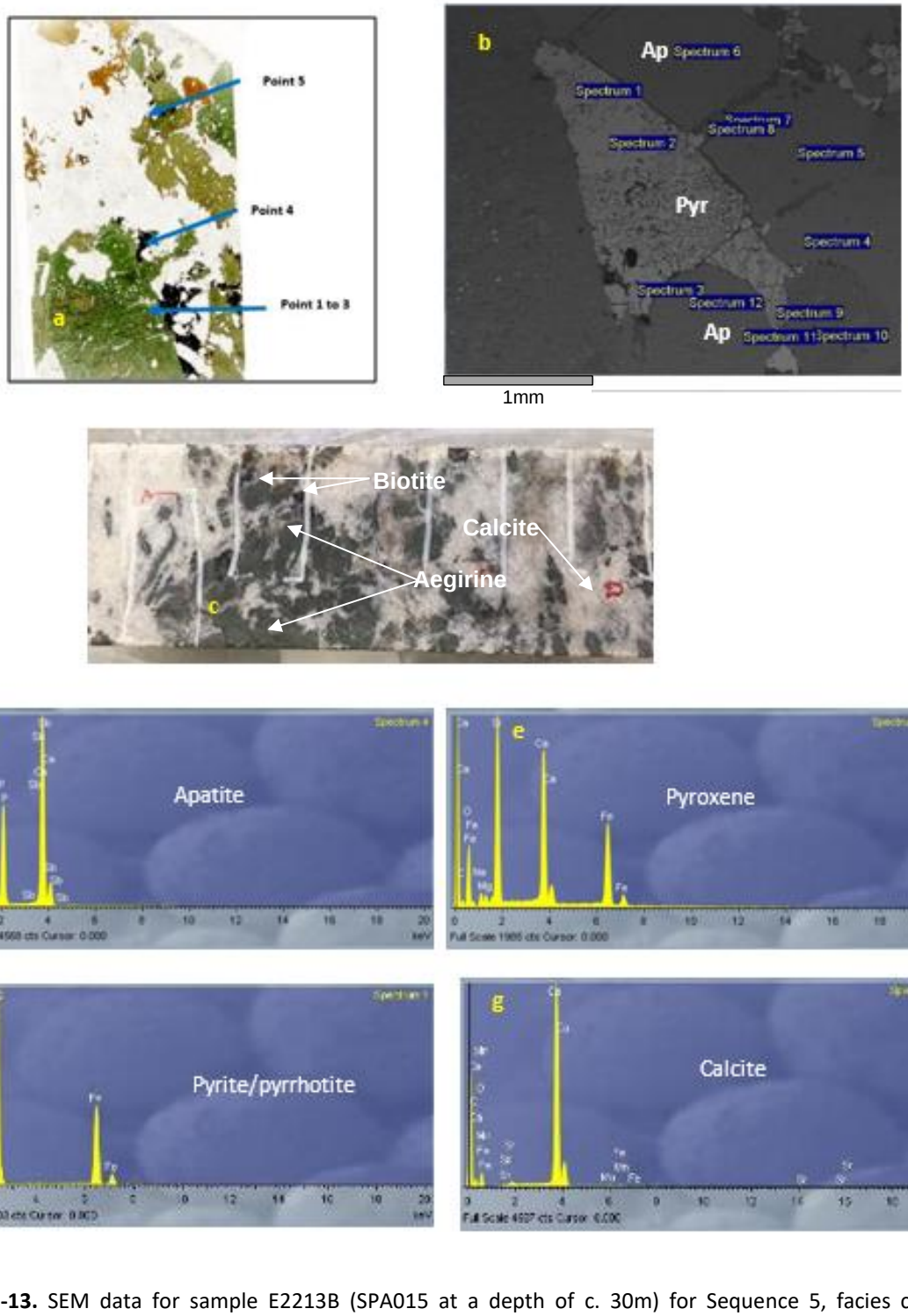

Figure 5-13. SEM data for sample E2213B (SPA015 at a depth of c. 30m) for Sequence 5, facies c, Shantumbu. (a) Thin section showing Points 1 to 5. (b) Backscattered electron image with locations of the eleven spectra; Ap – apatite, Pyr - pyrrhotite. (c) Half core sample from which the thin section was derived. (d) Mineral spectrum for apatite. (e) Mineral spectrum for pyroxene. (f) Mineral spectrum for pyrite/pyrrhotite. (g) Mineral spectrum for calcite.

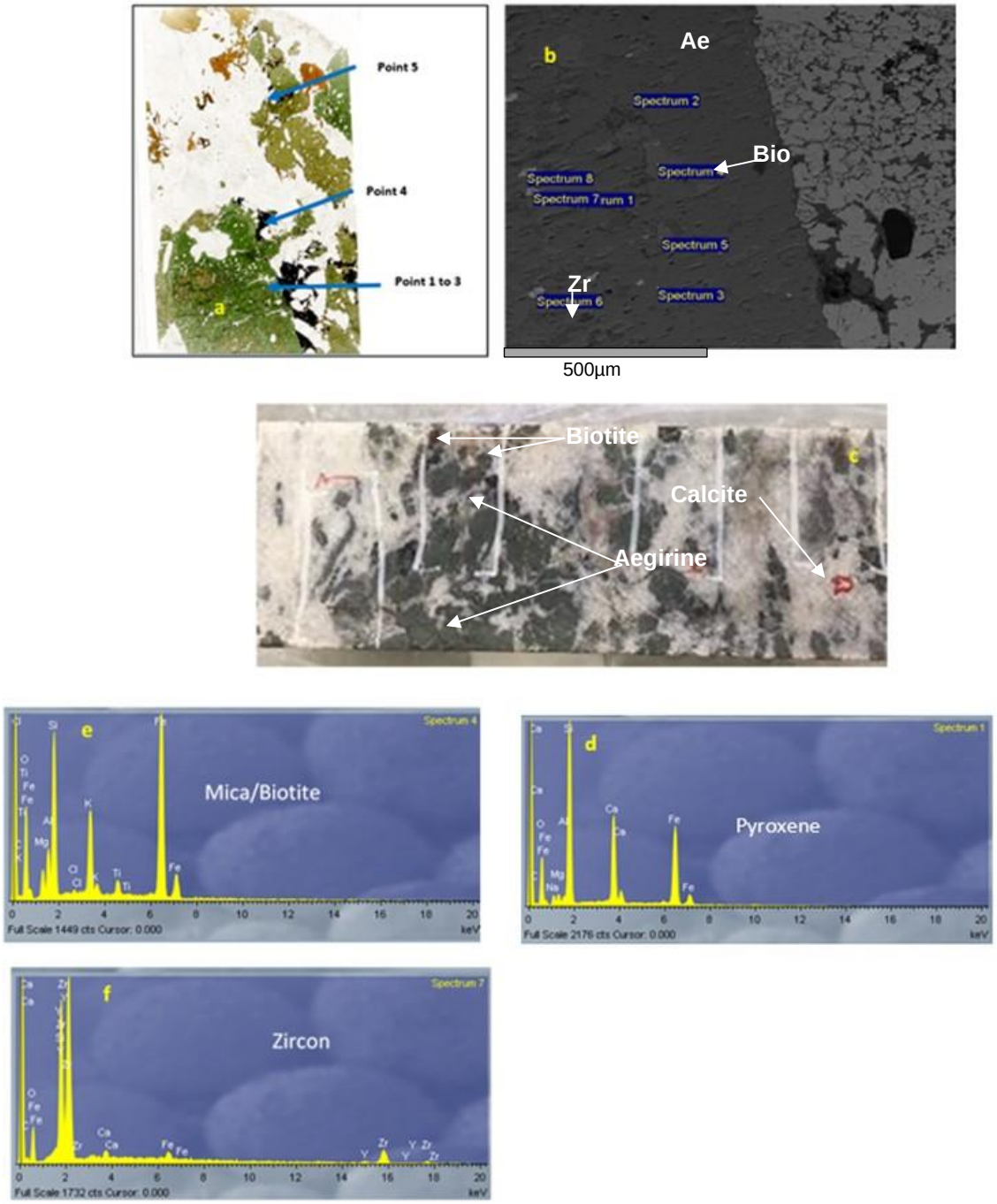

Figure 5-14. SEM data for sample E2213B (SPA015 at a depth of c. 30m) for Sequence 5, facies c, Shantumbu. (a) Thin section showing Points 1 to 5. (b) Backscattered electron image with locations of the eight spectra; Ae – aegirine, Bio – biotite, Zr - zircon. (c) Half core sample from which the thin section was derived. (d) Mineral spectrum for pyroxene. (e) Mineral spectrum for mica/biotite. (f) Mineral spectrum for zircon.

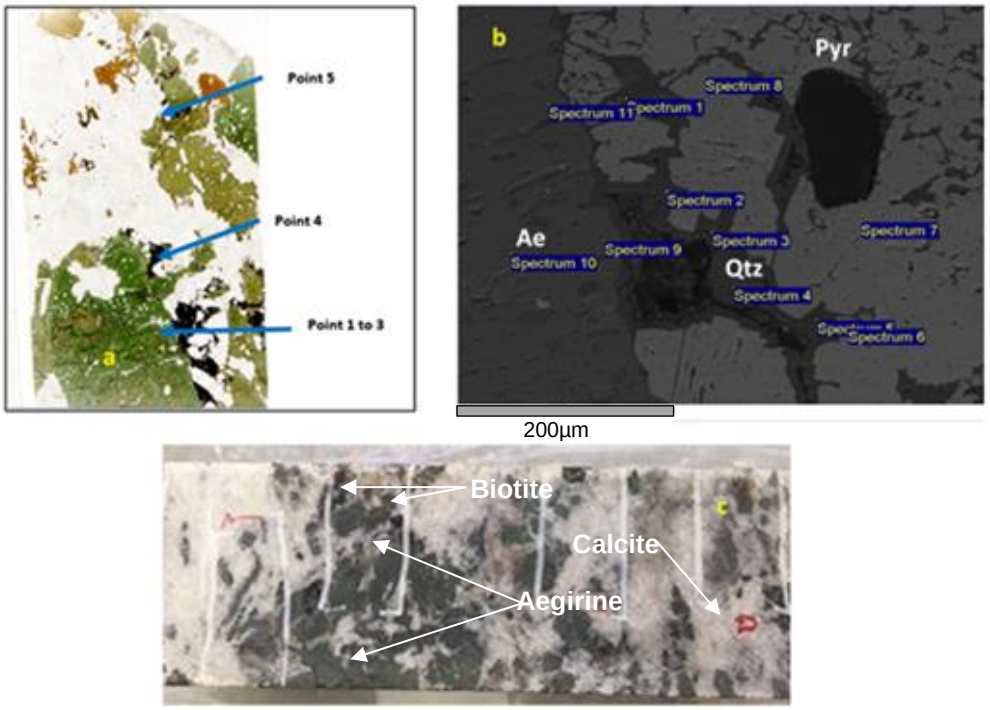

Figure 5-15. SEM data for sample E2213B (SPA015 at a depth of c. 30m) for Sequence 5, facies c, Shantumbu. (a) Thin section showing Points 1 to 5. (b) Backscattered electron image with locations of the eleven spectra; Ae – aegirine, Qtz – quartz, Pyr - pyrite. (c) Half core sample from which the thin section was derived. (d) Mineral spectrum for quartz. (e) Mineral spectrum for pyrite/pyrrhotite. (f) Mineral spectrum for pyroxene.

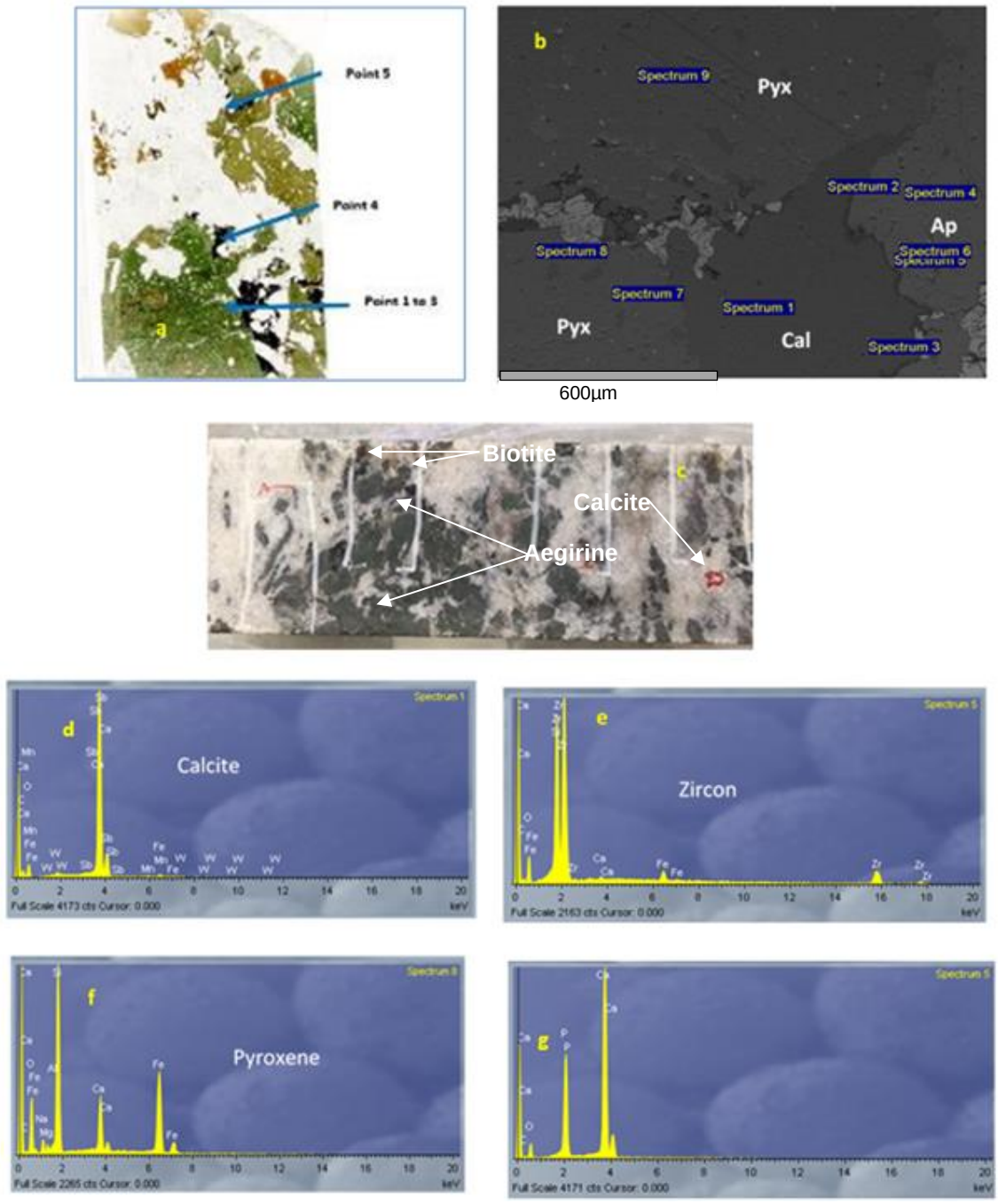

Figure 5-16. SEM data for sample E2213B (SPA015 at a depth of c. 30m) for Sequence 5, facies c, Shantumbu. (a) Thin section showing Points 1 to 5. (b) Backscattered electron image with locations of the nine spectra; Ap – apatite, Cal – calcite, Pyx - pyroxene. (c) Half core sample from which the thin section was derived. (d) Mineral spectrum for calcite. (e) Mineral spectrum for zircon. (f) Mineral spectrum for pyroxene. (g) Mineral spectrum for apatite.

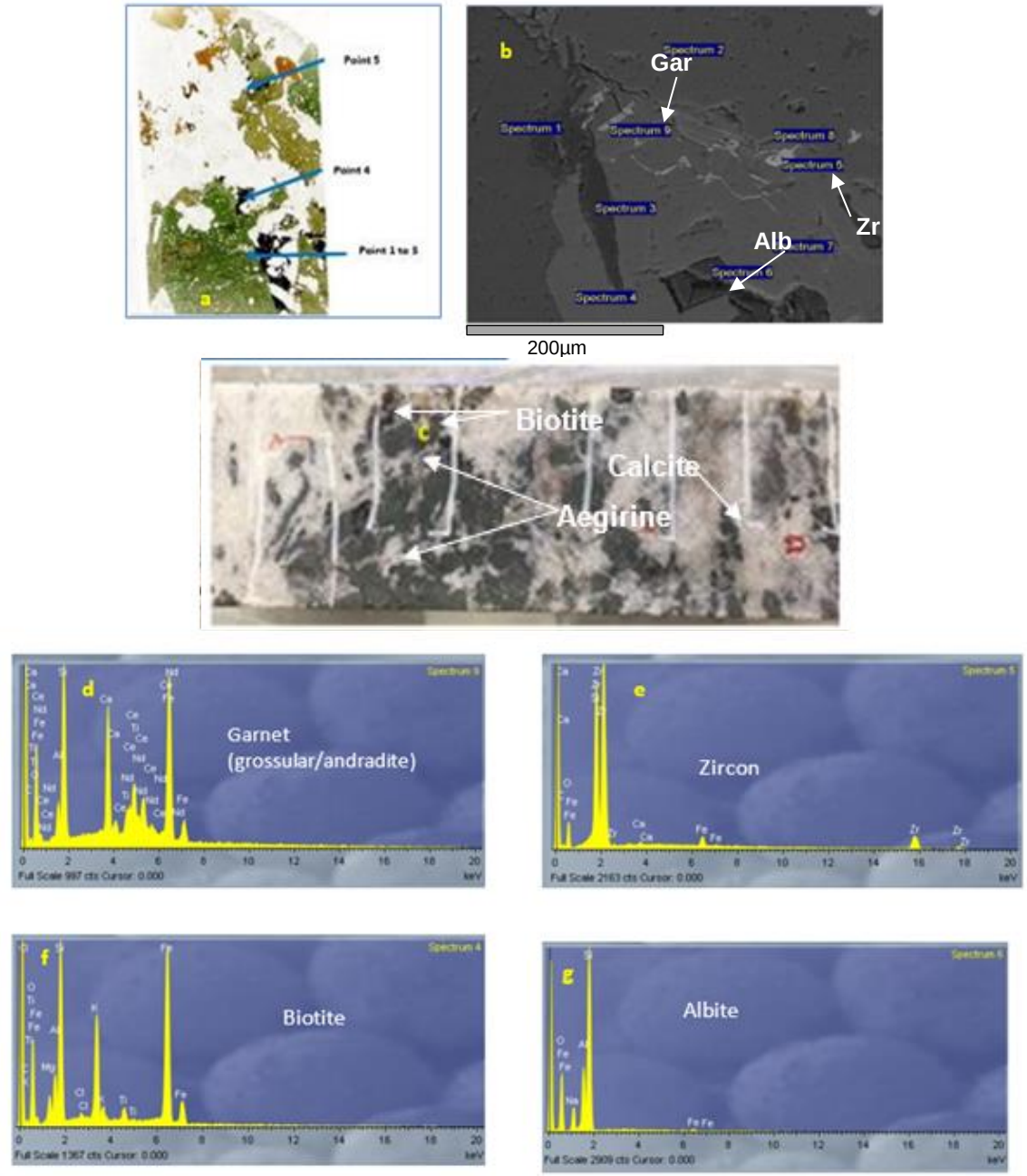

Figure 5-17. SEM data for sample E2213B (SPA015 at a depth of c. 30m), for Sequence 5, facies c, Shantumbu. (a) Thin section showing Points 1 to 5. (b) Backscattered electron image with locations of the nine spectra Gar – garnet, Cal – calcite, Zr - zircon, and Alb - albite. (c) Half core sample from which the thin section was derived. (d) Mineral spectrum for garnet. (e) Mineral spectrum for zircon. (f) Mineral spectrum for biotite. (g) Mineral spectrum for albite.

The mineral species of E2213C points 1 to 4 (Figure 5-18 and Figure 5-19) are similar to those noted in E2213B and include calcite, apatite, albite, aegirine-augite/omphacite/hedenbergite, stilpnomelane, biotite, accessory zircon and titanite/grossular/andradite.

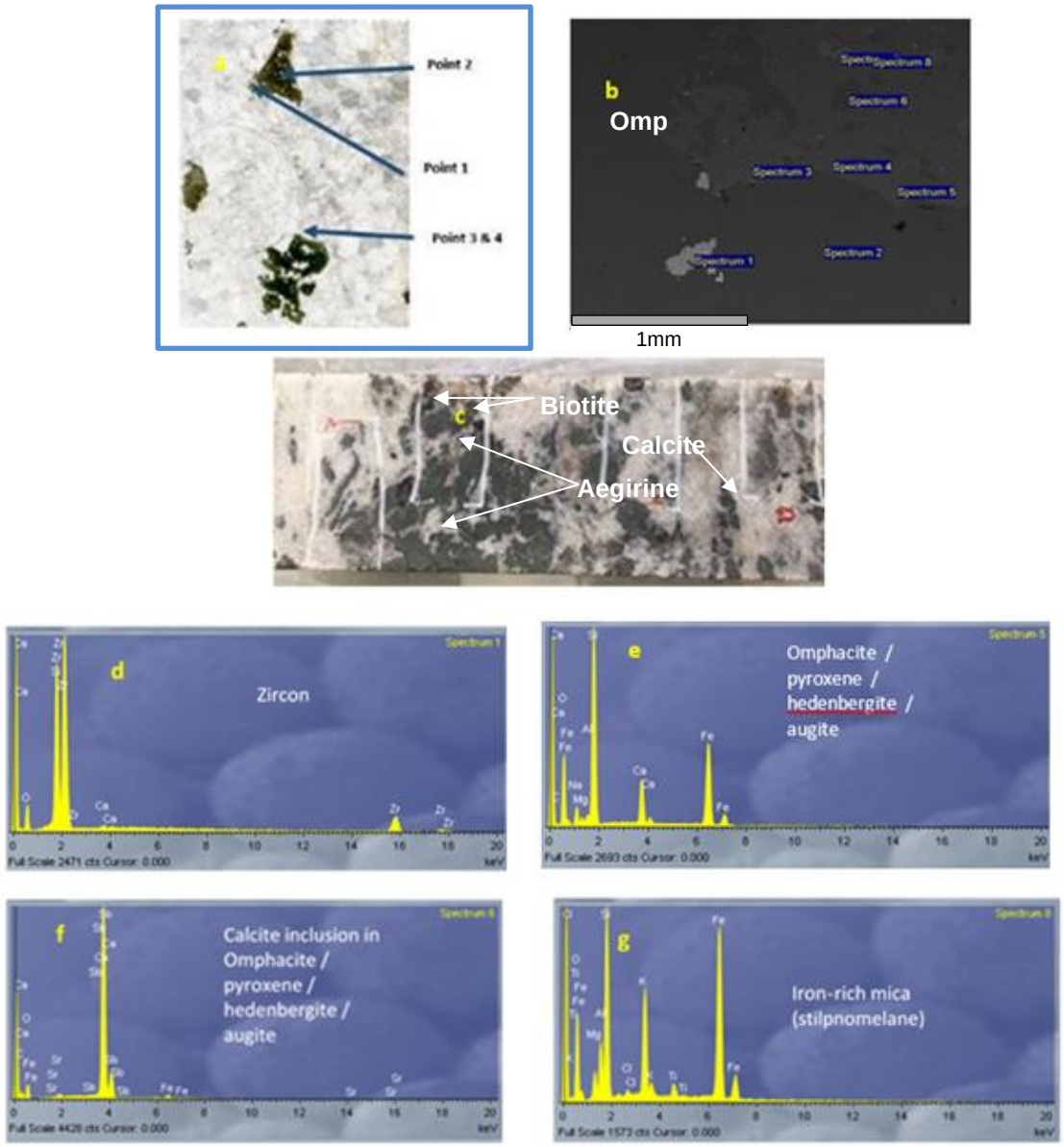

Figure 5-18. SEM data for sample E2213C (SPA015 at a depth of c. 30m), for Sequence 5, facies c, Shantumbu. (a) Thin section showing Points 1 to 4. (b) Backscattered electron image with locations of the eight spectra. (c) Half core sample from which the thin section was derived. (d) Mineral spectrum for zircon. (e) Mineral spectrum for omphacite/pyroxene/hedenbergite/augite. (f) Mineral spectrum for calcite inclusion in omphacite/pyroxene/hedenbergite/augite. (g) Mineral spectrum for iron-rich mica. OMP – omphacite.

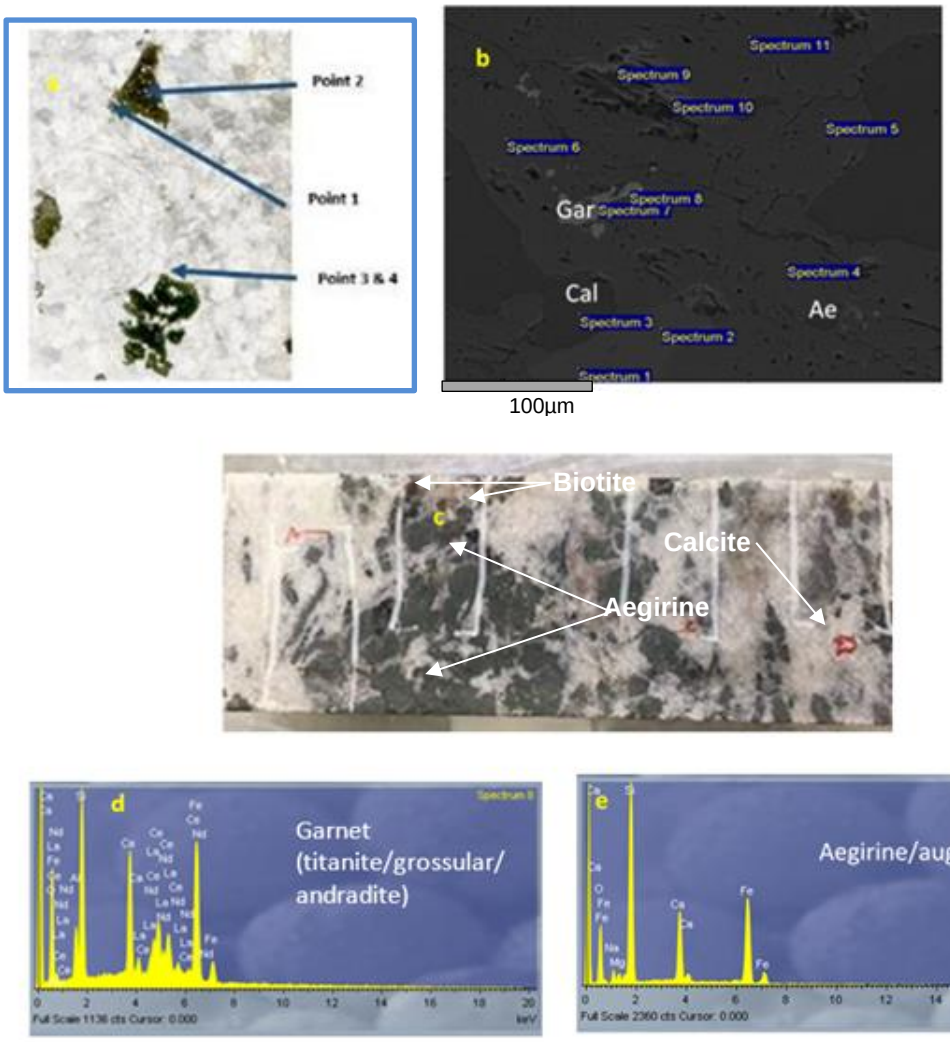

Figure 5-19. SEM data for sample E2213C (SPA015 at a depth of c. 30m), Sequence 5 facies c, Shantumbu. (a) Thin section showing Points 1 to 4. (b) Backscattered electron image with locations of the eleven spectra. (c) Half core sample from which the thin section was derived. (d) Mineral spectrum for garnet. (e) Mineral spectrum for aegirine-augite. Gar – garnet; Cal – calcite; Ae – aegirine.

The mineral species in E2213D Points of Interest 1 to 4 (Figure 5-20 to Figure 5-24) are also similar to those noted in E2213B and C but include hornblende, accessory barite and ankerite/ferroan dolomite. Barite has often been found in the Central African Copperbelt metasediments within the footwall or hanging wall units of the Copperbelt Orebody Member either above and/or below the mineralised units (Hayes *et al.*, 2015). Insufficient data is available at Shantumbu regarding the barite content of the lithologies, suffice to note that barite is a replacement mineral within carbonates. The sulphides present include pyrrhotite and pyrite.

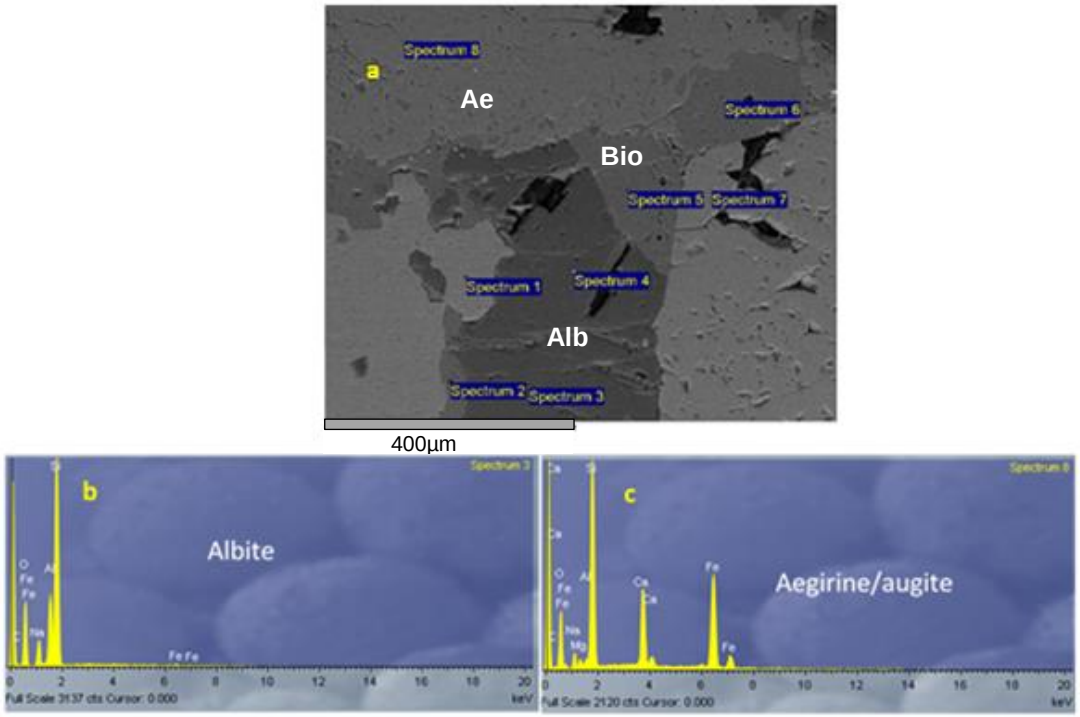

Figure 5-20. SEM data for sample E2213D. SPA015 at a depth of c. 30m, Sequence 5 facies c, Shantumbu. (a) Backscattered electron image with locations of the eight spectra. (b) Mineral spectrum for calcite. (c) Mineral spectrum for aegirine/augite. Alb – albite; Ae – aegirine; Bio – biotite.

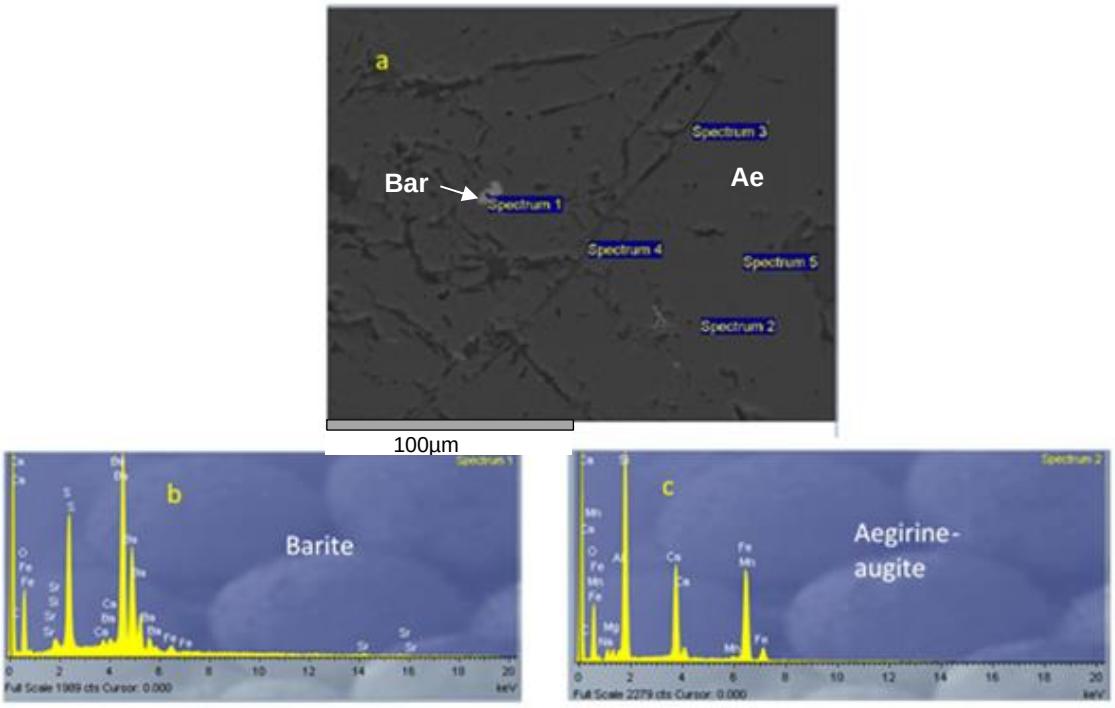

Figure 5-21. SEM data for sample E2213D (SPA015), Sequence 5 facies c, Shantumbu. (a) Backscattered electron image with locations of the five spectra. (b) Mineral spectrum for barite. (c) Mineral spectrum for aegirine/augite. Bar – barite; Ae – aegirine.

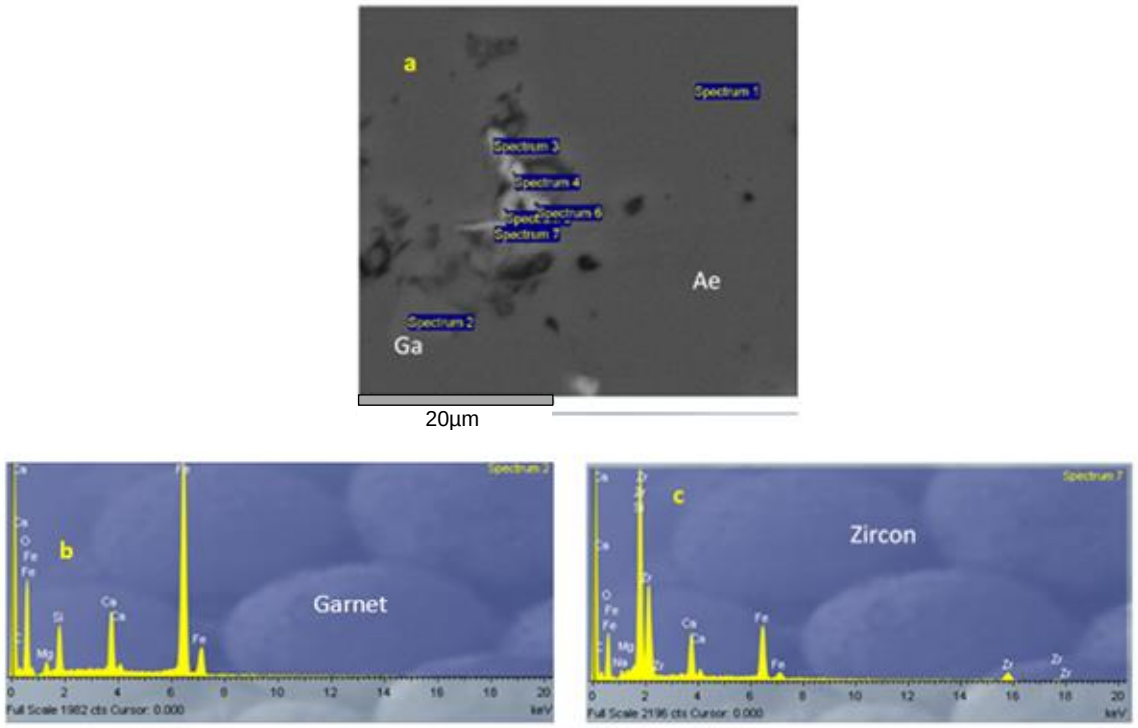

Figure 5-22. SEM data for sample E2213D (SPA015 at a depth of c. 30m), Sequence 5, facies c, Shantumbu. (a) Backscattered electron image with locations of the seven spectra. (b) Mineral spectrum for garnet. (c) Mineral spectrum for zircon. Ga – garnet; Ae – aegirine.

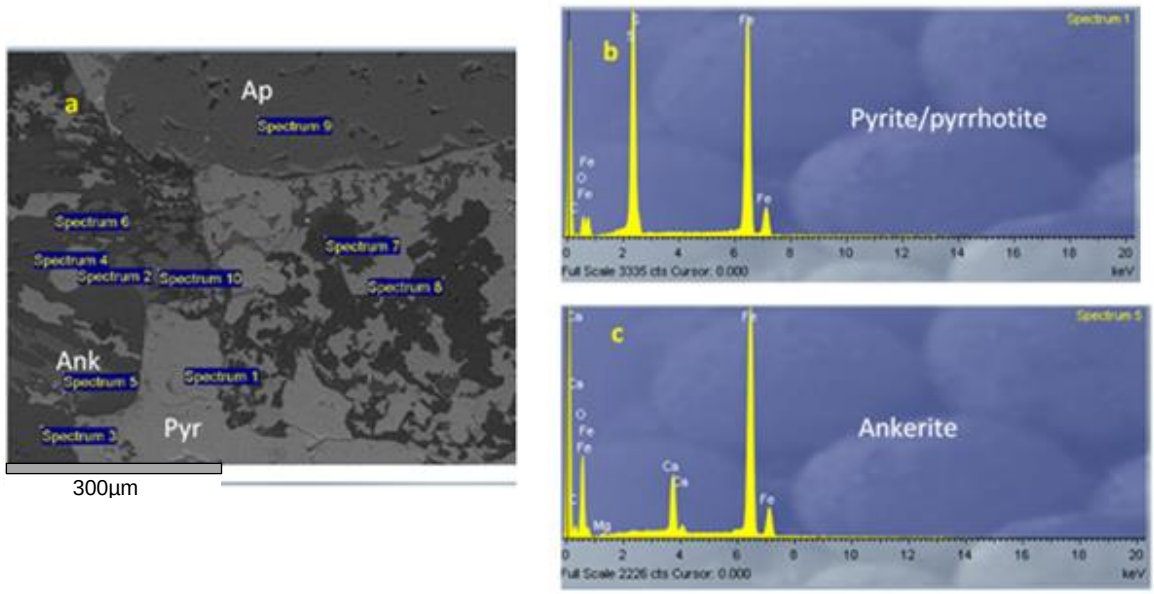

Figure 5-23. SEM data for sample E2213D, Sequence 5, facies c, Shantumbu. (a) Backscattered electron image with locations of the ten spectra. (b) Mineral spectrum for pyrite/pyrrhotite. (c) Mineral spectrum for ankerite. Ap – apatite; Ank – ankerite; Pyr – pyrite.

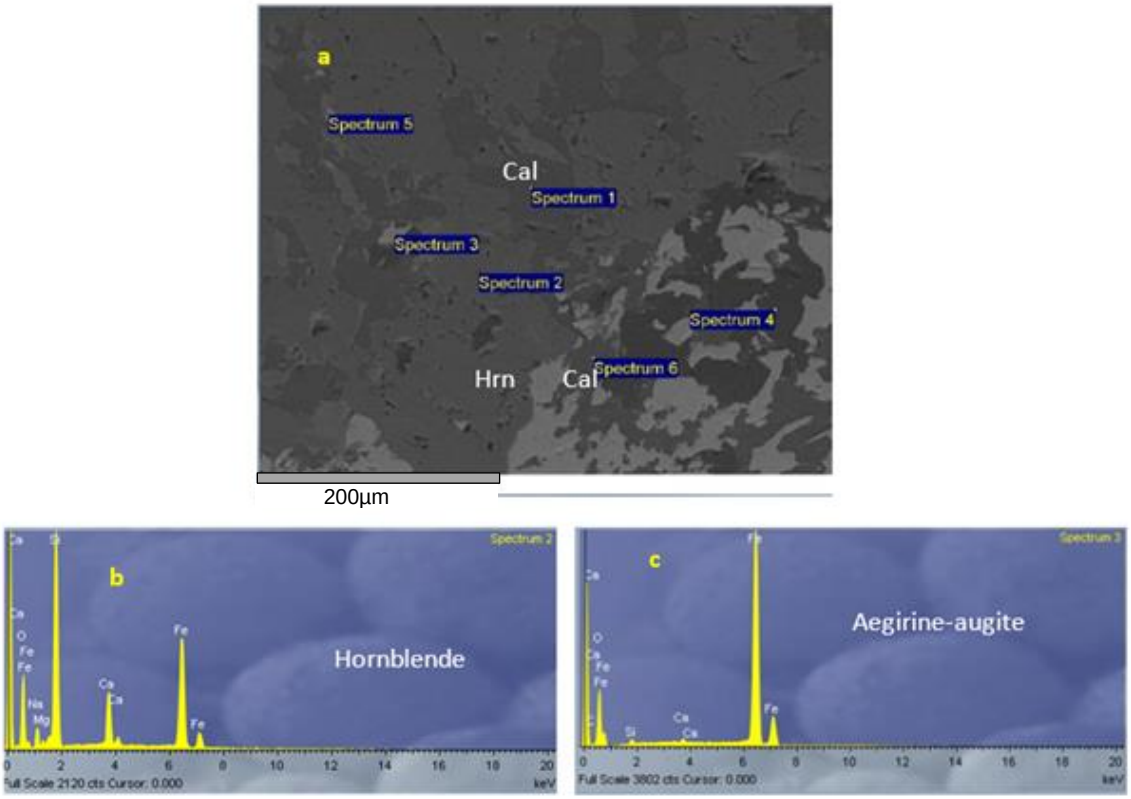

Figure 5-24. SEM data for sample E2213D (SPA015 at a depth of c. 30m), Sequence 5, facies c, Shantumbu. (a) Backscattered electron image with locations of the ten spectra. (b) Mineral spectrum for hornblende. (c) Mineral spectrum for aegirine-augite. Cal – calcite; Hrn – hornblende.

Sequence 6

The arenite units display a coarse-grained granoblastic texture (Figure 5-25), whereas the carbonate units are coarse-grained and interlayered with aegirine-biotite-rich layers. Cross-cutting veining is absent within the arenites, siltstones and carbonates, rather brecciation was noted. Minor carbonate-quartz veining within the brecciated arkosic units and these veins terminate at or near the siltstone/mudstone contacts. The arenite is chiefly composed of coarse-grained interlocking, anhedral orthopyroxene (with inclusions of anhedral clinopyroxene), plagioclase grains and sub-ordinate K-feldspar (orthoclase measuring up to 1.5cm in diameter), together with amphibole and sphene. Quartz is present to a lesser extent usually as microcrystalline grains up to 700µm. The mineralogy of the cement is primarily biotite, goethite and to a lesser extent calcite, apatite and chlorite; calcite may also be a major phase locally. Dolomite and calcite grains up to 6mm occur whilst hematite grains are microcrystalline.

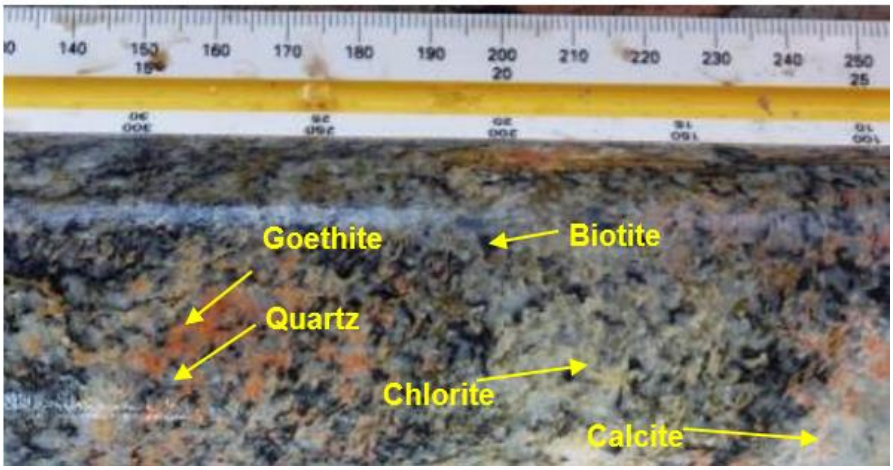

Figure 5-25. Granoblastic mosaic texture of the arenite in Sequence 6, Shantumbu, illustration of core from drill hole SPA027.

The protolith minerals of the siltstone have altered extensively to biotite and subsequently to chlorite. Plagioclase grains are present in the siltstone as anhedral to subhedral grains displaying carbonatisation, noted by the presence of microcrystalline calcite grains within the plagioclase grains.

Within the granoblastic texture, the mica grains display a preferred orientation. K-feldspar exhibits cross-hatching twinning and plagioclase formed irregular exsolution lamellae within K-feldspar grains. Apatite is present as microcrystalline grains within calcite. Microcrystalline goethite development is extensive (Figure 5-26) but a minor occurrence within veins. In places, purple to blue sodalite grains (Figure 5-27) measuring up to 8mm have formed a major mineral of the cement. Biotite, chlorite and dolomite are other common cementing minerals together with remnant pyrite grains. Goethite represents the complete alteration of pre-existing iron silicates, sulphides and oxides. The pyrite grains present measured up to c. 6mm, whereas magnetite grains noted measured up to 950µm.

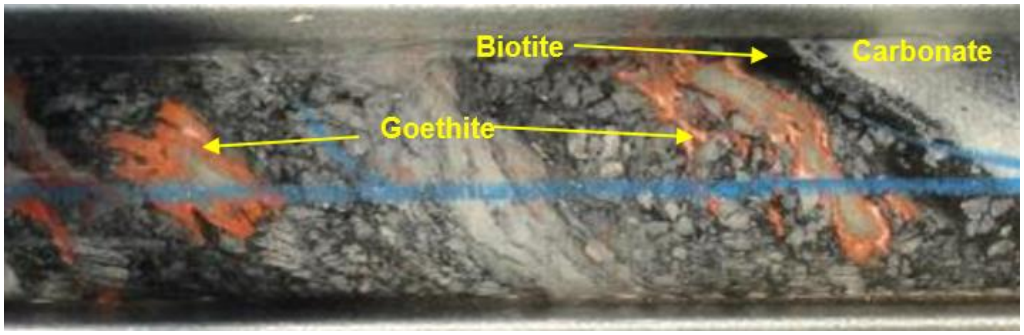

Figure 5-26. Pervasive goethite alteration within brecciated arenite of Sequence 6 Shantumbu, core sample (SPA018; drill core size is NQ).

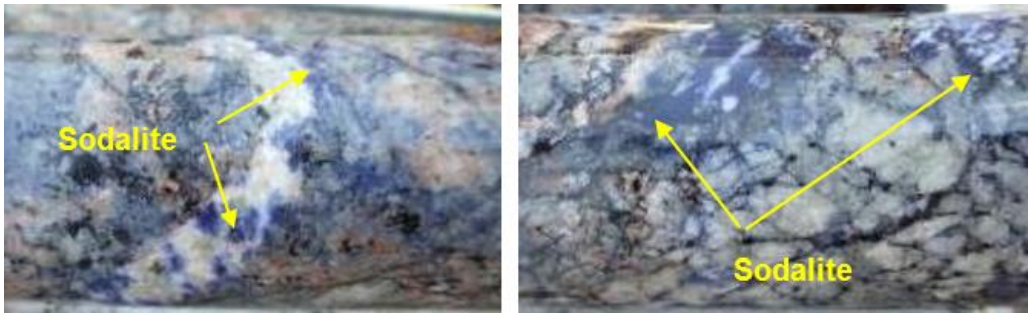

Figure 5-27. Coarse-grained sodalite pervasive through the brecciated arenite of Sequence 6, Shantumbu core sample (SPA018; drill core size is BQ; depth at c. 312m).

The arenites were subjected to albitisation (Figure 5-28 and Figure 5-29), carbonatisation, partial silicification and the retrograde alteration of biotite to chlorite. Retrograde metamorphism is further indicated by muscovite, which would not have survived the preceding high-grade metamorphism.

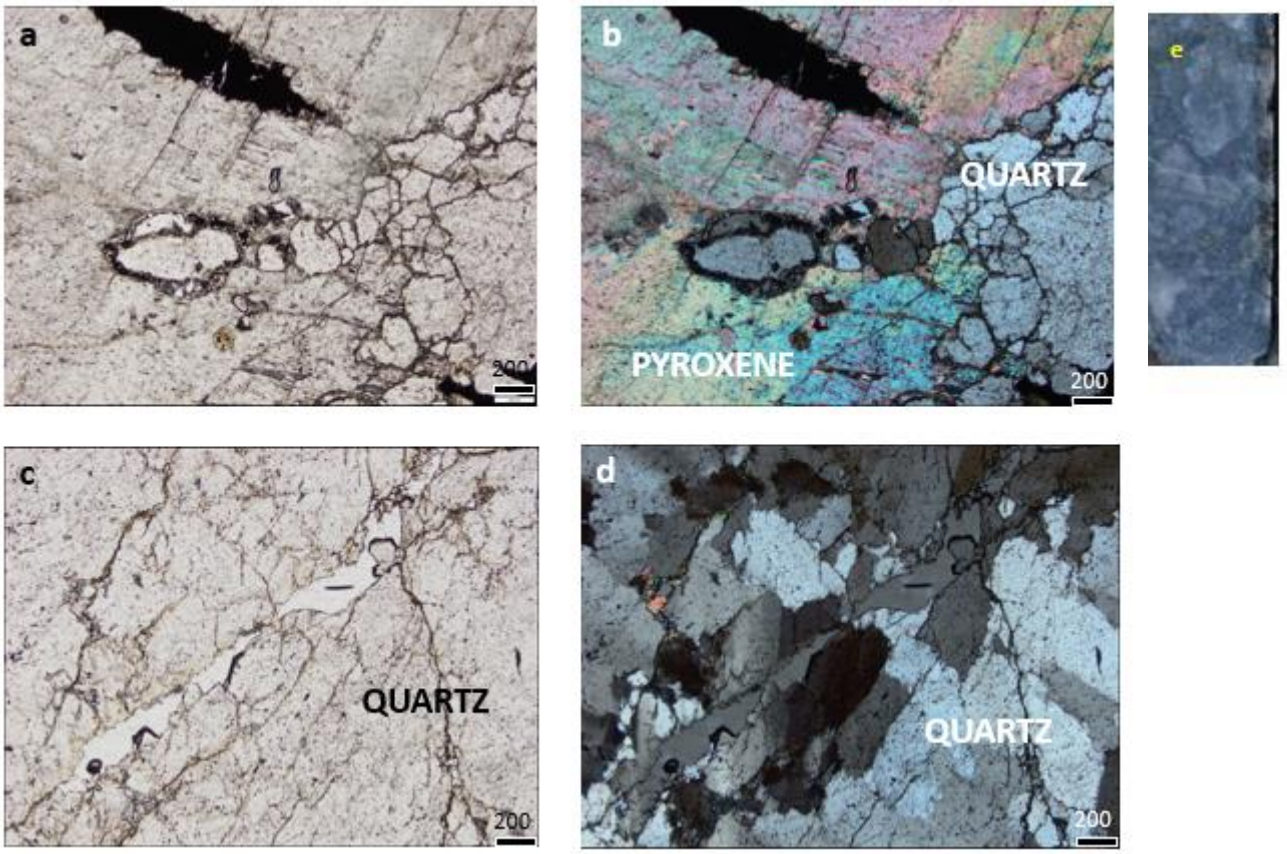

Continued next page

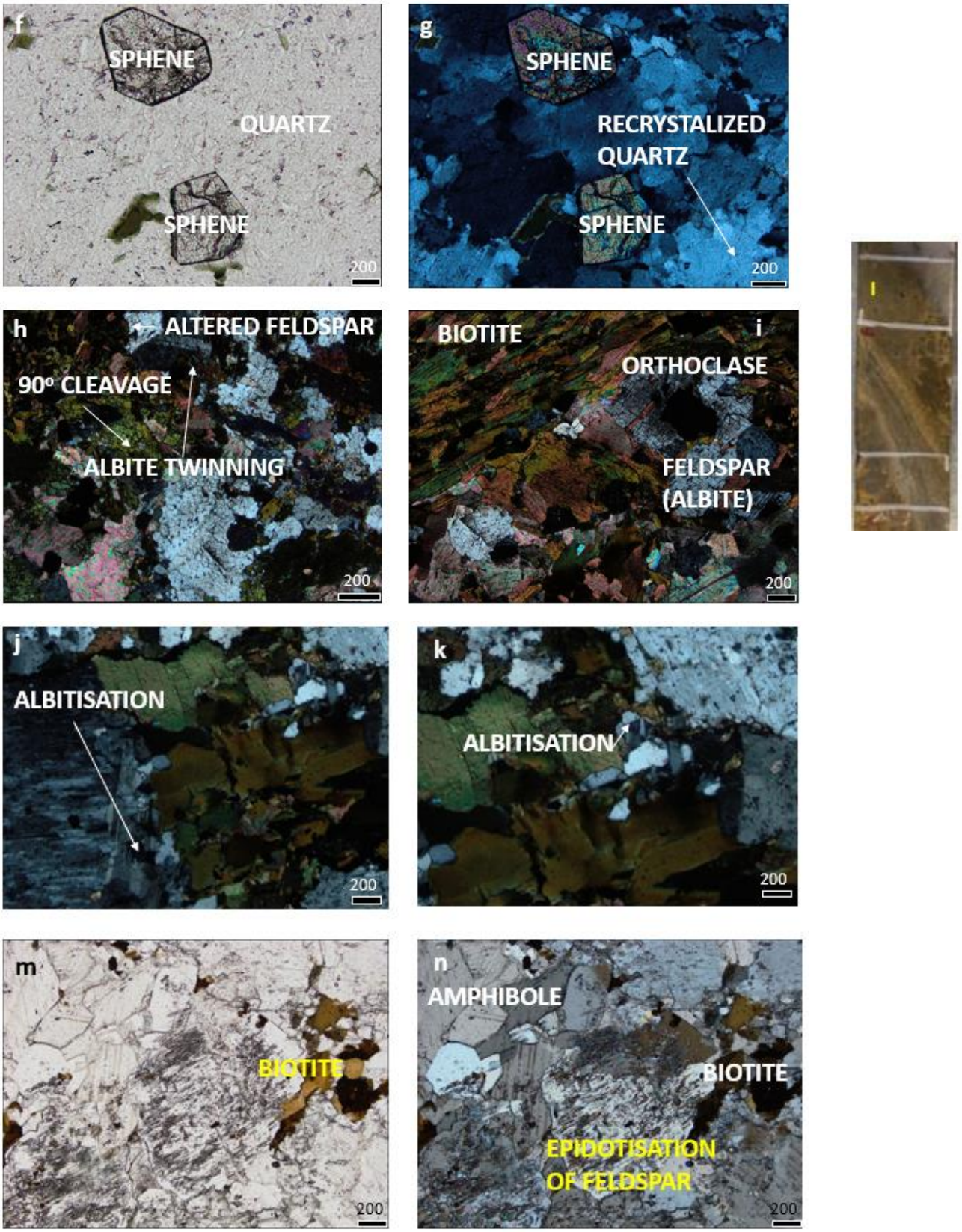

Figure 5-28. Alteration types and minerals within arenite of Sequence 6, Shantumbu. (a) Microcrystalline quartz. Sample E2240 plane polarised light (200µm) (SPQ002 c. 270m depth). (b) Microcrystalline quartz. Sample E2240 cross polarised light (200µm) (SPQ002c. 270m depth). (c) Undulose extinction within quartz grains; plane polarised light. Sample 2212 plane polarised light (200µm) (SPA015). (d) Undulose extinction

within quartz grains; cross polarised light. Sample E2212 cross polarised light (200µm) (SPA015). (e) Brecciated arenite core sample of Sequence 6. Sample E2240 (SPQ002 at c. 270m depth). (f) Sphene within recrystallised quartz; plane polarised light. Sample E2205 plane polarised light (100µm) (SPA015. c. 90m depth). (g) Sphene within recrystallised quartz; cross polarised light. Sample E2205 cross polarised light (100µm) (SPA015c. 90m depth). (h) Altered feldspar and albite twinning; plane polarised light. Sample E2215A plane polarised light (200µm) (SPA015 at c. 160m depth). (i) Alteration products albite, orthoclase, and biotite; cross polarised light. Sample E2215A cross polarised light (200µm) (SPA015 at c. 160m depth). (j) Albitisation; cross polarised light. Sample E2205 plane polarised light (200µm) (SPA015 at c. 90m depth). (k) Albitisation; cross polarised light. Sample E2205 cross polarised light (200µm) (SPA015 at c. 90m depth). (l) Pervasive iron oxide alteration of arenite within Sequence 6; core sample. Sample 2232 (SPQ002 SPA015 at c. 245m depth). (m) Sample E2243 plane polarised light (200µm) (SPA027c. 350m depth). (n) Sample E2243 cross polarised light (200µm) (SPA027 c. 350m depth).

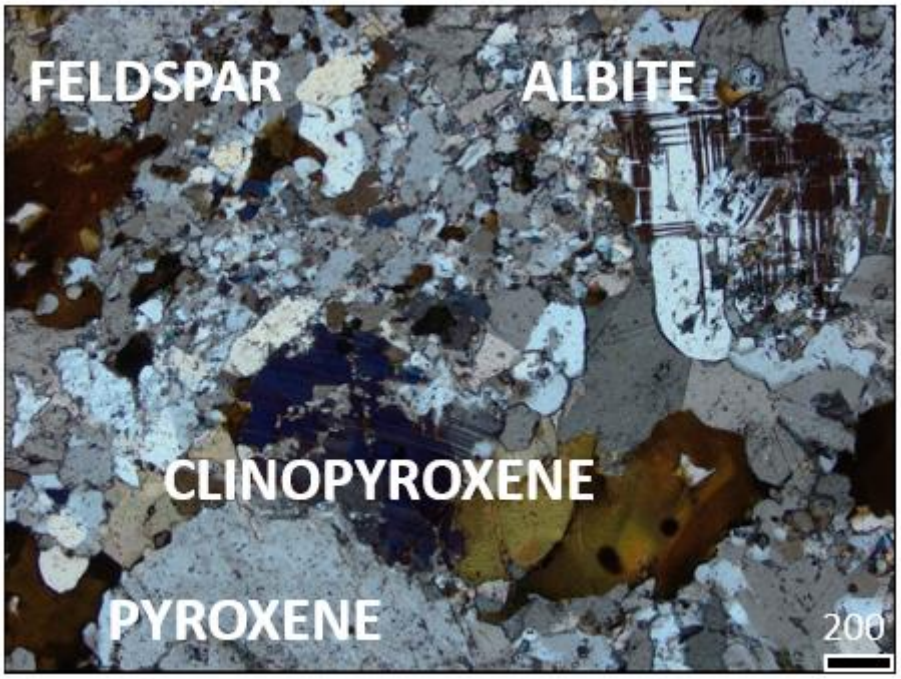

Figure 5-29. The chessboard twining of albite (upper right corner) and presence of clinopyroxene are indicative of sodic alteration within Sequence 6, Shantumbu. Thin section is cross-polarised light of Sample E2243B from SPA027 at a depth of c. 370m.

The foliation within the siltstones is defined both by the micas and the granular, interlocking layers of prismatic crystals, such as clinopyroxene, feldspar and amphiboles. The prismatic grains have a preferred orientation, which is parallel to the mica-dominated layers (Figure 5-30). The larger subhedral to anhedral grains did not follow the preferred orientation. The larger anhedral grains display varying degrees of sericitisation. Triple junctions are common within the prismatic crystal layers; however, the grain boundaries vary from irregular to decussate. The prismatic pyroxenes, feldspars (albite) and amphiboles display a mix of larger grain fragments and finer grain fragments. Sub-rounded quartz with undulose extinction was observed.

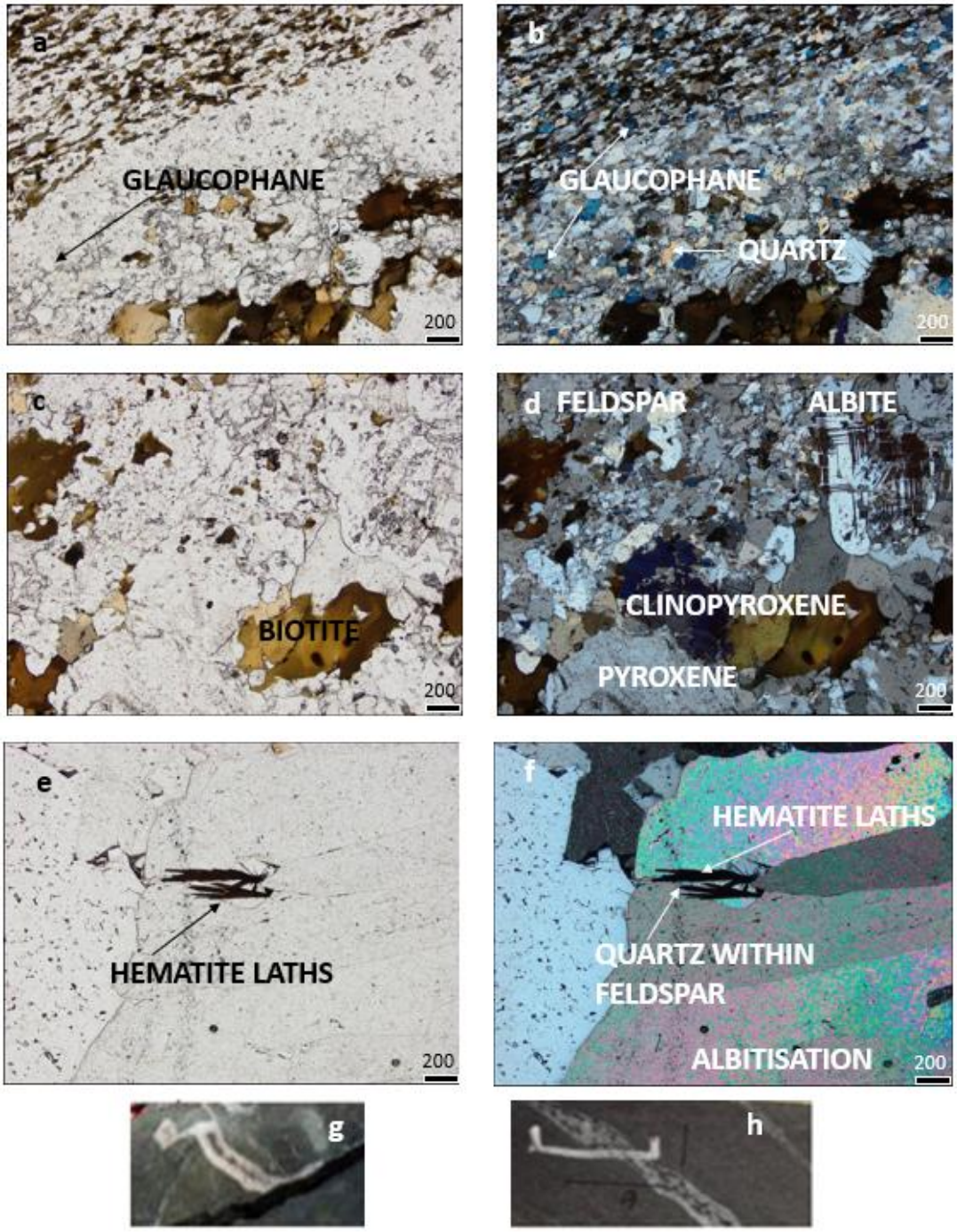

Figure 5-30. Alteration types and minerals within siltstones of Sequence 6, Shantumbu. (a) Foliation within rhythmite; elongated biotite grains with interstitial quartz and calcite and glaucophane. Preferred orientation of subhedral quartz and glaucophane grains in arenite layer adjacent to siltstone layer; plane polarised light. Sample E2243 plane polarised light (200µm) (SPA027 at a depth of c. 346m). (b) Foliation within rhythmite; elongated biotite grains with interstitial quartz and calcite and glaucophane. Preferred orientation of subhedral quartz and glaucophane grains in arenite layer adjacent to siltstone layer; cross polarised light. Sample E2243 cross polarised light (200µm) (SPA027 at a depth of c. 346m). (c) Clinopyroxene, feldspar, microcline, and biotite alteration minerals within siltstone; plane polarised light. Sample E2243 plane polarised light (200µm) (SPA027 at a depth of c. 346m). (d) Clinopyroxene, feldspar, microcline, and biotite alteration minerals within siltstone; cross polarised light. Sample E2243 cross polarised light (200µm) (SPA027 at a depth of c. 346m). (e) Hematite laths along grain boundaries between feldspar and quartz; plane polarised light. Sample E2207 cross polarised light (200µm) (SPA015). (f)

Hematite laths along grain boundaries between feldspar and quartz; cross polarised light. Sample E2207 cross polarised light (SPA015 at a depth of c. 90m). (h) Siltstone and quartz-glaucophane lamination; core sample. Sample position for a and b indicated on sample. Sample E2243 (SPA027 at a depth of c. 346m). (g) Siltstone and quartz-glaucophane lamination; core sample. Sample E2207 (SPA015 at a depth of c. 90m).

The carbonate layers are dominated by calcite, dolomite, chalcopyrite, pyrite and magnetite. Calcite formed anhedral grains. The largest magnetite grains present are hosted within the carbonate layers whilst smaller magnetite grains were observed within the siltstone layers.

Sequence 7

The contacts between the carbonate and calc-silicate layers in Sequence 7 are sharp. The layering observed in hand specimen is not noted in thin section, in that no preferred orientation or elongation was noted during the thin section microscopy.

The siltstone layers within Sequence 7 have altered extensively to biotite and aegirine and display tight folding and boudinaging (Figure 5-31). The white carbonate is the principal lithology present in Sequence 7 and consists of granoblastic calcite and quartz with accessory mica laths. Quartz grain boundaries are irregular and indicative of annealing and sutured boundaries between calcite and quartz are common (Figure 5-32). Fine-grained calcite forms the groundmass to larger calcite and quartz grains. Where this groundmass has a higher proportion of mica flakes, it is accompanied by goethite.

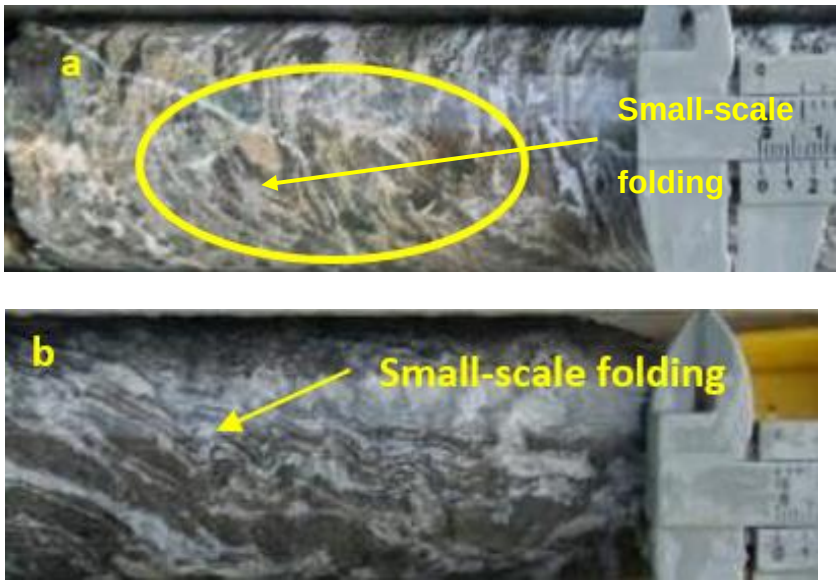

Figure 5-31. Siltstone layers made up of biotite and aegirine, displaying tight folding (a and b) Sequence 7, Shantumbu.

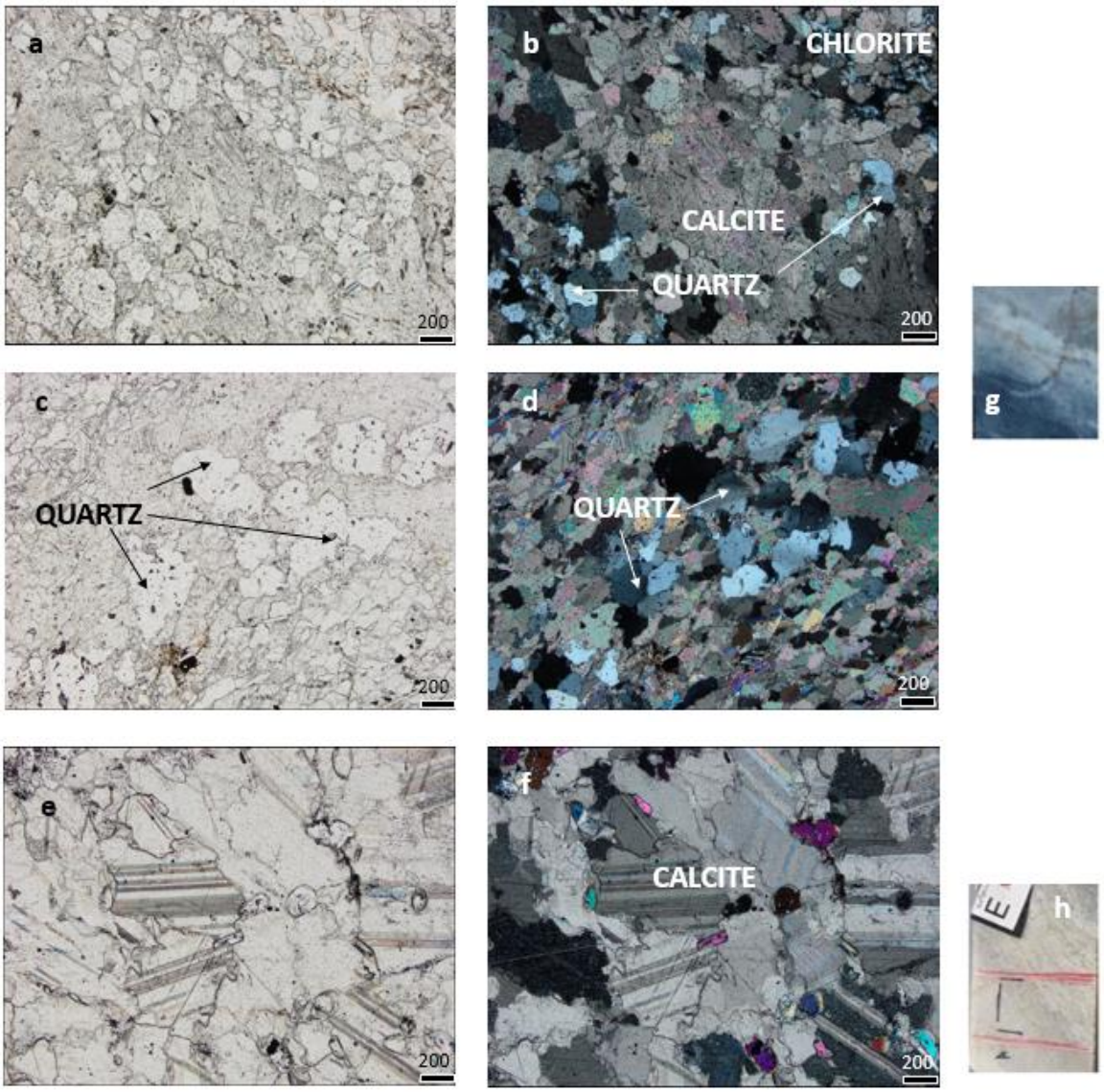

Figure 5-32. Irregular annealed and sutured grain boundaries of quartz grains; Sequence 7, Shantumbu. (a), (c) and (e) Illustrations in plane polarised light. (b), (d), and (f) Illustrations in cross polarised light. (g) Blue-white carbonate of Sequence 7; core sample. Sample E2239 (SPQ002 at a depth of c. 40m). (h). White carbonate of Sequence 7; core sample. Sample E2238 (SPQ002 at a depth of c. 40m). (a) Sample E2238 plane polarised light (200µm) (SPQ002 at a depth of c. 40m). (b) Sample E2238 cross polarised light (200µm) (SPQ002 at a depth of c. 40m). (c) Sample E2231 plane polarised light (200µm) (SPQ002 at a depth of c. 220m). (d) Sample E2231 cross polarised light (200µm) (SPQ002 at a depth of c. 220m). (e) Sample E2227A plane polarised light (200µm) (SPQ002 at a depth of c. 110m). (f) Sample E2227A cross polarised light (200µm) (SPQ002 at a depth of c. 110m).

The finely bedded grey-blue calcitic carbonate is composed of anhedral, medium-grained interlocking calcite grains with lesser quartz, iron oxides and muscovite. Quartz and muscovite represent 10 - 20% of the mineralogy of the calc-silicate units. Two generations of calcite

developed, the first generation consist of inequigranular and anhedral calcite grains and is fine- to medium-grained. The second generation of calcite forms coarser-sized grains with regular grain boundaries and the presence of annealing/triple junctions. The calcite grains are often 'grainy' suggestive of recrystallised grains. Calcite has also replaced silicate minerals to varying degrees. The mica-dominated bands host epidote porphyroblasts, granoblastic plagioclase and quartz and pervasive goethite.

The lithologies in Sequence 7 were subjected to numerous alteration processes (Figure 5-33), including saussuritisation (epidote), albitisation, sericitisation, the formation of sphene and amphiboles. Locally extensive iron oxidation has occurred (Figure 5-34).

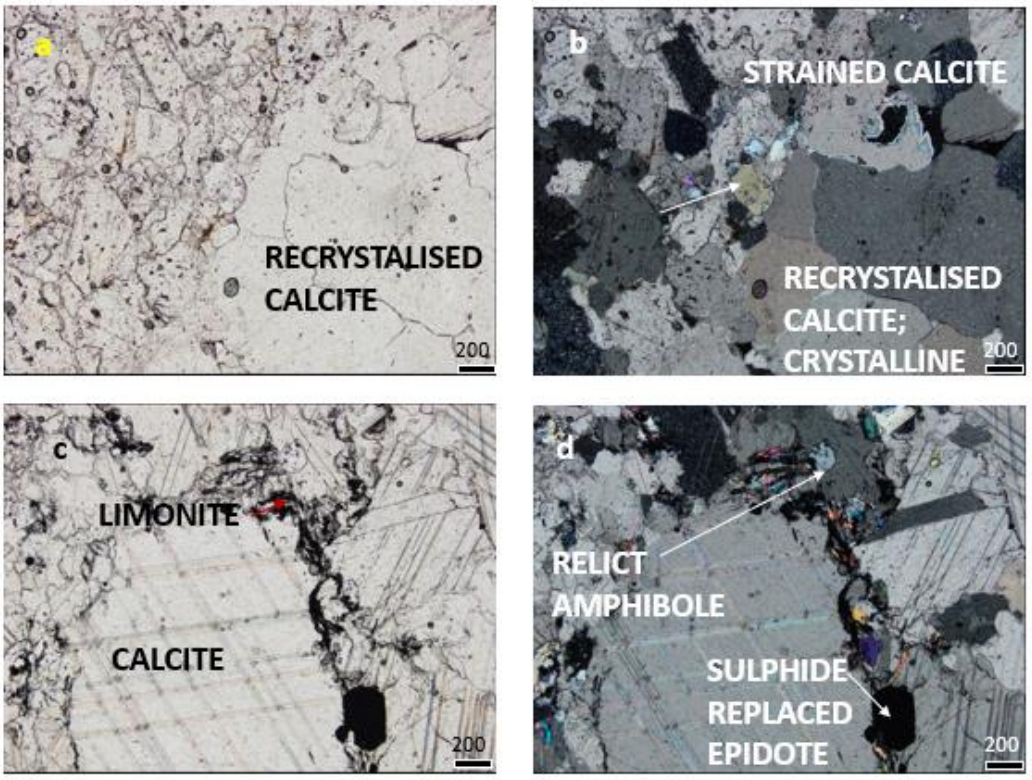

Continued next page

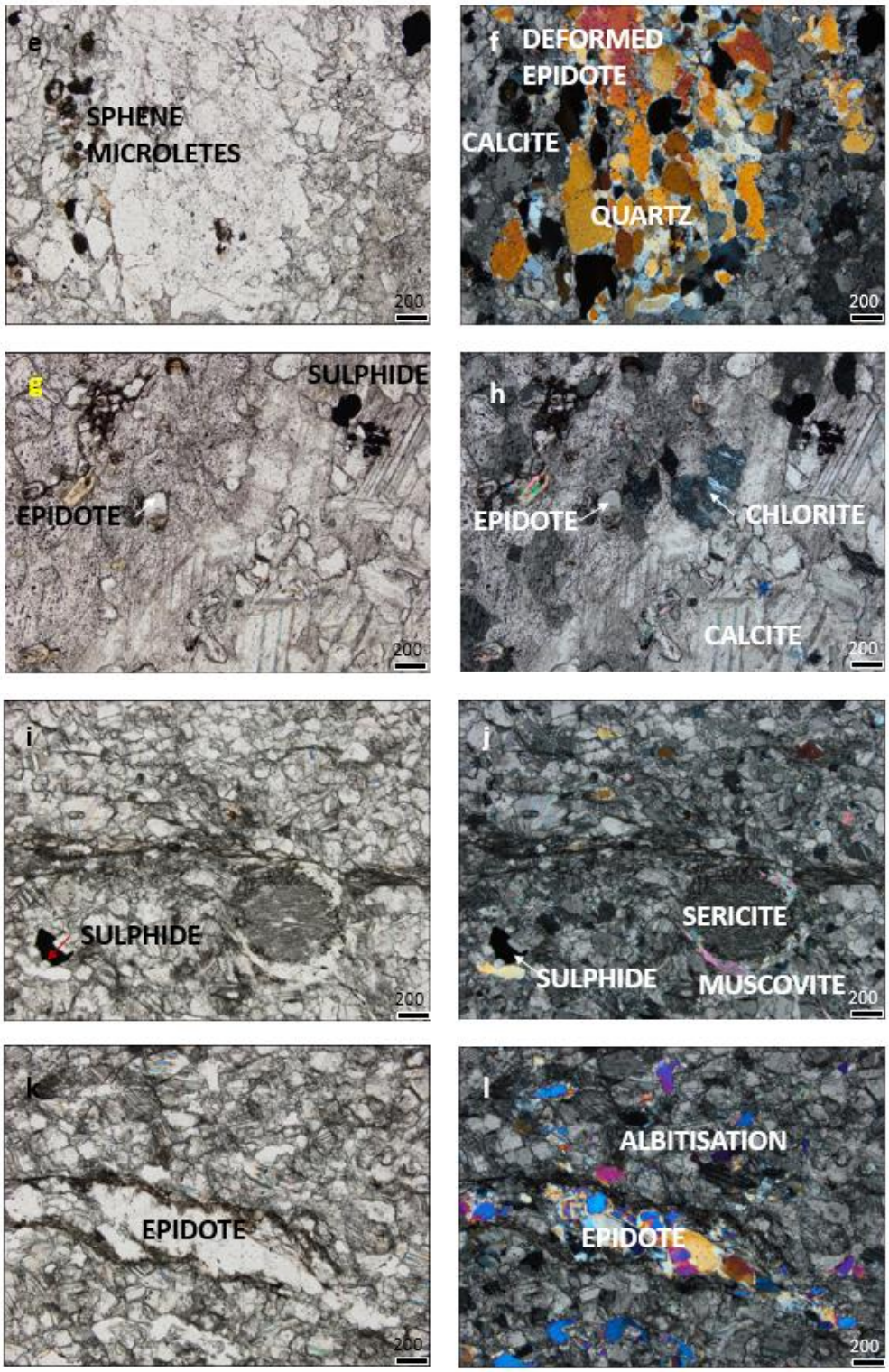

Figure 5-33. Alteration processes identified in Sequence 7, Shantumbu. (a) Rounded sphene crystals, relict amphibole, strained and recrystallised calcite; plane polarised light. Sample E2227B plane polarised light (200µm) (SPQ002 at a depth of c. 110m). (b) Rounded sphene crystals, relict amphibole, strained and recrystallised calcite; plane polarised light. Sample E2227B cross polarised light (200µm) (SPQ002 at a depth of c. 110m). (c) Relict amphibole, alteration to goethite, and sulphides replacing epidote; plane polarised light. Sample E2227C plane polarised light (200µm) (SPQ002 at a depth of c. 110m). (d) Relict amphibole, alteration to goethite, and sulphides replacing epidote; cross polarised light. Sample E2227C cross polarised light (200µm) (SPQ002 at a depth of c. 110m). (e) Sphene microlets accompanied by

calcite, quartz, and deformed epidote; plane polarised light. Sample E2238 plane polarised light (200µm) (SPQ002 at a depth of c. 40m). (f) Sphene microlets accompanied by calcite, quartz, and deformed epidote; cross polarised light. Sample E2238 cross polarised light (200µm) (SPQ002 at a depth of c. 40m). (g) Sub-hederal epidote grains with matrix of calcite, quartz, and plagioclase; plane polarised light. Sample E2230 plane polarised light (200µm) (SPQ002 at a depth of c. 200m). (h) Sub-hederal epidote grains with matrix of calcite, quartz, and plagioclase; cross polarised light. Sample E2230 cross polarised light (200µm) (SPQ002 at a depth of c. 200m). (i). Sericite/muscovite within a matrix of calcite, quartz, and plagioclase. Disseminated sulphides within matrix; plane polarised light. Sample E2239A plane polarised light (200µm) (SPQ002 at a depth of c. 40m). (j) Sericite/muscovite within a matrix of calcite, quartz and plagioclase. Disseminated sulphides also within a matrix; cross polarised light. Sample E2239A cross polarised light (200µm) (SPQ002 at a depth of c. 40m). (k) Sub-hederal epidote grains with a matrix of calcite, quartz, and plagioclase; plane polarised light. Sample E2239A plane polarised light (200µm) (SPQ002 at a depth of c. 40m). (l) Sub-hederal epidote grains with a matrix of calcite, quartz, and plagioclase. Albitisation present; cross polarised light. Sample E2239A cross polarised light (200µm) (SPQ002 at a depth of c. 40m).

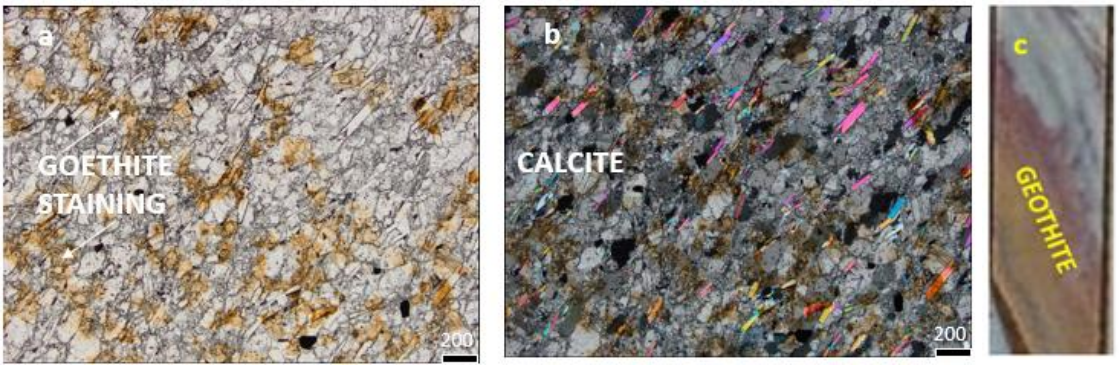

Figure 5-34. Pervasive iron oxidation, Sequence 7, Shantumbu. (a) Goethite interstitial to calcite, sericite/muscovite, and quartz; plane polarised light. Sample E2231A plane polarised light (200µm) (SPQ002 at a depth of c. 220m). (b) Goethite interstitial to calcite, sericite/muscovite, and quartz; cross polarised light. Sample E2231A cross polarised light (200µm) (SPQ002 at a depth of c. 220m). (c) Goethite layer in core sample. Sample E2231 (SPQ002 at a depth of c. 220m).

Disseminated fine-grained, anhedral pyrite is present and larger anhedral pyrite grains infrequent (Figure 5-35). Pyrite and chalcopyrite are closely associated with each other. Anhedral microcrystalline hematite and goethite grains are disseminated throughout the unit and form less than 1% of the mineral assemblage (Figure 5-35). Pyrite grains are typically a few microns in diameter and up to 5mm, whilst the largest chalcopyrite grain noted measured c. 700µm in diameter.

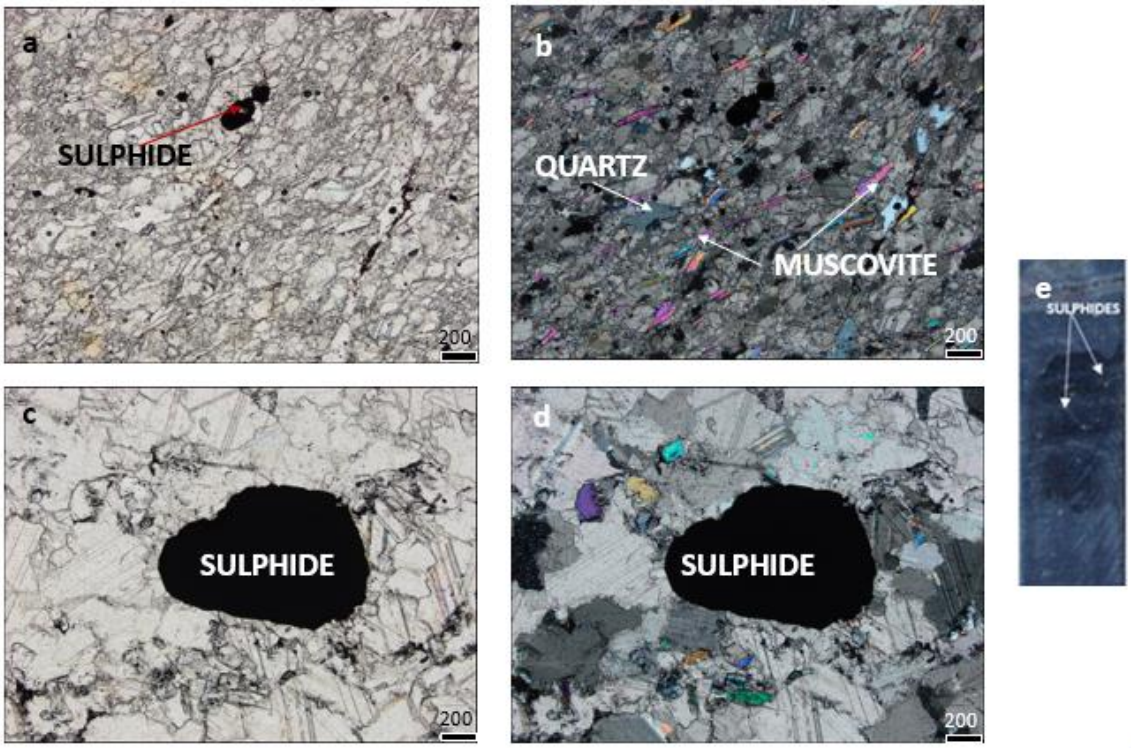

Figure 5-35. Sulphide mineralisation in Sequence 7 carbonates, Shantumbu. (a) Disseminated and rounded sulphide (pyrite) within matrix of muscovite and quartz; plane polarised light. Sample E2231A plane polarised light (200µm) (SPQ002 at a depth of c. 220m). (b) Disseminated and rounded sulphide (pyrite) within matrix of muscovite and quartz; cross polarised light. Sample E2231A cross polarised light (200µm) (SPQ002 at a depth of c. 220m). (c) Disseminated and rounded sulphide (pyrite) within matrix of muscovite and quartz; plane polarised light. Sample E2227B plane polarised light (200µm) (SPQ002 at a depth of c. 110m). (d) Disseminated and rounded sulphide within matrix of muscovite and quartz; cross polarised light. Sample E2227B cross polarised light (200µm) (SPQ002 at a depth of c. 110m). (e) Core sample of blue carbonate with disseminated sulphides. Sample E2227of drill hole (SPQ002 at a depth of c. 110m).

Microscopic to macroscopic calcite-goethite veins cross-cut the carbonate (Figure 5-36), where calcite is coarse-grained in comparison to the calcite grains constituting the bulk of the carbonate. Veins filled with plagioclase, quartz, muscovite, pyrite and chalcopyrite also cross-cut the carbonate; strain shadows are noted in several of the quartz grains. Alteration of the carbonate is limited to oxidation of the iron minerals and to a lesser extent albitisation along the vein contacts.

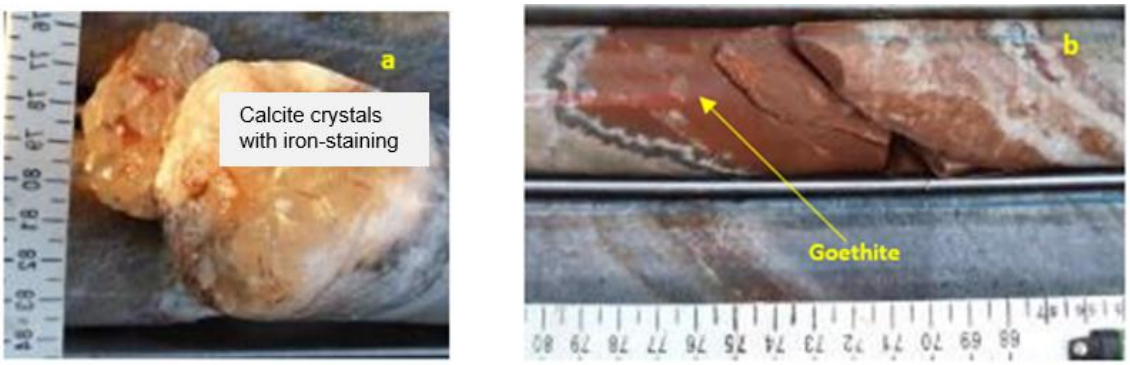

Figure 5-36. Veining within carbonates of Sequence 7 at a depth of c. 185m, Shantumbu. (a) Macroscopic calcite grains filling vein; core sample. (b) Pervasive goethite filled vein; core sample SPQ002 (c. 189.5m).

Veins

Three generations of veins were noted to have developed in the lithologies of Sequences 1 to 7, and include layer-parallel, cross-cutting and lastly irregular veins (Figure 5-37). Veins hosted by siltstones/mudstones and shales have sharp boundaries and limited alteration of the surrounding host rock while, the contacts between the veins and the arenite host rock vary from sharp to irregular and diffuse. Alteration progresses away from the veins which cross-cut arenite host rocks (Figure 5-38).

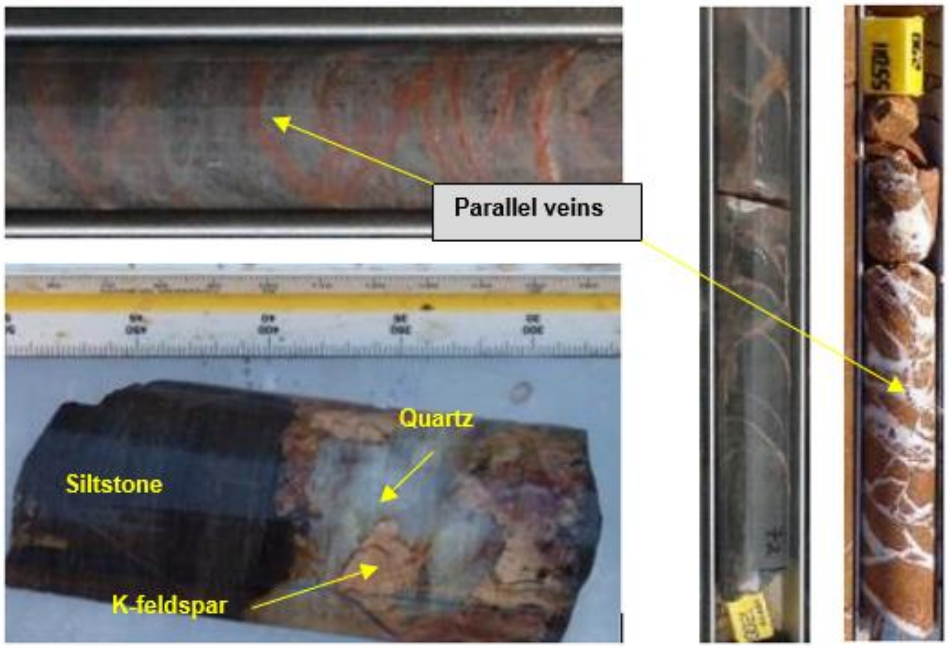

Figure 5-37. Layer parallel vein set at Shantumbu. (a) Layer parallel and irregular veins. (b) K-feldspar and quartz-bearing vein layer parallel with host siltstone (E2241 in SPQ002 at a depth of 344m).

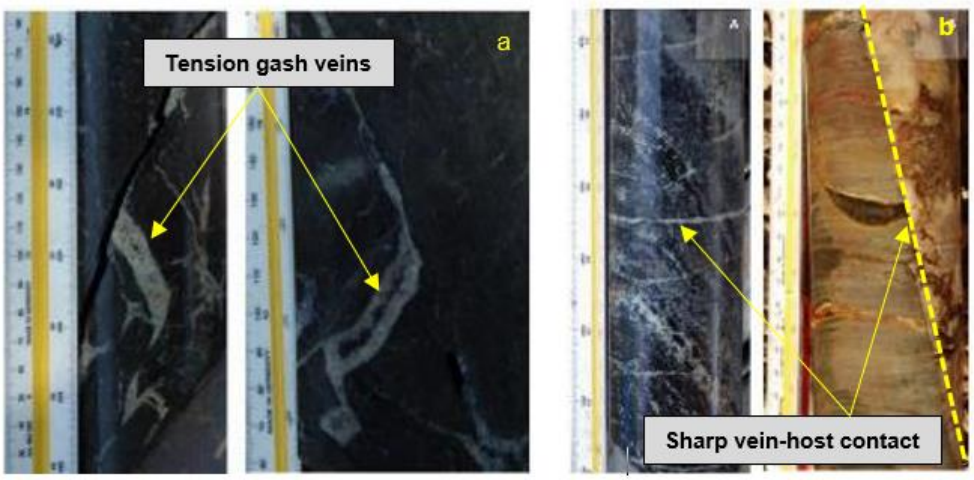

Figure 5-38. Types of veins at Shantumbu. (a) Tension gash vein in Siltstones of Sequence 6 (SPA015 Tray 24 c. 92m). (b) Sharp vein-host rock contacts and progressive alteration away from vein.

The mineral assemblage of the veins mirrors the mineral assemblage of the host rocks, indicative of remobilisation and reprecipitation. Two compositional variants are noted in the area; firstly, quartz + carbonate veins and veins with an identical mineral assemblage to the host rock. Veins vary from ± 0.1cm to several centimetres in width. Large quartz veins with dimensions varying between 0.5 to c. 1m in width and several tens of meters in length are less common and hosted by Sequences 1 and 2.

The layer-parallel vein set is composed of plagioclase, feldspar, quartz, muscovite, sericite, calcite, dolomite, goethite, malachite and various concentrations of iron and copper sulphides (Figure 5-37). The layer-parallel veins conform to the folding experienced by the host rock. An increase in the volume of sulphides within the fold hinges is observed at Shantumbu. The gangue and sulphides within the layer-parallel veins demonstrate various strain fabrics, such as stretching along the cleavage direction. A fourth vein type hosted in siltstones and shales was weakly developed in Sequences 5 to 7. This vein type is represented by tension gashes filled by carbonate minerals (Figure 5-38).

The mineral composition of the irregular veins mirrors that of the host-rock and is interpreted as remobilisation and reprecipitation and cementing of fractured host-rock in strained areas. The irregular veins cross-cut both bedding and folding. The sulphide content and textures within the irregular veins are identical to the layer-parallel vein set.

5.3 METAMORPHISM

The mineralogy and textures noted in Sequences 1 to 7 suggests both basinal and orogenic fluid migration occurred on Shantumbu. Metamorphism is considered to have assisted with fluid formation and movement, as supported by the observations of Munyanyiwa (1990) where retrograde metamorphism from amphibolite facies to greenschist facies occurred in the Lusaka Region, resulting from late-stage fluid movement.

Primarily potassic minerals form the bulk of the minerals of the detrital sediments of Sequences 1 and 2, and include K-feldspar, secondary plagioclase, quartz, ± muscovite. Sequences 3 to 7 are composed primarily of calcite, dolomite, aegirine, plagioclase, K-feldspar, biotite ± quartz, epidote, glaucophane, garnet and amphibole. In all sequences, biotite, muscovite/sericite, calcite, dolomite, quartz, hematite, goethite and magnetite form the interstitial minerals. The mineralogy, particularly of Sequences 3 to 7, are indicative of medium to high pressure-temperature metamorphism and retrograde metamorphism to greenschist facies.

Evidence for low temperature metamorphism or retrograde metamorphism, such as greenschist facies, is indicated by grain bulging noted for quartz and plagioclase and the undulose extinction observed in quartz grains (Cao *et al*., 2013).

Clinopyroxene and sodic amphiboles formed from the sodic metasomatism and low-temperature and high-pressure metamorphism, which occurred around Shantumbu. Retrograde metamorphism accounts for the conversion of clinopyroxene to amphibole, biotite and chlorite (Aivo and Whitehouse, 2011). The presence of clinopyroxene (aegirine) denotes amphibolite facies metamorphism, whilst glaucophane is suggestive of epidote amphibolite facies to blueschist facies metamorphism. Glaucophane may have also have formed via sodic metasomatic fluids, or from relatively high pressure and low temperature conditions and hence by itself cannot indicate the facies of metamorphism (Ernst, 1963).

It is proposed that the amphibole minerals were retrograde metamorphosed to biotite, pyroxene and chlorite, thereby explaining the lower number of amphiboles present in comparison to biotite. Biotisation is likely to have occurred during the Pan-African Orogeny. Introduction of high temperature hydrous and sodic- and potassic-rich sulphate fluids would facilitate alteration of hornblende to biotite + anhydrite + quartz (Brimhall *et al*., 1985). The completeness of the amphibole alteration to biotite and chlorite is considered to be largely time-dependent and the volume of fluids involved (Brimhall *et al*., 1985).

Amphibole/hornblende and garnet are characteristic of epidote-amphibolite and amphibolite metamorphic facies (Smulikowski *et al*., 2007). Garnet also forms from the interaction of Al-rich solutions, thereby explaining the formation of epidote (Moufti, 2011). Anhedral amphibole clasts are sporadic and found within brecciated clinopyroxene clasts in Sequences 5 and 6.

The scarcity of garnets is proposed to have resulted from absorption by biotite and replacement by sodic clinopyroxenes and amphiboles. Munyanyiwa (1985) indicated garnets in the Mapanza Region of Zambia occur only in amphibolites with Fe/(Fe + Mg) > 0.5. In the Mapanza Region of the Zambezi Belt, minor amphibolites sporadically occur as lenticular bodies, bands and boudins in marbles and calc-silicate rocks (Munyanyiwa, 1985).

Hornblende alteration of pyroxene was noted. Clinopyroxene (aegirine) underwent alteration to chlorite along grain boundaries and biotite constitutes the major cement mineral surrounding the clinopyroxene clasts. Scapolite, clinopyroxene, columbite and amphibole were noted in Sequences 5 and 6.

Katongo *et al. (*2004) acknowledged that the scapolitisation in the Munali Hills area (southern Zambezi Belt of Zambia) was due to metasomatism, where scapolite pervasively replaced plagioclase in the granite gneiss, amphibolites and metagabbros, indicating amphibolite facies metamorphism. Katongo *et al*. (2004) documented the similarity in composition of the Munali Hills scapolite to that known in the Zambian Copperbelt in former evaporite horizons, where metamorphism was accompanied by high-NaCl fluids, which formed from the dissolution of the evaporite horizons. Scapolite precipitated from the reaction of plagioclase + calcite + quartz + halite (Mora and Valley, 1989; Satish-Kumar and Harley, 1998), and suggested a sedimentary origin of the NaCl (Mora and Valley, 1989).

Scapolite was observed in the carbonate-rich units of Sequences 1 and 5. Scapolite-plagioclase-calcite suggests low to moderate chlorine activity whereas scapolite-quartz-plagioclase and scapolite-quartz-calcite suggests high chlorine activities during metasomatism. Scapolite-plagioclase-quartz-calcite also denotes high temperature and pressure metamorphism (Deer *et al*., 2004). Hence, high temperature and pressure metamorphism is suggested by the presence of scapolite-plagioclase-quartz-calcite at Shantumbu.

Simpson *et al.* (1963), Mallick (1966) and Cairney (1967) documented almandine-staurolite-kyanite schists at the base of the lithological package above the Basement in the Kafue-Lusaka region. Vrána (1975) documented eclogite in metagabbro bodies in a discontinuous belt south of Lusaka and east of Mpande Dome. Kyanite was not observed during the 2013 to 2015

exploration as exploration concentrated in the central and northern portions of Shantumbu, rather than on the margin of the Mpande Dome.

5.4 DISCUSSION

The lithostratigraphic correlation of Sequences 1 to 7 with the Roan Group in the Zambian Copperbelt was presented and deliberated in Chapter 4, together with the depositional environments of Sequences 1 to 7.

Sequences 1 and 2

The alteration mineralogy of Sequence 1 consists of plagioclase, K-feldspar, muscovite, sericite, dolomite, calcite, chlorite, goethite, covellite, chalcocite and secondary albite, indicating that the lithologies of Sequence 1 were subjected to sericitisation, saussuritisation, sodic and potassic alteration, minor albitisation and carbonatisation. Oxidation and weathering are represented by hematite, goethite and malachite.

Alteration is predominated by sodic, calcic and potassic alteration. Calcite precipitated from either or both the introduction of Ca in solution from circulating fluids and/or concentration of Ca during hydrothermal alteration of calcic-plagioclase. Dissolution of evaporites was a further source of Na for the circulating sodium and calcium-rich fluids. The mineral assemblage of the cross-cutting veins is the same mineralogy as the host rock, indicating crystallisation from solution during diagenesis and metamorphism.

The rapid sediment input responsible for Sequence 2 is considered responsible for the lack of intergranular spaces, which resulted in an impermeable unit. During deposition, it would be expected that clay sized material formed a significant part of the cementing material and layers deposited from suspension fallout. Together with the sutured boundaries, grain bulging and distorted lattices, due to pressure-related deformation, Sequence 2 formed an impermeable barrier to the flow of connate and basinal fluids. The lack of organic matter due to the high sedimentation rate and the high-energy environment of debris flows, impeded the reduction of sulphate and precipitation of copper and base metal sulphides during the deposition.

The scapolite present in Sequence 1 was either part of the protolith composition of the sediment or represents the alteration product of calcareous minerals related to mudstones with associated evaporitic deposits. Chlorite pseudomorphically replaces biotite to varying extents,

although not a common feature. Stain features within quartz grains resulted in undulose extinction.

Sericitisation, carbonatisation, silicification, albitisation and oxidation/hydration dominate the alteration. The products of feldspar alteration are silica and potassium and serve as sources for authigenic quartz and silicification and potassic alteration (El Desouky *et al*., 2008) noted in Sequence 2. Plagioclase displays Carlsbad twinning indicative of sodic alteration.

Sequences 3 and 4

The protolith of Sequence 3 is interpreted to have been an organic-bearing siliciclastic unit deposited during an emergence cycle, where silicate phases formed the major fraction and were mixed with calcareous material. The depositional environment evolved to evaporitic conditions following the high-energy debris flows, which resulted in the growth and increase in volume of evaporites. Dolomitisation has destroyed the original fine-grained textures.

Calcite and dolomite within the terrigenous sediments of Sequences 1 to 3 resulted from a combination of precipitation during sedimentation, from the introduction of carbonates in solution in circulating fluids and recrystallisation of carbonates. The carbonates represent remobilised components either from minor amounts of carbonate minerals present during deposition or from adjacent strata. Alternatively, circulating terrestrial fluids flowed towards the chemical gradient with the nearby seawater seepage and resulted in dolomitisation through the interaction between sulphates and carbonates with Mg, as summarised in Figure 5-39.

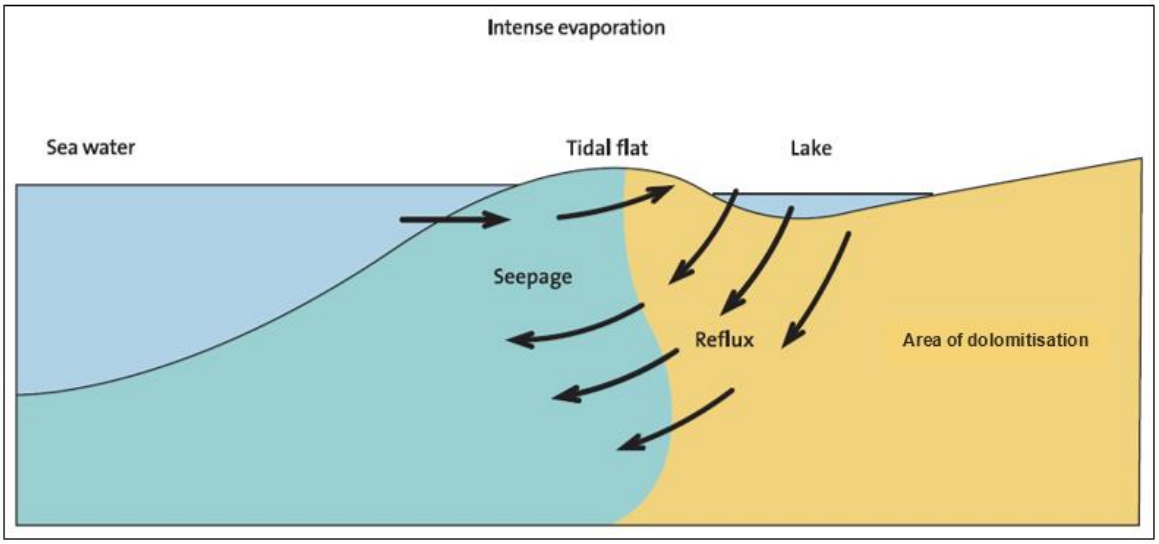

Figure 5-39. Area of dolomitisation and the seepage mechanism responsible for the development of the dolomitisation observed in Sequences 1 and 2, Shantumbu (After, Kendall, 1978, p143).

Sequence 5

Brecciation, migration of fluids through the strata and deformation altered the mineral assemblages within Sequence 5a to c. The alteration events which occurred in Sequence 5 included saussuritisation, carbonatisation, silicification, sodic alteration and sericitisation. The SEM work confirmed sodic metasomatism.

Alteration minerals in Sequence 5 a to c included aegirine, both green and tan brown, quartz, scapolite, hornblende, plagioclase (albite), K-feldspar, quartz, biotite and calcite, with accessory epidote, apatite, sphene, zircon, garnet, sericite and hematite. Iron oxides are common. Albitisation and epidotisation/saussuritisation are evident within the silicate mineralogy and calcite partially replaced silicate minerals. Zircon is interpreted as an original constituent of the carbonate rock, as it occurred as fine-grained inclusions within the aegirine-augite grains.

Epidote, associated with aegirine and biotite grains, replaced plagioclase. Epidote ($Ca_2(Al,Fe)_3Si_3O_{12}(OH)$) is a common retrograde product of Ca-bearing metamorphic rocks. Epidote replaced plagioclase frequently within Sequence 5 and is associated with iron sulphides and oxides; whether this is an indication that Fe-bearing fluids were involved in both the formation of epidote and sulphides is unclear. Recrystallisation of epidote from plagioclase may have occurred by introduction of Fe at the expense of Al. The highest temperature at which epidote is stable is c. 500°C (Harpum, 1954). Epidote together with albite, sphene and calcium- and sodium-rich silicates is suggestive of formation at temperatures of c. 300 - 400°C (Morad *et al*., 2010).

Hornblende is indicative of sodic alteration and together with garnet indicated that the sediments were subjected to medium-grade metamorphism. The garnets hold both lanthanides and titanium, and based on the calcium and iron present, is suggestive of grossular-andradite. The lanthanides probably originated from the Mpande Basement hinterland. Over and above the garnet containing Ti, both biotite and stilpnomelane were repositories of Ti. No definitive features were found for authigenic amphibole and the aegirine may have recrystallised to sodic amphiboles.

Scapolite is reported as evidence for former evaporites in the Katanga Supergroup of the Central African Copperbelt (Hanson *et al*., 1994; Johnson and Oliver, 1998). Scapolite may also result from transformation of plagioclase to scapolite (Moore, 2010) and may indicate the introduction of externally derived chlorine and/or CO_2-rich fluids or derived from organic matter such as graphite (Dombrowski *et al*., 1996). Scapolite within the dolomites around Lusaka was reported

by Drysdall and Stillman (1966) and abundant within metagabbro intrusive bodies and sporadic within pelitic schists in the Lusaka-Kafue Region. Hanson *et al. (*1994) attributed the presence of scapolite in the Zambezi Belt to high activities of Cl, CO_2 and SO_3 in the metamorphic fluids. The migration of moderate to high salinity (NaCl) fluid/s through the lithostratigraphy of Shantumbu is also indicated by the presence of sodalite and columbite.

The scarcity of aegirine in Sequences 1 to 4 and 7 indicates aegirine is an alteration mineral in Sequence 5. Na-bearing phases present in Sequence 5 are not pure end-member sodic clinopyroxenes and amphiboles, they are sodium minerals with variable Fe and Mg contents reflective of an iron- and magnesium-rich carbonate. It is proposed that through low-temperature-high pressure regional metamorphism and Na-metasomatism, biotite together with amphiboles, were replaced by sodic clinopyroxenes (aegirine-augite).

The presence of oxidised iron is a prerequisite, together with quartz and a Na-rich aqueous fluid, to form aegirine. The presence of oxidised iron required a pre-cursor oxidising event. An oxidised host unit and interaction with a Na-rich aqueous fluid was postulated by Tsikos and Moore (2005) to account for the aegirine in the Hotazel iron-formation in the Kalahari Manganese field in South Africa. Tsikos and Moore (2005) summarised the hypothetical chemical reaction as:

$$\underset{\text{Quartz + hematite}}{4SiO_2 + Fe_2O_3 + 2NaCl + H_2O} \longrightarrow \underset{\text{aegirine}}{2NaFeSi_2O_6 + 2HCl}$$

The low-temperature aqueous fluid was derived from formation of metasomatic Na-rich/saline fluids from near-surface waters and brines, and/or evaporite dissolution (Tsikos and Moore, 2005). Decarreau *et al.* (2004), through experimental synthesis, suggested aegirine crystallises at temperatures above 200°C and at a temperature of 200°C crystal growth is very slow and small aegirine crystals form. Below 200°C, ferric phyllosilicates develop in a Si-Fe-Mn-Na-H_2O system. With increasing pressure, the temperature at which aegirine formed was lowered, as summarised in the stability plot derived by Likhoydov (1981) (Figure 5-40). Decarreau *et al.* (2004) demonstrated that higher pH levels favoured growth of aegirine.

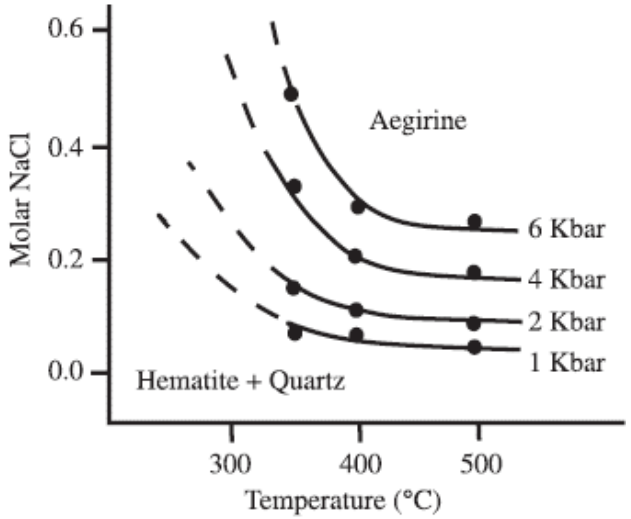

Figure 5-40. Stability of aegirine with NaCl molar quantity, temperature, and pressure. The plot indicates with increasing pressure, the temperature at which aegirine forms is lowered (Likhoydov 1981).

In the Sequence 5 carbonate samples which hosted large aegirine grains did not contain much biotite and in areas where biotite predominated, the aegirine grains tended to be finer-grained. The presence of aegirine indicated the minimum temperature sustained by Sequence 5 was in the order of 200°C but was dependent on both the prevailing pH and pressure at the time of alteration.

In the Hotazel Formation, Tsikos and Moore (2005) noted the earlier iron oxidation and hydrothermal leaching of the carbonate fraction were precursors to the sodic metasomatism. This earlier event assisted with an increase in secondary porosity of the carbonate units, particularly along layers which contained an increased amount of silicate minerals. Likewise, for Sequence 5, the circulating metasomatic fluids may have carried Fe. Both iron oxides and sulphides are associated with aegirine-bearing samples, suggesting Fe was present during alteration. Similarly, the low amounts of biotite noted within the aegirine-rich samples may suggest biotite was replaced by quartz-microcline-amphibole, followed by albite-aegirine-amphibole (Pirajno, 1992). The pyrrhotite + pyrite association with aegirine in Sequence 5c suggests the dominance of iron in the system.

The presence of albite with aegirine-bearing samples suggests albite formed from the Na-rich metasomatic fluids, akin to fenitisation associated with carbonatite/granitic intrusions. The presence of amphibole may or may not have been related to the sodic metasomatism, formed from the destabilisation of aegirine. The degree of albitisation varies throughout Sequence 5, but is concentrated in areas with aegirine, feldspar, epidote and quartz.

Circulating low salinity meteoric fluids resulted in the dissolution of the evaporite minerals within the siltstone/mudstone beds triggering brecciation in Sequence 5. Circulating magnesia, silica, carbonate and sulphide-bearing fluid subsequently formed the cement between the breccia clasts. Circulating basinal brines increasingly warmed and strengthened the salinity during progressive burial, diagenesis and dissolution of evaporite minerals. The fluid generated from the dissolution of the evaporite minerals would have produced the moderately to highly saline Na-Ca-Mg-bearing fluid.

Sequence 6

In Sequences 6 and 7, dissolution of the evaporite minerals by Na-, Fe- and Ca-bearing circulating connate fluids (dolomitisation) is proposed to have caused the collapse of the sediments, producing fine-grained granoblastic calc-silicate breccias.

The arenites of Sequence 6 are dominated by coarse-grained interlocking, anhedral pyroxene plagioclase grains, sub-ordinate orthoclase, clinopyroxene, amphibole, quartz, sodalite, sphene, biotite, calcite, apatite, chlorite, hematite and goethite grains. The arenite was subjected to carbonatisation noted by the presence of microcrystalline calcite within plagioclase grains. The presence of chessboard and polysynthetic twinning in the plagioclase grains is secondary plagioclase. The recrystallisation of calcite occurred after formation of the sulphides, noted by broken sulphide grains filled by calcite. Micro-crystallisation of quartz replaced calcite or vice versa.

The mineralogy of the siltstone layers within Sequence 6 are dominated by aegirine, feldspar, quartz and phyllosilicates. Calcite and sulphides are secondary. The mineralogy indicates the rock underwent low-grade metamorphism, specifically greenschist facies.

Sodalite indicated a high-temperature reaction between carbonates and silicates through hydrothermal alteration from a sodium chloride-rich solution (Jamtveit *et al*., 2004; Fall *et al*., 2006; Kovalskii *et al*., 2006). Silica precipitated as a by-product. The fundamental requirement for formation of sodalite is a calcic environment and displacement of the calcium during interaction with fluids. Sodalite may also form due to the presence of alkaline fluids and volatiles (Deer *et al*., 2004).

Introduction of hydrothermal fluids would require the presence of intrusions, of which none to date have been discovered on Shantumbu. The presence of sodalite in Sequence 6 may also be explained as a product of skarn activity, which indicated high temperature metasomatic fluids

which may have originated from pegmatite or granitic intrusions. It is more probable that the sodalite in Sequence 6 formed from sodic metasomatism, which also formed glaucophane. Glaucophane is indicative of low-temperature and high-pressure metamorphism, suggestive of blueschist (glaucophane schist) facies but is also indicative of a soda-rich environment or sodic metasomatism.

Sphene ($CaTiSiO_5$) (titanite) was noted in both Sequences 5c and 6 within impure carbonates and calc-silicates respectively and is associated with quartz and amphibole. Sphene is a common accessory mineral both in igneous and metamorphic rocks as it is found in rocks of calcic composition. Sphene is present in minor amounts in impure marbles, calc-silicate and to a lesser extent pelitic rocks (Frost *et al*., 2000). Within calcic environments, sphene is stable due to the Ca site within the crystal lattice, with the accommodation of various elements such as Al, Fe, U, Th, Mn and REEs, and the accommodation of elements is controlled by the bulk composition of the metamorphic host rocks. Sphene is known to occur in rocks subjected to amphibolite, eclogite and granulite facies metamorphism and may form in environments that were subjected to low temperature - high pressure and low temperature - low pressure metamorphism (Frost *et al*., 2000). The presence of orthopyroxene in Sequence 6 is indicative of granulite facies metamorphism, however granulite facies metamorphism requires high-temperature conditions which were not noted in Sequence 6.

Sequence 7

The lithologies in Sequence 7 have undergone various alteration processes, including saussuritisation, albitisation and sericitisation. The alternating micaceous and calcitic bedding of Sequence 7 resulted from cycles of short-lived and restricted sedimentation to chemical precipitation, with the bedding representing planar stromatolites. The monotonous succession of grey-blue calcitic carbonates are composed of anhedral, medium-grained interlocking calcite grains with lesser quartz, epidote, iron oxides, muscovite, biotite and chlorite. The biotite and chlorite are products of retrograde metamorphism. Quartz is predominantly recrystallised authigenic quartz and/or precipitated from the reaction of sulphate minerals dissolution during early diagenesis (Deer *et al*., 2004) and reduction of sulphates. Two generation of calcite were noted with the second generation being the result of alteration and metamorphism, which resulted in regular grain boundaries and annealed/triple junctions. The formation of sphene is a product of contact metamorphosed limestones.

Alteration

The alteration events on Shantumbu were both cross-strata and widespread within all the Sequences. Due to the widespread alteration, both at Shantumbu and in the Central African Copperbelt, differentiating the alteration event/s, which were responsible for the copper mineralisation is challenging. The mineralogical examination allowed a preliminary understanding of the probable alteration order, which occurred at Shantumbu.

The sodic alteration, which is more prolific in the lithologies above the Copperbelt Orebody Member than below, occurred after the dolomitisation and potassic alteration of the lithologies below the Copperbelt Orebody Member. The sodic alteration is indicated by the extensive development of secondary plagioclase feldspar, sodic feldspathoids, columbite, scapolite, sodic amphiboles and glaucophane present.

The dominance of potassic alteration in the lithologies below the Copperbelt Orebody Member correlated to the progressive burial of the sediments, which caused the dissolution of K-feldspar and the precipitation of albite. Minerals, which indicated the high-grade metamorphism include the sodic minerals and indicated that the sodic alteration occurred during or after peak metamorphism. Sodic minerals are related to the passage of basinal brines, which may or may not contain base metals in solution.

Alteration on Shantumbu was the result of diagenesis-compaction, dewatering of the terrestrial sediments and later stage remobilisation of potassic and sodium-bearing fluids. Based on the extensive alteration of Sequences 3 and 4, the basinal brines which developed were channelled through the permeable units of Sequences 3 and 4 and were responsible for the sodic alteration of the lithologies in Sequences 5 to 7 and the reprecipitation of copper. The sodic alteration resulted in the development of biotite in the lithologies of Sequences 5 and 6. The biotite has largely altered to aegirine, which is was a function of the extended sodic alteration phase. The final alteration event, which occurred at Shantumbu is the formation of ferric oxides.

5.5 CONCLUSION

The lithological and mineralogical examinations of Sequence 1 to 7 showed that the detrital and authigenic minerals of the metasediments on Shantumbu were subjected to a complex range of alteration and metasomatism. The alteration and metasomatism resulted from the circulation

of the basinal and orogenic fluids and from the high-pressure low temperature metamorphism. The fluids, which were responsible for the alteration of the sediments were formed by basinal processes such as diagenesis-compaction, dewatering of the terrestrial sediments and later stage remobilisation of potassic and sodium-bearing fluids.

The role of the sodic and potassic alteration episodes to the copper mineralisation events is not clear, other than both the presence of iron and the evaporites and anoxic versus oxic depositional environments played key roles in the formation of the copper sulphides, which occurred via bacterial sulphate reduction and remobilisation and reprecipitation. Chapter 6 delves further into the sulphide mineralisation within the seven sequences on Shantumbu.

The next step of this research, Chapter 7, examines the geochemical behaviour of elements in terms of oxic and anoxic conditions, as these conditions had a direct bearing on the precipitation of the sulphide mineralisation. Oxic and anoxic conditions affect the geochemical behaviour of elements and minerals, specifically the mobility of elements. Examination of geochemical profiles, Al_2O_3 - element scatter plots and element ratios provide support for the subdivision of the lithostratigraphy into Sequences 1 to 7.

CHAPTER 6

MINERALISATION

6.1 INTRODUCTION

Malachite hosted by the arenites of Sequence 1 outcrops on Shantumbu, whereas copper sulphide mineralisation was intersected in the drill cores within all the Sequences. The metasediments on Shantumbu host both disseminated copper sulphides and vein-hosted copper sulphides. Although the copper-bearing sulphides are not constrained to a specific lithology or Sequence at Shantumbu, however the highest concentrations of copper sulphides and oxides occur at or near the transgressive marine surface (Sequence 1, 2 to 4), to a lesser extent in the gneisses of Sequences 6 and 7.

6.2 PETROLOGY AND MINERALOGY

Sequences 1 and 2

The arenites of Sequence 1 and 2 adjacent to impermeable siltstone layers host sulphides concentrations of <1% of the mineral assemblage, as disseminations up to c. 20µm throughout the matrix of the arenite. Quartz veins hosting malachite (Figure 6-1) and hematite and sulphide-bearing veins cross-cut the Sequence. The copper sulphide minerals and oxides in Sequence 1 and 2 include chalcopyrite, chalcocite, bornite, covellite, digenite and malachite (Figure 6-2 and Figure 6-3). Chalcopyrite is always closely associated with pyrite in Sequences 1 and 2. Pyrite is the most abundant sulphide present in Sequence 1 however, chalcopyrite is the most abundant sulphide in Sequence 2. The progressive replacement of chalcopyrite to secondary copper sulphides is commonplace. The alteration of chalcopyrite typically progressed from alteration to bornite, digenite, covellite and lastly chalcocite. Digenite, covellite and chalcocite are finer-grained in comparison to chalcopyrite and grain sizes vary between 30 - 90µm. Alteration along the grain boundaries of the secondary digenite produced rims composed of goethite.

Within Sequence 1 arenites, the chalcopyrite and pyrite grains vary between c. 900µm and 4mm whilst covellite and chalcocite are finer-grained averaging 30 – 40µm in size. Bornite grains average c. 150µm in diameter. The chalcopyrite grains have similar sizes in Sequence 2, varying between c. 10µm and 3mm in size. Oxidation of pyrite resulted in the formation of both coarse-grained (up to c. 1mm) and microcrystalline hematite.



Figure 6-1. Outcrop of fine-grained arkose hosting malachite mineralisation at Copper Hill, Shantumbu.

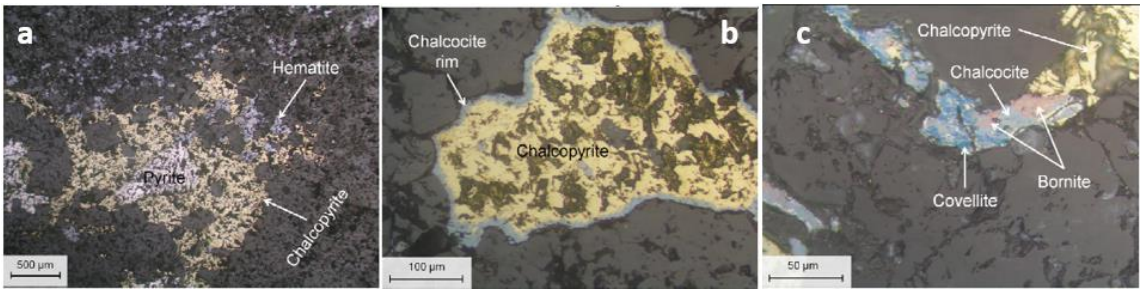

Figure 6-2. Copper-bearing sulphide veins and quartz-plagioclase-muscovite-bearing veins with accessory hematite ± malachite ± goethite, Shantumbu. (a) Rims of chalcopyrite and hematite on sulphides. (b) Chalcocite rim of a chalcopyrite grain (H08294 from PSH001 at a depth of 36.24m). (c) Vein-hosted copper-sulphides within arenite of Sequence 1 (H08300 from PSH001A at a depth of 43.42m). All images in plane polarised reflected light.

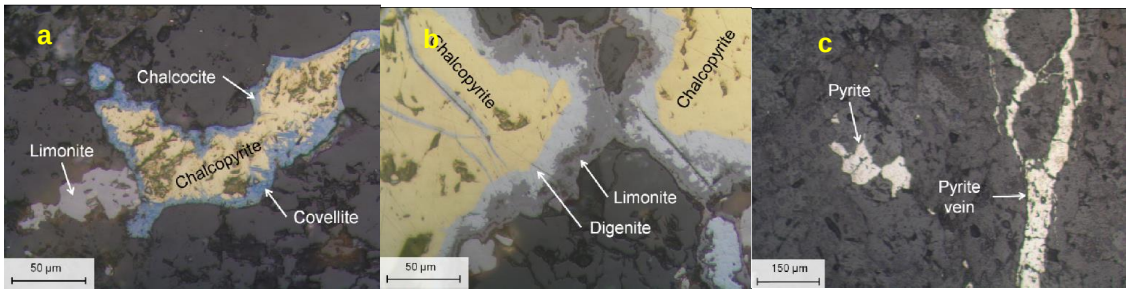

Figure 6-3. Vein hosted and disseminated chalcopyrite, digenite, chalcocite, covellite and pyrite of Sequence 2, Shantumbu. (a) Alteration of chalcopyrite to covellite and chalcocite (H08293 from PSH001 at a depth of 80.4m). (b) Alteration of chalcopyrite to digenite and goethite (H08293 from PSH001 at a depth of 80.4m). (c) Pyrite vein and disseminated pyrite (H08292 from PSH008 at a depth of 52m). All images in plane polarised reflected light.

Sequences 3 and 4

The calc-silicates and dolomitic carbonates of Sequences 3 and 4 underwent extensive oxidation to goethite. Although no copper sulphides were observed during the thin section microscopy, native copper (Figure 6-4) was observed although the presence thereof was not common. The native copper formed clusters of small copper grains, with grain size up to c. 10 - 15µm in diameter noted.

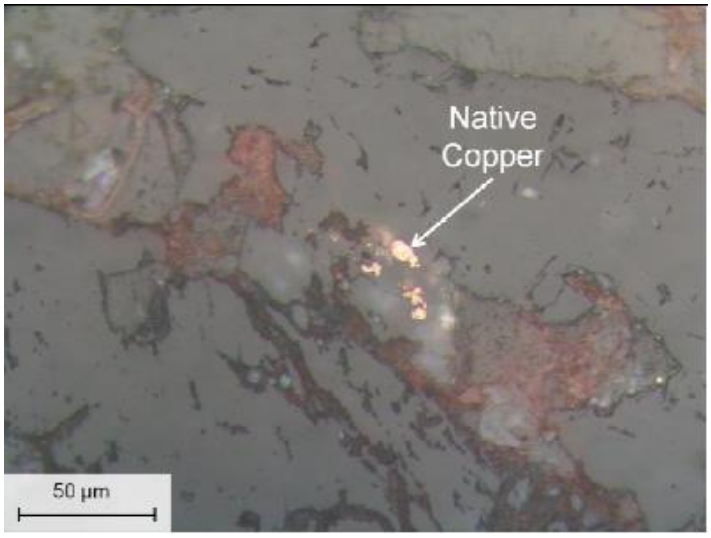

Figure 6-4. Native copper within the calc-silicates of the marine transgression zone from sample H08304 from PSH008 at a depth of 109.20m, Sequence 3/4, Shantumbu. Image in plane polarised reflected light.

Sequence 5

Anhedral and subhedral chalcopyrite within the brecciated siltstone of facies 5b (Figure 6-5 a to f) was noted where the chalcopyrite present occurred as fine disseminated grains within the matrix and in proximity to pyrite and magnetite grains. No copper sulphides were noted in facies 5a and 5c.

The relationship between adjoining chalcopyrite and pyrite grains indicates that the two sulphides crystallised simultaneously as separate sulphides. Both chalcopyrite and pyrite showed a close spatial relationship with biotite, calcite and quartz. The sulphide grains in proximity to coarse-grained biotite laths are significantly larger than the disseminated sulphides within the matrix of sericitic breccia clasts.

The iron and copper sulphide minerals within facies 5b include pyrrhotite, chalcopyrite and pyrite. Anhedral pyrrhotite is associated with hematite and often contains chalcopyrite inclusions. Remnant inclusions of pyrrhotite in hematite were observed. Sulphides are often

orientated in the same direction displayed by the carbonate and siltstone layers. Of the sulphides, chalcopyrite with grain sizes up to c. 550µm occur, whereas pyrite varies from 250µm to 4mm. Pyrrhotite, up to 1mm in size is present as anhedral grains closely associated with hematite and often with chalcopyrite inclusions or as remnant cores hosted in hematite. Magnetite grains vary in size from 250µm to 4mm.

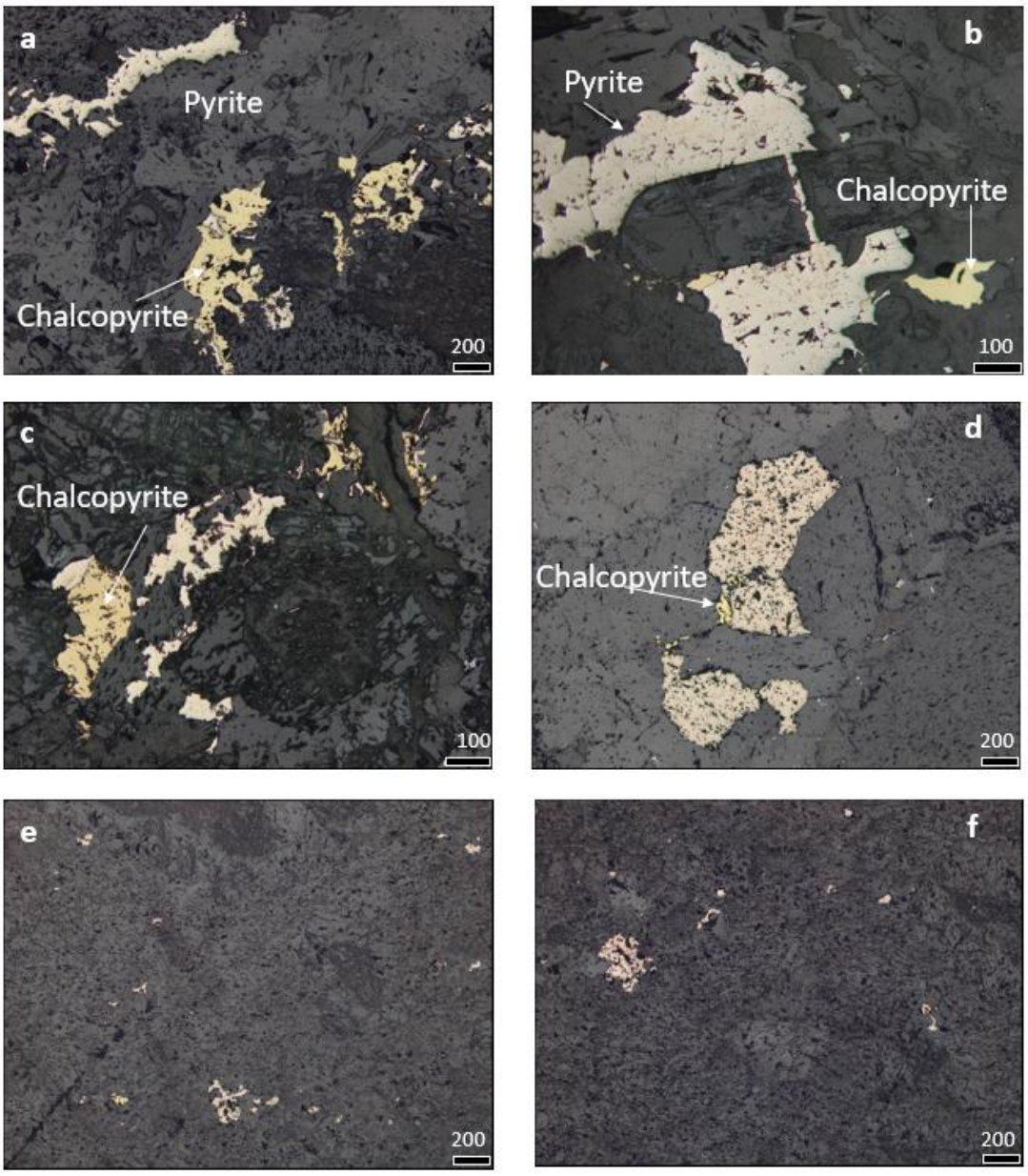

Figure 6-5. Anhedral to subhedral copper sulphides hosted by brecciated siltstones of facies 5b, Sequence 5, Shantumbu. (a) to (f) Disseminated chalcopyrite and pyrite within matrix of calcite and biotite. All illustrations in cross polarised light. (a) Sample E2257B plane polarised reflected light (200µm). (b) Sample E2257B plane polarised reflected light (100µm) (PSH003 at a depth of c. 165m). (c) Sample E2257BA plane polarised reflected light (100µm) (PSH003 at a depth of c. 165m). (d) Sample E2270A (200µm) (PSH003 at a depth of c. 175m). (e) Sample E2257B plane polarised reflected light (200µm) (PSH003 at a depth of c. 165m). (f) Sample E2257B plane polarised reflected light (200µm) (PSH003 at a depth of c. 165m). (g) Sample E2257 (PSH003 at a depth of c. 165m).

The largest pyrite grains are hosted in cross-cutting veins (Figure 6-6 a to h), where crystals display the characteristic cubic habit. Chalcopyrite was not found in the veins but was noted within the breccia clasts and adjacent to the veins.

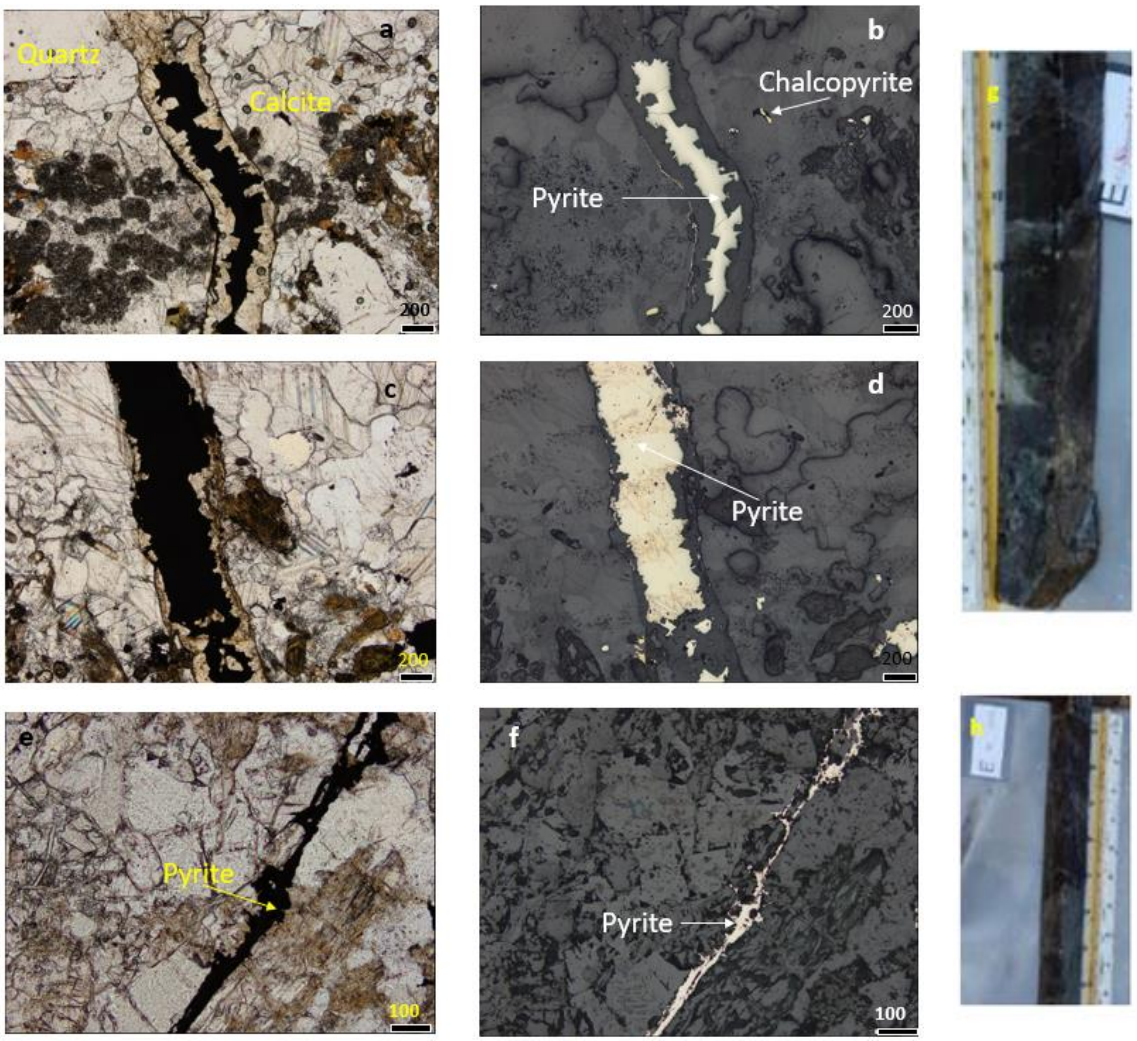

Figure 6-6. Cubic pyrite within veins whilst chalcopyrite is for the most part disseminated in the quartz and biotite host rock in Sequence 5, Shantumbu. (a) Cubic pyrite within vein hosted in calcite; plane polarised reflected light. Sample E2257A (200µm) (PSH003). (b) Cubic pyrite within vein hosted in calcite; Sample E2257A plane polarised reflected light (200µm) (PSH003 at a depth of c. 165m). (c) Sulphide bearing vein; Sample E2257A plane polarised reflected light (200µm at a depth of c. 165m) (PSH003). (d) Sulphide-bearing vein; Sample E2257A plane polarised reflected light (200µm) (PSH003 at a depth of c. 165m). (e) Sulphide bearing vein; plane polarised reflected light. Sample E2257 plane polarised light (PSH003 at a depth of c. 165m). (f) Sulphide-bearing vein; plane polarised reflected light. Sample E2258 plane polarised reflected light (100µm) (PSH003 at a depth of c. 165m). (g) and (h) Core samples of brecciated siltstone of Sequence 5. (g) Sample E2257A (100µm) (PSH003 at a depth of c. 165m). (h) Sample E2258 (PSH003 at a depth of c. 165m).

The post-brecciation veins are chiefly composed of anhedral pyrite, pyrrhotite and chalcopyrite (Figure 6-7). Chalcopyrite occurs in close association with pyrite.

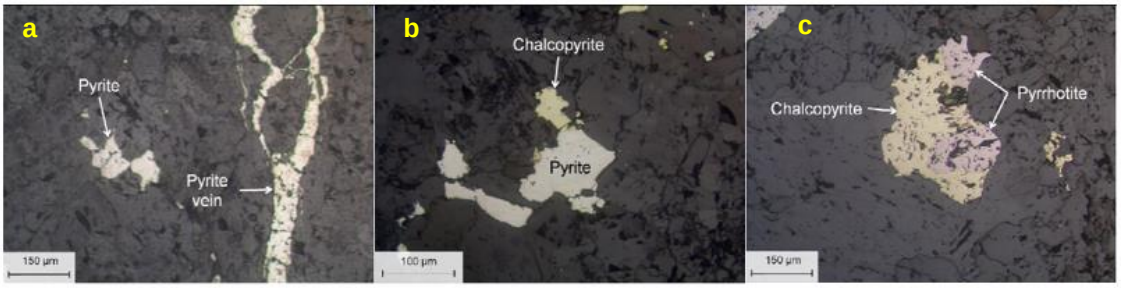

Figure 6-7. Sulphides within Sequence 5, facies b, Shantumbu. (a) Post-brecciation veins composed of anhedral pyrite, pyrrhotite and chalcopyrite (H08292 from PSH008 at a depth of 52m). Sulphide grains (H08292 from PSH008 at a depth of 52m) both within veins and the matrix of the breccia, as shown in (b) and (c) (H08295 from PSH007 at a depth of 136.47m). All illustrations are in plane polarised reflected light.

Sequence 6

The intercalated siltstone and carbonate layers of Sequence 6 both host sulphides. Pyrite and chalcopyrite occur throughout the unit as anhedral to subhedral grains, whilst the largest pyrite grains are hosted within veins (Figure 6-8 and Figure 6-9), where crystals display the characteristic cubic habit and as disseminations within the siltstone and carbonate layers. Chalcopyrite is present in close association with pyrite both within veins and within the host rock.

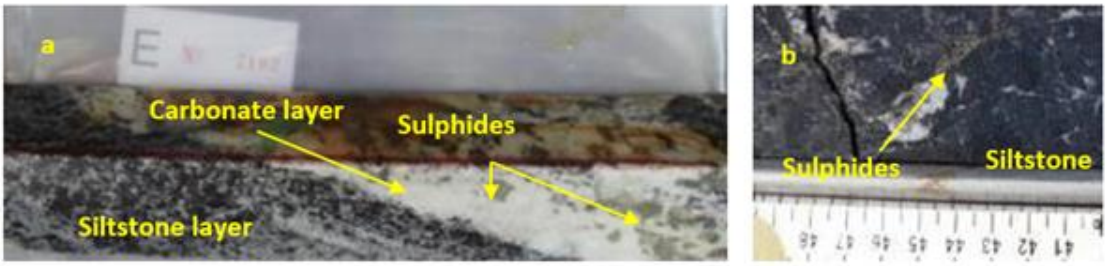

Figure 6-8. Sulphides are hosted by both siltstone and carbonate layers in Sequence 6, Shantumbu; quarter core sample. (a) Large anhedral sulphides grains within carbonate (E2192 from SPA014). (b) Fine-grained sulphide within siltstone; core sample.

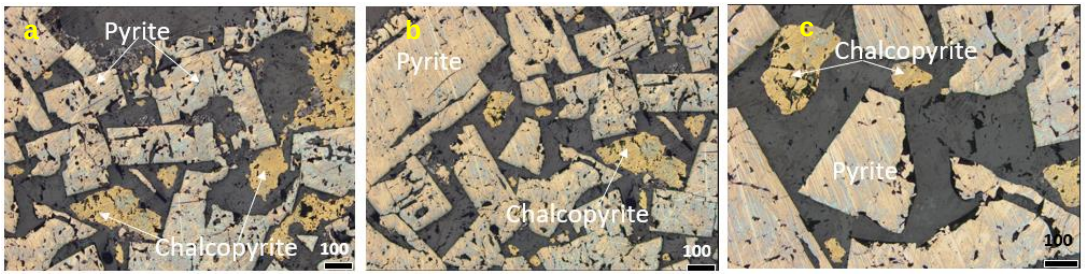

Figure 6-9. Cubic pyrite within siltstone and carbonate layers of Sequence 6, Shantumbu. Chalcopyrite (Ccp) is sub-hederal to anhedral (a to c). All images in plane polarised reflected light. (a) Sample E2215B

(200µm) (SPA015 at a depth of c. 160m). (b) Sample E2268 (200µm) (SPA015 at a depth of c. 175m). (c) Sample E2268 (100µm) (SPA015 at a depth of c. 175m).

Sequence 7

Pyrite, chalcopyrite and pyrrhotite are disseminated throughout the grey carbonate, but are preferentially located along bedding planes. The sulphides have been variably altered to hematite and goethite (Figure 6-10).

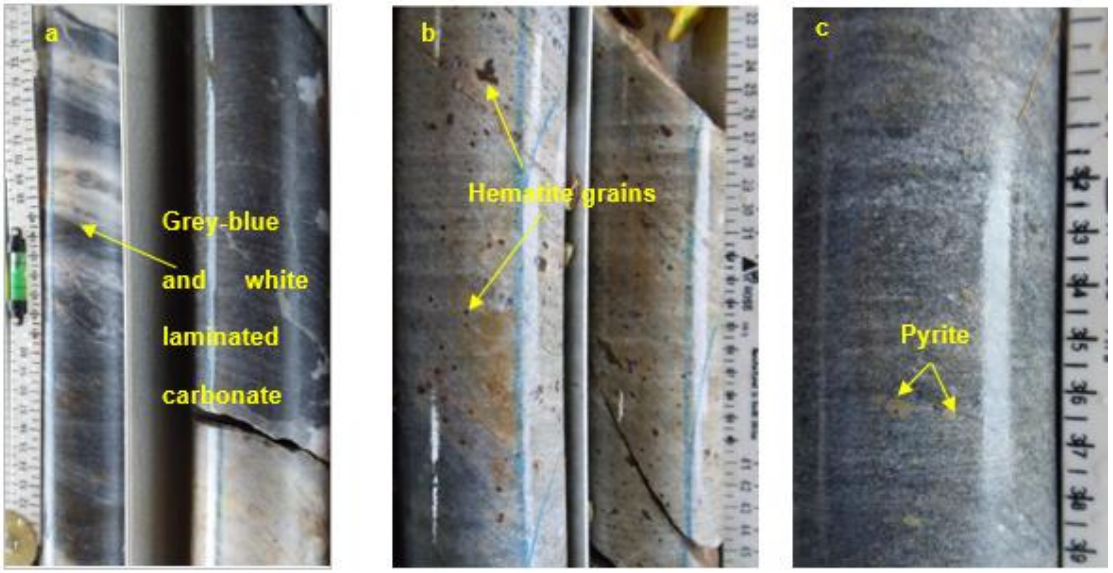

Figure 6-10. Lithologies of Sequence 7, Shantumbu. (a) Finely laminated grey-blue carbonate of Sequence 7 (SPQ002). (b) Hematite grains within laminations of Sequence 7. (c) Pyrite grains within the grey-blue carbonate in Sequence 7 (SPQ001).

6.3 DISCUSSION

Several generations of copper sulphides are noted at Shantumbu. The habit of the sulphides indicated that a significant portion of the sulphides were of early diagenetic origin, formed during shallow burial. Remobilisation and reprecipitation at impermeable barriers and within veins are evident. The abundance of sulphides in sediment-hosted, stratiform copper occurrences is influenced by the presence of organic matter, dissolved sulphate and reactive iron. Based on the mineralogy examination in Chapter 5, there was no shortage of iron within the sediments. Evidence for organic matter was however not found in the core samples for Shantumbu. The prevalence of sodic alteration minerals above the Copperbelt Orebody Member attests to the presences of saline basin fluids having migrated through the sediments.

Genetic Model

Diagenetic pyrite formed by the interaction of iron, sulphates, organic matter and dissolved evaporite material. This step of diagenetic pyrite precipitation was critical to the precipitation of the copper mineralisation on Shantumbu. Chalcopyrite formed diagenetically from the addition of copper to the pyrite crystal lattice and from brines carrying copper in solution. Progressive addition of copper to the crystal lattice of the primary pyrite formed bornite, covellite and chalcocite along the rims of the chalcopyrite or within vein structures.

Pyrrhotite, although a minor component, is interpreted to have formed from the conversion of pyrite during metamorphism. The transition to pyrrhotite indicated desulphidation during metamorphism however, the presence of pyrrhotite is not indicative of the grade of metamorphism, as pyrrhotite can form at all metamorphic grades depending on the lithologies present. The desulphidation to pyrrhotite may also be caused by the addition of iron to the rock, or without loss or gain in either sulphur or iron (Ferry, 1981).

The predominance of stratabound base metal sulphides in the detrital Sequences 1 and 2, versus the scarcity of copper sulphides in the marine-dominated successions of Sequences 5 to 7, suggests the copper was originally sourced from the Basement and/or metavolcanics rocks rather than introduced from a magmatic source. The precipitation of the copper and iron sulphides were deemed to have initially been of diagenetic origin, followed by the remobilisation and reprecipitation of the copper sulphides during the compressive and tectonic activity in the Shantumbu Region.

The formation of basinal brines and related sequence of alteration and copper mineralisation at Shantumbu can be summarised according to five points:

(1) Dewatering related to compression of the rift basin sediments and diagenesis resulted in the dissolution of evaporite units and absorption of base metals into brine solutions. The metals were probably transported as chloride complexes, as these complexes are far more effective in transporting copper, silver and mercury at low temperatures than complexes with OH^-, SO_4^{2-} and SO_3^{2-}. The source of the chloride complexes would be related to dissolution of evaporites which released Cl into the circulating fluids, sea water and evolved connate water moving out of marine sediments due to compaction or tectonic activities;

(2) Low-temperature fluids migrated through permeable strata and precipitated sulphides within the secondary porosity;

(3) Subsequent remobilisation and reprecipitation of the base metals were related to compressional tectonics which reached amphibolite facies metamorphism. Sulphides and host rock minerals were remobilised and precipitated in cross-cutting veins;

(4) Retrograde metamorphism to greenschist facies and related metasomatism followed and the migration of base-metal bearing fluids along structural features such as the D_1 fold axes; and

(5) Oxidation and weathering were the final alteration events which occurred on Shantumbu.

Widespread primary disseminated pyrite in the reduced/carbonate units is a characteristic of sediment-hosted, stratiform copper deposits globally. There is extensive fine-grained disseminated pyrite within the reduced fine-grained carbonate, rhythmites and fine arenaceous layers of Sequences 5 to 7. In Sequence 2, the sulphides are largely restricted to veins but are present as small disseminated grains up to c. 20µm throughout the matrix. Chalcopyrite is closely associated with pyrite in all the Sequences.

In Sequence 1 the sulphide minerals include chalcocite, bornite, covellite, in addition to pyrite and chalcopyrite, whilst pyrite is the most abundant sulphide present. The copper-sulphide/malachite-bearing veins are restricted to the arenite, whilst iron-oxide veins cross-cut both the siltstone and arenite units. In Sequence 2, sulphide minerals form <1% of the mineral assemblage and include chalcopyrite, digenite, chalcocite, covellite and pyrite. Sulphides are largely restricted to veins but are present as small disseminated grains throughout the matrix. Chalcopyrite is closely associated with pyrite and chalcopyrite is the most abundant sulphide present. Alteration along the grain boundaries of chalcopyrite grains was first to digenite and then goethite.

Sequences 3 and 4 are correlated with the Copperbelt Orebody Member of Roan Group in the Zambian Copperbelt, the main copper-bearing horizon. The considerable amount of goethite present in Sequences 3 and 4 suggests the sequences hosted significant amounts of syngenetic and diagenetic sulphides, which were later remobilised. Sequences 3 and 4 experienced intensive alteration but do not host copper sulphides however, native copper is present. Insufficient information is available to determine whether the native copper was originally introduced as native copper or the product of alteration and fluid migration. The dolomite, authigenic quartz and carbonate units of Sequence 3 may represent the altered products of a primary lithological unit, which contained vast amounts of evaporitic material. Such replacement of evaporites is well documented in the Zambian Copperbelt (Hayes *et al*., 2015).

The lack of base metal sulphides in Sequences 3 and 4 raises two questions regarding the copper mineralisation on Shantumbu: (1) Where did the copper migrate to if it was originally precipitated in the vast quantities of pyrite presumed to have been the primary mineral to the secondary goethite; and (2) was there sufficient thickness of copper-bearing detrital sediments at the base of the rift package on Shantumbu for copper to be remobilised into the brine solutions and reprecipitated further up the stratigraphy beneath impermeable lithologies? Lastly, was the rift basin responsible for the deposition of the metasediments bounded along the margins by faults, or were the copper-bearing fluids able to escape the basin?

Sequences 1 and 2 do not have the sulphate and chemical carbonate minerals, which are considered to have assisted the formation of the iron and copper sulphides in the Sequences above the Copperbelt Orebody Member. Organic matter is also a prerequisite for sulphate reduction and the formation of sulphides within a sedimentary environment. In areas where the permeable arenite layers of Sequences 1 and 2 are overlain by successions of black siltstone-shale, copper mineralisation is present, and vice versa. The source of the sulphur for the diagenetic sulphides of Sequences 5 to 7 is considered to have been the result of bacterially produced H_2S from seawater sulphate. Sulphate reduction is considered to have been a late-stage event and responsible for the precipitation of sulphides following remobilisation by circulating metasomatic and basinal brine fluids, during the Pan-African Orogeny and retrograde metamorphism. In Sequences 5 to 7, the diagenetic pyrite formation is considered to have been followed by the migration of the metalliferous fluid migration upward through the stratigraphy and led to the formation of chalcopyrite within the marine-dominated sequences.

Pyrrhotite formed during prograde metamorphism by pyrite-to-pyrrhotite desulphidation. The breakdown of pyrite allowed the metals to enter the fluids generated during metamorphism. Typically, copper is retained *in situ* during metamorphism and did not enter the fluids (Finch and Tomkins, 2017). This may have resulted in the growth and predominance of chalcopyrite as the common copper sulphide present noted in Sequences 5 to 7.

Pyrrhotite is closely associated with hematite, often occurring as remnant inclusions within hematite and hosting inclusions of chalcopyrite. The copper-bearing sulphides other than chalcopyrite, appear to be secondary, an alteration feature at Shantumbu.

The alteration succession of the sulphides developed from pyrite to chalcopyrite+pyrrhotite-chalcocite-digenite-bornite-covellite-native copper-malachite, and pyrite-magnetite-hematite-goethite. The sulphide and oxide mineralisation were that of replacement-style mineralisation.

Microscopic native copper was observed within the iron-rich calc-silicate of Sequence 4. The native copper is proposed to have formed from supergene activity, which resulted from complete alteration of the protolith silicates and sulphides. Most of the iron minerals were oxidised and hydrated, potentially releasing copper into its native form. It is postulated the absence of sulphides in the breccia and calc-silicate resulted from the removal of sulphur by the migrating basinal brines and prolonged alteration. Within sedimentary basins subjected to marine transgression and regression, circulating brines originate from dissolution of evaporites, compaction and the resulting expulsion of fluids, seawater percolation and tectonic activity (Shelton *et al*., 2009).

The presence of native copper at the White Pine Mine in Michigan was introduced as native metal after sedimentation (Walker *et al*., 1958). The introduction of native copper after sedimentation is plausible as a cause for the native copper noted in Sequence 4. Alternatively, the petrography of Sequence 4 has been highly altered, and the native copper may be of supergene origin, as noted in the Monwezi Sandstone of the Nguba Group in the Katanga Foreland (El Desouky *et al*., 2008). Native copper precipitates first from oxidised chloride-bearing fluids when encountering pH >6.0 conditions (Rose, 1976).

Based on the sequence of events from sedimentation to diagenesis, deformation and metamorphism and retrograde metamorphism, it is unlikely that bacterial sulphate reduction and hydrothermal fluids occurred in tandem. It is considered more likely that the mineralisation formed in anoxic conditions present during sedimentation by bacterial sulphate reduction and basinal brine, and from hydrothermal alteration thereafter.

Chongwe Copperbelt

To the north of Shantumbu, a copper- and gold-rich metallotect, informally termed the Chongwe Copperbelt, hosts several copper and gold occurrences over a strike of approximately 80km and a width of approximately three kilometres (Figure 6-11). The Mpande Dome is approximately 40km to the south east of the Chongwe Copperbelt. The copper mineralisation at Shantumbu is similar to that within the Chongwe Copperbelt, although the copper mineralisation of the Chongwe Copperbelt is described as an iron oxide-copper-gold (IOCG) style deposit, which may or may not be accurate.

Both the copper mineralisation at Shantumbu and within the Chongwe Copperbelt coincides with the contact between the Basement granitoid-gneisses and the overlying Katanga

metasediments. Within the Chongwe Copperbelt, malachite and chalcopyrite mineralisation in a close association with magnetite, are hosted by silicified quartz-hematite veining and within breccias. The copper mineralisation at both Shantumbu and in the Chongwe Copperbelt is disseminated through the brecciated assemblages of ferruginous altered carbonate, calc-silicate, and amphibole schist lithologies, and feldspar-quartz-biotite and quartz-biotite schists (Zambezi Resources, 2005; Zambezi Resources, 2007).

Within the Chongwe Copperbelt, sulphide mineralisation is hosted by Katanga Supergroup lithologies which overlie or are near the unconformity with the Basement, while the sulphides within the Basement occurs as structurally hosted copper oxide and sulphide mineralisation (Zambezi Resources, Prospectus, 2007). Sulphide mineralisation within the Basement was mined at Allies Mine in 1914 and 1922, and various small-scale artisanal workings in the Mulofwe Dome area. Diamond drilling at the Allies Mine during reconnaissance activities by an exploration company yielded copper values, the best of which was reported as 6.5m averaging 5.09% Cu (Zambezi Resources AIM admission document, 2004a).

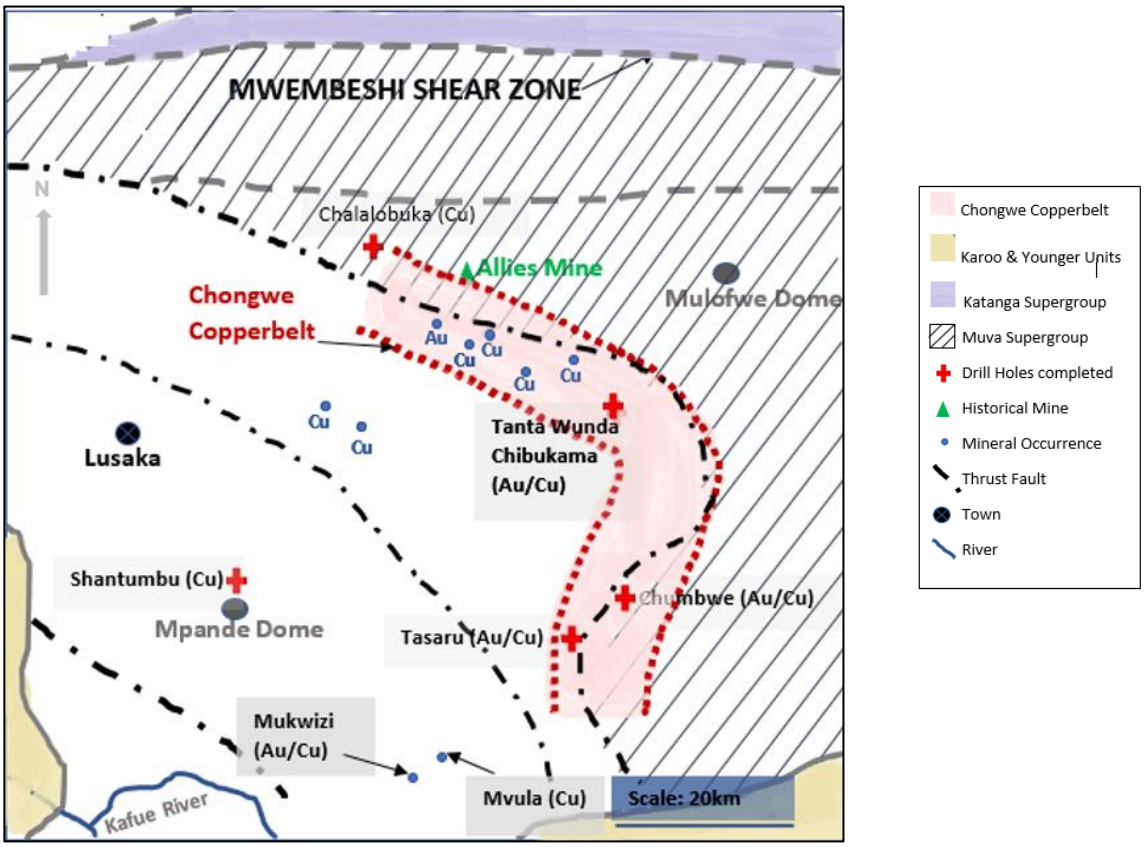

Figure 6-11. Locations of several known copper and gold occurrences within the Chongwe Copperbelt, indicating the location of Shantumbu, Mpande Dome, Mulofwe Dome, Allies Mine, Tanta Wunda Chibukama, Tasaru, Chumbwe and several other known copper and gold occurrences (Modified after, Zambezi Resources, 2007).

In the Mulofwe Dome area, structurally controlled anomalous copper, gold, silver, cobalt and bismuth mineralisation occurs in a shallow dipping zone (Zambezi Resources, 2005; Zambezi Resources Press Release, 2008). Bismuth was mined in the 1920s' at Mulofwe Dome (Zambezi Resources, 2004). First pass rock chip sample results for the Mulofwe Dome area returned a copper grade of 7.0% Cu. Further rock chip sampling render copper values between 1.5% Cu and 7.0% Cu. Arsenic values were observed to be elevated, as noted in a reported grade of 3,713ppm As. The mineralisation within the Mulofwe Dome area is hosted in structurally controlled, broad zones in chrysocolla-bearing veins, tourmaline-bearing iron oxide veins, in malachite iron oxide quartz rocks, in highly silicified malachite-bearing quartz and in iron oxide breccia (Zambezi Resources, 2005).

Exploration at the Mukwizi Copper-gold project, southeast of Shantumbu, intersected copper mineralisation in rock chip samples, which returned values of 11.4% Cu, 4.8% Cu and 4.0% Cu. The copper mineralisation consisted of malachite, azurite, chalcopyrite and bornite hosted by intensely fractured and brecciated assemblages of ferruginous altered carbonate, calc-silicate and amphibole schist lithologies (Zambezi Resources Press Release, 2008). At Chumbwe, approximately 60km east of Shantumbu, Reverse Circulation drilling intersected disseminated malachite hosted in feldspar-quartz-biotite schist and quartz-biotite schist with grades between 0.3 to 0.5% Cu as (Zambezi Resources, 2004; Zambezi Resources, 2005a).

At Tasaru in the Chongwe Copperbelt, surface sampling of historical trenches and mined material yielded malachite and traces of bornite, and copper grades between 0.83% Cu and 8.06% Cu (Zambezi Resources, 2004). Exploration by Zamanglo in the 1960s' noted drill intersections of copper within altered, brecciated, silicified and sulphidic lithologies (Zambezi Resources, 2005a).

At Cheowa, 130km east of Shantumbu, on the contact between mafic volcanics and shales, sandstones, dolomite and quartzite of the Muva Supergroup, chalcopyrite, pyrrhotite and pyrite are hosted in breccia zones. The width of the breccia is reported at 4.5m with a dip of 65° to the northwest (Zambezi Resources, 2007).

Central African Copperbelt

Haest and Muchez (2011) discussed the multiphase origin of the sulphide mineralisation in the Central African Copperbelt, which can be subdivided into two phases, the first precipitated as disseminated stratabound sulphides and sulphides cementing pores and replacing evaporites during diagenesis. The second phase involved the remobilisation and reprecipitation of

sulphides by high salinity and low to moderate temperature fluid during metamorphism and tectonic activity. The metalliferous fluids precipitated sulphides in successive vein generations and within brecciated units.

During the initial phase, the source of the sulphate (SO^{2-}) for bacterial sulphate reduction may have originated from seawater sulphates, sulphates from within the sedimentary units, from evaporite brines and/or from dissolution of calcium sulphate such as anhydrite and gypsum cements and nodules (Machel, 2001). Dolomite and calcite precipitated because of the sulphate reaction during bacterial sulphate reduction and precipitated in voids.

Hydrogen sulphide (H_2S) generated through bacterial sulphate reduction within sulphate and organic-rich sediments below the depth of oxygen penetration can precipitate iron sulphides. Elemental sulphur may form from partial re-oxidation of H_2S. The quantity of organic matter and sulphate is important for bacterial sulphate reduction, as is the presence and quantity of base and transitional metals; the metals place a limit on H_2S concentrations as well as effectively removing H_2S from the system (Machel, 2001).

Haest and Muchez (2011) perceived the precipitation of sulphides in the Central African Copperbelt as having occurred during diagenesis at low to moderate temperature (115 - 220°C) within open systems, and with the involvement of bacterial reduction of seawater sulphates, where the fluid was H_2O-NaCl bearing. During bacterial sulphate reduction, HCO^{3-} and H_2S were produced precipitating dolomite and sulphides. The fluid pH decreased during sulphide precipitation and resulted in the precipitation of quartz, hence the common association of quartz and sulphides in the ores of the Central African Copperbelt (Haest and Muchez, 2011). Precipitation of the metal sulphides may occur due to a change in the fluid pH, a decrease in temperature and dilution or migration into sediments (such as carbonates containing Mg^{2+} and Ca^{2+}) (Kamona and Friedrich, 2007).

Kamona and Friedrich (2007) advocated the sulphides hosted in carbonate-dominated lithologies formed during metasomatism. The high salinity metalliferous fluids deemed as the source of the mineralisation may have been derived from extensive evaporation of seawater, dissolution of evaporite minerals or a combination of both fluids. Metals were taken up in the high salinity fluids by a combination of the salinity and low H_2S content of the fluids, together with chloride complexing resulting in metals entering solution (Kamona and Friedrich, 2007). The solubility of copper and gold is significantly increased in the presence of chlorine bearing hydrothermal fluids (Webster, 2004).

Disseminated, anhedral to subhedral pyrite grains are hosted by many of the lithostratigraphic sequences on Shantumbu and the formation of the primary pyrite is attributed to the H_2S having been removed by Fe and precipitated as pyrite.

Although no direct evidence exists for intrusive bodies within Shantumbu, proximity to intrusion of igneous bodies would elevate fluid temperatures, form a source of fluids, assist the migration and precipitation of metals, or have acted as a heat pump for fluid movement.

6.4 CONCLUSION

The arenites below the transgressive marine surface are host to the higher-grade copper intersections on Shantumbu. The copper mineralisation is present as disseminated grains within voids and as a cementing mineral, within stratabound layers, and within veins.

The predominant copper sulphide is chalcopyrite, whereas malachite and azurite outcrop at Copper Hill. The progression of copper sulphide minerals after chalcopyrite is pyrrhotite, chalcocite, covellite, bornite and digenite. Chalcopyrite in many instances has progressively replaced pyrite, with both pyrite and hematite enclosed by chalcopyrite been noted. Chalcocite formed alteration rims surrounding chalcopyrite, covellite and bornite mineralisation. Bornite variably altered to covellite and chalcocite.

The several remobilisation and precipitation events, which affected the sediments on Shantumbu are attributed to several pressure-temperature events, from sediment-loading, diagenesis through to epidote-amphibolite metamorphism and retrograde greenschist facies metamorphism.

The low amount of copper and base metal mineralisation on Shantumbu is attributed to a poorly mineralised source area, and the remobilisation and reprecipitation of the base metal sulphides concentrated the mineralisation. Insufficient information exists to determine whether the erratic and low-grade copper mineralisation resulted from basinal brines, which escaped the Shantumbu Basin or the initial concentrations of copper in the source area was insufficient to develop into economical copper occurrences.

CHAPTER 7

GEOCHEMISTRY

7.1 INTRODUCTION

The metasediments of Sequences 1 to 7, Shantumbu underwent extensive alteration and remobilisation of elements from the time of deposition through to the Pan African Orogeny. The metasediments were geochemically affected at all stages, from weathering of the source granitic hinterland, during aeolian and/or aqueous transport and deposition, diagenesis, burial and metasomatism. The petrology of Shantumbu was subjected to high-grade metamorphism and retrograde metamorphosed to lower temperature minerals.

The mineralogy of the Mpande Gneiss and Munali Hills Granite is composed of microcline (often pink in colouration), quartz, plagioclase, biotite, muscovite, sericite with accessory minerals such as sphene, epidote, apatite, zircon, hornblende, garnet, scapolite, pyrite, chalcopyrite and opaque minerals (Katongo *et al*., 2004). The Mpande Gneiss and Munali Hills Granite are described as exhibiting A-type granite affinities, with the rocks being high in NaO and K_2O and low in CaO and MgO, and having ferromagnesium minerals such as biotite, alkali amphibole and sodic pyroxene (Katongo *et al*., 2004).

Chapter 7 examines both mobile and immobile elements to further understand the conditions during deposition, these being the anoxic and oxic conditions at the time of deposition and the geochemical trends of the altered petrology. The immobile elements examined included Al, Ti, Zr, Th and Sc. Zr tends to show little mobility even under extreme alteration (Middleburg *et al*., 1988), while the mobile elements examined included Mn, Ca, Na, K, Mg, Sr, Ba, Rb, Cu, Co, Zn and As.

Two data sets were available from the 2013 to 2015 exploration programme for the geochemical examination of Sequences 1 to 7, a portable XRF and an ICP-OES dataset. The drill cores which intersected Sequences 3, 6 and 7 did not contain copper mineralisation and were therefore not sampled for geochemical analyses by the owner of the exploration license. The geochemical characteristics of Sequences 1, 2, 4 and 5a to 5c, collectively termed Sequence 5 unless otherwise said, constituted the ICP-OES dataset available for examination. The portable

XRF dataset includes points completed on the entire lengths of the drill cores, except for drill holes SPA018 and SPA027, which have readings for a portion of the core length.

7.2 GEOCHEMICAL SAMPLING AND ANALYTICAL METHODOLOGIES

A total of 3,579 portable XRF readings were available for examination. Multi-acid digest ICP-OES analyses of the base metal-bearing samples where base metal mineralisation was expected, were undertaken at Intertek Genalysis laboratory in Perth, Australia. A total of 1,504 ICP-OES samples were available for examination.

Portable XRF measurements are inherently imprecise as the counts measure only a minute surface area of a sample. Variations in matrix and particle size, inter-element interference, homogeneity, sample form (solid or powder), moisture content and temperature of the sample influences the portable XRF readings, which are termed counts. To counteract the lack of precision of portable XRF values, both quality controls and assurance procedures were employed, which improved the semi-quantitative / qualitative aspect of this sampling technique.

The reduced representivity of the portable XRF readings was partially offset by averaging several readings taken along a sample length. Three individual reading points per one metre segment of core were undertaken and averaged, where the measurement time for each sample site was consistently 30 seconds. A manufacturer derived representative standard for Zambian Copperbelt samples was used to calibrate the portable XRF machine on a regular basis. The probe window was physically placed on the sample to reduce error introduced from varying distances of the probe to the sample. Energy calibration checks were routinely conducted and confirmed that the portable machine was operating with maximum resolution and X-ray drift had not occurred. The machine was warmed up prior to checks and reading of the samples. To ensure the uniformity of results per drill hole, the physical conditions, such as moisture and temperature, of the core during measurements was kept the same as far as possible. The core was not rotated to obtain readings over the surface area of the sample, and readings were taken in the metal core tray.

The portable XRF machine used was a Thermo Scientific NITON XL 3t 950 GOLDD. The elements read were Cu, Fe, Ti, Au, Mn, Ni, Ag, Sr, V, Cr, Co, Zn, As, Se, Rb, Zr, Nb, Mo, Pd, Cd, Sn, Sb, W, Pb and Bi. All units were recorded as percentage (%). Na, Mg, Al, Li and Si were not detected by the portable XRF machine. The portable XRF readings for the elements are available in APPENDIX 2.

Portable XRF values for the various elements were plotted against the lithostratigraphic logs for the Sequences. Box and whisker plots together with log-probability plots were constructed for several of the elements for each of the available sequences.

The ICP-OES analytical technique used an aliquot extracted from a pulverised and homogenised sample. The samples were subjected to a four-acid digest, these being hydrofluoric, nitric, perchloric and hydrochloric acids, in Teflon tubes and analysed by ICP-OES method at the Intertek Genalysis laboratory in Perth, Australia. The elements analysed included Al, Ag, As, Ba, Bi, Ca, Cd, Ce, Co, Cr, Cu, Fe, K, La, Li, Mg, Mn, Mo, Na, Ni, P, Pb, S, Sb, Sc, Sn, Sr, Te, Ti, Tl, V, W and Zn. The ICP-OES results are summarised in APPENDIX 3.

The ICP-OES samples included samples, which were read during the portable XRF screening, as well as samples anticipated to have hosted copper mineralisation. The ICP-OES dataset therefore represented a heterogeneous population distribution, comprised of samples taken in both the mineralised and unmineralised sections. The heterogeneity was offset by examination of only the ICP-OES samples which had a copper grades above 0.1% Cu. Scatter plots were compiled for oxide versus oxide from the stoichiometric conversion of the ICP-OES element values to oxide values and element ratios were calculated, such as the ratio of V/Cr.

The portable XRF and ICP-OES results correlated poorly due to the contrasting precision and accuracy characteristics of each dataset and hence the datasets were kept separate during examination of the geochemical characteristics.

7.3 GEOCHEMICAL RESULTS

7.3.1 Lithologies and Alteration

The detrital sediments of Sequences 1 to 7 were subdivided according to lithology, resulting in an arenite and arkose dataset, a siltstone and mudstone dataset and two carbonate datasets. The dolomitic carbonate of Sequence 4 (Copperbelt Orebody Member) formed one dataset and the second set incorporated the calcitic carbonates of Sequence 5 and 7 (Pelito-Arkosic and Chambishi members and Bancroft Member respectively.

The Copperbelt Orebody Member, represented by Sequences 3 and 4 (Copperbelt Orebody Member), is the first dolomitic carbonate in the Shantumbu Stratigraphy, hence using the composition of dolomite the MgO values were plotted against Al_2O_3 (Figure 7-1), which

confirmed the high MgO content of the dolomitic carbonate versus the calcitic carbonates of Sequence 5 (Pelito-Arkosic and Chambishi members).

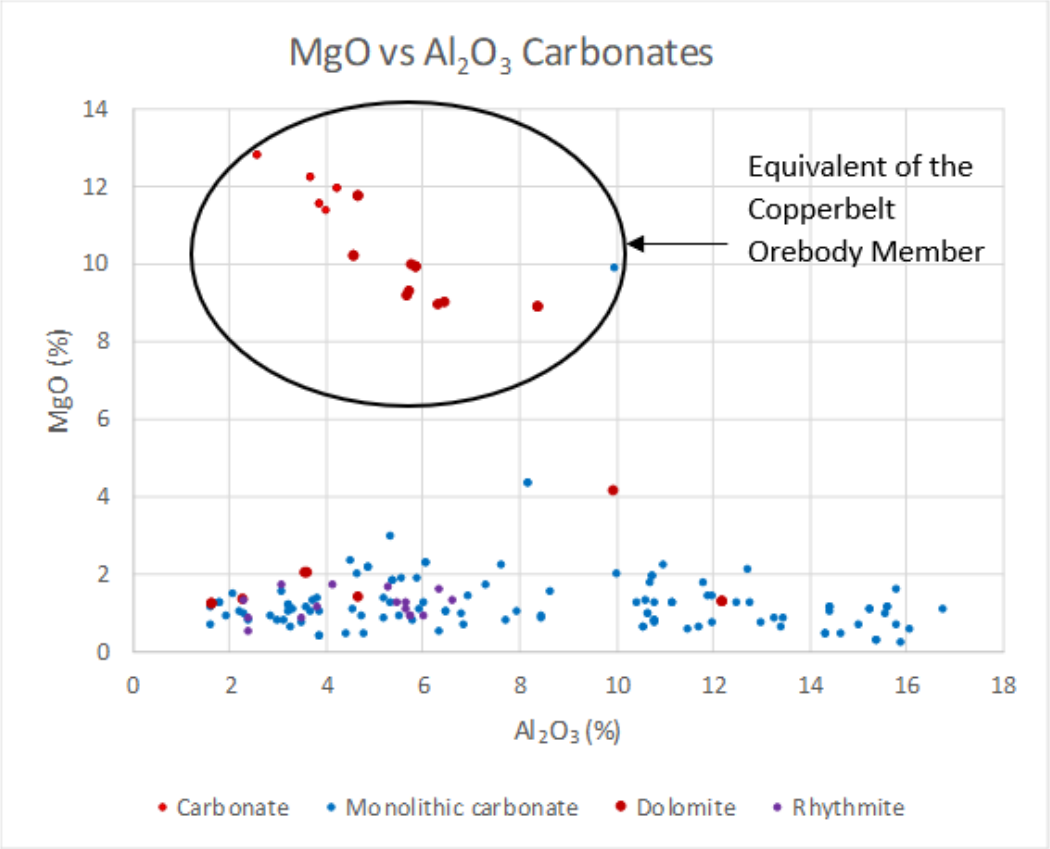

Figure 7-1. The ICP-OES dataset for MgO (%) versus Al_2O_3 (%) shows the dolomitic carbonate dataset for Sequence 4 is offset from the calcitic carbonates of Sequence 5, Shantumbu.

MnO plotted against Al_2O_3 to illustrate the calcitic carbonates had elevated Mn content in comparison to the dolomitic carbonate (Figure 7-2) dataset. MnO is an efficient indicator of oxic and anoxic conditions at the time of deposition, and the scatterplot for the dolomitic carbonate exhibited characteristics of deposition during oxic conditions, whilst the carbonates of Sequence 5 exhibited characteristics of deposition in alternating oxic and anoxic conditions. The MnO points plotted for the arenaceous debris flow deposits of Sequence 2 (Kafue Arenite Member) (Figure 7-3) are tightly grouped in comparison to the arenites and arkoses of Sequences 1, 2, 4 and 5, which is symptomatic of the high plagioclase and quartz content and the tight pore spaces related to the rapid sediment input which caused anoxic conditions. The MgO points of the debris flows versus the arenites and arkoses mirrored that of MnO (Figure 7-4).

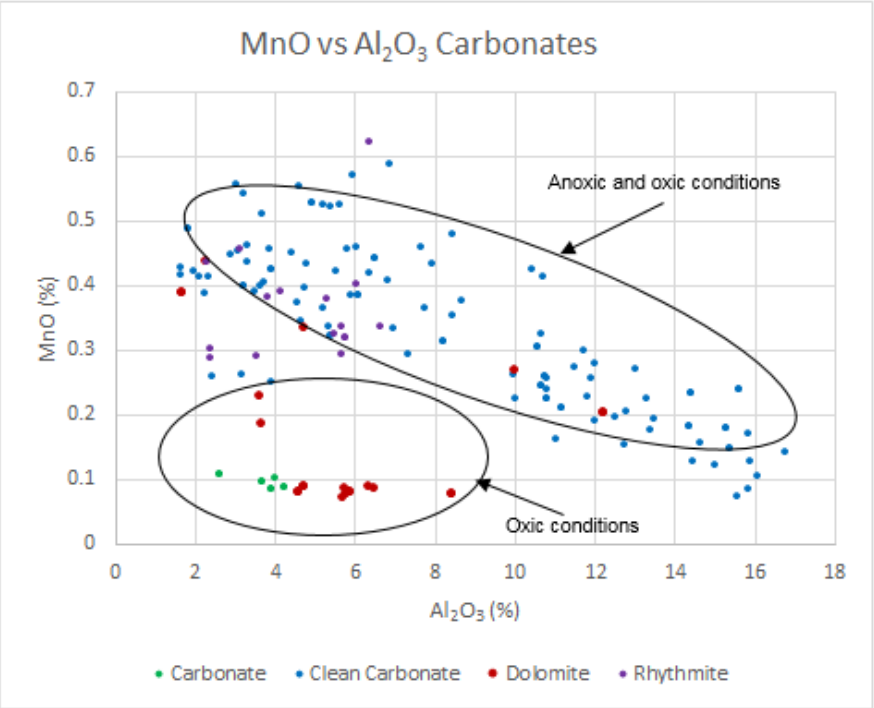

Figure 7-2. A scatterplot of the ICP-OES data for MnO (%) versus Al_2O_3 (%) for the dolomitic carbonate of Sequence 4 and the calcitic Sequence 5 (Pelito-Arkosic Member) carbonates, Shantumbu. The plot illustrates that the dolomites are clearly segregated from the remaining carbonates, which were deposited under oxic conditions.

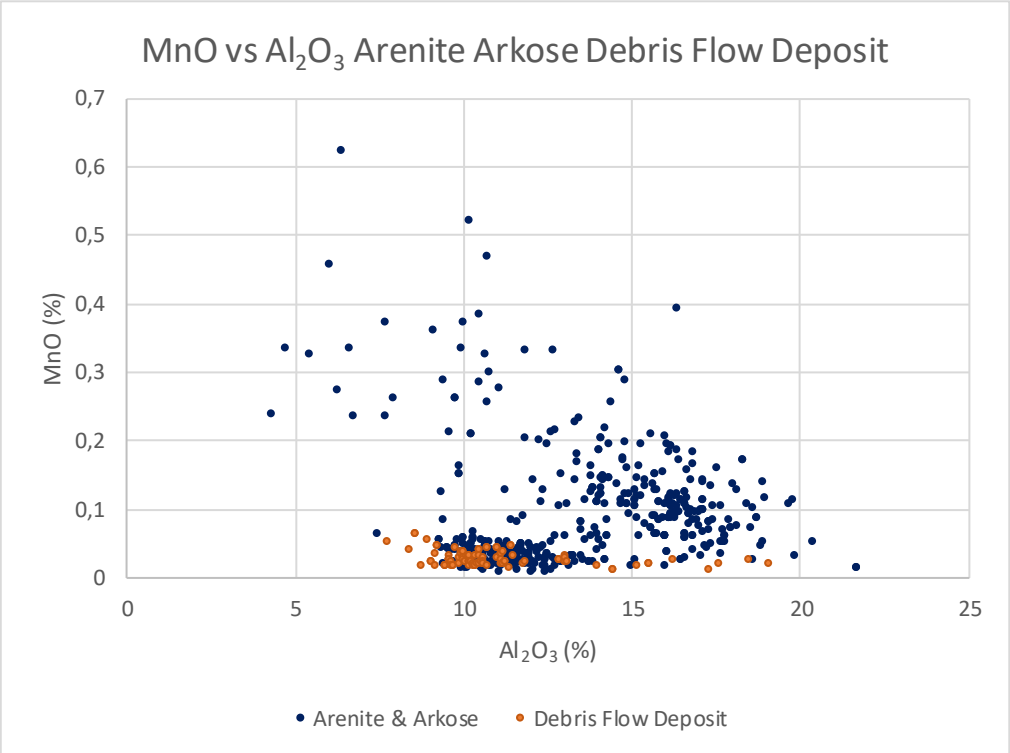

Figure 7-3. MnO (%) versus Al_2O_3 (%) for the debris flow deposits of Sequence 2 contrasted with the arenites and arkoses from Sequence 2 (Kafue Arenite Member), Shantumbu. The behaviour of Mn is segregated from the remaining detrital units of Sequence 2. ICP-OES data is presented.

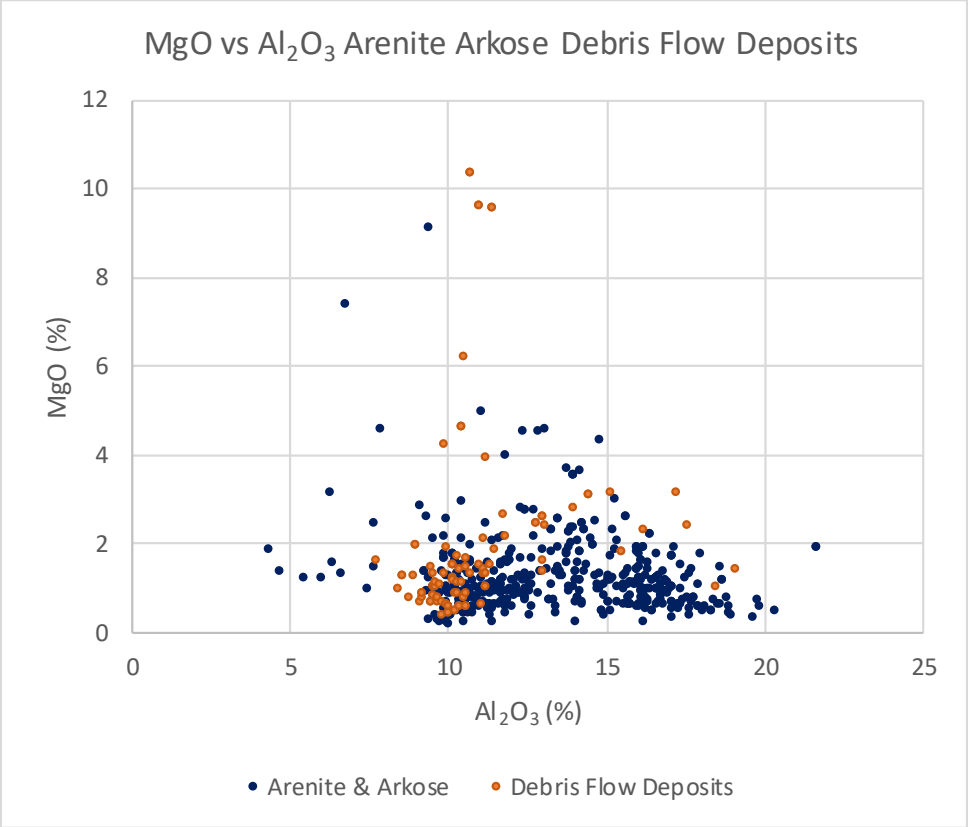

Figure 7-4. MgO (%) versus Al_2O_3 (%) for the debris flows deposits of Sequence 2 contrasted with the arenites and arkoses from Sequence 2 (Kafue Arenite Member), Shantumbu. The behaviour of Mg is segregated from the remaining detrital units of Sequence 2. ICP-OES data is presented.

The dolomitic carbonate of Sequence 4 (Copperbelt Orebody Member) displayed depressed K_2O values in the range of 0.5 to 2.5% (Figure 7-5) in comparison to the calcitic carbonates of Sequence 5. A positive correlation is strong between Na_2O versus Al_2O_3, where the Na_2O values for the dolomitic carbonate are grouped together at lower Na_2O values compared to the calcitic carbonates. The dolomitic carbonates underwent limited potassic alteration and were subjected to more extensive sodic alteration. The mineralogy of Sequences 5 and 6 (Pelito-Arkosic to Antelope members) is dominated by the sodic minerals such as aegirine, feldspar, glaucophane, sodalite and sericite. Biotite extensively altered to aegirine in Sequence 5 (Pelito-Arkosic and Chambishi members) supporting the sodic alteration illustrated by Figure 7-5.

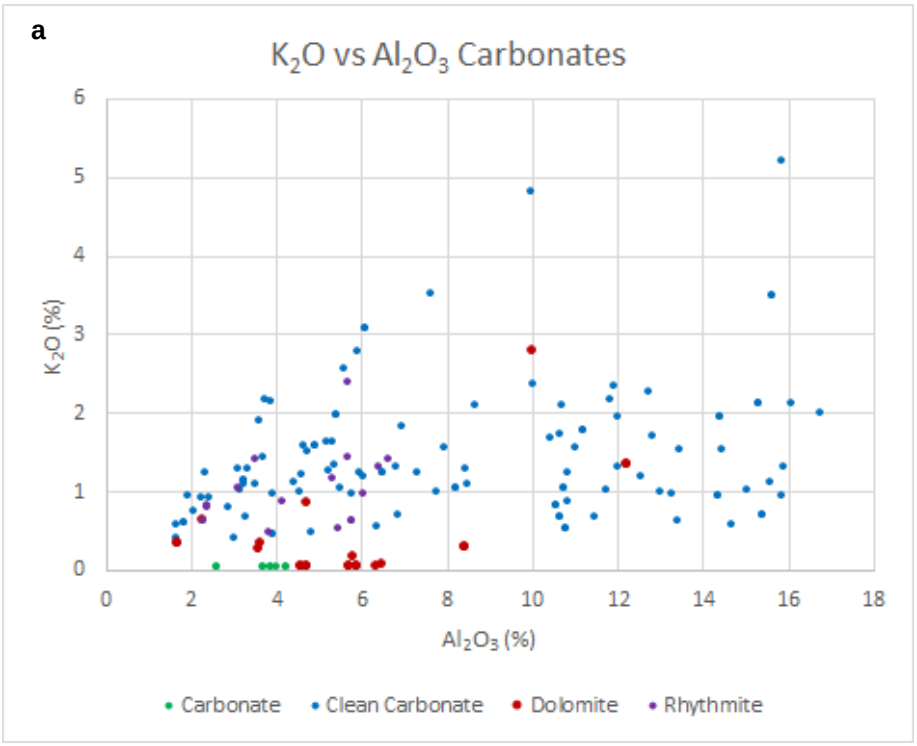

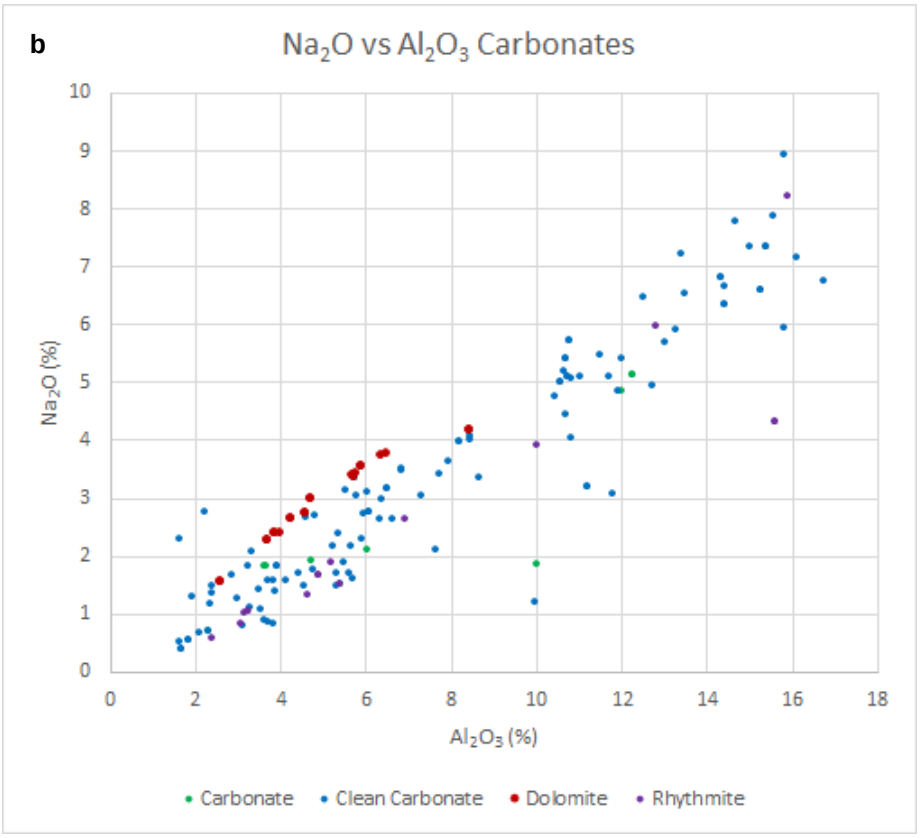

Figure 7-5. Scatterplot illustrating the alteration of the carbonates on Shantumbu. ICP-OES. (a) K_2O (%) versus Al_2O_3 (%) of the dolomite of Sequence 4 (Copperbelt Orebody Member), contrasted with the calcitic carbonates of Sequence 5. (b) Na_2O (%) versus Al_2O_3 (%) of the dolomite of Sequence 4, contrasted with the calcitic carbonates of Sequence 5 (Pelito-Arkosic and Chambishi members). The term 'Clean Carbonate' refers to monolithic carbonate rock without argillite interlayers.

The arenites of Sequences 1, 2, 4 and 5 and debris flow deposits of Sequence 2 (Kafue Arenite Member) underwent both potassic and sodic alteration (Figure 7-6). The arenites of Sequences 1, 2, 4 and 5 and the debris flow deposits of Sequence 2 have K_2O values between 0.1 to 7% K_2O, in comparison to the low K_2O values of between 0.1 to 3% K_2O for the carbonate lithologies (portable XRF data). The K_2O values of Sequences 1, 2, 4 and 5 (Figure 7-7a) range between 0.1 and 7% K_2O for the ICP-OES data. The spread of the K_2O values along the Al_2O_3 axis varies between Sequences 1, 2 and 4 to Sequence 5. The high mica content in Sequence 5 (Pelito-Arkosic and Chambishi members) is reflected in the K_2O content.

The Na_2O content of the detrital sediments of Sequences 1 and 2 (Mindola Formation) and the carbonates from Sequences 4 and 5 (Kitwe Formation) have elevated Na_2O, where the Na_2O values for Sequences 1, 2, 4 and 5 (Figure 7-7b) range between 0.1 and 9% Na_2O for the ICP-OES data, although the spread of Na_2O along the Al_2O_3 axis for Sequence 5 (Pelito-Arkosic and Chambishi members) is considerably greater than for the remaining Sequences.

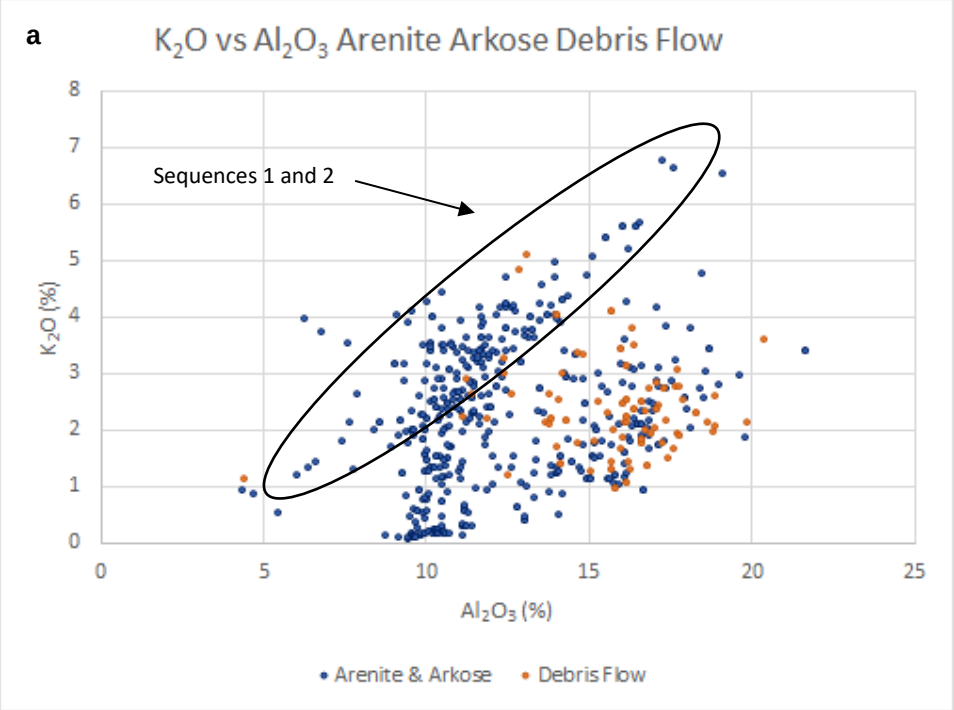

Continued next page

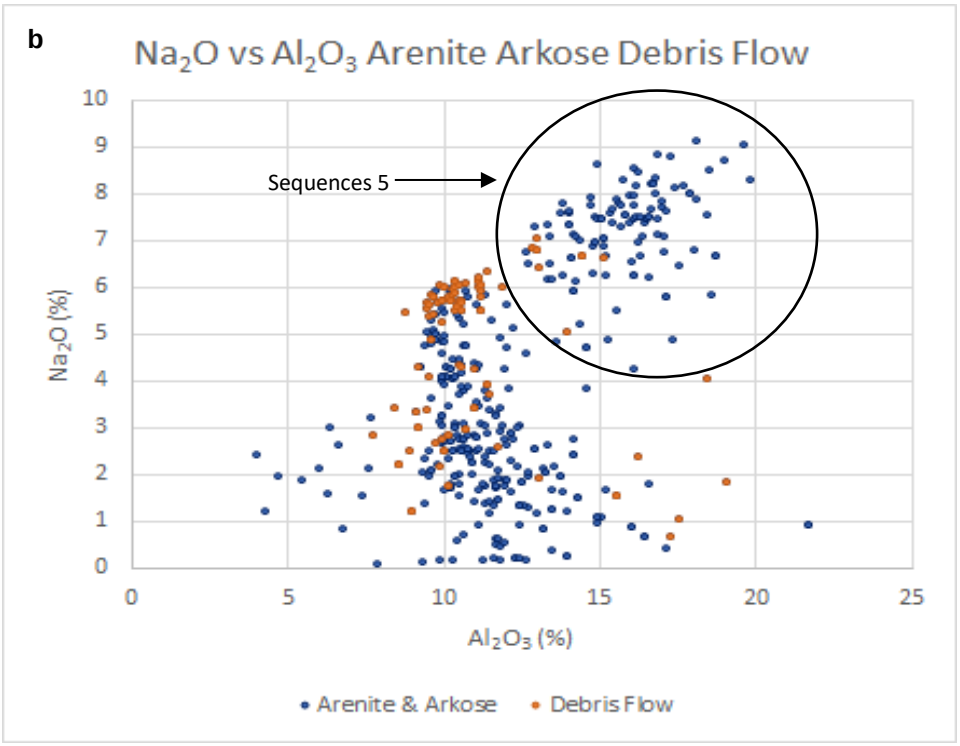

Figure 7-6. Scatterplot of the ICP-OES dataset illustrating the alteration of the detrital metasediments on Shantumbu. (a) K_2O (%) versus Al_2O_3 (%) of the Sequence 2 (Kafue Arenite Member) debris flows, contrasted with the arenite and arkoses of Sequences 1, 2, 4, and 5. (b) Na_2O (%) versus Al_2O_3 (%) of the Sequence 2 debris flows deposits, contrasted with the arenite and arkoses of Sequences 1, 2, 4, and 5.

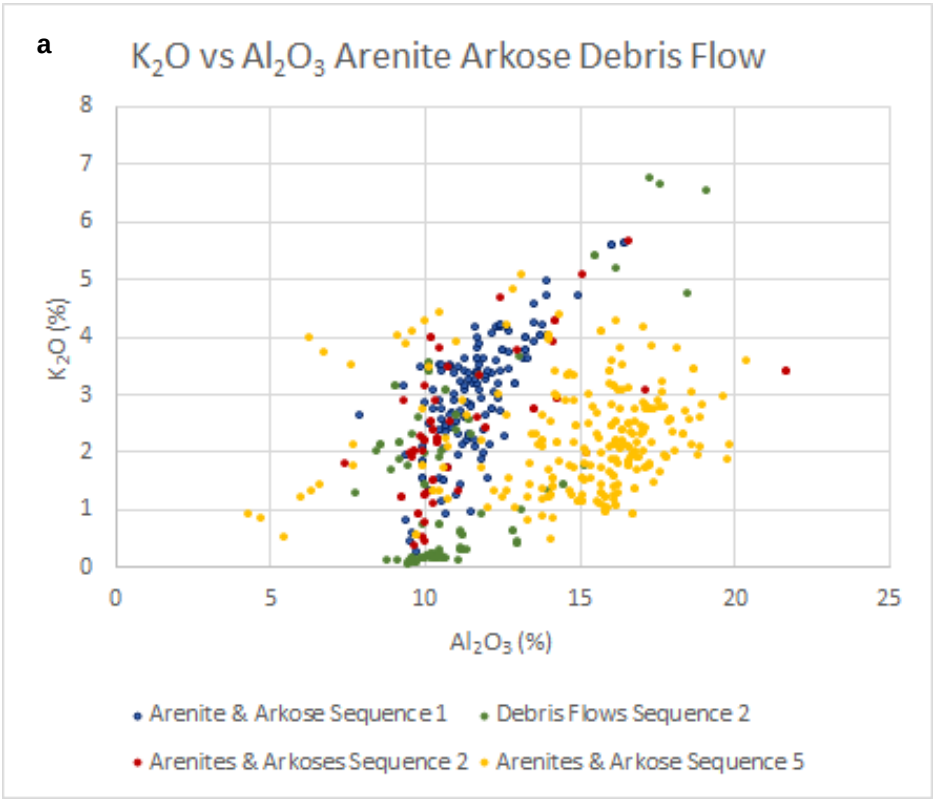

Continued next page

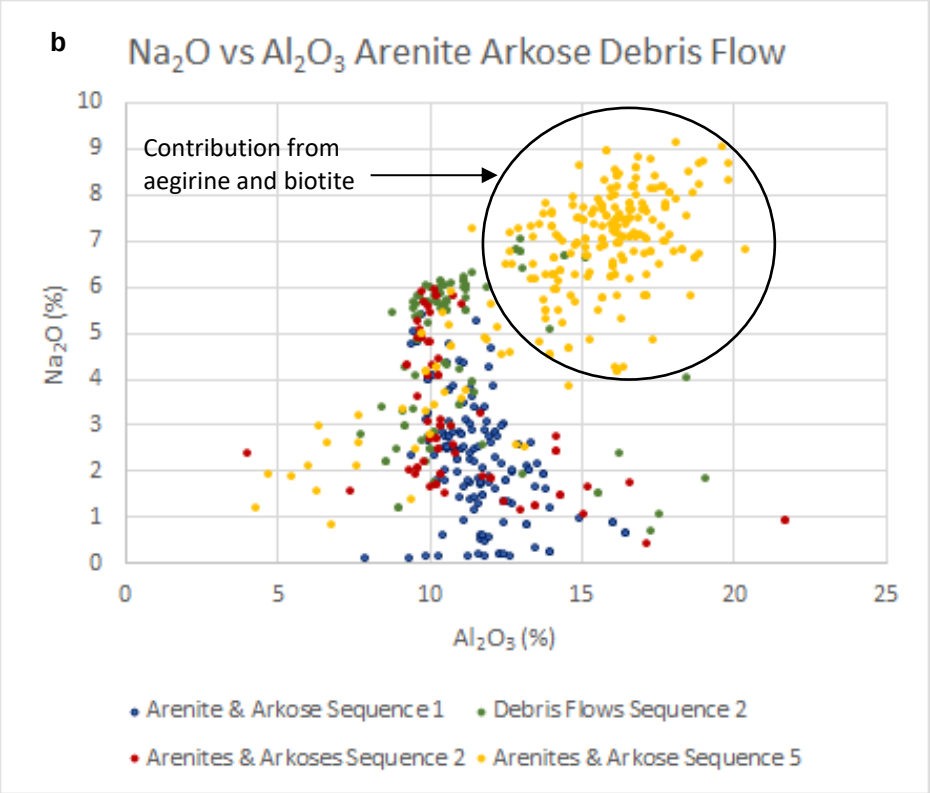

Figure 7-7. Scatterplot of the ICP-OES data illustrating K_2O versus Al_2O_3 per sequence, Shantumbu. (a) Scatterplot illustrating K_2O (%) versus Al_2O_3 (%) of the Sequences 1, 2, 4 and 5. (b) Scatterplot illustrating Na_2O (%) versus Al_2O_3 (%) of the Sequences 1, 2, 4 and 5.

The relationship between K_2O and Sc (scandium) has been used in the Central African Copperbelt to assist in identifying mineralised zones (Croaker, 2011, and references therein). The scatter plot of K_2O versus Sc (Figure 7-8a) for the dolomitic carbonate and the calcitic carbonates at Shantumbu demonstrated a tight grouping of the dolomitic carbonate points at very low K_2O content versus a more disperse grouping for the calcitic dolomites. The dolomitic carbonates are proximal to the sulphide mineralisation and have elevated Sc values in comparison to the calcite carbonates. The scatter plot of K_2O versus Sc (Figure 7-8b) for the arenite and arkoses and the debris flows from Sequences 1, 2, 4 and 5 illustrate higher Sc values for the debris flows deposits in comparison to the remaining detrital sediments. The Sc values for the arenites and arkoses of Sequence 1 (Basal Sandstone Member) are elevated in comparison to those of Sequences 2, 4 and 5.

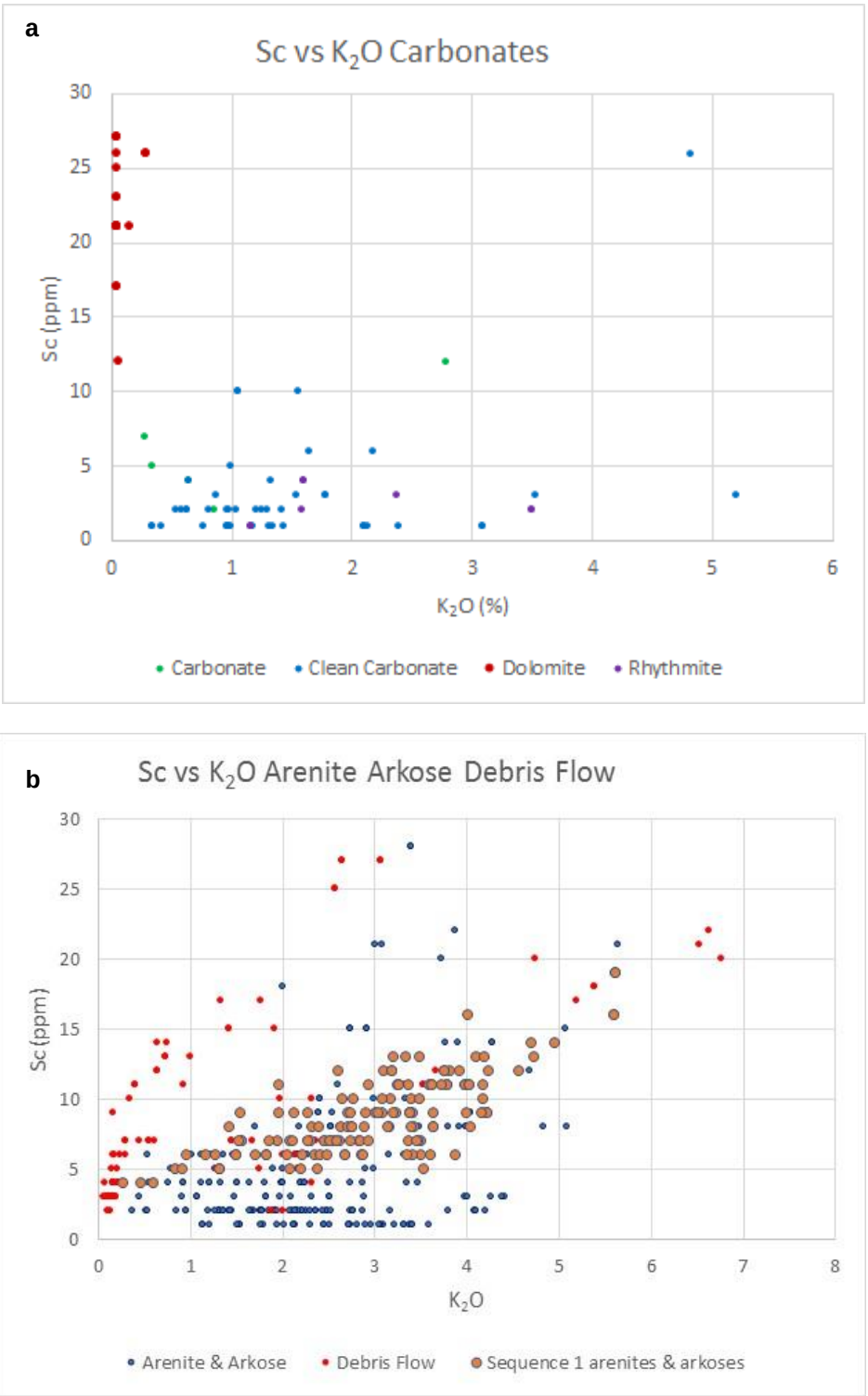

Figure 7-8. Scatterplot of the ICP-OES data for K_2O versus Sc per sequence (a) Sc (ppm) versus K_2O (%) for the dolomitic carbonate of Sequence 4 contrasted with the calcitic carbonates, Shantumbu. The dolomitic carbonate points are segregated from the remaining carbonates. (b) Sc (ppm) versus K_2O (%) for the arkose and arenite units versus the debris flows of Sequence 2; Sequence 1 values are coloured separately.

The debris flows of Sequence 2 (Kafue Arenite Member) displayed a subdued iron content in comparison to the arenites of Sequences 1, 2, 4 and 5 (Figure 7-9a). The iron content for all the sequences plotted is reflective of the high content of plagioclase and quartz and accessory Fe-bearing minerals. The lower iron content of the debris flow sediments reflected the tightly packed nature of the sediments due to the rapid deposition, which also formed an impermeable barrier to the migration of the basinal brines and movement of Fe and base metals. The calcitic carbonates of Sequence 5 (Pelito-Arkosic and Chambishi members) have elevated Fe content between 5 and 15% in comparison to the dolomitic carbonate (Figure 7-9b), related to the high content of biotite and aegirine and the interstitial goethite within the calcitic carbonates.

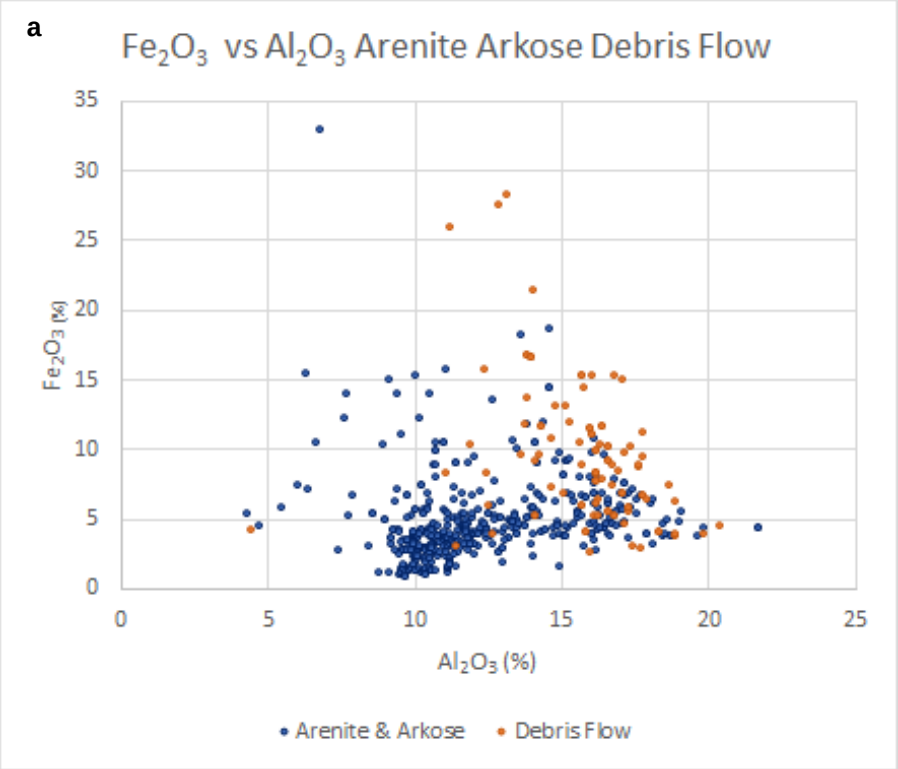

Continued next page

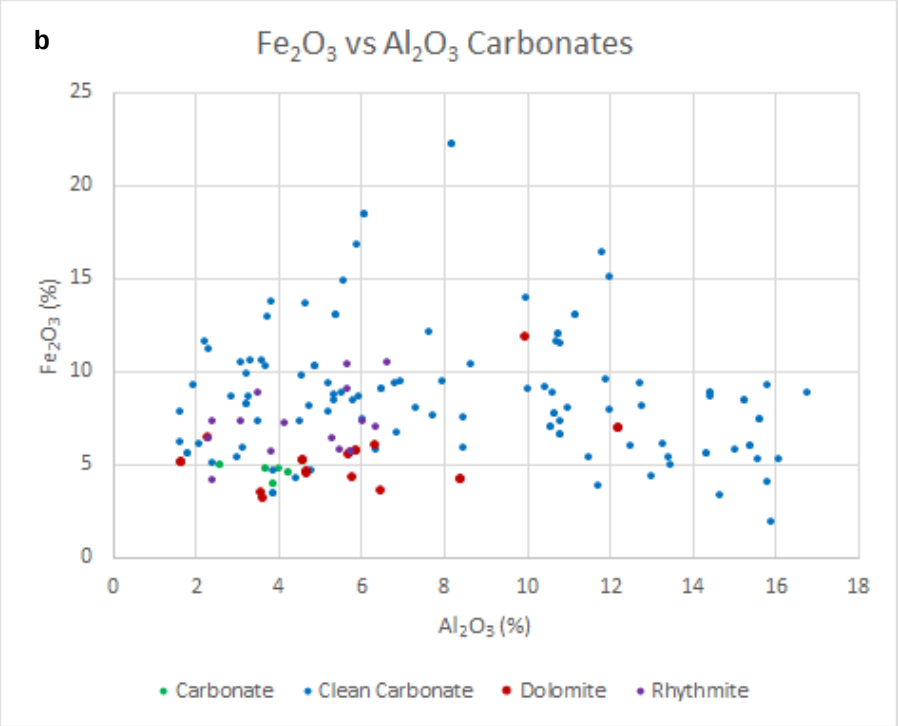

Figure 7-9. Scatterplot of the ICP-OES data for Fe_2O_3 (%) versus Al_2O_3 (%) for Sequences 1, 2, 4 and 5, Shantumbu. (a) Fe_2O_3 versus Al_2O_3 for the debris flow of Sequence 2 versus the arenites of Sequences 1, 2, 4 and 5. (b) Fe_2O_3 versus Al_2O_3 for the dolomitic carbonate of Sequence 4 on Shantumbu contrasted with the remaining carbonates. The dolomitic carbonate formed a tight grouping of values in comparison to the calcitic carbonates, perhaps because of less analyses. The calcitic carbonates reflect Sequence 5.

7.3.2 Immobile Elements

Al and Fe are considered immobile during weathering with the mobility influenced by grain size and redox conditions, while under reducing conditions, Fe and Mn are moderately soluble (Middelburg *et al.*, 1988). Al_2O_3 was used for correlation between various oxides and elements, such as Fe, K, Mg, Ca, Mn and Na oxides. Al, Fe, Ti and Zr were examined for Sequences 1, 2, 4 and 5 in terms of the immobile elements.

An iron source is a vital component for the formation of sedimentary-hosted stratiform copper deposits. Source rocks for the iron within this ore body style are of detrital origin such as red-bed arenites, siltstones and mudstones. Within sedimentary-hosted stratiform copper deposits, iron is both an early and late phase element and characterises both the mineralised and non-mineralised zones. The iron minerals which dominate on Shantumbu include micas, hematite, pyrite, clinopyroxenes and ferroan carbonate. The formation of pyrite was essential for the precipitation of the copper sulphides during the migration of basinal brines at Shantumbu.

The Fe content of the portable XRF dataset varies across the Sequences and is in the order of 4 - 5% Fe. Sequences 1 to 4 have Fe in the range of 2% to 3.5% (Figure 7-10) and Sequences 5 and 6 (Kitwe Formation) contained higher Fe values at 6 - 7%. The chemical sediments of Sequence 7 (Bancroft Member) contained the lowest Fe content at c. 1.8%.

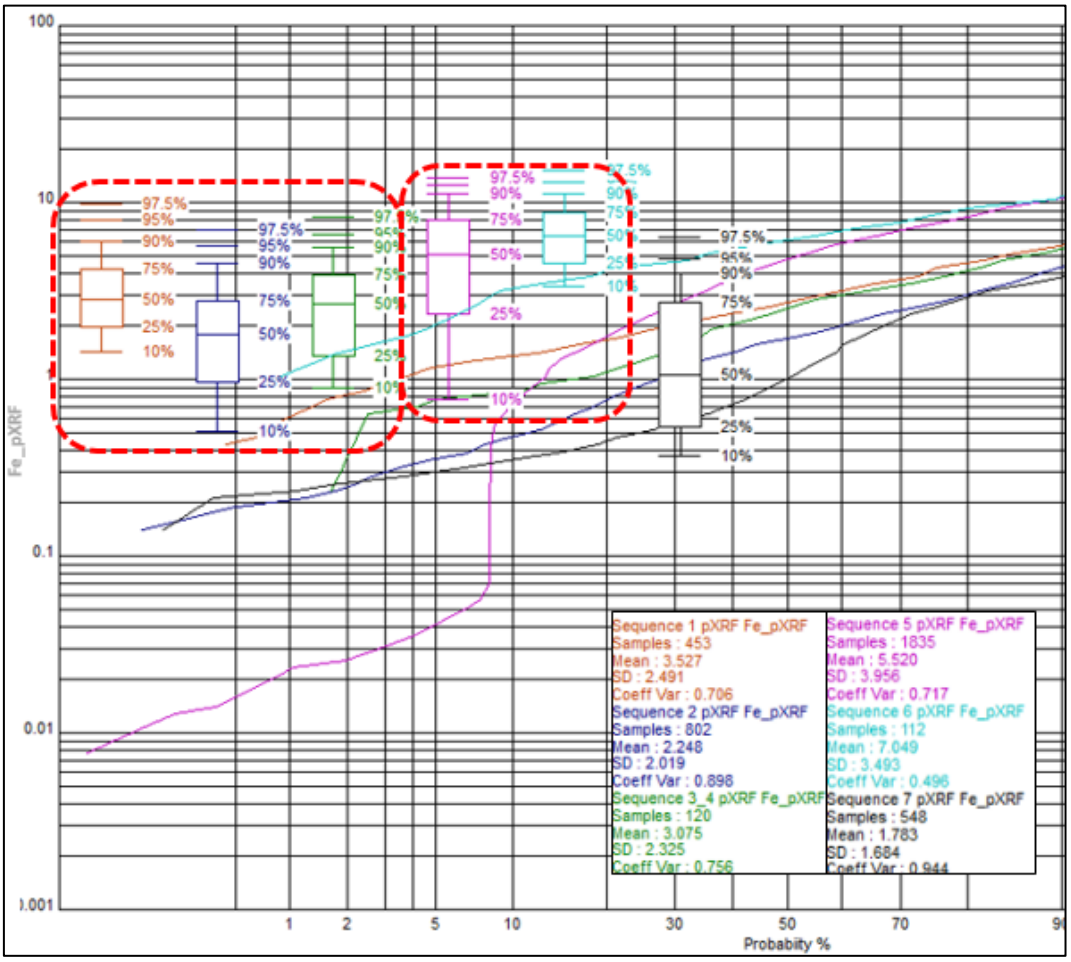

Figure 7-10. Box and whisker and log probability plots for Fe (%) within the Sequences 1 to 7 on Shantumbu. The plot represents the portable XRF dataset. The dotted red outlines illustrate the grouping of similar Fe contents of Sequences 1 to 4, and a separate grouping for Sequences 5 and 6. The probability plot is cut at 90% probability for illustration purposes.

The ICP-OES results for Sequences 1, 2, 4 and 5 (Figure 7-11) demonstrated the uniformity of the Fe_2O_3 concentrations through the stratigraphy. Nonetheless, the Fe_2O_3 concentrations for Sequences 1 and 2 (Mindola Formation) are persistently below 5% and within a narrow Al_2O_3 range of 8 - 15%, in comparison to the variability illustrated by Sequence 5 (Pelito-Arkosic and Chambishi members) against Al_2O_3. Sequences 5 is characterised by several values of ± 15% Fe_2O_3 and at higher Al_2O_3 concentrations (c. 11 - 18% Al_2O_3) for iron than in Sequences 1 and 2 (Mindola Formation). The Fe_2O_3 grades for facies 5 (a) and (b) are ≤6% Fe_2O_3, while the range for facies 5 (c) is between 5 - 10% Fe_2O_3. Facies 5 (c) includes a significant thickness of rhythmic

layers of carbonate and biotite-dominated laminations whereas facies 5 (a) and (b) are principally composed of intercalated carbonate and siltstone-arkose layers.

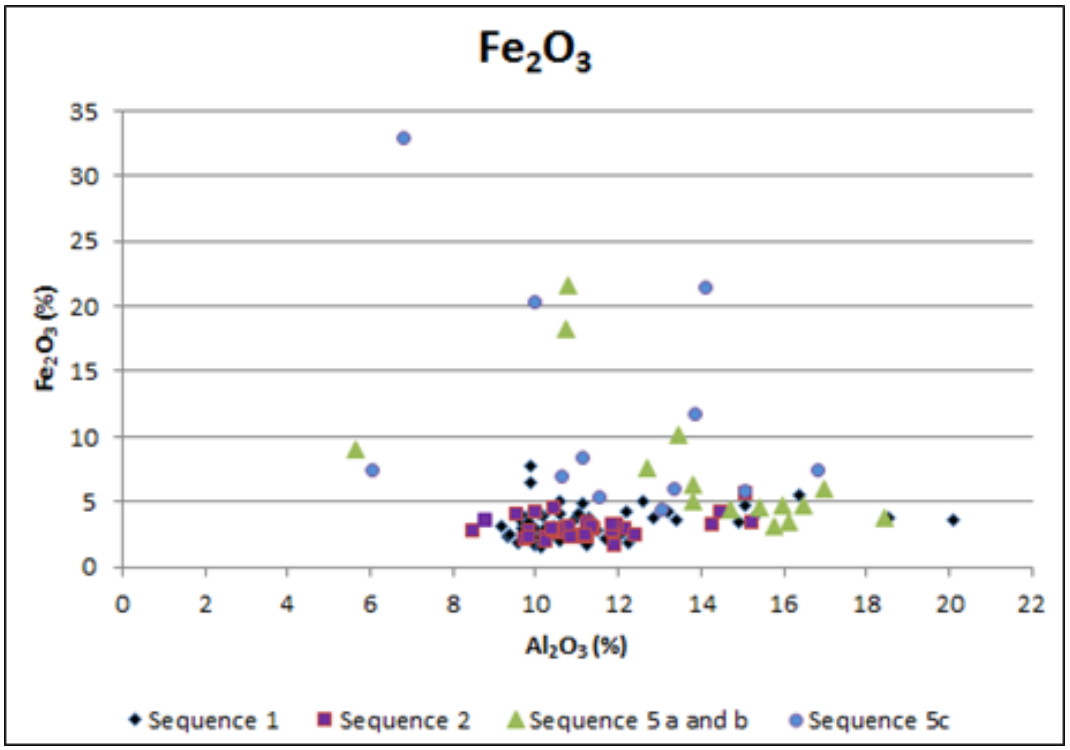

Figure 7-11. ICP-OES Fe_2O_3 values (%) for Sequences 1, 2 and 5 versus Al_2O_3, an immobile oxide, Shantumbu.

Sequences 1 to 7 host comparable Ti concentrations (Figure 7-12). The lowest Ti values are associated with Sequence 4 and 7, while the highest values are associated with Sequence 1. Sequence 1 has an average of 0.96% Ti whilst Sequences 2 to 7 ranged from 0.4 - 0.78% Ti.

Both Al and Ti are to some extent immobile elements. The debris flow deposits of Sequence 2 illustrate a tight grouping of the Ti points in comparison to the arenites and arkoses of Sequences 1, 2, 4 and 5. The tight grouping of points is related to the rapid sediment deposition process which occurred in Sequence 2 and the assumed restricted provenance for the debris flows deposits (Figure 7-13). The mineralogy of Sequence 2 (Kafue Arenite Member) consists primarily of recrystallised interlocking plagioclase (albite) and quartz, with accessory muscovite, scapolite, chlorite, biotite, malachite, hematite, goethite, dolomite, calcite and rutile. To a large extent, the Ti within the metasediments reflects rutile and Ti taken up in the micas.

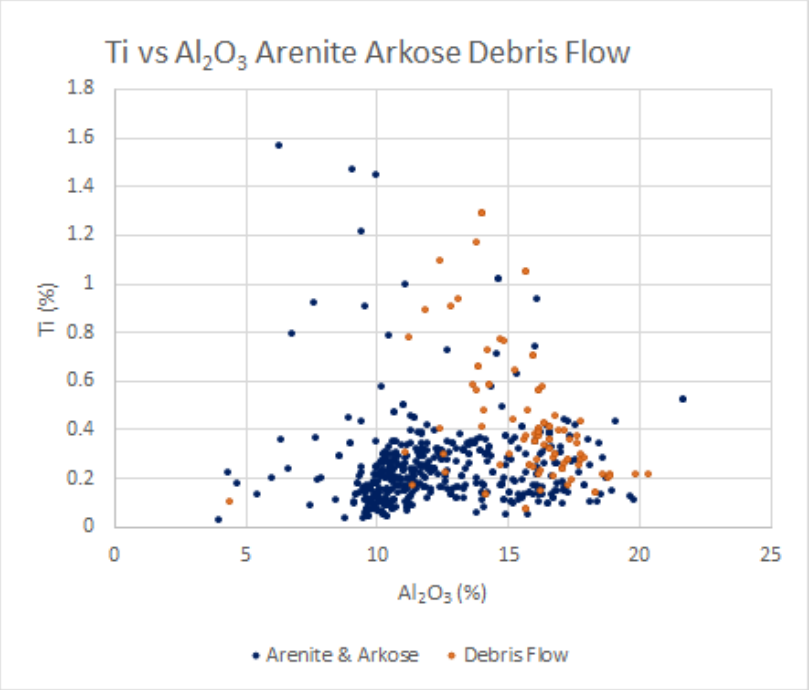

Figure 7-12. Scatterplot of the ICP-OES dataset for Ti (%) versus Al_2O_3 (%) for the detrital metasediments of Sequences 1, 2, 4 and 5, Shantumbu.

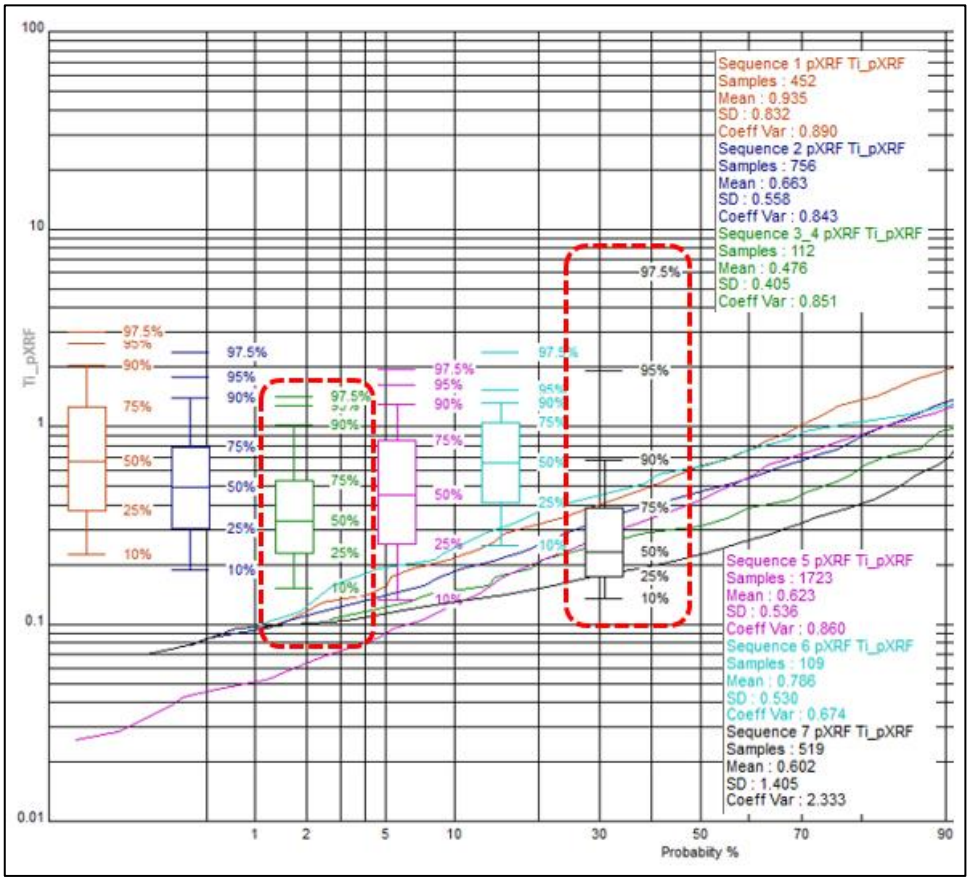

Figure 7-13. Box and whisker and log probability plots for Ti (%) within the Mindola, Kitwe and Kirilabombwe formations equivalents on Shantumbu. Portable XRF dataset presented. The dotted red outlines illustrate the onset of marine conditions and sediment starvation. The probability plot is cut at

90% probability for illustration purposes. The box and whisker plots for Sequences 1, 2, 5 and 6 show similar trends and variability of Ti.

7.3.3 Mobile Elements

The mobile elements examined included Mn, Ca, Na, K, Mg, Sr, Ba, Rb, Cu, Co, Zn and As. Of these elements Cu, Co, Ba, Zn, As and Mn tend to be affected by reduction-oxidation conditions and the salinity of the environment. Cu, Co, As and Mn tend to concentrate with pyrite (Croaker, 2011 and reference therein).

Feldspars, micas and apatite, which make up a significant part of the mineralogy in the Sequences on Shantumbu, are considered leachable minerals and the immobile element content is concentrated in resistant mineral phases or absorbed by secondary minerals. Interaction between feldspar and carbonate minerals may have resulted in the formation of secondary minerals such as sodalite. Sodalite is a feldspathoid and is related to feldspars except it contains Cl. Feldspars are Na, Ca and K-bearing minerals and the general formula is $X(Al, Si)_4O_8$ where X is Na, Ca, K or Ba. The depletion of Ca and Na during weathering and alteration is considered more rapid than that for potassium.

Sequences 1 to 4 and 7 displayed similar Mn characteristics, whilst Sequences 5 and 6 displayed the highest concentrations of Mn. The ICP-OES concentrations for MnO for Sequences 1 and 2 (Mindola Formation) averages less than 0.1%, while Sequence 5 (Pelito-Arkosic and Chambishi members). displays a range of MnO values from 0.05% to 0.45% MnO. Facies 5 (c) shows elevated MnO concentration in comparison to facies 5 (a) and (b) (Figure 7-14).

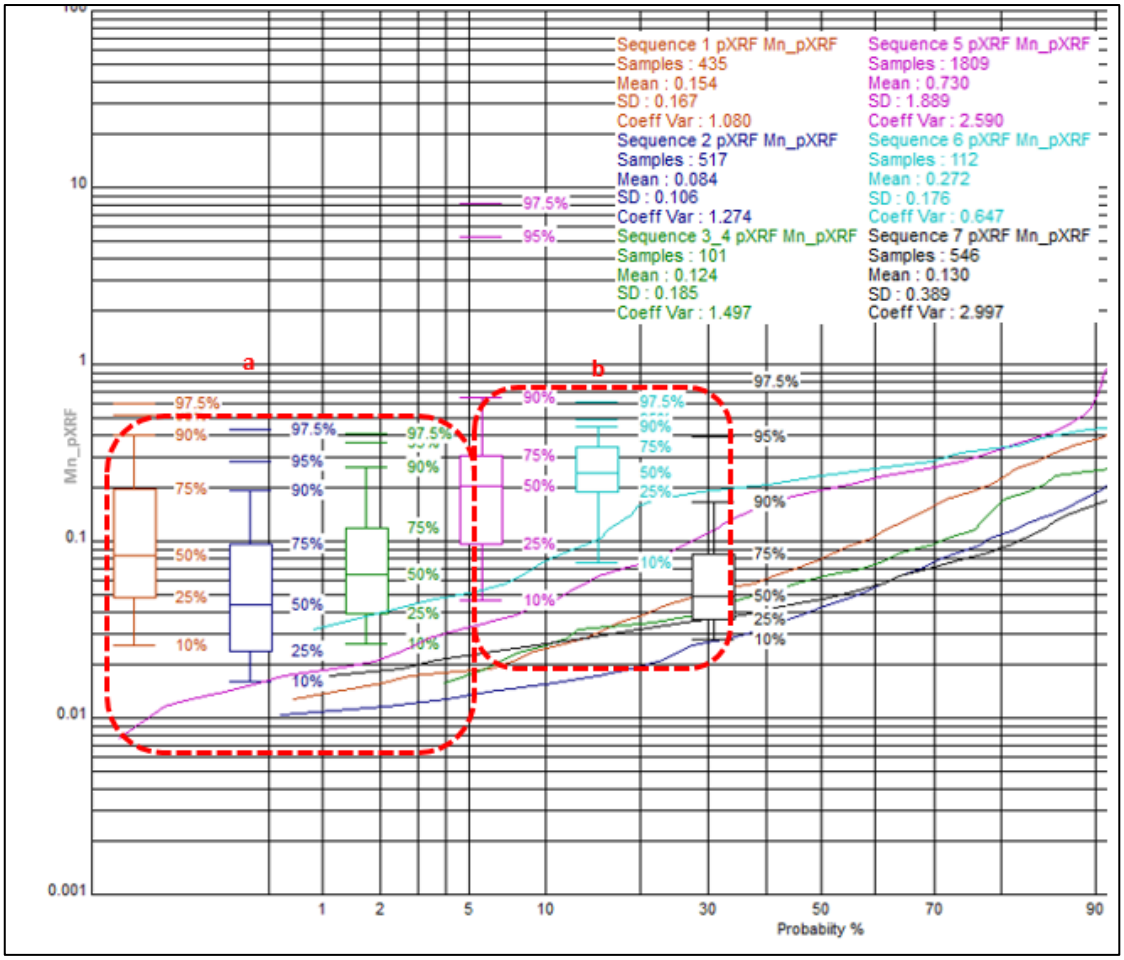

Figure 7-14. Box and whisker and log probability plots for Mn (%) within the Mindola, Kitwe and Kirilabombwe formations equivalent on Shantumbu. Portable XRF dataset presented. The probability plot is cut at 90% probability for illustration purposes. The box and whisker plots demonstrate distinctive trends for the terrestrial versus marine sequences. (a) The box and whisker plots for Sequences 1 to 4 which represent sediments deposited in terrestrial to shallow water environments. (b) The box and whisker plots for Sequences 5 and 6, which were deposited under subaqueous conditions.

The Sequence 1 (Mindola Formation) has very low Sr values in the order of c. 35ppm. A thirty-fold increase to c. 1,100ppm Sr was noted for the Sequence 3 to 6 (Kitwe Formation), specifically within the siltstone and carbonate lithologies. Sr increased vertically upwards through Sequences 4 and 5 (Copperbelt Orebody and Pelito-Arkosic members), and the highest Sr values of c. 4,840ppm were noted in the Sequence 6 (Antelope Member). The Sr values followed with lower values in Sequence 7 (Bancroft Member) at c. 370ppm (Figure 7-15 and Figure 7-16).

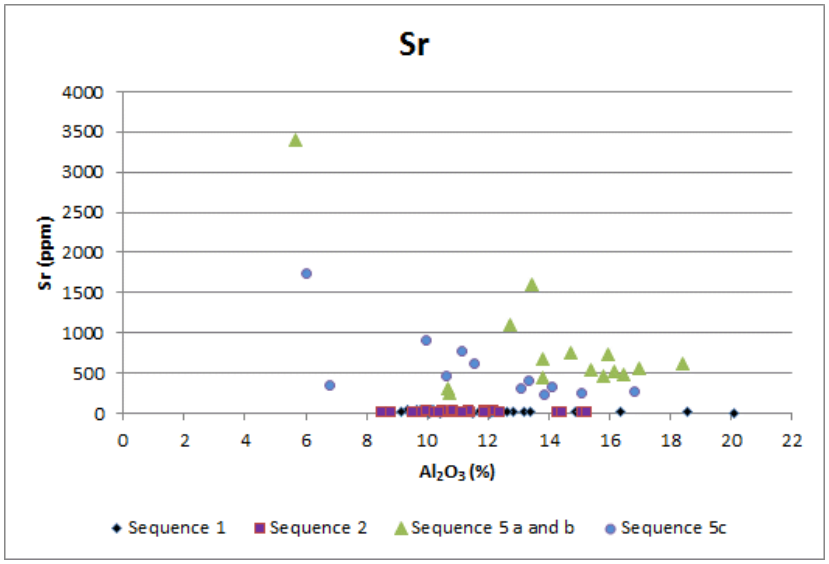

Figure 7-15. ICP-OES Sr values (ppm) for Sequences 1, 2 and 5 against Al_2O_3, an immobile oxide, Shantumbu.

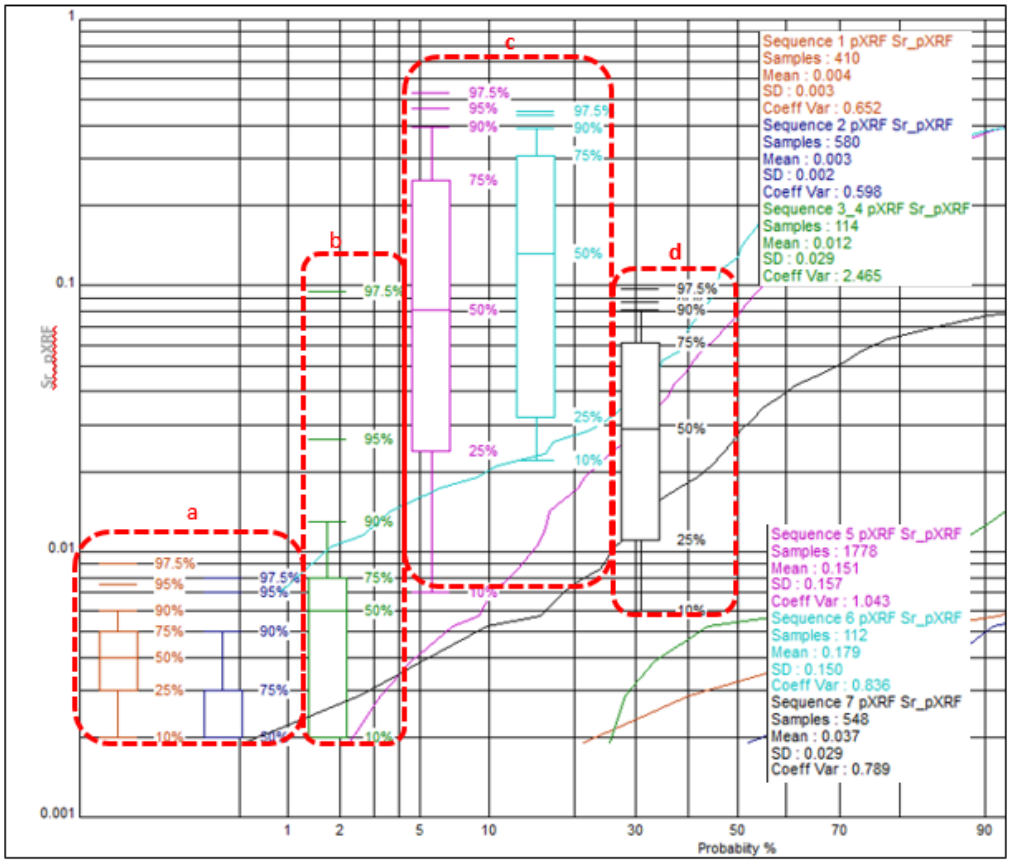

Figure 7-16. Box and whisker and log probability plots for Sr (%) within the Mindola (Sequence 1 and 2), Kitwe (Sequences 3 to 6) and Kirilabombwe (Sequence 7) formations on Shantumbu. Portable XRF data is plotted. The probability plot is cut at 90% probability for illustration purposes. The box and whisker plots show distinctive trends for the terrestrial versus marine sequences. (a) The box and whisker plots for Sequences 1 to 2 reflect terrestrial sediments. (b) The box and whisker plots for Sequences 3 and 4 reflect marine transgression environments. (c) The box and whisker plots for Sequences 5 and 6 reflect

marine depositional environments. (d) The box and whisker plots for Sequence 7 reflects a closed marine depositional environment.

All the metasediments sequences on Shantumbu had elevated arsenic levels, ranging from 10 to 995ppm, in comparison to the crustal abundance, which was determined at 5.7 ± 1.2ppm by Hu and Gao (2008). Sequences 3 and 4 (Copperbelt Orebody Member) have the highest arsenic grades of the sequences considered, whilst Sequence 6 (Antelope Member) has the lowest degree of variability in the arsenic content.

Sequence 2 (Kafue Arenite Member) demonstrated considerable variability in K_2O concentrations followed closely by Sequence 1 (Basal Sandstone Member), whilst Sequence 5 (Pelito-Arkosic and Chambishi members) demonstrated the least variability. Detrital sequences 1 and 2 have K_2O values in the range from c. 8% to 16% Al_2O_3, whilst Sequence 5 had a greater K_2O range from c. 6% to 21% Al_2O_3 (Figure 7-17).

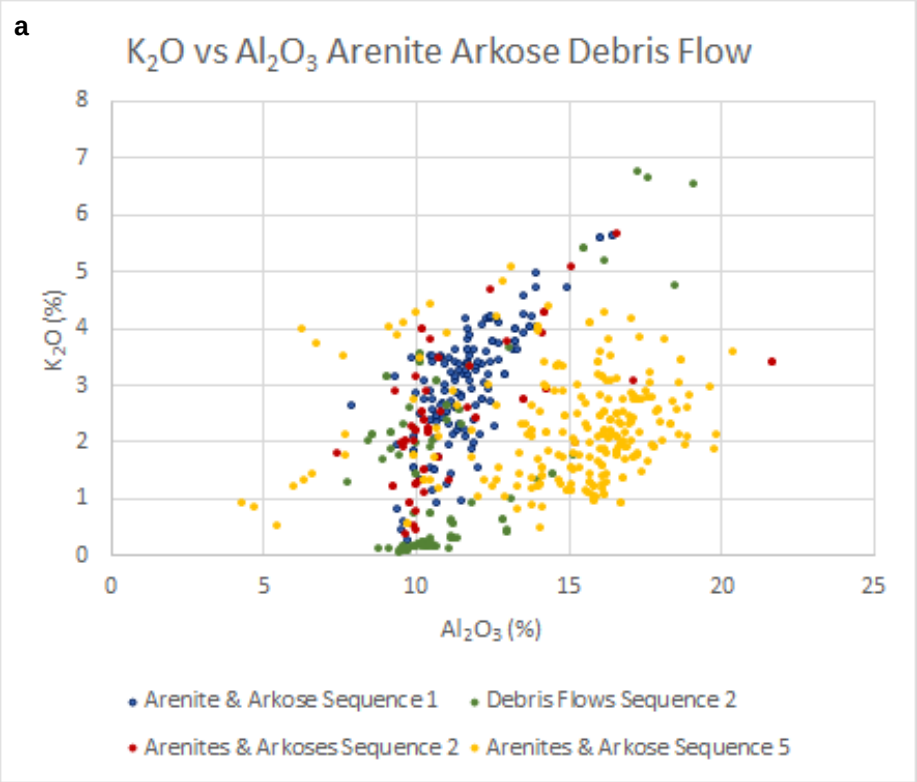

Continued next page

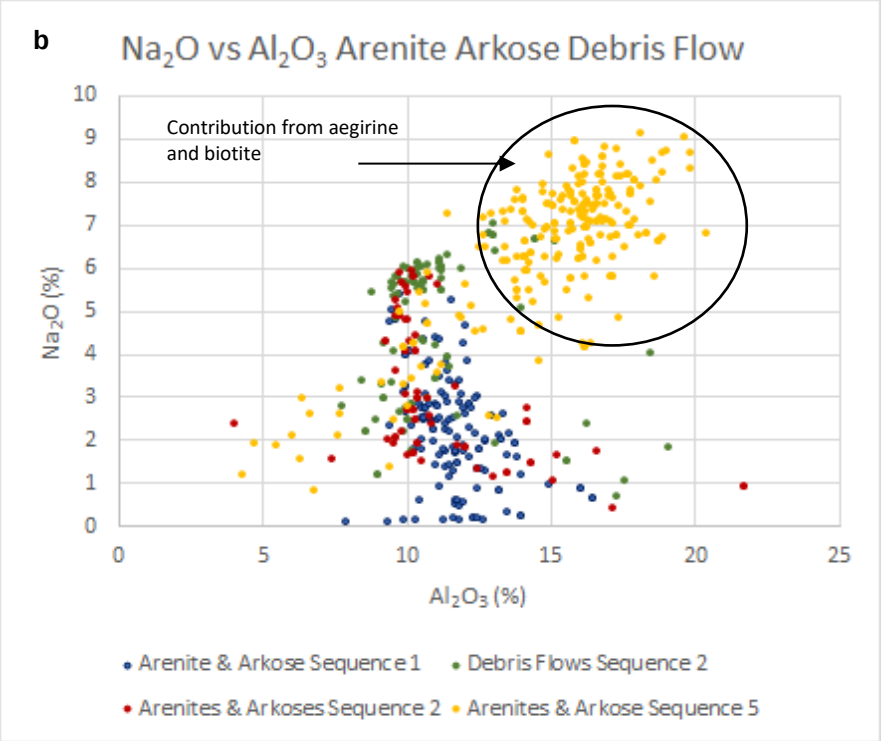

Figure 7-17. Scatterplot of K_2O versus Al_2O_3 per sequence. ICP-OES data, Shantumbu. (a) Scatterplot illustrating K_2O (%) versus Al_2O_3 (%) of the Sequences 1, 2, 4 and 5. (b) Scatterplot illustrating Na_2O (%) versus Al_2O_3 (%) of the Sequences 1, 2, 4 and 5.

The mobile elements of Co and Zn did not display a clear correlation with K_2O. The copper-bearing detrital sequences (Sequences 1 and 2) have elevated K_2O but suppressed Na_2O values (Figure 7-16 above), whilst Sequence 5 a to c, a subaqueous-marine succession, has elevated Na_2O and suppressed K_2O values. A positive correlation between K and Ba is illustrated in Figure 7-18 and Figure 7-19 and for K and Fe in Figure 7-20. Ba (Figure 7-21) is concentrated mainly in K-feldspar and has a similar geochemical distribution to K.

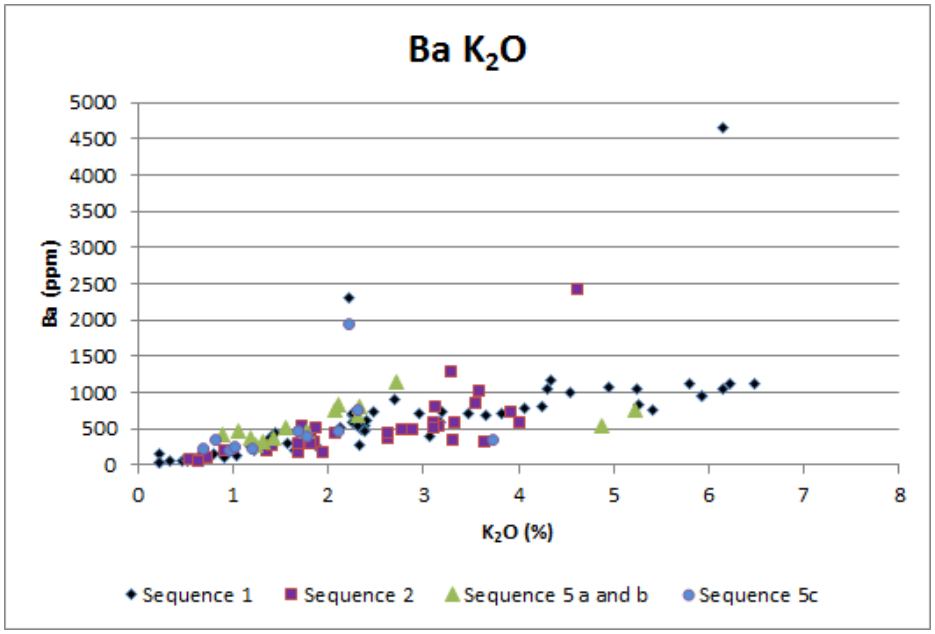

Figure 7-18. ICP-OES Ba values (ppm) for Sequences 1, 2 and 5 against K_2O, a mobile oxide, Shantumbu.

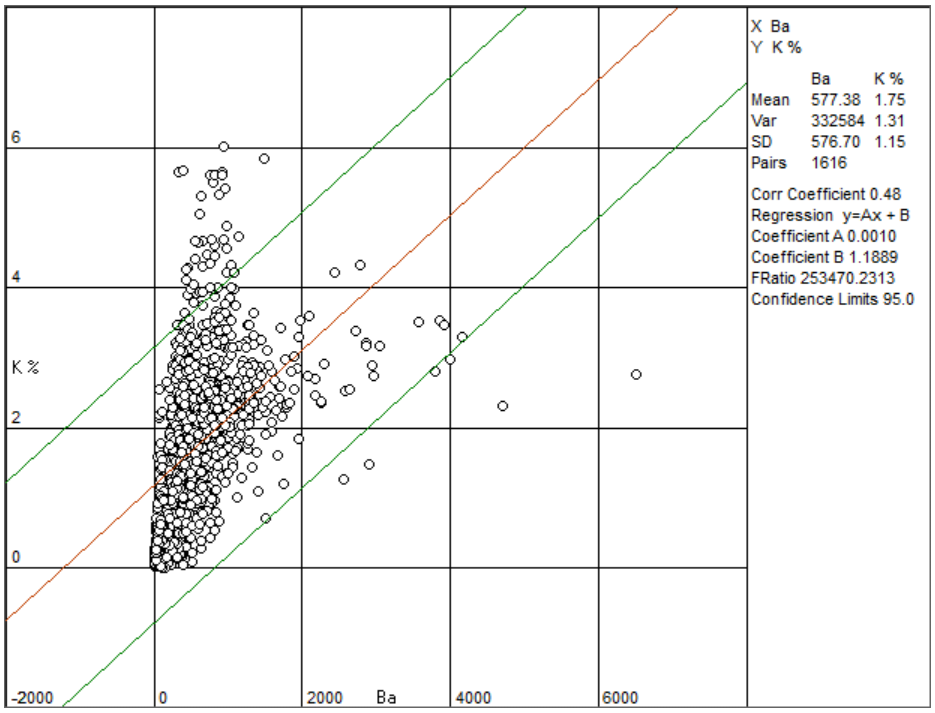

Figure 7-19. Positive correlation (48%) between K and Ba (%) for the ICP-OES dataset; all Sequences are combined into a single plot, Shantumbu.

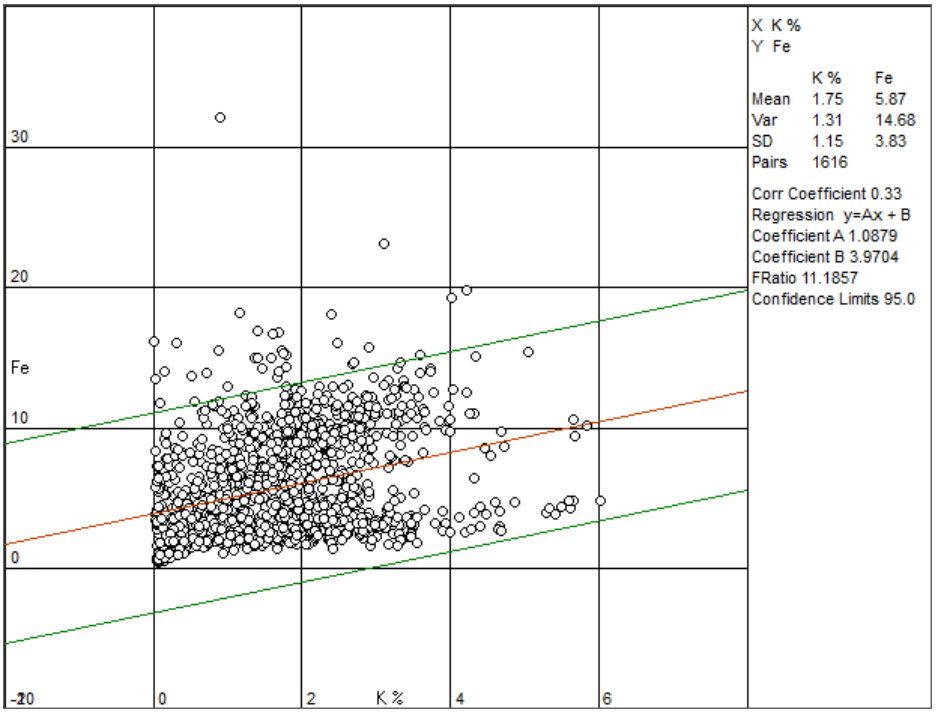

Figure 7-20. Positive correlation (33%) between K and Fe (%) for the ICP-OES dataset; all Sequences are combined into a single plot, Shantumbu.

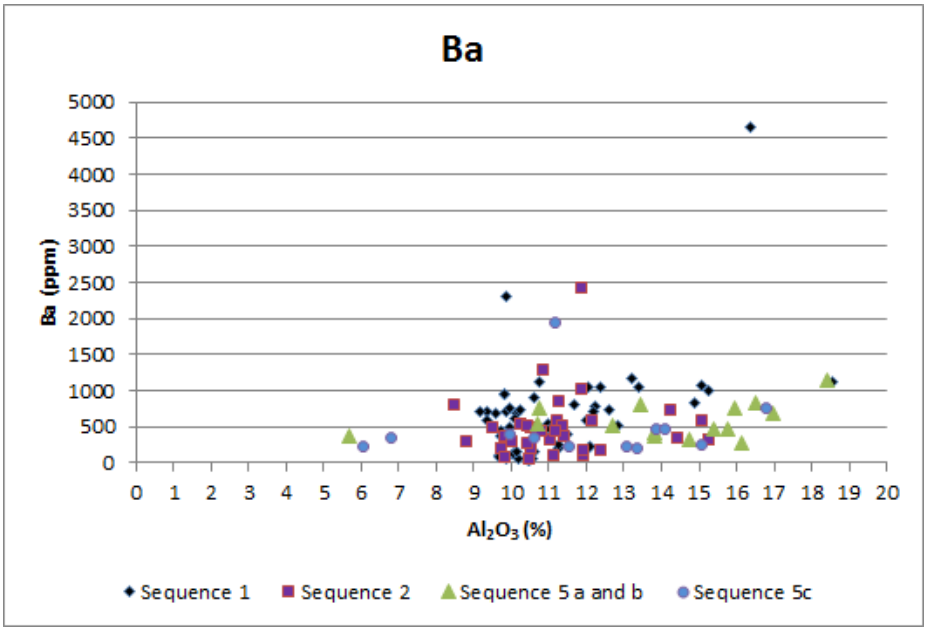

Figure 7-21. ICP-OES Ba values (ppm) for Sequences 1, 2 and 5 against Al_2O_3, an immobile oxide, Shantumbu.

Both the Rb and Cs distributions are closely linked with K and K-feldspars often have higher concentrations of Rb and Cs than biotite (Middelburg *et al.*, 1988). Rb and K exhibit similar geochemical behaviour in the Zambian Copperbelt lithologies (Croaker, 2011). Micas absorb many accessory minerals such as zircon, apatite, rutile, monazite, sillimanite and ilmenite

(Middelburg *et al.*, 1988). With the abundance of biotite found in the mineralogy of Shantumbu, the relationship between K and Rb was examined (Figure 7-22). The siltstones of Sequences 1 and 2 (Mindola Formation) averages 156ppm Rb and 174ppm Rb respectively, while the arenites and siltstones have an average of Rb concentration of 89ppm for Sequence 1 and 100ppm for Sequence 2 (Kafue Arenite Member). Rb analyses were not undertaken for the samples of Sequence 5 (Pelito-Arkosic and Chambishi members).

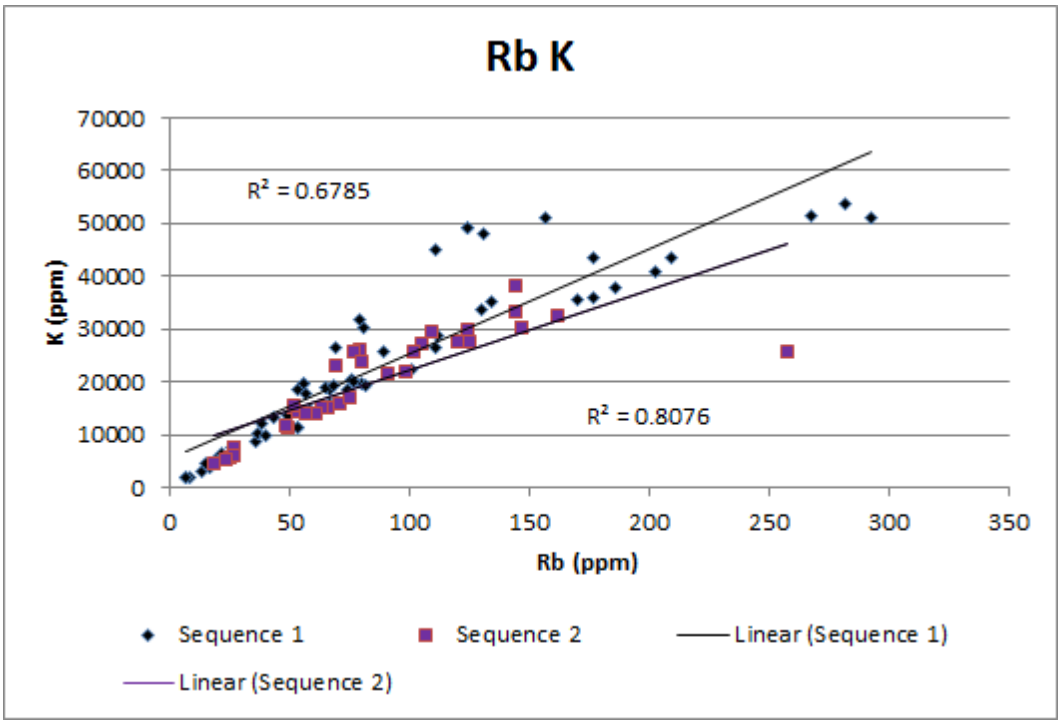

Figure 7-22. Correlation plot of ICP-OES data for Rb versus K in Sequences 1 and 2, Shantumbu.

V/Cr Trace Element Ratio

Palaeo-oxygenation indices provide an understanding of oxic versus anoxic conditions during deposition. V/Cr is a moderately reliable indicator of palaeo-oxygenation in fine-grained rocks such as mudstones and shales (Jones and Manning, 1994). The V/Cr ratio per sequence and lithology (Table 7-1) was determined from the available ICP-OES data and the acceptability of the V/Cr ratio was confirmed via the correlation between V and Cr for each Sequence.

Sequences 1 to 5 display a moderately positive correlation between V and Cr with the strongest correlation noted in Sequences 1 and 2. The arenite and siltstone components for Sequences 1 and 2 (Mindola Formation) had comparable V/Cr ratios. The V/Cr ratio for the siltstones in Sequences 3 and 4 (Copperbelt Orebody Member) were greater than those of the arenites and carbonates.

Table 7-1. V/Cr (ICP-OES) per lithology for Sequences 1, 2, 3 and 5, Shantumbu. ICP-OES analyses not undertaken for Sequence 6 and 7.

Formation	Sequence	Arenite	Argillite	Arkose	Debris Flow	Carbonate	Rhythmite	White Carbonate
Mindola	Sequence 1	1.37	1.32	1.54	-	-	-	-
	Sequence 2	1.36	1.58	1.49	1.36	-	-	-
Kitwe	Sequence 4	1.85	5.3[1]	-	-	1.47	-	-
	Sequence 5	2.43	2.30	3[1]	-	2.77	1.38	2.19

[1] One sample

Three Cr outlier points in Sequence 5 (Pelito-Arkosic and Chambishi members) were removed from the scatter plot due to the bias incurred from these high Cr grades, following which Sequence 5 kept its variability. The average Cr range for Sequence 1 to 5 was between 20 and 68ppm, with the upper range supporting the Cr average of 68ppm for alluvial sedimentary rocks determined by Hu and Gao (2008). The V grade for Sequences 1, 2 and 5 varied between 6 and 243ppm (Figure 7-23). The average grade for Sequences 1 and 2 (Mindola Formation) were 70ppm V, whilst Sequence 5 (Pelito-Arkosic and Chambishi members) averaged 40ppm V. The upper continental crustal average for V is 106ppm (Hu and Gao, 2008).

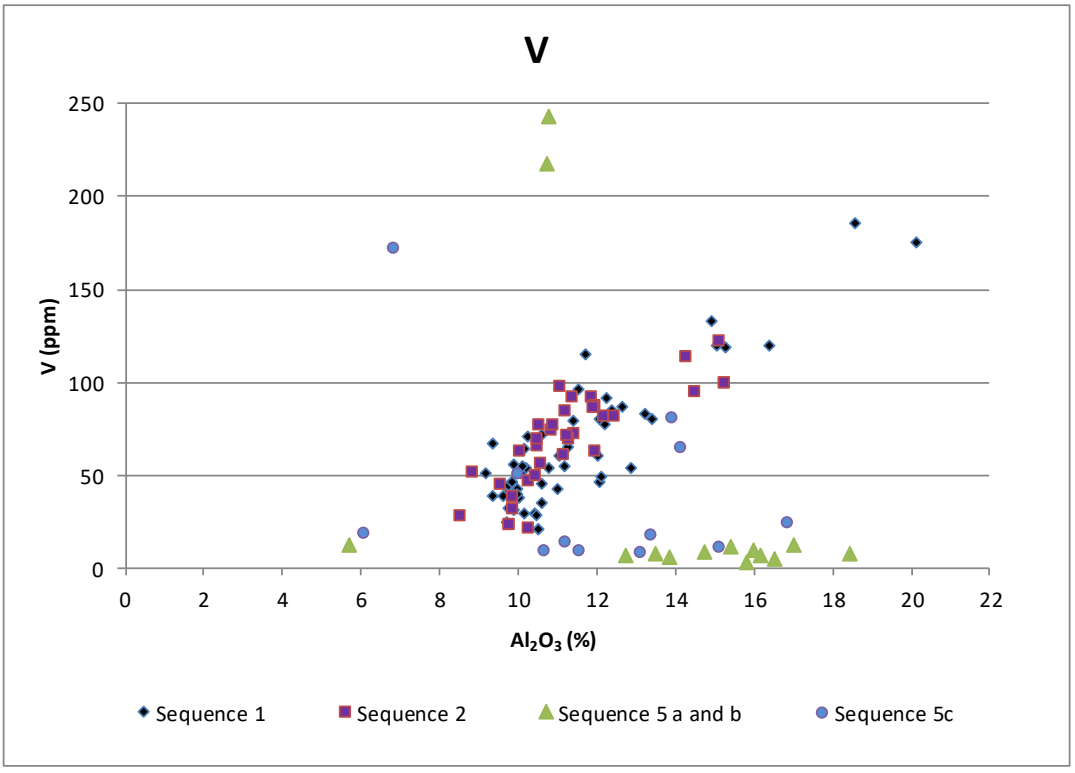

Figure 7-23. Correlation plot of ICP-OES data for V (ppm) in Sequences 1, 2 and 5 against Al_2O_3 (%), Shantumbu.

Sequence 5 (Pelito-Arkosic and Chambishi members) had the lowest and least variable V values compared against Sequences 1 and 2 (Figure 7-24). V is a useful element to determine anoxic

conditions, a V/Cr ratio greater than 2 is indicative of anoxic conditions (Porter *et al.*, 2014). Identical trends to V for Sequences 1, 2, 4 and 5 are noted for Cr (Figure 7-25).

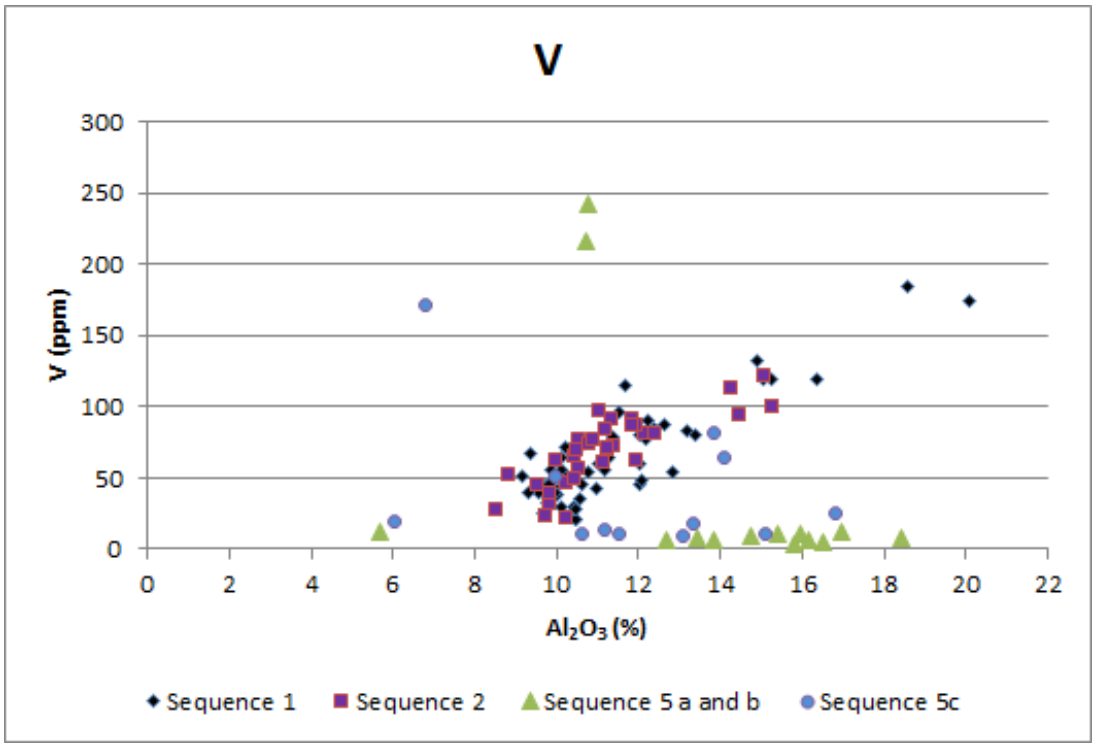

Figure 7-24. ICP-OES V values (ppm) for Sequences 1, 2 and 5 against Al_2O_3 (%), an immobile oxide, Shantumbu.

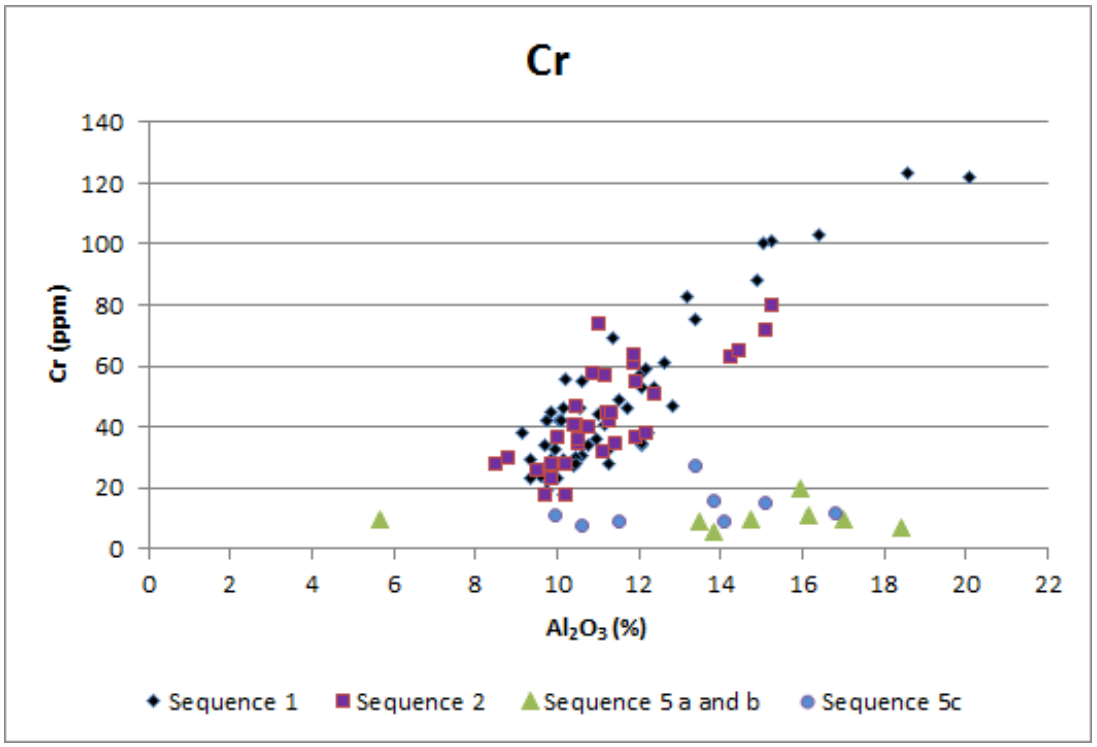

Figure 7-25. ICP-OES V values (ppm) for Sequences 1, 2 and 5 against Al_2O_3 (%), an immobile oxide, Shantumbu. Three outlier samples were top cut due to the bias incurred.

7.3.4 Mineralisation

The upper crustal estimate for copper abundance is 27 ± 2ppm (Hu and Gao, 2008). The copper concentration in Sequence 1 (Basal Sandstone Member) averages 1,890ppm ranging from c. 30 to 2,080ppm, while the siltstone layers within Sequence 1 averages 620ppm Cu, ranging from 40 to 2,540ppm Cu, and the arenites average 1,950ppm Cu with a range from 30 to 20,800ppm.

The portable XRF readings for Sequence 2 (Kafue Arenite Member) averaged 750ppm Cu within a range of c. 20 and 7,350ppm. Elevated Cu concentrations from c. 20 to 6,000ppm were noted in the arenites of Sequences 3 to 7, with Sequence 5 having the highest grades of the five sequences, bearing in mind the lack of precision of portable XRF values. Copper sulphides were not observed in Sequence 3 and 4 (Copperbelt Orebody Member), however native copper was observed and the likely source of the Cu grades. The arenites have higher grades of Cu than the siltstones in the five sequences considered, and the carbonate units contain background Cu grades (Figure 7-26 and Figure 7-27). Figure 7-27 illustrates the ICP-OES values obtained for the copper grades in Sequences 1 to 7, reflecting similar characteristics noted from the portable XRF readings.

Figure 7-28 reflects the copper grades obtained from portable XRF readings for each of the sequences and illustrates that Sequences 1 and 2 have a lower variability in copper grades than Sequences 5 and 7.

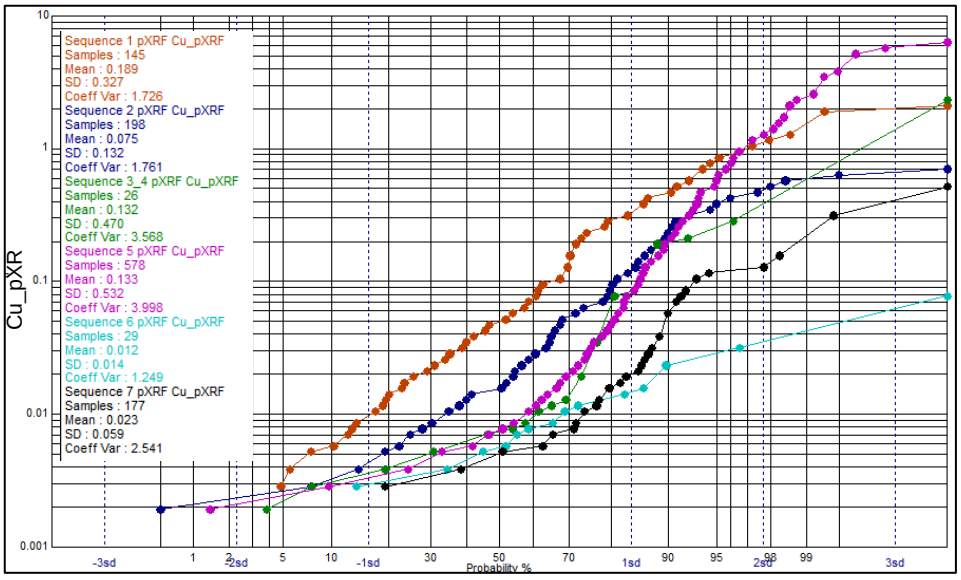

Figure 7-26. Log probability plot for the portable XRF copper readings for each Sequence individually, Shantumbu. Sequence 5 is the combination of 5a, 5b and 5c.

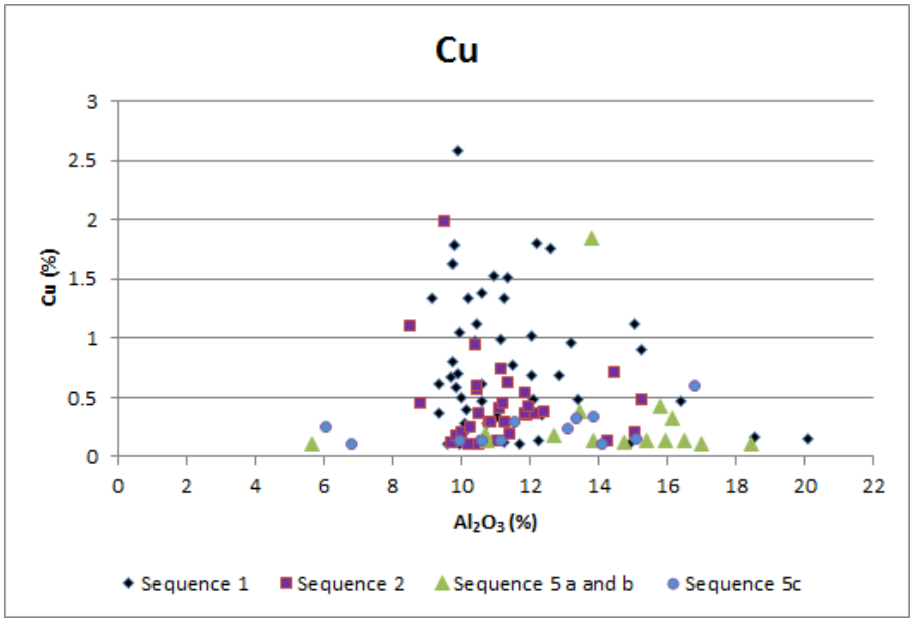

Figure 7-27. ICP-OES copper values (%) for Sequences 1, 2, and 5 against Al_2O_3, an immobile oxide, Shantumbu.

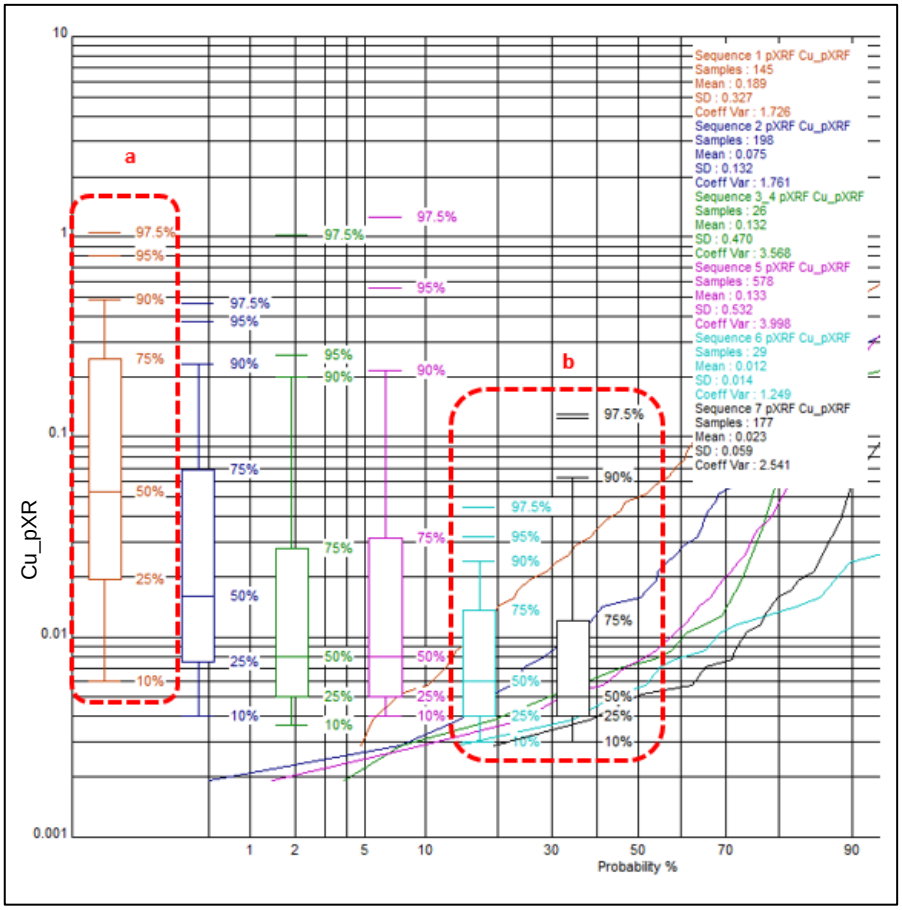

Figure 7-28. Box and whisker and log probability plot for copper (%) within sequences 1 to 7 on Shantumbu. Portable XRF dataset presented. The probability plot is cut at 90% probability for illustration purposes. (a) The box and whisker plots demonstrate distinctive trends with Sequences 1 and 2 being

the highest grade. (b) The box and whisker plots for Sequences 6 and 7 are markedly lower than the remaining sequences.

The copper mineralisation within the carbonates showed that the dolomite contained very low copper grades whilst the carbonates and rhythmites of Sequence 5 (Pelito-Arkosic and Chambishi members) host slightly elevated copper values (Figure 7-29).

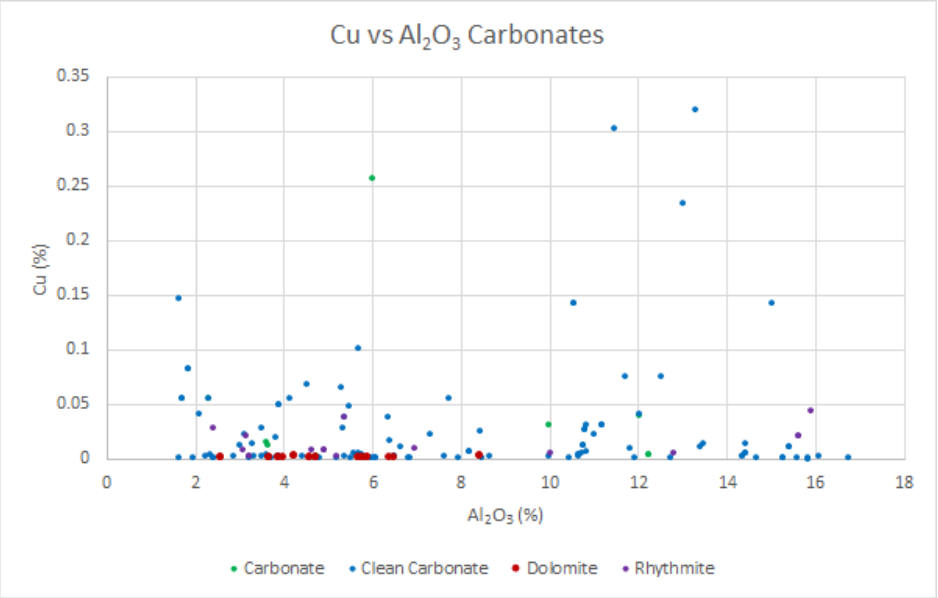

Figure 7-29. ICP-OES copper values (%) for Sequences 1, 2 and 5 against Al_2O_3, an immobile oxide, Shantumbu.

The higher sulphur (S) values from the ICP-OES dataset occurred in Sequence 5 a to c, in comparison to Sequences 1 and 2 (Mindola Formation) (Figure 7-30 and Figure 7-31). The S values were for the most part less than 4,000ppm.

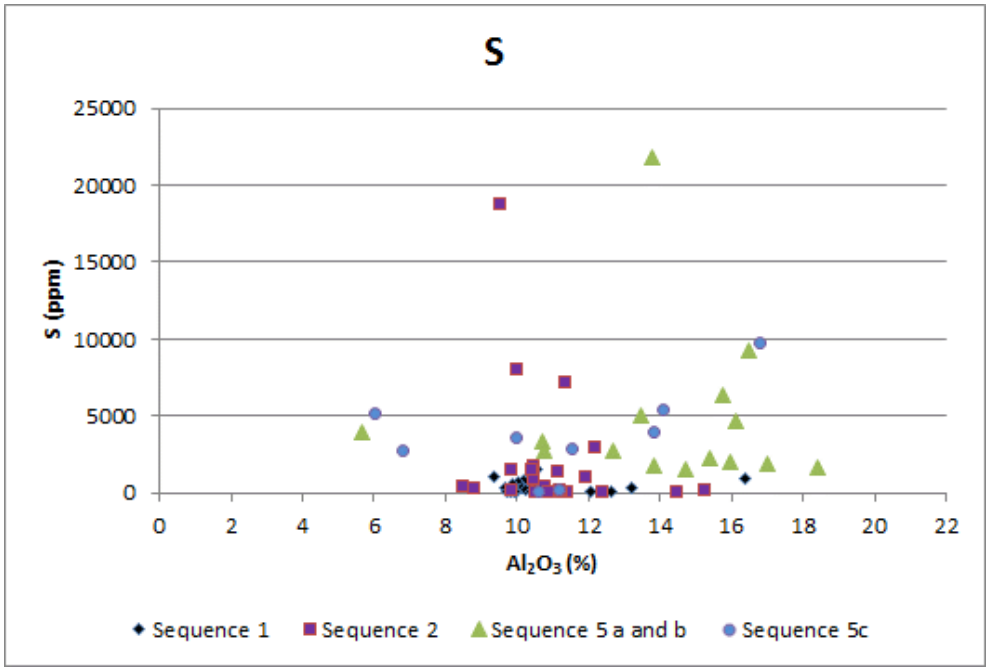

Figure 7-30. ICP-OES dataset for Sequences 1, 2 and 5 a to c illustrating S (ppm) against Al_2O_3 (%), Shantumbu.

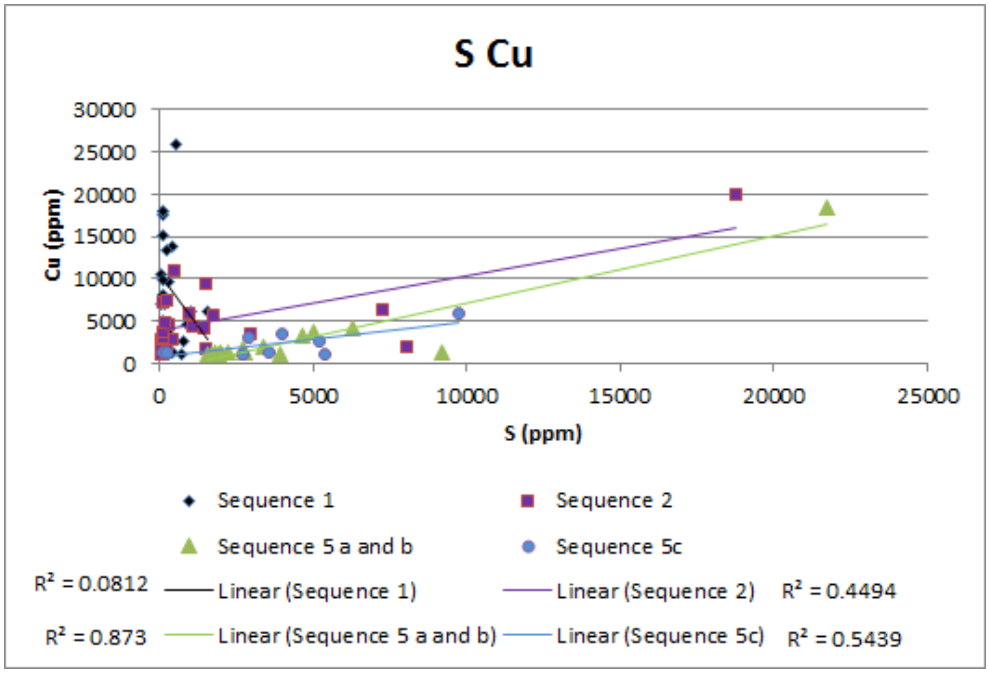

Figure 7-31. ICP-OES dataset for Sequences 1, 2 and 5 a to c illustrating S (ppm) against copper (ppm), Shantumbu.

Cobalt (Co) is a transition metal with an affinity for Cu, Ni, Au, Ag, Bi, As, Mo, U and Zn (Annels and Simmonds, 1984). Co has greater mobility than copper before being precipitated by reduced sulphur (Annels and Simmonds, 1984). Higher copper grades did not always have coincident elevated Co concentrations on Shantumbu. In several of the drill holes, the Co

profile mirrored the spikes in other metals such as Cu, Zn and Ni, as well as Fe. The Co spikes were however, offset from the copper spikes, peaking above and below elevated copper concentrations.

Using the portable XRF dataset, the Co values for Sequence 1 (Basal Sandstone Member) ranged from 0.013 to 1.3%, the average being 0.18%. Within Sequence 2 (Kafue Arenite Member), the Co values ranged from 0.007 to 0.97%. Sequences 3 and 4 averaged 0.26% whilst Sequences 5 to 7 had negligible Co, averaging c. 0.1%. Background grades of Co in Sequence 1 (Basal Sandstone Member) occur along the vertical length of the drill core intersections, while Co is restricted to erratic spikes in Sequences 3 to 7 (Figure 7-32).

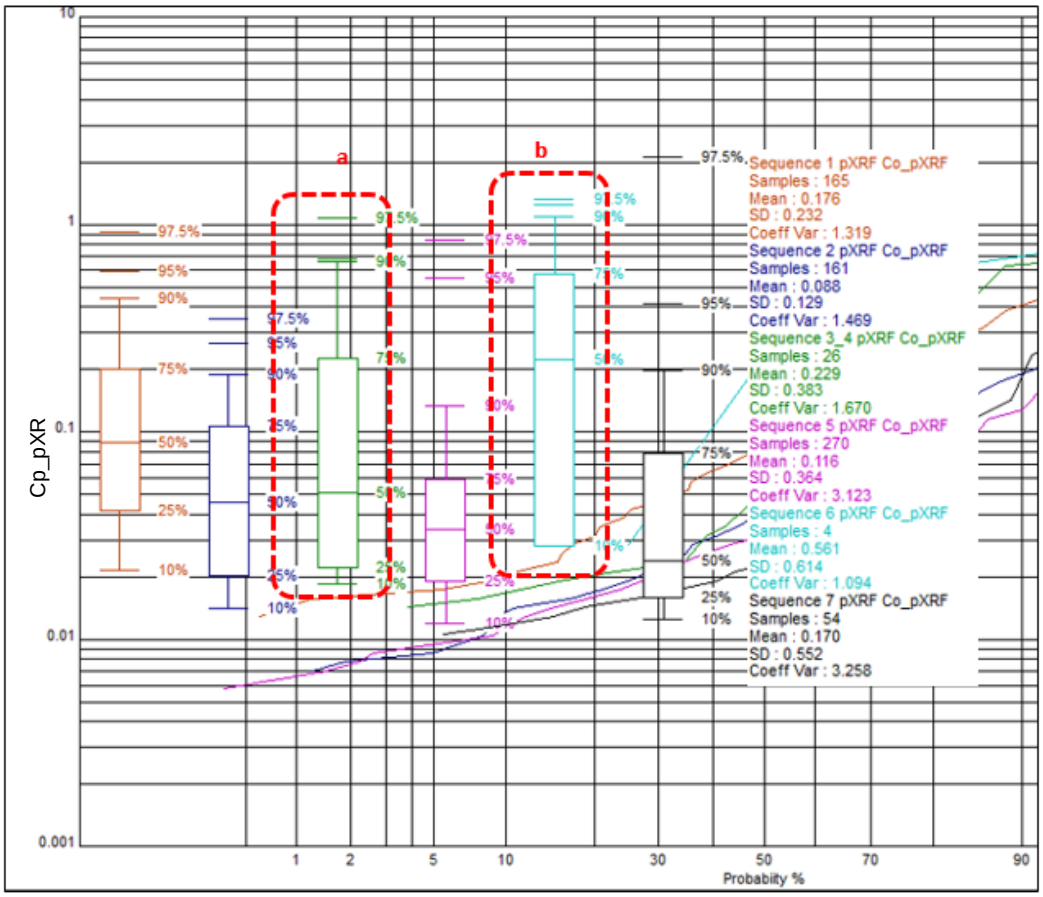

Figure 7-32. Box and whisker and log probability plots for Co (%) within sequences 1 to 7. Portable XRF dataset presented. The probability plot is cut at 90% probability for illustration purposes. (a) Co displays the greatest range in C values in Sequences 3 and 4. (b) as well as in Sequence 6.

The breccias of Sequence 5 (Pelito-Arkosic and Chambishi members) did not have elevated Co values while, the four values available for Sequence 6 contained Co ranging between 0.028% to 1.416% Co (portable XRF values). Only one Co bearing sample was available for Sequence 7 (SPQ001). The ICP-OES values obtained for the Co grades in Sequences 1 to 7 (Figure 7-33) reflected similar findings of the portable XRF readings.

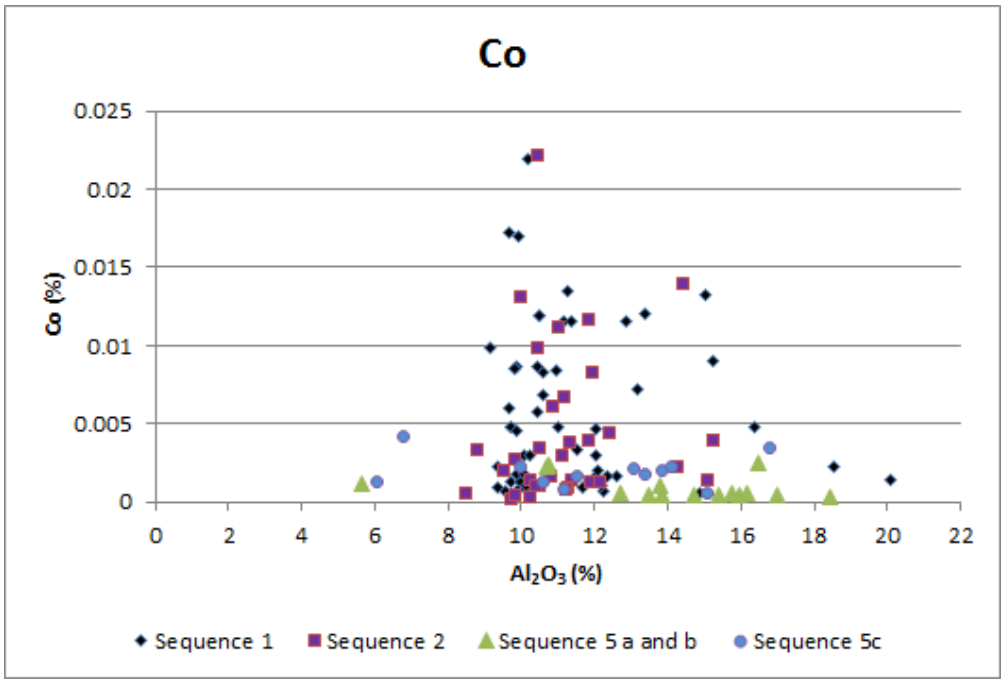

Figure 7-33. ICP-OES Co values (%) for Sequences 1, 2 and 5 against Al_2O_3, an immobile oxide, Shantumbu.

The Zn values for Sequences 1 and 2 (Mindola Formation) were for the most part less than 10ppm, whilst Sequence 5 a to c contained higher Zn values of 10ppm and higher (Figure 7-34). The trends noted for Zn were in opposition to the copper trends, but had a similar distribution across the Sequences as Fe and S. The two Zn grade populations may be used as a proxy for copper during exploration.

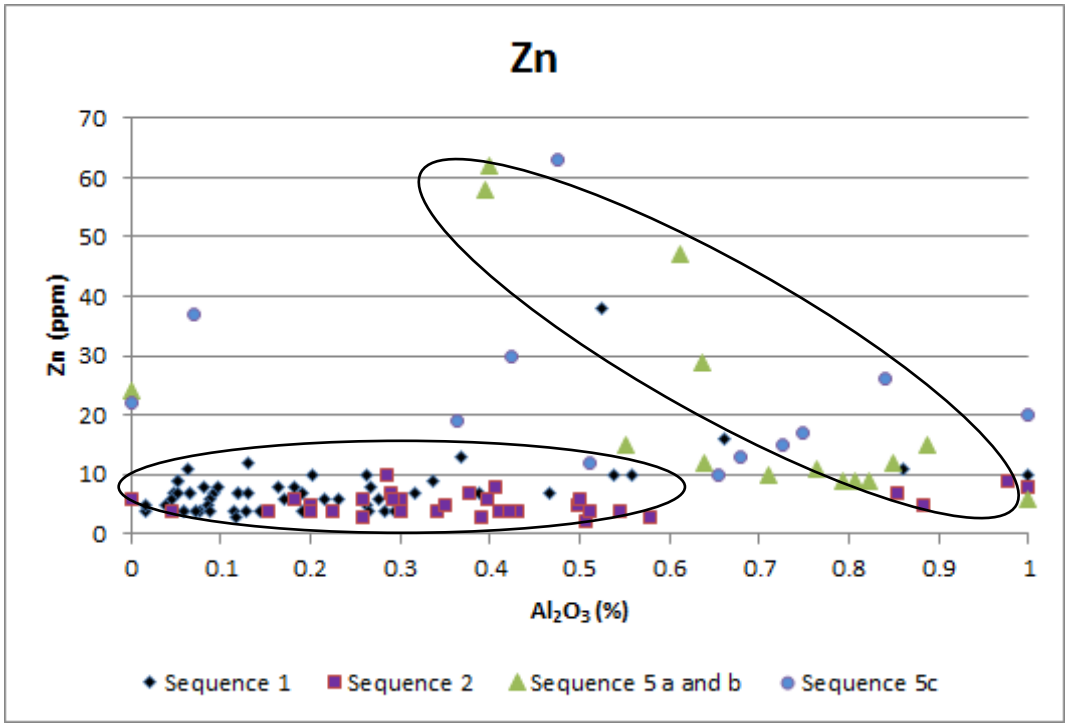

Figure 7-34. ICP-OES Zn values (ppm) for Sequences 1, 2 and 5 against Al_2O_3, an immobile oxide, Shantumbu. The two populations are noted by the inserts.

7.4 DISCUSSION

The distinct geochemical populations in the scatterplots for both immobile and mobile elements for Sequences 1 to 7, confirmed that each sequence was a discrete lithostratigraphic event. Examination of the geochemical profiles, scatter plots of elements/oxides with Al_2O_3, and element ratios gave support to the subdivision of the lithostratigraphy into the seven Sequences. The progression from detrital siliciclastic deposition to the introduction of carbonate as a major contributing phase, and to the stratigraphy being dominated by carbonates and subordinate calc-silicates, was supported by the geochemical examinations.

Cu, U, Th and As are enriched compared to continental crustal averages. V, Cr, Sc and Zn of Sequences 1 and 2 (Mindola Formation) are depleted relative to continental crustal averages. Table 7-2 summarises the arithmetic means for various trace elements (ppm) within Sequences 1, 2 (Mindola Formation) and 5 (Pelito-Arkosic and Chambishi members) versus the upper continental crust abundances as determined by Hu and Gao (2008). Ni abundance on Shantumbu compared with the average upper continental crustal abundance, while Co, Cu, Rb and Mo were enriched.

Table 7-2. Trace element abundances (ppm) of the upper continental crust (Hu and Gao, 2008) versus arithmetic averages (ppm) for Sequences 1, 2, 5 (a) to (c) for Cu ≥0.1% at Shantumbu.

Element	Hu and Gao (2008) (ppm)	Shantumbu			
		Sequence 1 (ppm)	Sequence 2 (ppm)	Sequence 5 facies a and b (ppm)	Sequence 5 facies c (ppm)
Sc	14	8	8	14	5
V	106	64	69	40	40
Cr	73	47	44	75	13 (164)[1]
Zn	75	7	5	22	24
Ni	34	47	34	29	24
Co	15	57	44	9	20
Cu	27	7,482	4,356	2,989	2,336
Rb	94	91	85	Not sampled	Not sampled
Mo	0.6	6	10	7	8
Sn	2.2	6	-	-	-
Bi	0.23	16	8[2]	-	6
U	2.6	19[3]	17	Not sampled	Not sampled

[1] One outlier of 1,365ppm; including outlier give a result of 164ppm; [2] One sample; [3] One outlier of 255ppm.

Sequences 1 and 2 (Mindola Formation) were deposited within an alluvial fan environment and MnO supports that finding that Sequences 3 and 4 (Copperbelt Orebody Member) were deposited in a nearshore environment. The Mn content of the marine sediments probably originated from transportation via wind, rivers and from shelf sediments, and the diffusion of Mn-enriched surface waters into the anoxic shelf environment. Mn precipitated in anoxic sulphidic waters and concentrations were greater immediately below the oxygen/sulphide boundary in the anoxic waters. In general, Mn actively cycles between oxidised and reduced forms across a redox front within the water column-sediment interface (Calvert and Pedersen, 1993). In the nearshore environment Mn enrichment is also a factor related to the supply of aluminosilicate sediments.

Mn diffused downward into sediment and upward into the overlying oxic zone where it is reprecipitated, thereby enriching the nearshore sediments in Mn. Alkalinity exerts a control on the concentration of Mn in sedimentary systems and Mn carbonate often precipitated in alkaline anoxic sediments in deep basins. An increase in alkalinity of the pore waters of the sediments occurred due to sulphate reduction (Calvert and Pedersen, 1993). Calvert and Pedersen (1993) concluded that high concentrations of Mn carbonate indicate accumulation under oxic bottom water conditions and concluded that anoxic basins with sulphidic waters at the sediment interface do not contain authigenic Mn enrichment.

The enrichment of Mn in Sequences 3 and 4 (Copperbelt Orebody Member) in comparison to Sequences 1 and 2 (Mindola Formation) is interpreted to represent Sequences 3 and 4 having

formed in a near-shore environment at the oxic-anoxic boundary involving a detrital shallow water to marine depositional environment. The highest concentrations of Mn within the sequences occur in Sequences 5 and 6, which is related to the deposition in fluctuating oxic and anoxic conditions and the detrital layers contributing Mn. The closed-sediment anoxic depositional environment of Sequence 7 (Bancroft Member) is reflected by a lower concentration of Mn in comparison to Sequences 5 and 6.

Strontium (Sr) is associated with gypsum-bearing and carbonate units formed in lacustrine and marine depositional environments (Warren, 1999), and hence is a key identifier for lacustrine and marine depositional settings and highlights transgressive/regressive events. Sr substitutes for K, Ca and Na due to their atomic structure (Croaker, 2011, p237). Strontium is significantly enriched in Sequence 5, as is CaO and Fe_2O_3, confirming the dominance of fan-delta and marine basin depositional settings. Sequences 1 and 2 (Mindola Formation) have negligible Sr (c. 35ppm) consistent with deposition in aerial and sub-aerial environments, whilst the several-fold increase in Sr through Sequences 3 and 4 is consistent with a nearshore to closed marine setting and the affinity for Ca-bearing minerals. The lower Sr content of Sequence 7 (Bancroft Member) in comparison to the other two marine Sequences (5 and 6) indicate curtailed replenishment of the oceanic water during deposition of Sequence 7 (Bancroft Member).

Arsenic has an affinity for iron oxides, Mn-bearing rocks, phosphate and carbonates. Reducing conditions are favourable for release of arsenic from hosting oxides, which may then be taken up by other iron oxides, phosphates and carbonates (Smedley *et al*., 2003). Arsenic is strongly chalcophile and occurs in association with copper sulphides and the arsenic content is released during oxidation (Plant *et al*., 2007). When arsenic levels in silicate minerals is lower than that for sulphides, arsenic competes for sites held by Fe and Al during alteration. In sedimentary rocks, higher arsenic concentrations are found in organic and sulphide-rich shales and phosphate rocks as well as in rocks containing abundant secondary Fe oxides (Plant *et al*., 2007).

Arsenic displays little variation amongst the Sequences, except for the elevated values within Sequence 3, when nearshore conditions were prevalent. Sequences 3 and 4 (Copperbelt Orebody Member) have the highest arsenic grades of the Sequences being considered. Sequences 3 and 4 represented the onset of marine transgression and hence increase in carbonate content. Additionally, Sequences 3 and 4 (Copperbelt Orebody Member) have elevated iron content interpreted as representing syngenetic pyrite, which subsequently altered to goethite, accounting in part for the elevated arsenic concentrations. If it is

considered that arsenic was derived from the Basement lithologies, circulation of arsenic - bearing fluids upon encountering carbonates and elevated iron-bearing Sequences 3 and 4 (Copperbelt Orebody Member), would more readily precipitate the arsenic content. The arsenic values for Sequences 3 and 4 suggest that the sequences originally hosted sulphides which were remobilised therefore releasing arsenic into the iron oxides thereby altered and/or precipitated. Within the Chongwe Copperbelt, arsenic values are reported to be elevated (Zambezi Resources, 2005).

The lower iron content of Sequences 1 and 2 (Mindola Formation) in comparison to Sequences 5 and 6 suggests oxidising conditions were dominant during deposition of Sequences 1 and 2, and an absence of bacterial sulphate reduction. In part, the low iron (c. 8 - 12% Fe) content is attributed to the mineral assemblages being dominated by plagioclase and quartz; plagioclase and quartz account for 20 - 100% of the mineralogy.

Sediments can contain both reactive iron and non-reactive iron. Pyrite is a reactive version of iron and is deposited in an environment where H_2S from bacterial sulphate reduction is available. The activity of bacterial sulphate reduction is limited by the abundance of reactive Fe available (Sun and Püttmann, 1996). Pyrite is found primarily as disseminated grains formed by the fixation of the sulphides within the anoxic sediments of the restricted marine setting.

Sequences 3 and 4 (Copperbelt Orebody Member) were deposited during marine transgression hence, anoxic conditions would alternate with oxic conditions. The anoxic conditions are considered responsible for the fixation of iron during pyritisation of the carbonate layers. The goethite-rich carbonates are interpreted to have formed from oxidation of the pyrite.

Sequences 5 and 6 were also deposited in a deposition environment, which experienced alternating anoxic and oxic conditions. Iron is soluble in anoxic conditions and together with a continual replenishment of detrital sediments, a continuous supply of iron is available. The lower average Fe_2O_3 concentration in facies 5 a and b reflected fluctuating oxic and anoxic bottom water conditions in comparison to the dominantly anoxic bottom water environment of facies 5c. The variability in Fe_2O_3 concentrations in Sequences 5 reflected the availability of H_2S in anoxic conditions for the reduction of Fe.

Sequence 7 (Bancroft Member) was deposited within a sediment-starved, closed anoxic marine environment and the replenishment of iron phases was limited. The iron content noted in Sequence 7 may relate to the disseminated pyrite and pyrrhotite, and ankerite present.

Ankerite is a Fe, Mg, Mn bearing carbonate where Mn has been replaced to varying degrees by iron and to a lesser degree by iron oxidation along fractures.

Titanium (Ti) is commonly found in stable primary minerals such as rutile and ilmenite (Middelburg *et al*., 1988). As a low solubility element, Ti tends to concentrate in a sedimentary system, particularly in a closed sedimentary system such as the marine transgression sequences on Shantumbu. Sequences 3 and 4 (Copperbelt Orebody Member) have low Ti values corresponding with deposition in a near shore marine environment and the decline in detrital sediments delivered. The increased detrital component of Sequences 1, 2, 5 and 6 resulted in an elevated Ti content, and/or the predominance of biotite within Sequences 5 and 6. Sequences 1 to 6 host comparable Ti concentrations. The lowest Ti values are associated with Sequence 7 (Bancroft Member), corresponding to deposition within a sediment starved closed marine environment Ti spikes noted in the Kirilabombwe Formation (Sequence 7) (SPQ001 and SPQ002).

The TiO_2 ranges encountered on Shantumbu are similar to concentrations encountered in the RAT and Mines Subgroup rocks in the Kolwezi, Kabolela, Kambove and Luiwishi areas (Kampunzu *et al*., 2005). The equivalent of Sequences 3 and 4 (Copperbelt Orebody Member) in the Nkana-Mindola deposit is reported by Croaker (2011) to range from 0.05 – 1% TiO_2, with the Sequences 3 and 4 values within this range and at 0.48%.

Micas absorb a multitude of accessory elements, such as Zr. The altered detrital sediments of Sequences 1 and 2 (Mindola Formation) and the granitic Basement source is reflected in the abundant micas, while the wider range of Zr in Sequences 5 and 6 is interpreted to reflect the increase in biotite. Sequence 7 (Bancroft Member) demonstrates a sediment-starved depositional environment, containing fewer siltstone layers and hence biotite within the terrestrial related units.

Sequence 4 (Copperbelt Orebody Member) represented the first discernible dolomitic carbonate on Shantumbu, which is reflected in the elevated Mg values. The remaining Sequences, both detrital and marine reflect the carbonate component being that of calcite. The fluctuations in MgO for Sequences 5 facies a to c relate to an increase in carbonates and biotite.

The copper-bearing detrital succession of Sequences 1 and 2 (Mindola Formation) have suppressed Na_2O trends in comparison to the carbonate units of Sequences 3 to 7. The variability in Na_2O of Sequences 1 and 2 reflects the sodic alteration of the detrital sediments

and the dissolution of evaporitic layers, and remobilisation of Na from these sequences. The calcitic carbonates of Sequences 3 to 7 are dominated by several sodic minerals (aegirine, feldspar, glaucophane, sodalite and sericite) and biotite was extensively altered to aegirine in Sequence 5, supporting the sub-aqueous Sequences underwent extensive sodic alteration.

Sequences 1 and 2 (Mindola Formation) have concentrations of Ba greater than that noted in Sequence 5. Ba may have originated from either, or both, Ba-bearing fluids, or the destruction of detrital K-feldspar (Woodhead, 2013). The absence of barite and the elevated occurrence of Ba silicates together with ore metals according to Heijlen *et al.* (2008) is indicative of sulphide mineralisation formed in a reducing H_2S-rich setting, although bacterial sulphate reduction is only expected to have occurred within Sequences 3 to 7.

Rb and K have similar ionic radii and tend to be closely affiliated (Horstman, 1957). Nonetheless, during weathering K is more mobile compared to Rb, therefore concentrating Rb. During low-temperature recrystallisation, Rb does not enter either feldspar or quartz structures and is preferentially absorbed by clay particles (Horstman, 1957). The average Rb concentration of sedimentary rocks according to Horstman (1957) is 110ppm where the bulk of Rb is found in illite. Both Sequences 1 and 2 (Mindola Formation) underwent potassic alteration, reinforced by the strong correlation between Rb and K.

The geochemical behaviour of iron, Cr, V and Mn are dependent on the reduction-oxidation conditions during deposition. Cr and V are considered soluble in oxic conditions and are reactive or insoluble species under anoxic conditions (Calvert and Pedersen, 1993). Both trace elements, V and Cr, form elements of silicate minerals. V is enriched in oxic conditions, as demonstrated by Sequences 1 and 2 (Mindola Formation), whilst V has an affinity for organic matter and concentration of V is favoured in reducing conditions. The low averages for V in the calcitic carbonates indicated anoxic conditions, the dominance of carbonate and siltstone layers, and a lack of sulphides in Sequence 5 (Pelito-Arkosic and Chambishi members).

Cr readily substitutes for Mg in ferromagnesian minerals (Calvert and Pedersen, 1993) and iron and Al scavenge Mg in suboxic conditions. The absence of Cr, V, Cd, Ni and Zn, is a guide to sedimentation conditions under oxygenated bottom water conditions. The Cr content of Sequence 5 (Pelito-Arkosic and Chambishi members) is negligible reflecting the dominance of carbonate and siltstone layers and predominance of anoxic conditions.

The lithologies of Sequences 1 and 2 (Mindola Formation) have a consistent V/Cr ratio, while the V/Cr ratios for both arenites and carbonates of Sequences 3 and 4 (Copperbelt Orebody

Member) are similar to that of Sequences 1 and 2. The arenite units of Sequence 5 contain a higher V/Cr ratio in comparison to Sequences 1 to 4, indicating a shift away from oxygenated conditions toward alternating oxygenated - anoxic conditions.

A V/Cr ratio above 2 is suggestive of anoxic conditions where H_2S is present within the water above the sediment. A V/Cr ratio of below 2 suggests primarily oxidising conditions and V/Cr ratio below 1 is suggestive of the palaeo-oxygenation – H_2S interface located within the sediment (Jones and Manning, 1994). An anoxic environment is indicated by the V/Cr ratio for Sequence 5 versus a dominantly oxic environment for Sequences 1 and 2. The V/Cr ratio for Sequence 5 confirms alternating oxic and anoxic conditions prevailed in facies 5 a and b whilst, the V/Cr ratio for Sequence 7 confirmed the anoxic bottom water conditions.

The geochemical composition of the Mpande Gneiss and granite is summarised in Table 7-3. As only two samples were available, the V/Cr ratio was expanded to the Munali Hills Granite (Table 7-4), which is to the south of Shantumbu. Review of the V/Cr ratios for the Mpande and the Munali Hills granites is comparable to the V/Cr ratios determined for the lithologies on Shantumbu (Table 7-5).

Table 7-3. V/Cr ratio of the Mpande Gneiss and Granite - V/Cr ratios (Source: Katongo *et al*., 2004).

Element	MPD1	MPD2	Average
V	30.1	25.9	28.0
Cr	9.77	17.3	13.54
V/Cr Ratio	**3.08**	**1.50**	**2.07**

Table 7-4. Geochemical composition of the Munali Hills Granite – V/Cr ratios (Source: Katongo *et al*., 2004).

Element	MHG1	MHG2	MHG3	MHG4	MHG9	MHG10	Average
V	24.8	36.5	35.5	17.3	82.2	17.7	35.67
Cr	17.3	16.8	13.1	16.0	22.4	7.19	15.47
V/Cr	**1.43**	**2.17**	**2.71**	**1.08**	**3.67**	**2.24**	**2.31**

Table 7-5. V/Cr (ICP-OES) per lithology for Sequences 1, 2, 3 and 5, Shantumbu. ICP-OES analyses not undertaken for Sequence 6 and 7.

Formation	Sequence	Arenite	Argillite	Arkose	Debris Flow	Carbonate	Rhythmite	White Carbonate
Mindola	Sequence 1	1.37	1.32	1.54	-	-	-	-
	Sequence 2	1.36	1.58	1.49	1.36	-	-	-
Kitwe	Sequence 4	1.85	5.3[1]	-	-	1.47	-	-
	Sequence 5	2.43	2.30	3[1]	-	2.77	1.38	2.19

[1] One sample

7.5 CONCLUSIONS

The mineralogy presented in Chapter 5 and the geochemistry examined in Chapter 7 have provided support for the depositional environments interpreted from the petrographic and lithostratigraphic examinations of the Shantumbu Drill cores, along with the clarification of the oxic and anoxic conditions during deposition. The Geochemistry Chapter has recognised several characteristics of the metasediments and the depositional environments, and which are summarised as follows:

- Granitic Basement was a source for the detrital components and elements including Cu, Ba, Zr, K, Na, V, Cr, Ti and Rb;
- The geochemical trends of the debris flow deposits or sediments of Sequence 2 exhibited restricted groupings, indicating that the close-packed nature of the protolith debris flows sediments probably formed an impermeable barrier to basinal brines from the underlying lithologies. The debris flow sediments do not exhibit the same characteristics for iron as the arenites and arkoses of Sequences 1, 2, 4 and 5;
- The low Mg and Ca for Sequences 1 and 2 (Mindola Formation) is related to the low concentrations of these elements in the Basement hinterland, as well as lack of dolomitisation;
- Sequences 1 and 2 (Mindola Formation) have higher K_2O values than Sequence 5, which is related to the alkali provenance of the sediments, and/or the extensive potassic alteration, which affected the sediments;
- The Mg content and the mineralogy of Sequence 4 (Copperbelt Orebody Member) confirms that this sequence was the first occurrence of dolomitic carbonate in the lithostratigraphy, corresponding to the onset of a marine transgression;
- Sequence 5 (Pelito-Arkosic and Chambishi members) has the highest Mn values, which reflected alternating of oxic and anoxic conditions during deposition of this sequence. The brecciated siltstones, which resulted from dissolution of the evaporite content also attest to a fluctuating oxic-anoxic environment;
- The increase in sulphur in Sequence 5 (Pelito-Arkosic and Chambishi members) was interpreted to relate to bacterial sulphate reduction activity and anoxic conditions;
- The V/Cr ratio of greater than 2 for Sequence 5 (Pelito-Arkosic and Chambishi members) indicate the dominance of anoxic conditions during deposition;
- The V/Cr ratios for the Mpande and the Munali Hills granites were comparable to the V/Cr ratios determined for the lithologies on Shantumbu; and

- The similarities between the geochemistry and mineralogy of the Shantumbu rift-related metasediments with those of the surrounding granites and gneisses are significant, although detailed work on the zircons of the Shantumbu metasediments and those within the granites and gneisses would need to be undertaken.

CHAPTER 8

DISCUSSIONS, CONCLUSIONS AND RECOMMENDATIONS

8.1 INTRODUCTION

The detrital and chemical metasediments at Shantumbu were recently drilled as part of an exploration programme to determine the existence of sediment-hosted, stratiform copper mineralisation. Shantumbu is located immediately south of the world's largest copper-cobalt province, the Central African Copperbelt. The succession of arenites, arkoses, siltstones and carbonates at Shantumbu have numerous similarities in terms of tectonic setting, mineralogy, alteration, mineralisation and metasomatism with the Roan Group within the Proterozoic Rift basins of the Central African Copperbelt.

At the time of the exploration little information about the lithostratigraphy, copper mineralisation and geochemistry were available for the metasediments around Shantumbu. The most complete accounts of the lithostratigraphy prior to the 2013 to 2015 exploration were conducted by Simpson *et al*. (1963), Smith (1964) and Mallick (1966), which examined the southern flank of the Mpande Dome. Shantumbu is found on the northern flank of the Mpande Dome. Smith (1964) and Mallick (1966) described the stratigraphy with rhyolite, of the Kafue Rhyolite and the Nazingwe formations, above the Basement Granite and at the base of the metasediments succession. Overlying the rhyolites are altered fine-grained muscovite-bearing quartzite and quartz-muscovite schists intercalated with minor acid and mafic volcanic rocks and further rhyolite (Mallick, 1966).

Mallick (1966) described the stratigraphy with the Kafue Rhyolite and the Nazingwe formations above the Basement Mpande granites and gneisses and overlain by a succession of metasediments. The lower parts of the metasediments, which were made up of altered fine-grained muscovite-bearing quartzite and quartz-muscovite schists, were intercalated with minor acid and mafic volcanic rocks and rhyolite.

Smith (1964) assigned the Kafue Rhyolite and the Nazingwe formations to the Basement stratigraphy and designated the overlying metasediments to the Chunga Group and the younger Cheta Group of the Katanga System. The Chunga Group is floored by the Mulola Formation overlain by the Funswe Pelite Member. The youngest unit of the Chunga Group was the Chipongwe Psammite Member. The overlying Cheta Group consisted of two members, the basal

Mampompo Limestone Member, and the overlying Chilanga Psammite Member. The Cheta Group was capped by the Lusaka Dolomite Formation along a tectonic contact.

Mallick (1966) assigned the stratigraphy to the Katanga System, starting at the base with the Kafue Rhyolite Formation of the Shamazio Group, followed by the Mulola Formation, the Schist-Marble Formation and the Chipongwe Semipelite Formation of the Kafue (Chunga) Group respectively. The Mampompo Limestone Formation, of the Cheta Group, formed the topmost stratigraphic unit below the Lusaka Dolomite Formation.

Following the detailed examination of the lithostratigraphy at Shantumbu during this study, an alternate stratigraphic classification to the Chunga and Cheta groups has been presented, where the metasediments represent the southernmost occurrence of the Roan Group of the Katanga Supergroup. It therefore appears that the Katanga Supergroup rift-related terrigenous and marine sediments at and around Shantumbu represent a rift basin analogous to the interlinking rift basins hosting the Zambian Copperbelt.

The copper sulphides intersected in drill core at Shantumbu and the copper oxides which outcrop, are comparable to the sediment-hosted, stratiform copper deposits of the Zambian Copperbelt, and other sediment-hosted, stratiform copper occurrences globally, such as White Pine in Michigan, the Zechstein Basin in Europe, Spar Lake in Montana, the copper occurrences in Namibia and Botswana on the Kalahari Craton, and the Mangula and Mhangura deposits in Zimbabwe.

8.2 TECTONIC FRAMEWORK OF SHANTUMBU

The Katanga Supergroup in the Central African Copperbelt was deposited in rift-related basins during passive continental extension during the breakup of Rodinia c. 880 Ma (Master and Wendorff, 2011). The examination of the lithostratigraphy at Shantumbu confirms that the metasediments were deposited within a rift basin analogous to basin metasediments in the Central African Copperbelt.

The Proterozoic rifting in the Central African Copperbelt eroded the Basement granites and gneisses, and the sediments were deposited within braided streams, alluvial fans, fan-deltas, and a marine shelf environment. The exploration conducted on Shantumbu confirmed an equivalent tectonic setting for the sediments at Shantumbu.

8.2.1 Regional Structure

Shantumbu straddles the junction between the Zambezi Belt, the Irumide Belt and the Lufilian Arc, and underwent Pan African deformation and high-grade metamorphism. The initial deformation phase, termed D_1 or the Kolwezian Phase (Kampunzu and Cailteux, 1999), involved northward-directed folding and thrusting with related back-folding in the Lufilian Arc and the Zambezi Belt. The peak of the ductile D_1 deformation has been dated at c. 790 - 750 Ma and ceased completely by c. 710 Ma (Kampunzu and Cailteux, 1999).

Within the Zambezi Belt, the D_1 event was southwest verging which resulted in amphibolite facies metamorphism c. 535 - 517 Ma (Naydenov *et al*., 2015). West-northwest trending S_1 foliation in the Lusaka-Kafue Region was axial planar to the regional-scale southwest vergence and overturned to form recumbent F_1 folds (Hanson *et al*., 1994).

Initial thrusting related to D_1 propagated northward and was succeeded by back folding and thrusting during the progressive contraction during Pan African orogenesis (D_2 and D_3); D_1 structures were overprinted by D_2 structures. Southward thrusting and transcurrent to oblique-slip ductile shear zones accommodated the crustal shortening during the Pan African orogenesis of the Zambezi Belt (Hargrove *et al*., 2003). The south to southwest (back folding) verging folding of the sedimentary rocks from Lusaka southwards to the Mpande Dome were re-iterated by Porada and Berhorst (2000). The southwest folds were considered to represent F_1 structures (Hanson *et al*., 1994).

Naydenov *et al*. (2014) gave an emplacement age range for the Hook Batholith, north of the Mwembeshi Zone. The emplacement age of c. 550 to 533 Ma is syn-tectonic with the D_1 event of the Lufilian Orogeny.

Brittle deformation characterised the second phase, D_2 or Monwezi, dated at c. 690 - 540 Ma. Brittle deformation was accommodated along sinistral strike slip faults, such as the Mwembeshi Zone. The Mwembeshi Zone has been suggested to have been most active during the D_2 phase. Naydenov *et al*. (2014) indicated the Mwembeshi Zone developed during the D_2 north-south shortening event.

Clockwise rotation of the Lufilian Arc began during the D_2 phase (Kampunzu and Cailteux, 1999) and this period was characterised by north-south to north northeast-south southwest compression. The D_2 brittle deformation has been attributed to the convergence of the Congo

and Kalahari cratons and the progression of strike slip faults northwards across the Pan African orogenic belts (Kampunzu and Cailteux, 1999).

On Shantumbu, F_2 folds mantling the Mpande Dome mimic the margin of the Mpande Dome although Hanson *et al*. (1994) noted the F_2 folds were coaxial with, and overprinted, the overturned to recumbent F_1 folds in the Zambezi Belt. The F_2 folds later experienced upright, open and northeast-trending folding, F_3 (Hanson *et al*., 1994). The F_3 folding included irregularly developed upright, open, northeast-trending folds. The up-warping of the Mpande Gneiss was proposed to have occurred during D_2 deformation at c. 530 Ma (Naydenov *et al*., 2015).

The D_3 or the Chilatembo Phase was the third and final phase of Pan African deformation which affected the Lufilian Arc and Zambezi Belt. The D_3 deformation was dominated by structures transverse to the trends of the Pan African belts and hypothesised to be of Palaeozoic age (Kampunzu and Cailteux, 1999). High-angle NE-SW faulting and open folding related to NW-SE compression affected the Lufilian Arc and Zambezi Belt and resulted in the reactivation of several strike slip faults (Kipata *et al*., 2013).

Crustal thickening due to compressional deformation resulted in high-pressure metamorphism within the Zambezi Belt. Peak metamorphism in the Lufilian Arc has been dated at c. 566 - 550 Ma (Kröner and Stern, 2005; Reinaud *et al*., 2005). Irregular occurrences of eclogite facies metamorphism within the Katanga Supergroup metasediments of the Zambezi Belt are related to subduction of oceanic crust and ocean basin closure during the collision of between the Congo and Kalahari cratons c. 659 and 595 Ma (De Waele *et al.*, 2008).

Peak metamorphic grades encountered along the Mwembeshi Zone occurred during the Late Proterozoic, attaining greenschist facies (Yemane *et al*., 2002). The Mwembeshi Zone is broadly taken as the junction between greenschist metamorphism characteristic of central and northern Zambia, and the amphibolite metamorphism of southern Zambia. The Mwembeshi Zone experienced prograde metamorphism to amphibolite and locally eclogite facies and was retrograde metamorphosed to greenschist facies. Amphibolite and eclogite metamorphism require both high temperatures and pressures and the required pressure-temperature regime has been attributed to tectonic thickening related to the Pan African deformation (Porada and Berhorst, 2000).

8.2.2 Local Structure

The structures observed on Shantumbu during the 2013 to 2015 exploration were consistent with the work of Mallick (1966), Hanson *et al*. (1994), Porada and Berhorst (2000) and Hargrove *et al*. (2003). The large-scale recumbent folding, in the order of 10km, and limbs overturned to the southwest confirmed that compressional deformation dominated the structural setting at Shantumbu following the deposition and lithification of the basin sediments. Co-axial folding open to the southwest on the limbs of earlier structures followed (Hanson *et al*., 1994; Porada and Berhorst, 2000).

Both the faults and the large-scale recumbent folds at Shantumbu acted as the conduits along which basinal fluids migrated, an example of which is the copper mineralisation within the hinge of a D_1-D_2 fold axis at Copper Hill, in the southern part of Shantumbu.

Circulating basinal fluids were channelled through the more permeable horizons and along structural pathways, such as that noted at the Konkola Deposit, which concentrated the copper in a particular lithology/ies and stratigraphic level/s. Fluctuations in the amount of fluids migrating through the permeable lithologies may account, amongst other reasons, for the erratic base metal sulphide mineralisation noted at Shantumbu and at various Zambian Copperbelt occurrences.

Further structural investigation is required to determine whether the rift basin at Shantumbu is fault-bounded along the entire length of the basin margin, as in Figure 8-1A. Sediment-hosted, stratiform copper occurrences have a greater chance of developing in these basins where the circulation of metal-bearing basinal brines were confined to the basin sediments due to the fault-bounded nature of the basin margin, rather than in basins which which are not bounded on all margins by faults, as illustrated in Figure 8-1B.

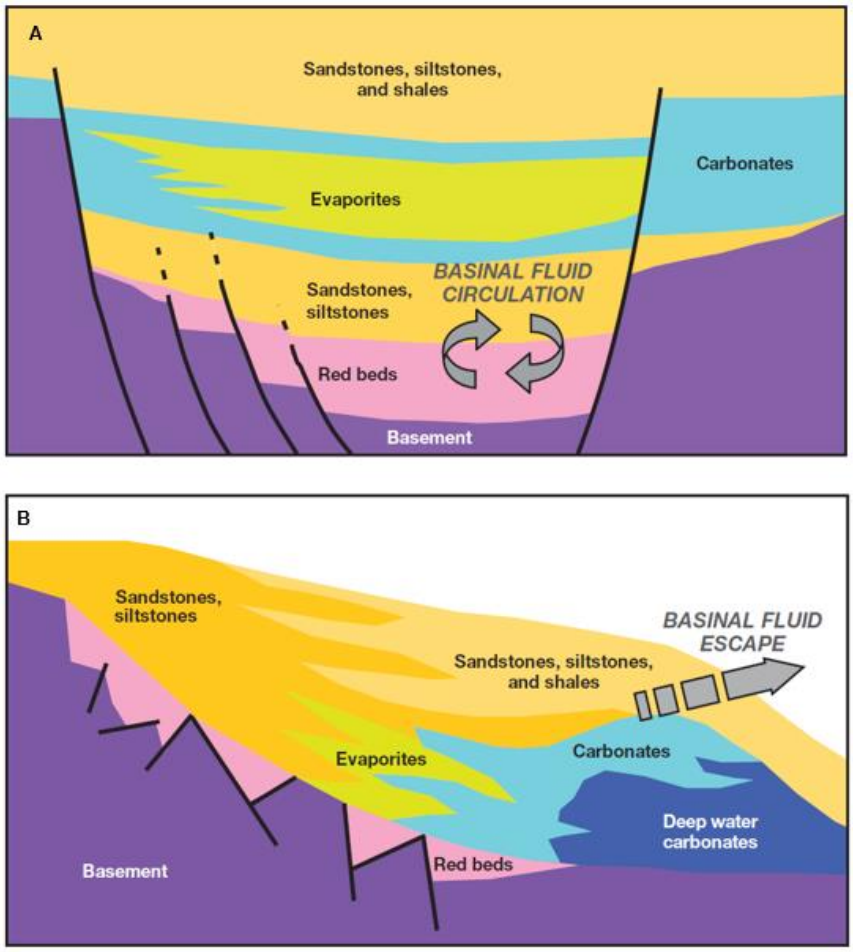

Figure 8-1. Schematic cross sections of sedimentary basins, placing the Shantumbu Basin in context of the two types of basins reported by Hitzman *et al*. (2010). (A). Cross section of an intracratonic rift basin with a basal red-bed sequence and overlying siliciclastic, carbonate, and evaporite sediments. Basinal fluids in this system are trapped by confining basement and lateral sediment pinch-outs. (B). Cross section of a passive margin basin with a thin rift sequence overlain by continental siliciclastic sediments (sandstones and siltstones) that grade seaward into evaporates and then carbonates. The carbonate sediments prograde seaward and overlap deeper water carbonates. This carbonate-rich sequence is covered by deltaic to slope basin siliciclastic sediments (sandstones, siltstones, and shales). Basinal fluids in this system are able to escape from the sedimentary sequence vertically and laterally, the rift-basin at Shantumbu may be an example of this type, although further structural work would be required to verify. (Source: Hitzman *et al*., 2010, p633).

The copper mineralisation at Shantumbu is erratic and low-grade which is the result of several reasons/processes, including a low-grade hinterland, a thin stratigraphic succession above the Basement but below the marine units, and the high-grade prograde and low-grade retrograde metamorphism. Alternatively, the metal-bearing basinal brines may have escaped from the rift-basin due to the absence of block-faulted basement highs and lateral pinch-outs of the host lithologies, as illustrated in Figure 8-1B (Hitzman *et al*., 2010).

8.2.3 Magmatism

In the Lusaka-Kafue-Shantumbu Region, various within-plate-type granitoid bodies, which intruded the metasediments, are known collectively as the Lusaka Granite (Johnson *et al*., 2007). The age of intrusion for the Lusaka Granite is specified at 846 ± 68 Ma (Barr *et al*., 1977), while various metaluminous, monzogranitic plutons in the Munali Hills area, south of the Mpande Dome, which intruded the metasediments were age dated at 820 ± 7 Ma (Johnson *et al*., 2007).

During the exploration of Shantumbu, no granitic intrusions were intersected in the drill core, although the presence of skarn metasomatism is a possibility. Extensive and pervasive sodalite was intersected in the drill core in the northern region of Shantumbu. The sodic alteration may be related to the presence of igneous bodies, or form part of the extensive sodic alteration characteristic of the upper members of the Kitwe Formation (Sequence 3 to 6) on Shantumbu.

8.3 SHANTUMBU LITHOSTRATIGRAPHY AND CORRELATION WITH THE ROAN GROUP

Petrographic inspection of the drill cores, together with mineralogy studies and geochemical analyses, presented new insight into the depositional environments related to the Proterozoic rifting, rift climax and cessation, and the related sulphide mineralisation at Shantumbu.

Seven metasedimentary sequences were identified at Shantumbu, and termed Sequences 1 to 7. The detrital metasediments of Sequence 1 form the basal unit of the rift basin succession, whilst Sequence 7 is the youngest / top most Sequence. The metasediments of Sequence 1 progress from arenites and siltstones above what is interpreted to be Kafue Rhyolite and Nazingwe metavolcanics, and the proportion of arenites diminished upwards giving way to an increased number of siltstone units. The siltstone-arenite succession is in turn was overlain by carbonate and siltstone units and capped by the marine carbonates of Sequence 7.

8.3.1 Lithostratigraphic Correlation with the Roan Group

The Roan Group siliciclastic and carbonate sedimentary rocks within the Zambian Copperbelt were deposited during rifting, subsequent marine transgression and rift climax and conclusion. The lowermost formation of the Roan Group, the Mindola Formation (Sequence 1 and 2), was deposited during rift initiation, whilst the overlying Kitwe (Sequences 3 to 6) and Kirilabombwe (Sequence 7) formations were deposited during rift-climax and conclusion. The Mindola Formation (Sequence 1) within the Zambian Copperbelt comprises supratidal to peritidal clastic

sequences, whereas the Kitwe Formation (Sequences 3 to 6) comprises platform carbonates, breccias (stratiform and discordant), and subordinate siliciclastic rocks, and the Kirilabombwe Formation (Sequence 7) consists of marine carbonate sediments (Table 4-2).

In the Zambian Copperbelt, the transition from the supratidal clastic rocks to the shallow water subtidal zone carbonate rocks is represented by the Copperbelt Orebody Member (Sequence 3 and 4), alternatively known as the Ore Shale Unit of the Kitwe Formation. The Copperbelt Orebody Member represents a transgressive sequence which separated the subaerial clastic lithologies from the marine lithologies of the Kitwe and Kirilabombwe formations (Hitzman *et al.,* 2012). The Copperbelt Orebody Member is commonly the host of the copper mineralisation at several occurrences and deposits within the Zambian Copperbelt. The Copperbelt Orebody Member has a negative $\delta^{13}C$ isotopic value of -10 to -16 $\delta^{13}C$ ‰ (Theron, 2013).

The basal rhyolites below the Mindola Formation were not intersected during the drilling campaign on Shantumbu but are proposed to underlie the siliciclastic succession of Sequences 1 and 2. These two sequences were deposited in an alluvial fan environment, during a period dominated by extensional rift tectonics on Shantumbu. The mineralogy of these terrestrial sediments is dominated by feldspar, quartz, hematite, goethite, sericite/muscovite and dolomite/calcite. Potassic alteration is characteristic of both Sequence 1 and 2. The K_2O values for Sequences 1 and 2 are elevated confirming the alkali provenance of the sediments.

Sequence 1 consists of iron-rich arenites at the base with an increasing number of interspersed siltstone layers towards the top of the sequence and was deposited in a medium-energy, sub-aerial to shallow fluviatile - alluvial fan environment. The Basal Sandstone Member of the Mindola Formation, in the Zambian Copperbelt consists of the same succession of arenites, siltstones and subordinate carbonate layers, and was also deposited in a sub-aerial to shallow fluviatile environment. Within the Roan Group in the Zambian Copperbelt, the conglomerates characteristic of the base of the Mindola Formation were not identified at Shantumbu, due to the limited drilling depth undertaken. The base of Sequence 1 was not penetrated during the drilling campaign.

Within the Zambian Copperbelt, the Basal Sandstone Member was deposited in a fluvial, alluvial fan, aeolian and fan-delta environments of limited strike extent (Selley *et al*., 2005), which often pinched out against the Basement lithologies (Croaker, 2011). Episodic low- and high-energy conditions characterised the sedimentation of this member. The arkose varies between grey, pink and white (Croaker, 2011) and from arkosic to subarkosic. Sequence 1 is interpreted as the

equivalent of the upper portions of the Basal Sandstone Member, Mindola Formation of the Roan Group in the Zambian Copperbelt (Table 4-2 above).

Sequence 2 (Kafue Arenite Member, Mindola Formation) at Shantumbu is a thick, massive to finely laminated dark grey arenite succession with subordinate siltstone layers and overlain by mottled pink and grey arenite alternating with pink arenite. Sequence 2 was deposited within a prograding alluvial fan environment which experienced rapid sediment input of medium- to coarse-grained arkosic sediments. The siltstone layers, subordinate in number to the arenites, were deposited from suspension fallout following the high-energy events.

The high-energy events are interpreted as debris flows which were deposited in a floodplain or fan apron within the peritidal to supratidal zone of the rift basin. The contact with the overlying Sequence 3 is sharp, and the lithologies above and below the contact characterised by extensive goethite alteration.

The Kafue Arenite Member is the upper unit of the Mindola Formation of the Roan Group and consists of pink to grey medium-grained feldspathic and micaceous arenites below the marine transgression lithologies of the Copperbelt Orebody Member. The Kafue Arenite Member was deposited during rift initiation within an alluvial fan environment dominated by debris flows and lesser channel flow. The pink to grey arkosic mass flow units and subordinate siltstone beds of Sequence 2 are comparable to the Kafue Arenite Member in the Zambian Copperbelt.

Copper mineralisation is erratically developed in the Mindola Formation of the Zambian Copperbelt and is for the most part hosted by the arkose units, which are capped by siltstone, as in Sequence 1 at Shantumbu.

Rift climax resulted in a marine transgression event and the accumulation of the carbonate and calc-silicate successions of Sequences 3 and 4. These two Sequences have several characteristics similar to those of the Copperbelt Orebody Member, of the Kitwe Formation in the Zambian Copperbelt. Sequence 3 consists of a carbonate and a siltstone unit, where the siltstone has variable carbonaceous content, alternating between a black and grey colouration. Sequence 3 signified the onset of sub-aqueous conditions and a gradual deepening of the basin. Sequence 4 started with a calcareous arkose overlain by alternating calc-silicates and dolomitic carbonates.

Sequence 3 was deposited in a nearshore or shallow water environment with restricted input of clastic sediments. Sequence 4 was deposited as a laterally extensive calc-silicate sequence reflecting the continuation of detrital sediment supply to the nearshore or shallow water

environment. The thick expanse of siliciclastic units interlayered with carbonate-dominated units and siltstone layers from suspension fallout, indicate that periodic uplift and subsidence characterised the mode of deposition on Shantumbu.

The Copperbelt Orebody Member in the Zambian Copperbelt was deposited in a low energy, shallow marine-peritidal depositional environment subjected to periodic dry and wet cycles. At the Nkana-Mindola Deposit in the Zambian Copperbelt, four facies types occur. The four facies include the Northern facies composed of dolomitic argillite, argillite, fine-grained sandstone and an upper carbonaceous argillite; the Southern facies is composed of black carbonaceous shale, argillite and an upper carbonaceous argillite; the sandstone-argillite facies consists of a dolomitic carbonaceous argillite and a massive dolomite facies consists of a carbonaceous argillite (Croaker, 2011).

The chemical sediments of Sequence 3 correlate with the start of the Copperbelt Orebody Member of the Roan Group in the Zambian Copperbelt, whilst the dolomitic carbonate breccia of Sequence 4 is analogous to the dolomitic facies of the Copperbelt Orebody Member, as noted at the Nkana-Mindola, Chambishi SE and Mwanbashi B deposits, where the dolomite facies is interpreted to represent a restricted subtidal environment and isolated stromatolitic biotherm structures (Croaker, 2011). The elevated MgO noted in Sequence 4 confirmed the Sequence was the first occurrence of dolomitic carbonate and related to a major flood event.

The copper mineralisation in the DRC Copperbelt is hosted by the high-energy conglomeratic arkoses of the Mutonda Formation and within the low-energy sediments of the overlying Musoshi Formation, the Copperbelt Orebody Member and Sequences 3 and 4 equivalents (Lefebvre, 1986). The Lower Roan Rift basin stratigraphy in the DRC Copperbelt sediments were deposited in large fan-delta environments, which graded both vertically and laterally into lacustrine silts and dolomites (Lefebvre, 1986).

The MnO content of Sequences 3 and 4 equivalent to the start of the Kitwe Formation, corroborates that deposition occurred within a nearshore environment, whilst the MnO contents of Sequences 1 and 2 indicated deposition occurred within an alluvial fan environment. A characteristic of sediment-hosted, stratiform copper deposits is the elevated Mg values adjacent to the copper-bearing horizons, such as the association of Mg with the copper mineralisation in the Congolese Copperbelt (Hayes *et al*., 2015).

Sequence 5 was deposited in a subtidal to tidal flat environment which underwent periodic subaerial exposure. The package of gritty to pure carbonates of facies 5a, the carbonate and

siltstone of facies 5 and carbonate-siltstone rhythmites of facies 5c, denoted the progression to a shallow subtidal to tidal flat environment, with cycles of subaerial exposure related to periodic uplift. The succession of alternating detrital and carbonate layers of facies 5c, was deposited in a distal to turbidity current-dominated platform environment. The elevated Sr values, and CaO and Fe_2O_3 contents of Sequence 5 at Shantumbu, support a fan-delta and nearshore depositional setting. The subtidal to platform sediments of Sequence 5 were succeeded by the deposition of shallow/marginal restricted marine sediments of Sequence 6.

The Pelito-Arkosic Member within the Zambian Copperbelt consists of quartzites interbedded with siltstones and silicified dolomites, as well as dolomite and laminated to thinly bedded argillite and dolomitic argillite (Croaker, 2011). The Chambishi Member consists of a thick unit of dolomite and argillite which is overlain by thinly bedded siltstone-mudstone and sandstone units (Croaker, 2011).

Sequences 5 on Shantumbu correlates with the Pelito-Arkosic Member of the Kitwe Formation in the Zambian Copperbelt. The basal gritty carbonate of facies 5a which is overlain by siltstone lenses, correlates with the basal facies of the Chambishi Member of the Kitwe Formation. The Chambishi Member at the Nkana-Mindola Deposit in northern Zambia consists of a basal laminated dolomite and argillite which is overlain by a thicker succession of carbonate layers, subordinate argillite and sandstone.

The gritty carbonate and siltstone layers at Shantumbu are considered to be the equivalent of the Chambishi Member contact with the underlying Pelito-Arkosic Member in the Zambian Copperbelt. The alternating siltstone-arkose-carbonate layers of facies 5b is considered to be the equivalent of the siltstone, arkose and carbonate succession of the Pelito-Arkosic Member of the Roan Group.

Many of the siltstones of facies 5b were brecciated by the dissolution of the evaporite content and the subsequent collapse of the siltstone, during the migration of basinal fluids. The distinguishing feature of the Pelito-Arkosic Member of the Roan Group was the presence of evaporites. The Member is split into two facies, the lower Rokana Evaporite facies and the overlying Nchanga Quartzite facies (Croaker, 2011). The stratabound monolithic and lesser polymictic breccias within the Roan Group in the Zambian Copperbelt are frequent and attributed to strata with an originally evaporitic content (Bull *et al*., 2011).

Both the breccias at Shantumbu and within the Kitwe Formation in the Zambian Copperbelt, are related to post-lithification chemical changes. In the carbonate-hosted Omar Copper deposits in

Alaska, Folger (1986) noted the cross-cutting texture of the veins and the angular fragments of the carbonate breccia indicated the brecciation was post-lithification. The brecciated facies 5b correlates with the Rokana Evaporite facies within the Zambian Copperbelt.

The highest Mn values of the Sequences was noted in Sequence 5 which related to the fluctuating oxic and anoxic conditions during deposition. The V/Cr ratio for Sequence 5 is above 2 which implies anoxic conditions at the time of deposition. The V/Cr ratios for the Mpande and the Munali Hills granites, to the south of Shantumbu, have comparable V/Cr ratios to the Mindola and Kitwe formation lithologies on Shantumbu.

There is an abrupt change from the carbonate-siltstone rhythmite stratigraphy of Sequence 5 to the alternating arenite-carbonate-siltstone succession of Sequence 6. The sediments of Sequence 6 were deposited below the storm-wave base or within an inner shelf lagoon to tidal flat environment, which experienced minor sea-level fluctuations. The lithological contacts within Sequence 6 were erosional, which suggests fluctuating energy levels occurred during deposition. The arkosic units were deposited by the periodic influx of siliciclastic material related to storm and wind activity.

The base metal sulphide content of the siltstone units of Sequences 5 and 6 is less than the sulphides present within the arenite-dominated units of Sequence 5 and 6. This characteristic of Sequence 5 and 6 is related to the permeability of the arkoses in comparison to that of the siltstones, and from the fluctuation from oxidised to reduced conditions during deposition of the siltstones.

Sequence 6, a succession dominated by calc-silicates and lesser carbonates, is interpreted as an equivalent of the Antelope Member of the Kitwe Formation in the Zambian Copperbelt. The Antelope (Clastic) Member consists of interbedded shales, argillite and fine-grained sandstone and reflects an abrupt transformation from carbonate-dominated stratigraphy to the increased deposition of calc-silicate layers (Croaker, 2011; Woodhead, 2013). In the Zambian Copperbelt, the Pelito-Arkosic Member is succeeded by the Chambishi Member, which is overlain by the Antelope Member.

The thick succession of grey to blue, finely laminated calcitic carbonate of Sequence 7 lacks the rhythmic banding of the underlying Sequence 6. The infrequent calc-silicate layers and a thick succession of monotonous carbonate indicated an open marine environment with limited input of terrestrial sediments during subsidence of the rift basin which existed at the time Sequence 7 was deposited.

The noncyclical succession of monolithic carbonates and subordinate calc-silicates sediments of Sequence 7 correlate with the Bancroft Member of the Roan Group. Croaker (2011) described the Bancroft Member of the Roan Group as consisting of grey arenaceous dolomite, light-grey massive dolomite, grey slightly carbonaceous dolomite, dark carbonaceous dolomite and grey to pink argillaceous dolomite.

Croaker (2011) noted the marine carbonate succession in the Zambian Copperbelt is dominated by dolomite, whereas the mineralogy of Sequence 7 is mainly that of calcite. The dominance of calcite over dolomite is attributed to the high degree of deformation and alteration that occurred at Shantumbu area in comparison to that experienced in the Zambian Copperbelt.

In summary, the Kafue Rhyolite and Nazingwe formations, and Sequences 1 and 2 represented the initiation and early stages respectively of rift basin development. The incursion of the marine units, Sequences 3 and 4, were related to rift climax, whilst the dominance of carbonates and lesser siliciclastic and siltstone units were related to deposition during rift cessation and basin subsidence. The progression to rift climax is represented by the metasediments of Sequences 5 and 6, and rift cessation is represented by Sequence 7. Each stage of the rift basin evolution was characterised by the evolution of the depositional environments from sub-aerial to sub-aqueous. The depositional environments during the Proterozoic rifting at Shantumbu are summarised in Table 4-2 and the correlation of the Sequences 1 to 7 with the Mindola and Kitwe formations within the Zambian Copperbelt is summarised in Table 4-1.

The geochemical characteristics and element ratios of the Sequence 1 to 7 lithologies indicated that multiple fluctuations between oxic and anoxic conditions occurred. The V/Cr ratio confirmed alternating oxic and anoxic conditions prevailed in Sequence 5, that is during deposition of the Pelito-Arkosic and Chambishi members, whilst the V/Cr ratio for Sequence 7 (Bancroft Member) confirmed the predominance of anoxic bottom water conditions. Sequences 1 and 2 represent deposition during oxic conditions.

Table 8-1. Depositional environments on Shantumbu during the development of the Neoproterozoic rift basin.

Sequence	Depositional Environment
7 (Youngest)	Carbonate platform or shelf characterised by gradual subsidence and stability – anoxic; marine platform / shelf.
6	Shallow/marginal restricted marine setting with influx of siliciclastic material - oxic-anoxic; inner shelf lagoon.
5	Progression to fan-delta – Sequence 5 represented shallow subtidal through to tidal flat environments with cycles of subaerial exposure during falling sea level. Primary precipitation of carbonate with subordinate input of detrital material from up-platform areas – sub-aqueous/marine conditions – Sequence 5. Platform to basin transition; carbonate-pelite rhythmite - Sequence 5 – anoxic; Sub-tidal to tidal flat.
4	Emergence to shallow water conditions – first siliciclastic unit – oxic-anoxic Deepening of water conditions – calcareous dolomitic arkose - anoxic Emergence to shallow water environment and hiatus – second, third and so on siliciclastic layer of Sequence 4 - oxic-anoxic.
3	Increased subsidence and marine transgression. Nearshore or shallow water environment with restricted input of clastic sediments; subtidal.
2	Prograding alluvial fan and debris flows; peritidal to subtidal.
1 (Oldest)	Alluvial fan - sub-aerial to shallow fluviatile environment.
Metavolcanics	Rifting represented by the rhyolites south of Mpande Dome.

The lithostratigraphy of the Shantumbu Rift basin supports the interpretation that the metasediments are the equivalent of the Roan Group Rift basin sediments within the Zambian Copperbelt (Figure 8-2). The correlation of the Shantumbu stratigraphy with that of the Roan Group in the Zambian Copperbelt therefore extends the boundary of the Roan Group south of the Mwembeshi Zone and Lusaka, as illustrated in Figure 8-3.

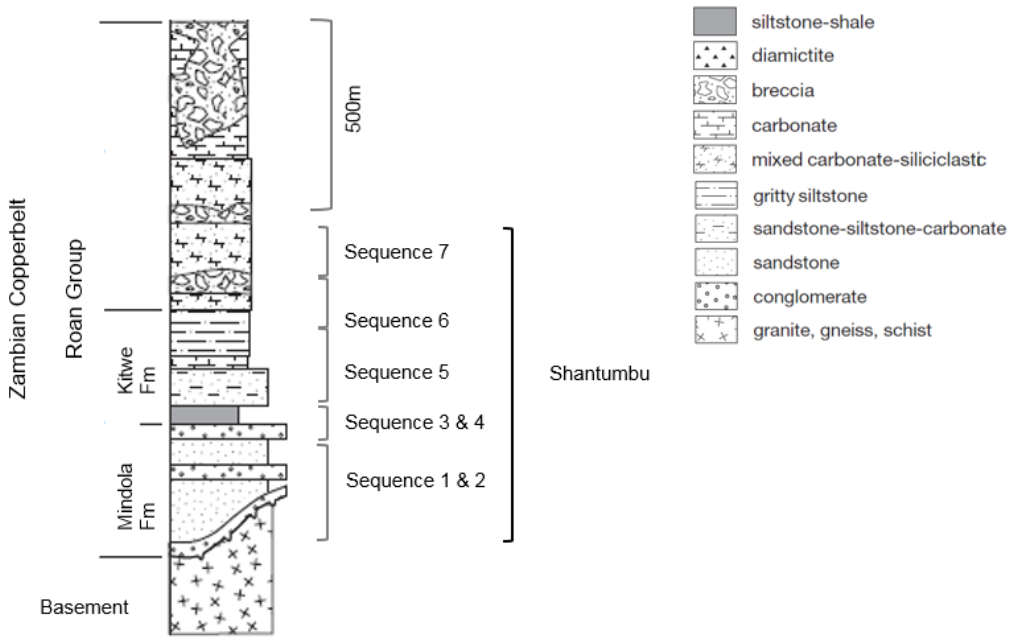

Figure 8-2. Lithostratigraphic column for the Roan Group in the Zambian Copperbelt with the authors interpretation of the position of Sequences 1 to 7 at Shantumbu (modified from, Selley *et al*., 2005).

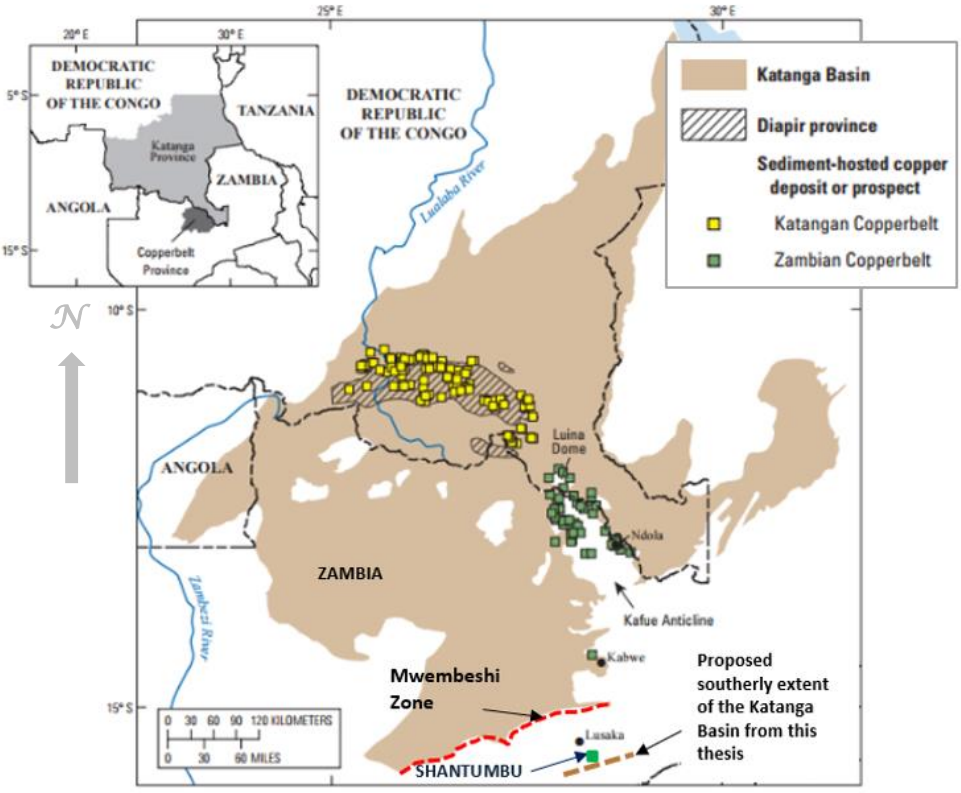

Figure 8-3. The location of the Katanga Basin, Mwembeshi Zone, Zambian and the Congolese Copperbelts, with the proposed southerly extent of the Katanga Supergroup to Shantumbu, from this study (Source: Zientek *et al*., 2014).

The stratigraphy of the rift-basin at Shantumbu has many similarities with other rift-basin which formed during the breakup of Rodinia, such as the rift stratigraphy along the northern margin of the Kalahari Craton where several Late Proterozoic continental rift basins occur along the 2,500km length of the Kalahari Craton margin, for example the Damara and Kaoka belts. These continental red bed sediments are underlain by volcanic rocks and overlain by clastic sediments, which are capped by carbonates. The carbonates were deposited within a shallow marine environment. The arenite to carbonate succession of rift-basin lithologies were subjected to lower greenschist facies metamorphism and underwent deformation during the Damaran event (Borg and Maiden, 1986).

8.3.2 Metamorphism

Epidote-amphibolite facies prograde metamorphism and subsequent retrograde greenschist facies metamorphism was identified at Shantumbu during this study. The identification of amphibole, glaucophane, biotite, orthopyroxene, clinopyroxene, plagioclase, epidote and titanite/grossular indicated the stratigraphy was initially subjected to medium and high pressure-temperature metamorphism.

Evidence for the retrograde greenschist facies metamorphism includes the grain bulging noted for quartz and plagioclase and the undulose extinction observed by quartz grains (Cao *et al.*, 2013).

A notable difference between Shantumbu and the Zambian Copperbelt is the prograde epidote-amphibolite facies metamorphism which occurred on Shantumbu, in contrast to the greenschist facies metamorphism which occurred to the north of the Mwembeshi Zone. The Domes Region to the west of the Zambian Copperbelt in comparison underwent amphibolite-grade metamorphism.

Retrograde metamorphism from amphibolite facies to greenschist facies suggested that late-stage fluid movement occurred in the Shantumbu Basin and the effect thereof on the copper mineralisation at Shantumbu is considered to have been significant.

The comparison of the grade of metamorphism and the grade of the sediment-hosted, stratiform copper deposits globally shows that the calibre of the mineralisation does not appear to be directly associated with the grade of metamorphism undergone (Zientek *et al.*, 2014, and references therein). Examples of this association include the Aynak Deposit in Afghanistan, which hosts stratabound disseminated bornite and chalcopyrite within the Neoproterozoic to

Early Cambrian amphibolite-grade rocks, the Oamites Deposit in Namibia, where the copper mineralisation is hosted by upper greenschist to probably lower amphibolite grade metamorphosed rocks, the Zambian Copperbelt mineralisation, which is hosted by rocks which underwent greenschist facies metamorphism (Hayes *et al*., 2015), and the Paleoproterozoic Mangula Cu-Ag-Au Deposit, in Zimbabwe which underwent four deformations and two metamorphic events, which result in partial remobilisation and reprecipitation of the sulphides (Treloar, 1988; Hitzman *et al*., 2010).

The Mangula Sediment-hosted, stratiform copper deposit is located adjacent to a fault-bounded granitic Basement high, within the alluvial and braided stream sediments of the Paleoproterozoic Deweras Group (Maiden and Master, 1986) of the Magondi Mobile Belt. The Mangula sediments were deposited c. 2.1 Ga to 2.2 Ga and metamorphosed between c. 2.0 Ga and 1.8 Ga (Master, 1996). Relict textures indicate the copper sulphides were initially disseminated throughout the clastic sediments and were remobilised into veins during deformation at Mangula. The deformation resulted in brecciation of the arkoses, dykes and granites. Subsequent deformation under greenschist facies metamorphism, deformed these early mineralised quartz-K-feldspar-carbonate vein structures and shearing. Boudinaging and fracturing of the earlier veins occurred and was accompanied by pressure-related redistribution of the copper sulphides (Maiden and Master, 1986). At the Mesoproterozoic Spar Lake post-metamorphic veinlets have the same mineralogy as the host rocks (Hitzman *et al*., 2010), akin to veinlets which have sulphides and host-rock mineralogy at Shantumbu.

The description of the Mangula Deposit introduced an important characteristic of sediment-hosted, stratiform copper deposits, in that this type of deposit is formed by multiple remobilisation and reprecipitation of the base metals events during the tectonic history of the basin. The genetic model for sediment-hosted, stratiform copper deposits is the precipitation of base metals during deposition and the remobilisation and reprecipitation thereof during the circulation of basinal brines related to both diagenetic processes and temperature and pressure pumping during deformation. The high-grade metamorphism and deformation that occurred in the Shantumbu area is in part, one of the reasons for the erratic and low-grade copper mineralisation. The circulating basinal fluids are considered to have transported the copper either upward into the overlying marine carbonate units or out of the Shantumbu metasediments during the high-grade metamorphism and retrograde metamorphism.

Schrijver *et al*. (1986) recognised that within cupriferous carbonate rocks hosting copper mineralisation of the sediment-hosted copper deposit type, that reconcentration of sulphides

within dolospar-quartz veins occurred during low grade metamorphism. “During a late, post metamorphic event, sulphides were leached from ‘in-situ mineralisation’ and veins, and replaced by iron hydroxides and hydroxides, while the dolospar cement recrystallised.”

8.3.3 Alteration

The sediments at Shantumbu were subjected to both syngenetic and post-diagenetic alteration events. Many of the original mineralogical textures and associations did not survive the protracted alteration events and the high-grade metamorphism. The alteration sequence at Shantumbu began with the dissolution of the evaporites and the migration of the oxidised brines, which was followed by dolomitisation, potassic and sodic alteration, biotisation, saussuritisation and silicification.

A common alteration characteristic of the copper-bearing strata in the Zambian Copperbelt is the predominance of sodic alteration in the lithologies above the marine transgression surface, the Copperbelt Orebody Member, and the extensive potassic alteration in the stratigraphy below the marine transgression surface. The potassic and sodic alterations occurred during diagenesis-compaction, the dewatering of the terrestrial sediments, and the remobilisation of potassic and sodium-bearing fluids. The sequences above the Copperbelt Orebody Member on Shantumbu are dominated by sodic alteration minerals, including sodalite, plagioclase feldspar, sodic amphiboles such as glaucophane and scapolite. Scapolite is characteristic of the alteration of evaporite minerals in highly altered environments. The sediments below the Copperbelt Orebody Member on Shantumbu were noted to have undergone potassic alteration, whilst the sequences above the Copperbelt Orebody Member had undergone predominantly sodic alteration.

Sodalite ($Na_8(Al_6Si_6O_{24})Cl_2$), which extensively developed in the brecciated feldspathic arenite of Sequence 6 represented a high-temperature reaction between the calc-silicate and the carbonate components of Sequence 6. Sodalite, a feldspathoid, is the product of contact metamorphism of limestone and indicative of intense and localised carbonate alteration. Columbite, a niobium-bearing mineral with the chemical formula of ($(Fe,Mn)Nb_2O_6$), was observed in the calc-silicates of Sequence 6 and indicated the sediments underwent metasomatic alteration.

In comparison, saussuritisation of plagioclase to epidote indicated that Sequence 6 was also subjected to a second alteration stage of lower temperature to that which formed the sodalite.

Epidote resulted from the reaction between the silicate and carbonate components of the rock during low temperature alteration.

Cluzel and Guilloux (1986) noted three stages of mineral formation in many of the copper occurrences in the DRC Copperbelt. Firstly, an aluminous stage represented by chlorite + clinochlore + phengite + kyanite + dolomite + quartz. Secondly, a magnesian stage represented by clinochlore + phlogopite + magnesite (+ quartz). Lastly, a potassic stage occurred, represented by microcline + phengite + quartz. Cluzel and Guilloux (1986) noted that the potassic minerals formed after the early albite and paragonite-bearing minerals. The alteration resulted from regional hydrothermal alteration with temperatures in the range of 300 to 350°C and pressures in the range of 1 to 2kbar. Eugster (1986) noted that the temperatures present during circulation of the hydrothermal fluids was a function of the depth of circulation.

Copper mineralisation is more abundant, albeit low-grade, within the detrital metasediments of Sequences 1 and 2, as is the potassic alteration, than in the metasediments of Sequences 5 to 7, which underwent sodic alteration. An inference is drawn between the copper mineralisation and potassic alteration on Shantumbu however, insufficient data is available to test this proposal. The copper-bearing detrital units at the Konkola Deposit in the northern part of the Zambian Copperbelt (Zientek *et al*., 2014) has elevated potassic concentrations, as too do the copper deposits at Spar in the USA.

The metal-bearing basinal brines at Shantumbu originated from the compaction of the sedimentary column, chemical gradients caused by the alternating arid and marine periods, and tectonic activity. The brines mobilised the base metals and led to the potassic, sodic, dolomitic and carbonatisation alteration of the sediments. The dissolution of the evaporite minerals and the sulphate content of the basinal brines were critical for the precipitation of sulphides during bacterial sulphate reduction within the anoxic environments on Shantumbu. The progressive loading of the lithologies may have increased the pressure and temperature conditions to the extent that thermal bacterial sulphate reduction may have occurred, although this has not been determined on Shantumbu. Intrusion of igneous bodies may have contributed to the temperature regime, although no intrusive rocks were noted during the exploration activities at Shantumbu.

The extensive alteration within the goethite-bearing arenites and dolomitic carbonate lithologies of Sequences 3 and 4, the Copperbelt Orebody Member, formed due to the inflow of oxidising basinal fluids into this permeable layer, which may have resulted in the remobilisation

of the base metals from this succession, as Sequences 3 and 4 contain hardly any copper mineralisation. Sediments which were deposited under reducing conditions underwent diagenetic hematisation suggested by the transgressive contact of red-stained sediments over sulphide-bearing deposits (Oszczepalski, 1986).

Sequences 3 and 4 have a negligible amount of copper sulphides, which raises the question whether the arenites originally hosted base metal sulphides, or otherwise. Native copper was identified during the mineralogical examination of Sequence 4 and is interpreted as evidence that copper sulphides were part of the mineralogical composition of the protolith arenites, or the arenites were favourable for the migration of copper-bearing fluids and formation of sulphides, which were remobilised at a later stage. Copper present in the basinal brines may have also been deposited as a native metal and not as a sulphide due to the possibility that the sediments had low levels of sulphate and organic matter content.

In the Mangula Cu-Ag-Au Deposit of the Lower Proterozoic Deweras Group, in Zimbabwe, pervasive hematite alteration as well as the occurrence of magnetite, silica, K-feldspar, carbonate and tourmaline rich zones, are related to the secondary development of veins which host the metal sulphides (Maiden and Master, 1986). Three sets of veins cross-cut the lithological sequences on Shantumbu and all three vein sets have the same mineralogy as the host strata. The pyrite content of the veins has been altered to hematite to varying extents at Shantumbu.

Alteration of the sediments during early diagenesis released the metals, and Walker (1986) reported that alteration may continue for many tens of millions of years with the following alteration sequence: (1) dissolution of silicates; (2) replacement of silicates by smectite; (3) leaching of biotite; and (4) conversion of magnetite to hematite. Diagenetic alteration includes: (1) conversion of amorphous and poorly crystallised ferric oxides to well-crystallised hematite; (2) conversion of smectite to illite; (3) replacement of feldspar and other silicates by carbonates; (4) albitisation of clays and feldspar; and (5) dissolution of earlier-formed ferric oxides (bleaching) (Walker, 1986).

8.4 SHANTUMBU COPPER MINERALISATION IN THE CONTEXT OF SEDIMENT-HOSTED, STRATIFORM COPPER DEPOSITS

The oxidising conditions necessary for the development of sediment-hosted, stratiform copper mineralisation have restricted the earliest occurrence of these deposits to intracontinental rift

basins after the Earth's atmosphere was oxygenated, which occurred in the Paleoproterozoic, circa 2.45 - 2.32 Ga (Brown, 1997, and reference therein; Hitzman *et al*., 2010; Zientek *et al*., 2014 and references therein). Sediment-hosted, stratiform copper deposits therefore can range in age from the Proterozoic to the Triassic (LaPoint, 1986).

The genetic model for this type of deposit requires the addition of copper and other base metals to the host rocks after sedimentation, and the early syndiagenetic accumulation of sulphate and sulphides, such as anhydrite and pyrite. The copper and base metal mineralisation were later remobilised and reprecipitated by the actions of the circulating basinal fluids (Brown, 1986). Sediment-hosted, stratabound copper deposits have two overriding controls, the thickness of the underlying red beds and the calibre of the basement or underlying volcanic successions in terms of copper content.

The Proterozoic Zambian Copperbelt, the White Pine District in Michigan (Proterozoic), Spar Lake in Montana (Proterozoic), and the Permian-Triassic Kupferschiefer of the Zechstein Basin in Poland and Germany, are the archetypal examples of sediment-hosted, stratiform copper deposits, where the copper mineralisation overprinted the sedimentary rocks during diagenesis, tectonism and metamorphism (Brown, 1997; Brown, 2014). Maiden *et al*. (1986) noted that the "unfolding" of the deformed sedimentary sequences of the Upper Proterozoic Klein Aub – Lake Ngami province of Namibia and Botswana, and the Lower Proterozoic Lomagundi Basin in Zimbabwe, showed that the copper occurrences are hosted in paleotopographic depressions bounded by the basement highs and related faults. Maiden *et al*. (1986) proposed that by undertaking a similar "unfolding" of the Zambian Copperbelt and the Zechstein Basin, that a similar depositional environment setting would be recorded.

The conditions and processes necessary for the formation of sediment-hosted, stratiform copper deposits were summarised by Hayes *et al*. (2015) as: (a) source rocks containing copper, such as red beds and/or igneous rocks such as flood basalt; (b) dissolution of the copper by sedimentary brine, which were typically more than 100°C; (c) migration of the metal-bearing brine; (d) non-oxidised, pyrite-bearing host rocks through which the brine migrated; (e) impermeable rocks which acted as a trap restricting the movement of the brine; and (f) physical and chemical reductants to precipitate the copper out of solution.

The copper mineralisation on Shantumbu postdates the deposition of the host detrital and carbonate sedimentary units, precipitated by the replacement of diagenetic pyrite, primarily as chalcopyrite, chalcocite and to a lesser extent bornite and digenite. At the Kupferschiefer

Deposit, the disseminated pyrite was replaced by chalcopyrite, chalcocite, bornite and hematite which were hosted by light grey to white sandstones, dark grey to black shale and mudstone, carbonates and veins that cross-cut these lithologies (Hayes *et al*., 2015).

Based primarily on the high-grade metamorphism at Shantumbu, the retrograde greenschist metamorphism, extensive alteration and the presence of extensive late phase iron oxides, multiple fluids migrated through the sediments. Both the Zambian Copperbelt and Kupferschiefer deposits experienced multiple episodes of fluid migration (Hitzman *et al*., 2010).

Shantumbu and the Zambian Copperbelt are two of many sediment-hosted, stratiform copper deposits located in proximity to a marine transgression surface. Although the copper mineralisation is most commonly associated with arenites capped by siltstone at and below the Copperbelt Orebody Member at Shantumbu, erratic copper mineralisation was intersected in the overlying marine lithologies akin to the copper occurrences along the northern margin of the Kalahari Craton in Namibia and Botswana. The copper occurrences along the northern margin of the Kalahari Craton in Namibia and Botswana are hosted by siltstone, sandstone, and the limestone sediments (Borg and Maiden, 1986). Most copper deposits in the Zambian Copperbelt are located within 200 metres of a marine transgression event, either within or adjacent to the Copperbelt Orebody Member (Hitzman *et al*., 2012).

The copper occurrences along the northern margin of the Kalahari Craton host stratabound chalcocite, bornite and chalcopyrite mineralisation, though the mineralisation is not limited to a specific unit or horizon. Copper mineralisation occurs in association with pyrite (Borg and Maiden, 1986) where the copper precipitated as early- to late-diagenetic sulphides from metal-bearing fluid which leached metals from the volcanic succession and precipitated the metals in the overlying permeable clastic units (Borg and Maiden, 1986).

As with the copper mineralisation at Shantumbu and in the Zambian Copperbelt, the copper mineralisation at White Pine, Kupferschiefer and within the upper Grinnell and lower Siyeh formations of the Purcell Supergroup, in Alberta and British Columbia, are located at the transition between terrestrial (oxidised) sediments and marine/lacustrine (reduced) sediments (Binda *et al*., 1986; Hooeve and Quirt, 1986). Conversely, though at White Pine, multiple transgression surfaces are evident before a completely reduced environment formed (Brown, 2014).

The copper deposits within the Roan Group in the Zambian Copperbelt have a considerable range in size and may be either persistent or erratically developed along strike. The larger

deposits are in general hosted within or adjacent to the Copperbelt Orebody Member. Sweeney and Binda (1986) reported the Ore Shale unit developed in a subtidal to intertidal setting, subjected to marine transgressions and regressions. Smaller deposits are typically located within the footwall arenites of the underlying Mindola Formation, whilst similar sized deposits occur in the immediate footwall to the Copperbelt Orebody Member (Annels, 1986).

As an analogy to Shantumbu, the low-grade calibre of the sediment-hosted, stratabound copper occurrences in the Cobalt Group in Ontario, is due to the lack of copper-rich material in the arenites even though the quantity of pyrite and reductants was greater than the quantity of copper sulphides (Chandler, 1986). Similarity is drawn with Shantumbu, specifically the low calibre of source copper resulted in the sporadic and low-grade copper intersections.

8.4.1 Bacterial Sulphate Reduction

Hoy *et al*. (1986) observed through sulphur isotope studies of red-bed stratiform copper deposits that low-temperature bacterial sulphate reduction resulted in the precipitation of sulphides within anoxic environments. The values obtained during sulphur isotope studies at Kamoto (DRC), Musoshi (Zambia) and White Pine (USA) were not fully supported by only low temperature sulphide reduction of sulphates. Hoy *et al*. (1986) proposed the secondary addition of reduced sulphur at Kamoto (DRC), Musoshi (Zambia) and White Pine (USA) may explain the sulphur isotope values obtained. The additional reduced sulphur was deemed to have resulted in sulphides being generated during abiogenic reduction of sulphate during introduction of copper-bearing fluid.

At Shantumbu, syngenetic pyrite was precipitated and preserved during the anoxic cycles of the alternating arid (oxic) and wet (anoxic) cycles. Bacterial sulphate reduction is considered responsible for the formation of the pyrite. Iron was scavenged by H_2S, which formed from bacterial sulphate reduction of the organic and calcareous content and precipitated disseminated iron sulphide (Machel, 2001) (Figure 8-4). The low amount of organic material inferred in Sequence 3 would have retarded bacterial sulphate reduction and copper mineralisation.

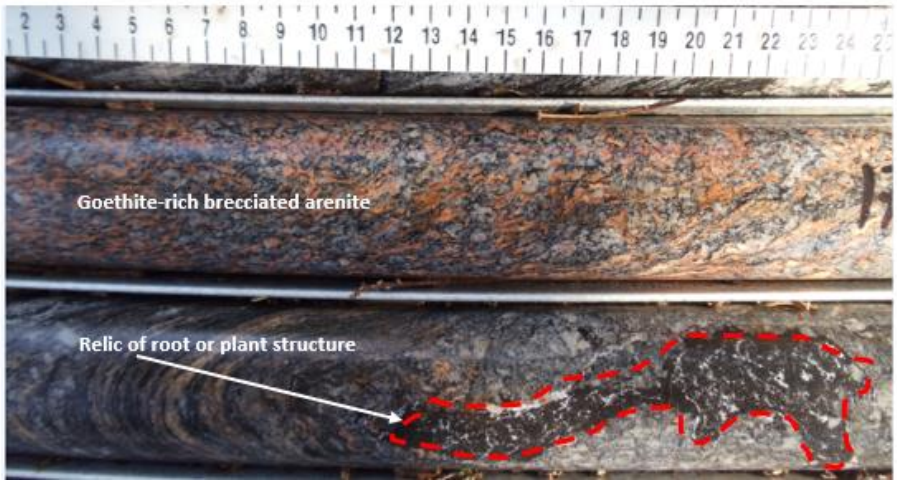

Figure 8-4. Remnant organic cast, possibly of a plant or root within brecciated arenite of Sequence 6, Shantumbu. Cast composed of biotite and aegirine. The overlying strata included fine siltstone laminations and brecciated arenite pervasively altered by goethite. The arenite consists of albite, plagioclase, amphibole, calcite, quartz and goethite. Drill core is from SPA015 at a depth of c. 177m.

The copper enrichment in the Mindola Formation (Sequences 1 and 2) on Shantumbu is largely restricted to the arenites bounded by siltstones. The correlation between copper and sulphur is low within Sequences 1 and 2 but increases in the overlying marine sequences, and this is considered as an indication that bacterial sulphate reduction precipitated pyrite within the anoxic marine sequences as the presence of H_2S and pyrite, causes copper and iron sulphides to precipitate (Rose, 1986).

Sverjensky (1986) advocated that evaporites within the context of sediment-hosted, stratiform copper deposits were a source of salinity and oxidised sulphur of the circulating basinal brines, which provided the high $f(O_2)$ required to transport copper in chloride complexes. The interaction of these oxidised basinal brines with organic matter and pyrite precipitated native copper followed by chalcocite, bornite, chalcopyrite, pyrite, sphalerite and galena (Sverjensky, 1986). At Shantumbu, dissolution of evaporitic units is deemed to have contributed to the salinity of the basinal brines. Cluzel and Guilloux (1986) related the copper mineralisation in sediment-hosted, stratiform copper deposits to intra- or extra-sedimentary metal and Cl-bearing enriched water, which leached the metals from the underlying volcanic units and precipitated the metal sulphides in the overlying permeable horizons within the sedimentary sequence. Hydrothermal fluids circulated during sedimentation and continued during compaction and tectonic activities.

In comparison to Shantumbu, LaPoint (1986) proposed the copper sulphides formed via pH neutral, bicarbonate-rich and low-saline fluid which caused the iron to be immobile and precipitated as iron hydroxides in the Permian and Triassic sandstone-hosted copper deposits in

New Mexico. Copper within the system was mobile within the fluids as copper-carbonate species ($CuCO_3^o$), which migrated to the nearby reducing sediments and precipitated as chalcocite. The fluids evolved into more saline basin fluids, which transported the copper as copper-chloride complexes.

8.4.2 Basement as a Source of Copper

Although the mechanisms responsible for the precipitation of the copper sulphides within the Zambian Copperbelt and at Shantumbu are moderately understood, the source of the copper is still implied at Shantumbu. The Basement to the Katanga Supergroup within the Central African Copperbelt is deemed the most probable source for the base metals which were subsequently concentrated within the Katanga Supergroup sediments forming the world-renowned sediment-hosted, stratiform copper deposits. Remobilisation and reprecipitation are largely accepted to have concentrated the copper sulphides within specific stratigraphic levels in the Central African Copperbelt.

At White Pine, in Michigan, the original source of the copper has been proposed by many authors as the hinterland basement and volcanic succession to the sedimentary basins. Seasor and Brown (1986 and references therein), noted copper entered the basin as complexes on clay minerals and as soluble species in basin waters.

On Shantumbu, the probable source for the base metals is the Mpande Basement rocks and the overlying volcanic strata. Johnson *et al*. (2007) recorded that chalcopyrite and bornite are randomly distributed in the Kafue Rhyolite Formation where copper sulphides accounted for 1 - 2% of the whole rock volume. Shantumbu is underlain by the Basement alkali granites and gneisses, and the metasediments on Shantumbu have the same mineralogical suite as the Basement. Examination of the geochemical characteristics of Cu, Ba, Zr, K, Na, V, Cr, Ti and Rb for the detrital Sequences 1 and 2 show similar trends with those of the granitic and gneissic Basement. Insufficient information is currently available on the petrology of the Mpande Dome Basement and overlying metavolcanics to prove whether the Basement and/or metavolcanics were wholly or partially responsible for the metal supply, or otherwise.

The Chongwe Copperbelt which is situated a short distance northeast of Shantumbu has a strike of c. 80km, and the copper mineralisation coincides with the contact between Basement granitoid-gneisses and the overlying Katanga metasediments and marbles. At the Allies Mine in the Mulofwe Dome area of the Chongwe Copperbelt, the sulphide mineralisation within the Basement was mined sporadically between 1914 and 1922. Various small-scale artisanal copper

workings in the Mulofwe Dome area are recorded. At the Allies Mine, base metals are hosted within basement rocks of the Mulofwe Dome. It is postulated that the basement rocks in the Shantumbu area was the source of the copper although the amount of base metals added to the sedimentary system is inferred as having been diminutive in comparison to the copper supply to the Central African Copperbelt.

The largest copper deposits in the Redstone Copper Belt, in the Northwest Territories, are associated with basins which have the thickest stratigraphic sequences (Jefferson, 1986). Although the base of the Roan Group stratigraphy was not intersected during the drilling on Shantumbu, based on the occurrences of volcanic units which have a limited thickness and the similar sedimentary successions on the southern flank of the Mpande Dome, the rift-basin successions is considered to be relatively thin on Shantumbu which is, perhaps, a contributor to the low-grade localised copper mineralisation.

8.5 AIMS AND OBJECTIVES ACHIEVED

The aim of the study was to examine the metasedimentary stratigraphy and copper mineralisation at Shantumbu and provide support, or otherwise, that the area represented the southerly extension of the Roan Group and the related sediment-hosted, stratiform copper mineralisation. Seven hypotheses were defined in Chapter 4, and all seven have now been verified.

The first assumption was the depositional basin at Shantumbu was a basement-proximal and restricted rift basin. The stratigraphy on the southern flank of the Mpande Dome is floored by a granitic and gneissic Basement overlain by rhyolitic units. Rhyolite clasts were found during the mineralogical examination of the clastic units of Shantumbu. Hence, the presence of rhyolite is assumed to floor the package of metasedimentary lithologies on the northern margin of the Mpande Dome. The presence of the rhyolites and abutment against the Mpande Dome supported the hypothesis that Shantumbu was a basement-proximal rift basin.

Based primarily on the low-grade and erratic copper occurrences, the rift basin at Shantumbu is interpreted to have been an open basin and not bounded by fault blocks along the entire margin of the basin. The basinal brines responsible for the remobilisation and reprecipitation of the copper therefore may have managed to escape the basin, though further detailed structural research is needed to unanimously confirm this.

The second assumption assumed the metasediments at Shantumbu were siliciclastic sediments, which were derived from the Basement lithologies. Based on the mineralogy and geochemistry of the Shantumbu metasediments, the matching mineralogy to the Mpande Dome granite and gneiss, and the correlation with the Roan Group of the Zambian Copperbelt, indicates that this assumption is appropriate. The alkali and potassic nature of the metasediments have been correlated to the erosion of K-feldspar-, biotite-, phlogopite- and muscovite-bearing sediments from the granitic and gneissic Basement. The basement and overlying volcanic units have been proposed as the source of the copper occurrences at Shantumbu.

The third assumption is Shantumbu represented a restricted basin. The extent and shape of the basin hosting Shantumbu has not been explored sufficiently to present an estimate of the basin size and shape, and whether the margins of the basin are fault-bounded. However, the thin arenite and siltstone layers hosted by the carbonates of the Bancroft Formation (Sequence 7) is indicative of a restricted marine environment.

Three of the initial assumptions were not validated or disproved during examination of the basin and structure characteristic at Shantumbu. The existence of thick conglomerates within the basal units of the rift-related lithologies were not observed, nor were the metavolcanics units identified. This may have been a function of the limited drilling depth, which was aimed at finding mineralisation, and not intersecting the full stratigraphic succession. Further drilling will be needed to prove the presence of metaconglomerates and metavolcanics at the base of the Mindola Formation.

Asymmetrical rift-related normal faults which dipped to the north and northeast along the northern flank of the Mpande Dome were assumed. Structural work to confirm this assumption will need to be undertaken. Faults and folds are an important part of sediment-hosted, stratabound copper deposits, however the limited drilling and poor outcrop did not facilitate a comprehensive understanding of the structures on Shantumbu.

Two of the assumptions related to the detrital and marine depositional environments of the sediments. A moderate to high energy depositional environment was assumed during the deposition of the older/lower siliciclastic rocks on Shantumbu. The environment was ascertained to represent an alluvial fan environment, which progressed into a fan-delta environment. It was assumed that due to basin subsidence, the marine transgression characterised the post-rift depositional environment. This assumption was proved valid by the research undertaken.

The final assumption was that Shantumbu was the most southerly rift basins which were responsible for the deposition of the Roan Group in the Zambian Copperbelt. The lithostratigraphic interpretation and correlations of the Shantumbu metasediments to the Roan Group in the Zambian Copperbelt has provided considerable weight to the validity of this assumption.

8.6 CONCLUSIONS

The extension of the Roan Group of the Katanga Supergroup, to the Mpande Dome region has implications for the area being prospective for sediment-hosted, stratabound copper mineralisation / Zambian Copperbelt style mineralisation. The copper mineralisation on Shantumbu is consistent with the genetic model for sediment-hosted, stratiform copper deposits, examples of which include the Central African Copperbelt, White Pine, Spar Lake, and the Kupferschiefer deposits.

The examination of the Shantumbu lithostratigraphy demonstrated a close correlation with the Roan Group, with the members and facies of the Mindola, Kitwe and Kirilabombwe formations of the Roan Group being identified on Shantumbu. An alternative stratigraphic classification of metasedimentary rocks at Shantumbu to that of Smith (1964) and Mallick (1966), is therefore recommended.

The metasediments of Shantumbu flank the basement Mpande Dome. Uplift of the Mpande Dome preceded the Neoproterozoic continental rifting and the onset of continental rift-related sediment deposition (Selly *et al*., 2005). The position of the Mpande Dome is related to a single or multiple pre-Katangan orogenic events (Hanson *et al*., 1994). The uplift of the basement Mpande Granites and gneisses during sedimentation and diagenesis acted as driver of metal-bearing basinal fluid migration from the basal rift-related volcanic rocks and clastic sediments both vertically and laterally. The oxidised saline fluids migrated and encountered the anoxic reduced sediments, where bacterial sulphate reduction produced copper sulphides. Circulation of the basinal fluids and the regional deformation assisted the remobilisation and reprecipitation of the metal sulphides within vein structures.

The area south of the Mwembeshi Zone has been described as a ‘thick succession of low-grade metamorphic carbonates with intercalations of quartz-muscovite-chlorite schists, carbonaceous schists, slates, phyllites and thin quartzite layers (Cheta Formation)’ (Porada and Berhorst, 2000, p.746). The Chunga Formation has been described as a succession of ‘quartz-muscovite-biotite schists containing a few lenses of impure dolomitic limestone and layers of quartzite’ that

underwent amphibolite facies metamorphism during strong Lufilian shearing (Porada and Berhorst, 2000, p.746).

The stratigraphy immediately north of the Mwembeshi Zone consists of low-grade metamorphosed arkoses, quartzites, phyllites, banded slates and thin dolomites and belongs to the Kangomba Formation, which Moore (1964) assigned to the Roan Group. The succession is overlain by a thick succession of carbonates intercalated with mudstones, slate and schist horizons, which were assigned to the Nyama Formation (Porada and Berhorst, 2000, and references therein). Porada and Berhorst (2000) correlated the Kangomba and Nyama formations to the Mindola to Kitwe formations, and the Bancroft Formation of the Roan Group.

The continuation of the metasediments from Shantumbu north through the Chongwe Copperbelt and the continuation of the Roan Group on the northern margin of the Mwembeshi Zone were described above and summarised in Figure 8-5. This continuation of the Roan Group on the other side of the Mwembeshi Zone strengthens the argument that Shantumbu is an extension of the Roan Group of the Katanga Basin. The age of the Kafue Rhyolite and Nazingwe formations in the Mpande Dome region, have been age dated at 879 ± 19 Ma (Hanson *et al*., 1994; Selley *et al*., 2005; Johnson *et al*., 2007), providing further support that Shantumbu is part of the Neoproterozoic Katanga Basin system rather than the rift systems to the south of Zambia, such as the Zambezi Belt or the Magondi Mobile Belt.

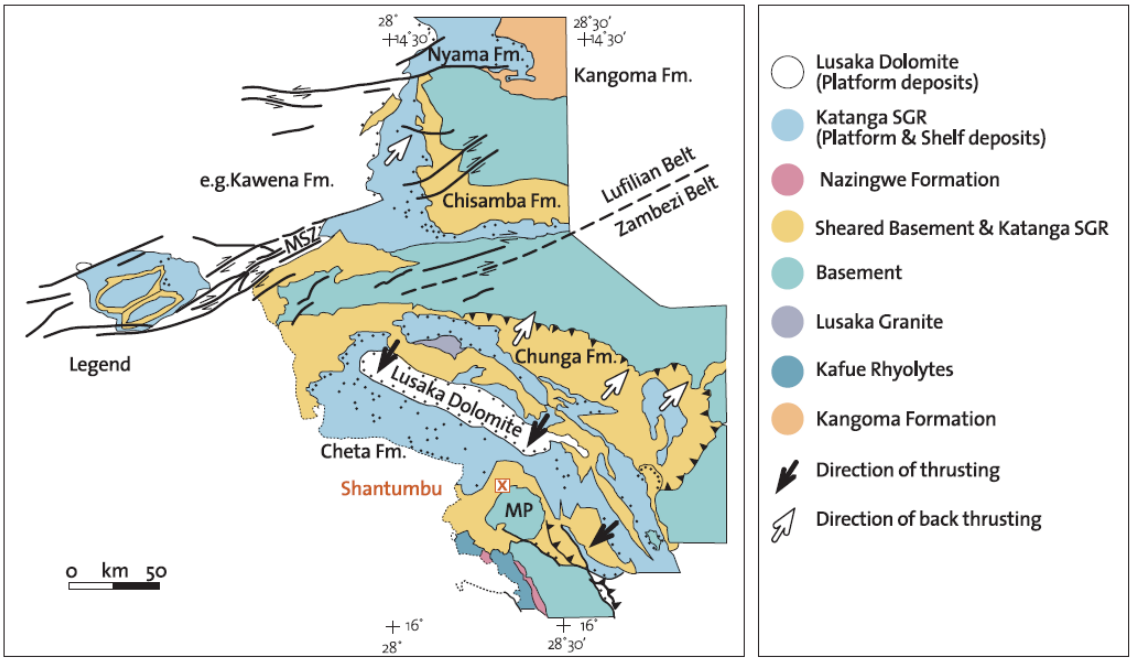

Figure 8-5. Regional basement and sedimentary geology at and around Shantumbu. The tectonic contact of the Lusaka Dolomite Formation and the Katanga Supergroup is illustrated. The continuation of the

platform-shelf carbonates and the terrestrial siliciclastic sediments on either side of the Mwembeshi Zone and south to the Shantumbu /Mpande Dome (MP) area is evident, and these areas have been assigned to the Katanga Supergroup (Porada and Berhorst, 2000). Fm = Formation. 'X' denotes locality of Shantumbu.

Shantumbu may alternatively represent a rift basin unrelated to the continental rifting responsible for the Roan Group in the Zambian Copperbelt and may perhaps be correlated to the rift systems on the Kalahari Craton, such as the Damara which extends from Namibia into Zambia where it is termed the Zambezi Belt (Longridge *et al*., 2011), or the Mesoproterozoic Botswana Rift.

The full width of the Zambezi Belt is exposed in southern Zambia, which consists of an east-west trending, intermediate- to high-grade metamorphosed intracontinental rift basin sediments capped by marine chemical sediments. The age dating of the sediments indicated deposition occurred c. 880 Ma to 820 Ma (Hanson *et al*., 1994). Porada and Berhorst (2000) envisaged two separate basins formed north and south of a pre-existing high, the Katanga High, during continental rifting. Following deposition of the rift-basin sediments and volcanic units, the Mwembeshi Zone, a north northeast – south southwest trending shear zone, separated the Lufilian Arc from the Zambezi Belt (Daly, 1988; Yemane *et al*., 2002; Selley *et al*., 2005; Miller, 2013).

The copper mineralisation at Shantumbu has many similarities with the copper mineralisation of the Zechstein Basin, the type area for the Kupferschiefer-type deposits, and the Central African Copperbelt. The geological features comparing the pertinent characteristics of the Kupferschiefer, Shantumbu and Zambian Copperbelt sediment-hosted, stratiform copper deposits are summarised in Table 8-2.

Table 8-2. Comparison of the geological features of the Kupferschiefer, Shantumbu and Zambian Copperbelt sediment-hosted, stratiform copper deposits.

Kupferschiefer deposits of the Zechstein Basin	Shantumbu, the southern extension of the Zambian Copperbelt rift-related basins	Roan Group deposits of the Zambian Copperbelt / Katanga Basin
Continental rift basin with basal basaltic or bimodal igneous rocks (Jowett, 1986).	Continental rift basin with basal rhyolite units. The lithostratigraphic, geochemical, alteration and metamorphic information showed the sediments at Shantumbu area were deposited in an intracontinental rift basin.	The Katanga Supergroup in the Zambian Copperbelt and the metasediments rocks at Shantumbu formed during passive continental extension related to the breakup of Rodinia c. 880 Ma (Master and Wendorff, 2011).
Isolated, closed basins hosting immature clastic and evaporite sediments (Jowett, 1986).	Isolated, closed basin on the flanks of the Mpande Dome, hosting clastic sediments and evaporite sediments.	Isolated, closed basin on the flanks of the basement domes, hosting clastic sediments and evaporite sediments.
Fault-controlled sedimentation (Jowett, 1986).	Tectonic control on the sedimentation.	The Roan Group was deposited within half-graben sub-basins where the underlying growth-faults remained active during the deposition of the overlying Kitwe Formation. Master faults exerted a greater control after the deposition of the Kitwe Formation (Selley *et al*., 2005).
Volcanic detritus providing source of metals (Jowett, 1986).	Copper sulphides within the Kafue Rhyolite Formation (by Johnson *et al*., 2007). In the Mulofwe Dome area structurally controlled anomalous copper, gold, silver, cobalt and bismuth mineralisation (Zambezi Resources, 2005; Zambezi Resources Press Release, 2008).	Copper mineralisation within basement lithologies provided source of metals.
Saline brine development (Jowett, 1986).	Saline brine development noted by the extensive sodic alteration and development of stratabound breccias.	The Copperbelt Orebody Member is locally characterised by evaporitic textures, and the upper part of the Roan Group has further evaporitic textures. Evaporites also developed throughout the Katanga Supergroup (Hitzman *et al*., 2012).

Kupferschiefer deposits of the Zechstein Basin	Shantumbu, the southern extension of the Zambian Copperbelt rift-related basins	Roan Group deposits of the Zambian Copperbelt / Katanga Basin
Migration of brines along faults where brines migrated from the oxidised lower detrital units along faults (Hayes *et al*., 2015).	Migration of copper-bearing brines along faults and folds, an example is the D_1-D_2 fold axis at Copper Hill, which hosts extensive copper oxide mineralisation. Base and precious metal mineralisation occurs in a shallow dipping zone within the Mulofwe Dome (Zambezi Resources, 2005; Zambezi Resources Press Release, 2008).	Migration of copper-bearing brines along faults and folds, transgressing across stratigraphic sequence. Annels (1986) reported structures within the basement at the Chambishi deposit that may have allowed metal-rich fluids to penetrate the overlying Roan Group sediments.
Circulation of oxidising fluids to reduced sediments during early or late diagenesis (Jowett, 1986).	Circulation of low-temperature oxidising fluids to reduced sediments of Sequences 3 to 7 during early to late diagenesis.	Circulation of oxidising fluids to reduced sediments during early to late diagenesis.
Reduced strata acted as chemical traps for the copper mineralisation during calm rifting period (Jowett, 1986).	Copper mineralisation hosted by the Sequences 1 and 2 arenites capped by siltstone, and adjacent to the marine transgression surface of Sequences 3 and 4. Reduced conditions during deposition of the siltstone and carbonate units of Sequences 3 and 4.	Reduced strata acted as chemical traps for the copper mineralisation.
Copper mineralisation overprinted the sedimentary rocks during diagenesis, tectonism, and metamorphism	Copper mineralisation overprinted the sedimentary rocks during diagenesis, tectonism, and metamorphism.	Copper mineralisation overprinted the sedimentary rocks during diagenesis, tectonism and metamorphism.
Ore formation during thermal and tectonic events which caused the migration of diagenetic fluids to the overlying reduced strata (Jowett, 1986).	Pan African deformation resulted in the intensive folding and faulting at Shantumbu. These structural features acted as thermal and tectonic pumps for the basinal brines.	Pan African deformation resulted in the intensive folding and faulting. These structural features acted as thermal and tectonic pumps for the basinal brines.
Disseminated sulphides deposited in anoxic marine sediments which are underlain by continental clastic sedimentary rocks (Kirkham, 1986).	Disseminated mineralisation precipitated during the deposition of the clastic sediments. Disseminated sulphides in anoxic marine sediments of Sequences 5 to 7, underlain by continental clastic sedimentary rocks of Sequences 1 and 2. Bacterial sulphate reduction activity has been implied in the marine/anoxic units, whilst remobilisation of metal-bearing brines occurred in the siliciclastic sequences.	Disseminated mineralisation precipitated during the deposition of the clastic sediments, and within the overlying anoxic marine sediments.

8.7 RECOMMENDATIONS

The study recommends the following research:

1. The examination of the metasediments on Shantumbu has shown that further research would advance the understanding of the rift basin stratigraphy and related sediment-hosted, stratiform copper mineralisation. Such research topics include the investigation of the presence of metavolcanics on the northern margin of the Mpande Dome and the Kafue Rhyolite and Nazingwe Formation hosting copper sulphides, and a comparison and correlation, or otherwise, of the metasediments comprising the Chongwe Copperbelt to the Shantumbu metasediments;
2. The role of structures as conduits for the migration of copper-bearing basinal brines and the timing of the mineralisation on Shantumbu would provide beneficial information for the exploration potential of the area;
3. Age dating of the Mpande Dome and the surrounding metavolcanics and metasediments will increase the current level of understanding of the rift system, and sediment-hosted, stratabound copper mineralisation potential. The 2013 to 2015 exploration activities at Shantumbu did not extend to the examination of the basement for copper sulphides and further research of the Mpande Dome granites and gneisses may answer whether the provenance for the Roan Group surrounding Dome had a hinterland with sufficient base metal mineralisation to form deposits of economic concentration;
4. Exploration of the Kafue Rhyolites to examine the copper endowment of this unit and whether the rhyolites were a source of the copper enrichment within the metasediments stratigraphically above;
5. The metasediments to the south of the Mpande Dome should be explored to determine the potential to host sediment-hosted, stratabound copper deposits. The connection, or otherwise, of the metasediments and mineralisation of the Chongwe Copperbelt to the Shantumbu and Kafue regions will provide valuable information on the areal extent of the copper metallotect south of the Mwembeshi Zone, and potentially the size and shape of the basin or basins hosting the Shantumbu metasediments, and whether the basins were linked by master faults;

6. Exploration of the footwall to the metasediments would assist in determining whether the Shantumbu area has a sufficient thickness of sediments to have formed economic copper mineralisation;
7. Future exploration should consider the role of faults and folding in the migration of fluids at Shantumbu. In-depth examination of the D_1 to D_3 structural features on Shantumbu, may assist future exploration for copper mineralisation on Shantumbu;
8. "Unfolding" of the Shantumbu basin may aid in the discovery of copper occurrences, although such "unfolding" would be thwart with difficulties as Shantumbu is found at the triple junction of the Zambezi and Irumide Belts and the Lufilian Arc;
9. Research into the isotopic signature of the dolomitic carbonate of Sequence 4 may facilitate correlation with the unique $\delta^{13}C$ (PDB) and $\delta^{18}O$ (SMOW) signature of the Copperbelt Orebody Member in the Zambian Copperbelt. In addition, research into the C and O isotope signatures of the Roan Group on Shantumbu will provide insight into the pressure and temperature conditions experienced during deformation of the metasediments. Stable S isotope research will assist in understanding the depositional environments which existed on Shantumbu;
10. Age or isotope research is recommended, as without age or isotope data for the Lusaka Dolomite Formation, the relationship, albeit unconformable, to the Bancroft Member, previously the Mampompo Limestone Formation of the Cheta Group, is not well understood; and
11. U-Pb zircon geochronology dating of both the metasediments and veins within the Shantumbu metasediments and those within the granites and gneisses is recommended to assist in the age dating of crystallisation, dating the deformation events on Shantumbu, and correlation with the age dates determined for the Katanga Basin and underlying Basement.

REFERENCES

Aivo, L. and Whitehouse, M.J. 2011. Metamorphic alteration, mineral paragenesis and geochemical re-equilibration of early Archaean quartz-amphibole-pyroxene gneiss from Akilia, southwest Greenland. International Journal of Earth Sciences, 100, 1, 1-22.

Annels, A.E. and Simmonds, J.R. 1984. Cobalt in the Zambian Copperbelt. Precambrian Research, 25, 75-98.

Annels, A.E. 1986. Ore genesis in the Zambian Copperbelt, with particular reference to the northern sector of the Chambishi Basin. Symposium on sediment-hosted stratiform copper deposits, Ottawa May 17 - 19 1986. Canadian Mineralogist, Vol. 24, 169-214.

Bailey, D.K. and Woolley, A.R. 2005. Repeated, synchronous magmatism within Africa: timing, magnetic reversals, and global tectonics. Geological Society of America, Special Paper, 388, 365-377.

Barr, M.W.C., Cahen, L. and Ledent, D. 1977. Geochronology of syntectonic granites from central Zambia: Lusaka Granite and granite NW of Rufunsa. Annals of the Society of Geology Belgium, 100, 47-54.

Berner, R.A. 1984. Sedimentary pyrite formation: an update. Geochimica et Cosmochimica Acta, 48, 605-615.

Binda, P.L., Koopman, H.T. and Koopman, E.R. 1986. A stratiform copper occurrence in the Helikian Siyeh Formation of Alberta and British Columbia. Symposium on sediment-hosted stratiform copper deposits, Ottawa May 17 - 19 1986. Canadian Mineralogist, Vol. 24, 169-214.

Boni, M., Terracciano, R., Balassone, G., Gleeson, S.A. and Matthews, A. 2011. The carbonate-hosted Willemite Prospects of the Zambezi Metamorphic Belt Zambia. Miner Deposita, DOI 10.1007/s00126-011-0338-7.

Borg, G. and Maiden, K. 1986. Stratabound copper-silver-gold mineralisation of late Proterozoic age along the margin of the Kalahari Craton in SWA/Namibia and Botswana. Symposium on sediment-hosted stratiform copper deposits, Ottawa May 17 - 19 1986. Canadian Mineralogist, Vol. 24, 169-214.

Brimhall, G.H., Agee C. and Stoffregen R. 1985. The hydrothermal conversion of hornblende to biotite. Canadian Mineralogist, 23, 369-379.

Broughton, D. 2002. Comparative study of drill core from the Konkola North orebody and barren gap. AMIRA P544 Progress Report, June 2002, 19-35.

Brown, A.C. 1986. A case for exhalative or pene-exhalative hydrothermal activity in the genesis of sediment-hosted, stratiform copper deposits. Symposium on sediment-hosted stratiform copper deposits, Ottawa May 17 - 19 1986. Canadian Mineralogist, Vol. 24, 169-214.

Brown, A.C. 1997. World-class sediment-hosted stratiform copper deposits: characteristics, genetic concepts and metallotects. Australian Journal of Earth Science, 44, 317-328.

Brown, A.C. 2014. Low temperature sediment-hosted copper deposits. Treatise on Geochemistry 2nd Edition, 251-271.

Bull, S., Selley, D., Broughton, D., Hitzman, M., Cailteux J., Large, R. and McGoldrick, P. 2011. Sequence and carbon isotopic stratigraphy of the Neoproterozoic Roan Group strata of the Zambian Copperbelt. Precambrian Research, 190, 70-89.

Cailteux, J.L.H., Kampunzu, A.B. and Lerouge, C. 2007. The Neoproterozoic Mwashya-Kansuki sedimentary rock succession in the Central African Copperbelt, its Cu-Co mineralisation, and regional correlations. Gondwana Research, 11, 414-431.

Cairney, T. 1967. The Geology of the Leopards Hill Area: Explanation of Degree Sheet 1528, SE. Quarter. Government Printer. 64pp.

Calvert, S.E. and Pedersen, T.F. 1993. Geochemistry of recent oxic and anoxic marine sediments: implications for the geological record. Marine Geology, 113, 67-88.

Cao, S., Neubauer, F., Bernroider, M. and Liu, J. 2013. The lateral boundary of a metamorphic core complex: the Moutsounas shear zone on Naxos, Cyclades, Greece. Journal of Structural Geology, 54, 103-128.

Chandler, F.W. 1986. Stratabound copper mineralisation in Early Proterozoic marine-transgression-related quartz arenite, Cobalt Group, Ontario. Symposium on sediment-hosted stratiform copper deposits, Ottawa May 17 - 19 1986. Canadian Mineralogist, Vol. 24, 169-214.

Clemmey, H. 1976. Aspects of stratigraphy, sedimentology and ore genesis on the Zambian Copperbelt with special reference to Rokana mines: Unpub. Ph.D. thesis, Univ. Leeds.

Cluzel, D. and Guillous, L. 1986. Hydrothermal Character of the Shaba Cu-Co-U mineralisation. Symposium on sediment-hosted stratiform copper deposits, Ottawa May 17 - 19 1986. Canadian Mineralogist, Vol. 24, 169-214.

Croaker, M. 2011. The Geology of the Nkana-Mindola sediment-hosted copper cobalt deposit, Zambian Copperbelt, Zambia. PhD Thesis, University of Tasmania.

Daly, M.C., Chakraborty, S.K., Kasolo, P., Musiwa, M., Mumba, P., Naidu, B., Namateba, C., Ngambi, O. and Cowrad, M.P. 1984. The Lufilian Arc and Irumide Belt of Zambia: results of a geotraverse across their intersection. Journal of African Earth Science, 2, 4, 311-318.

Daly, M.C. 1988. Crustal shear zones in Central Africa: a kinematic approach to Proterozoic tectonics. Episodes, 11, 1, 5-11.

Daly, M.C., Chorowicz J. and Fairhead J.D. 1989. Rift Basin Evolution in Africa: the influence of reactivated steep basement shear zones. In, Cooper, M.A. and Williams, G.D., (Eds). Inversion Tectonics: Geological Society of London, Special Publication 44, 309-334.

Decarreau, A., Petit, S., Viellard, P. and Dabert, N. 2004. Hydrothermal synthesis of aegirine at 200°C. European Journal of Mineralogy, 16, 85-90.

Deer, W.A., Howie, R.A., Zussman, J., Chang, L.L.Y and Wise, W.S. 2004. Rock-forming Minerals, Vol. 4B. Second Edition. Framework silicates: silica minerals, feldspathoids and the zeolites, London (The Geological Society), 982pp.

De Swardt, A. M. J and Drysdall, A.R. 1964. Precambrian Geology and Structure in Central Northern Rhodesia. Northern Rhodesia Geological Survey, Issues 1-2, 82pp

De Waele, B., Johnson, S.P. and Pisarevsky, S.A. 2008. Paleoproterozoic to Neoproterozoic growth and evolution of the eastern Congo Craton: its role in the Rodinia puzzle. Precambrian Research, 160, 127-141.

Dombrowski A., Hoernes S., and Okrusch A. 1996. Scapolitization in the Kuiseb Formation of the Damara Orogen: geochemical and stable isotope evidence for fluid infiltration along deep crustal shear zones. Communs. Geological Survey of Namibia, 11, 23-31.

Drysdall, A.R. and Stillman, C.J. 1966. Scapolite from the Katanga carbonate rocks of the Lusaka district. Records Geological Survey Northern Rhodesia, 10, 20-24.

El Desouky, H.A., Muchez, P., De Waele, S., Boutwood, A. and Tyler, R. 2008. Postorogenic origin of the stratiform Cu mineralisation at Lufukwe, Lufilian Foreland, Democratic Republic of Congo. Economic Geology, 103, 555-582.

Elrick, M. 1996. Sequence stratigraphy and platform evolution of Lower-Middle Devonian carbonates, eastern Great Basin. GSA Bulletin, 108, 4, 392-416.

Ernst, W.G. 1963. Petrogenesis of glaucophane schists. Journal of Petrology, 4, 1-30.

Eugster, H.P. 1986. Geochemical environments of sediment-hosted ore deposits. Symposium on sediment-hosted stratiform copper deposits, Ottawa May 17 - 19 1986. Canadian Mineralogist, Vol. 24, 169-214.

Fall, A., Bodnar, R.J. and Szabo, C. 2006. Fluid evolution in the nepheline syenites of the Ditrau Alkaline Massif, Transylvania, Romania. Lithos - DOI: 10.1016/j.lithos.2006.08.2005), 1-15.

Ferry, J.M. 1981. Petrology of graphitic sulphide-rich schists from south-central Maine: an example of desulfidation during prograde regional metamorphism. American Mineralogist, 66, 908-930.

Finch, E.G. and Tomkins, A.G. 2017. Pyrite-pyrrhotite stability in a metamorphic aureole: implications for orogenic gold genesis. Economic Geology, 112, 661-674.

Folger, P.F. 1986. The geology and geochemistry of the carbonate-hosted Omar Copper Deposit, Baird Mountains, Alaska. Symposium on sediment-hosted stratiform copper deposits, Ottawa May 17 - 19 1986. Canadian Mineralogist, Vol. 24, 169-214.

Fraser, A. 2010. Introduction: Boom and Bust on the Zambian Copperbelt. In, Fraser A. and Larmer M. (Eds). Zambia, mining, and neoliberalism, Palgrave Macmillan, 1-30.

Frost, B.R., Chamberlain, K.R. and Schumacher, J.C. 2000. Sphene (titanite): phase relations and role as a geochronometer. Chemical Geology, 172, 131-148.

Haest, M. and Muchez, P. 2011. Stratiform and vein-type deposits in the Pan-African Orogen in central and southern Africa: evidence for multiphase mineralisation. Geologica Belgica, 14, 23-44.

Hanson, R.E., Wilson, T.J. and Munyanyiwa, H. 1994. Geologic evolution of the Neoproterozoic Zambezi Orogenic Belt in Zambia. Journal of African Earth Science, 18, 2, 135-150.

Hargrove, U.S., Hanson, R.E., Martin, M.W., Blenkinsop, T.G., Bowring, S.A., Walker, N. and Munyanyiwa, H. 2003. Tectonic evolution of the Zambezi orogenic belt: geochronological, structural, and petrological constraints from Northern Zimbabwe. Precambrian Research, 123, 159-186.

Harpum, J.R. 1954. Formation of epidote in Tanganyika. Bulletin of the Geological Society of America, 65, 1075-1092.

Hayes, T.S., Cox, D.P., Piatak, N.M., and Seal, R.R. II 2015. Sediment-hosted stratabound copper deposit model: U.S. Geological Survey Scientific Investigations Report 2010/5070-M, 147pp.

Heijlen, W., Banks, D.A., Muchez, P., Stensgard, B.M. and Yardley, B.W.D. 2008. The nature of mineralising fluids of the Kipushi Zn-Cu deposit, Katanga, Democratic Republic of Congo: quantitative fluid inclusion analysis using laser ablation ICP-MS and bulk crush-leach methods. Economic Geology, 103, 1459-1482.

Hitzman, M.W., Selley, D. and Bull, S. 2010. Formation of sedimentary rock-hosted stratiform copper deposits through Earth history. Society of Economic Geologists, Inc., Economic Geology, 105, 627-639.

Hitzman, M.W., Broughton, D., Selley, D., Woodhead, J., Wood, D. and Bull, S. 2012. The Central African Copperbelt: diverse stratigraphic, structural, and temporal settings in the World's largest sedimentary copper district. Society of Economic Geologists Special Publication 16, 487-514.

Hooeve, J. and Quirt, D. 1986. A diagenetic-hydrothermal origin for unconformity-related and stratiform copper deposits in the Central African and Michigan Copper Districts. Symposium on sediment-hosted stratiform copper deposits, Ottawa May 17 - 19 1986. Canadian Mineralogist, Vol. 24, 169-214.

Horstman, E.L. 1957. The distribution of lithium, rubidium, and caesium in igneous and sedimentary rocks. Geochimica et Cosmochimica Acta, 12, 1-28.

Horton, B.K. and Schmitt, J.G. 1996. Sedimentology of a lacustrine fan-delta system, Miocene Horse Camp Formation, Nevada, USA. Sedimentology, 43, 133-155.

Hoy, L.D., Ohmoto, H., Rose, A.W., Dimanche, F. and Coipel, J. 1986. Constraints for the genesis of red-bed-associated stratiform Cu deposits from S and C mass-balance relations. Symposium on sediment-hosted stratiform copper deposits, Ottawa May 17 - 19 1986. Canadian Mineralogist, Vol. 24, 169-214.

Hu, Z. and Gao, S. 2008. Upper crustal abundances of trace elements: a revision and update. Chemical Geology, 253, 205-221.

Jamtveit, B., Dahlgren, S. and Austrheim, H. 2004. High-grade contact metamorphism of calcareous rocks of the Oslo Rift, southern Norway. American Mineralogist, 82, 11-12, 1241-1254.

Jefferson, C.W. 1986. Stratigraphic, tectonic, and sedimentological setting of deposits in the Redstone Copper Belt, Mackenzie Mountains, Northwest Territories. Symposium on sediment-hosted stratiform copper deposits, Ottawa May 17 - 19 1986. Canadian Mineralogist, Vol. 24, 169-214.

Johnson, S.P. and Oliver, G.J.H. 1998. A second natural occurrence of yoderite. Journal of Metamorphic Geology, 16, 809-818.

Johnson, S.P. and Oliver, G.J.H. 2004. Tectonothermal history of the Kaourera Arc, northern Zimbabwe: implications for the tectonic evolution of the Irumide and Zambezi Belts of south central Africa. Precambrian Research, 130, 71-97.

Johnson, S.P., De Waele, B., Evans, D. and Banda, W. 2006. A record of Neoproterozoic divergent processes along the southern Congo Craton margin. Abstract from 21st Colloquium on African Geology, Maputo.

Johnson, S.P., De Waele, B., Evans, D., Banda, W., Tembo, F., Milton, J.A. and Tani, K. 2007. Geochronology of the Zambezi Supracrustal sequence, Southern Zambia: a record of Neoproterozoic divergent processes along the southern margin of the Congo Craton. Journal of Geology, 115, 355-374.

Jones, B. and Manning, A.C. 1994. Comparison of geochemical indices used for the interpretation of palaeoredox conditions in ancient mudstones. Chemical Geology, 111, 111-129.

Jowett, E.C. 1986. Effects of tectonic environment on Kupferschiefer-type deposits. Symposium on sediment-hosted stratiform copper deposits, Ottawa May 17 - 19 1986. Canadian Mineralogist, Vol. 24, 169-214.

Kamona, A.F. and Friedrich, G.H. 2007. Geology, mineralogy and stable isotope geochemistry of the Kabwe carbonate-hosted Pb-Zn deposit, Central Zambia. Ore Geology Reviews, 20, 217-243.

Kampunzu, A.B. and Cailteux, J.L.H. 1999. Tectonic evaluation of the Lufilian Arc Central Africa Copper Belt during Neoproterozoic Pan African Orogenesis. Gondwana Research, 2, 401-421.

Kampunzu, A.B., Cailteux, J.L.H., Moine, B. and Loris, H.N.B.T. 2005. Geochemical characterisation, provenance, source and depositional environments of 'Roches Argilo-Talqueses' (RAT) and Mines Subgroups sedimentary rocks in the Neoproterozoic Katangan Belt (Congo): Lithostratigraphic implications. Journal of African Earth Science, 42, 119-133.

Kampunzu, A.B., Cailteux, J.L.H., Kamona, A.F., Intiomale, M.M. and Melcher, F. 2009. Sediment-hosted Zn-Pb-Cu deposits in the Central African Copperbelt. Ore Geology Review, 35, 263-297.

Katongo, C., Koller, F., Kloetzli, U., Koeberl, C., Tembo, F. and De Waele, B. 2004. Petrography, geochemistry, and geochronology of granitoid rocks in the Neoproterozoic-Palaeozoic Lufilian-Zambezi belt, Zambia: Implications for tectonic setting and regional correlation. Journal of African Earth Sciences, 40, 219-244.

Kendall, A.C. 1978. Facies models 11. Continental and supratidal (sabkha) evaporites. Geoscience Canada, 5, No. 2, 66-78.

Kipata, M.L., Delvaux, D., Sebagenzi, M.N., Cailteux, J.L.H. and Sintubin, M. 2013. Brittle tectonic and stress field evolution in the Pan African Lufilian Arc and its foreland Katanga, DRC: from orogenic to extensional collapse, transpressional inversion and transition to rifting. Geologica Belgica, 16, 1-2, 1-17.

Kirkham, R.V. 1986. Distribution of sediment-hosted stratiform copper deposits: an introduction. Symposium on sediment-hosted stratiform copper deposits, Ottawa May 17 - 19 1986. Canadian Mineralogist, Vol. 24, 169-214.

Kovalskii, A.M., Kovalskaya, T.N. and Kotelnikov, A.R. 2006. Tiksheozerskit massif. Composition, conditions of formation, experimental modelling of mineralogenesis. Informational Bulletin of the Annual Seminar of Experimental Mineralogy, Petrology and Geochemistry, 1-2.

Kröner, A. and Stern, R.J. 2004. Pan-African Orogeny North African Phanerozoic Rift Valley. Encyclopaedia of Geology 2004, 1, Elsevier Ltd Amsterdam, 1-12.

LaPoint, D.J. 1986. Genesis of Permian and Triassic sandstone-hosted copper deposits in New Mexico. Symposium on sediment-hosted stratiform copper deposits, Ottawa May 17 - 19 1986. Canadian Mineralogist, Vol. 24, 169-214.

Lefebvre, J. 1986. Lithostratigraphy of copper occurrences in southern Shaba (Zaire), and correlations with the Zambian Copperbelt. Symposium on sediment-hosted stratiform copper deposits, Ottawa May 17 - 19 1986. Canadian Mineralogist, Vol. 24, 169-214.

Likhoydov, G.G. 1981. Stability of the aegirine–quartz–hematite association as shown by experimental data. Doklady Academy of Sciences of the USSR, Earth Sciences Section, 242, 174–176.

Longridge, L., Ginson, R.L., Kinnaird, J.A. and Armstrong, R.A. 2011. Constraining the timing of deformation in the southwestern Central Zone of the Damara Belt, Namibia. In, Van Hinsbergen, D. J. J., Buiter, S. J. H., Torsvik, T. H., Gaina, C. and Webb, S. J. (Eds) The Formation and Evolution of Africa: A Synopsis of 3.8 Ga of Earth History. Geological Society, London, Special Publications, 357, 107–135.

Machel, H.G. 2001. Bacterial and thermochemical sulphate reduction in diagenetic settings – old and new insights. Sedimentary Geology, 140, 143-175.

Maiden, K.J., Borg, G. and Master, S. 1986. Structural traps for stratabound copper deposits. Symposium on sediment-hosted stratiform copper deposits, Ottawa May 17 - 19 1986. Canadian Mineralogist, Vol. 24, 169-214.

Maiden, K.J. and Masters, S. 1986. The Mangula copper-silver-gold deposit, Zimbabwe: A Lower Proterozoic Olympic-Dam-type deposit? Symposium on sediment-hosted stratiform copper deposits, Ottawa May 17 - 19 1986. Canadian Mineralogist, Vol. 24, 169-214.

Mallick, D.I.J. 1966. The stratigraphy and the structural development of the Mpande Dome, southern Zambia. Transactions of the Geological Society of South Africa, 69, 211-230.

Master, S. 1996. IGCP Project 363: Lower Proterozoic of Sub-equatorial Africa. Post-Conference Field Excursions No. 2: The Palaeoproterozoic Magondi Mobile Belt, NW Zimbabwe. Excursion Guide, 27pp.

Master, S. and Wendorff, M. 2011. Neoproterozoic glaciogenic diamictites of the Katanga Supergroup, Central Africa. In: Arnaud, E., Halverson, G.P. and Zhou-Shields, G. (Eds). The Geological Records of Neoproterozoic Glaciations. Geological Society Memoir, No. 36, IUGS, London, 173-184.

Middleburg, J.J., Van Der Weijden, C.H. and Woittiez, J.R.W. 1988. Chemical processes affecting the mobility of major, minor and trace elements during weathering of granitic rocks. Chemical Geology, 68, 253-273.

Miller, R. McG. 2013. Comparative stratigraphic and geochronological evolution of the northern Damara Supergroup in Namibia and the Katanga Supergroup in the Lufilian Arc of Central Africa. Journal of the Geological Association of Canada, 40, 2, 118-140.

Mitchell, C.J., Inglethorpe, S.D.J., Tawodzera, P., Bradwell, S. and Evans, E.J. 1998. Local development of affordable lime in southern Africa. Technical Report WC/97/20, British Geological Survey.

Moore, T. A. 1964 The geology of the Chisamba area: Explanation of degree sheet 1428, SW quarter. Report Geological Survey Zambia 5, 32pp.

Moore, J.M. 2010. Comparative study of the Onganja Copper Mine, Namibia: a link between Neoproterozoic mesothermal Cu (-Au) mineralisation in Namibia and Zambia. South African Journal of Geology, 113, 4, 445-460.

Mora, C.I. and Valley, J.W. 1989. Halogen-rich scapolite and biotite: implications for metamorphic fluid-rock interaction. American Mineralogist, 74, 721-737.

Morad, S., El-Ghali, M.A.K., Caja, M.A., Sirat, M., Al-Ramadan, K. and Mansurbeg, H. 2010. Hydrothermal alteration of plagioclase in granitic rocks from Proterozoic basement of SW Sweden. Geological Journal, 45, 105-116.

Moufti, A.M.B. 2011. Mineralogy of metacarbonate rocks and garnet deposits at two selected areas at Asir Region, southwestern USA. International Journal of Geosciences, 2, 657-668.

Munyanyiwa, H. 1985. The geochemistry and metamorphism of calc-silicate rocks, marbles and amphibolites in a portion of the Zambezi belt, southern Zambia. Master's Thesis, University of Zambia. 110pp

Munyanyiwa, H. and Hanson, R.E, 1988. Geochemistry of marbles and calc-silicate rocks in the Pan-African Zambezi Belt, Zambia. Precambrian Research, 38, 177-200.

Munyanyiwa, H. 1990. Mineral assemblages in calc-silicate and marbles in the Zambezi mobile belt: their implications on mineral-forming reactions during metamorphism. Journal of African Earth Sciences, 10, 4, 693-700.

Naydenov, K.V., Lehmann, J., Saalmann, K., Milani, L., Kinnaird, J.A., Charlesworth, G., Frei, D. and Rankin, W. 2014. New constraints on the Pan-African Orogeny in Central Zambia: a structural and geochronological study of the Hook batholiths and the Mwembeshi Zone. Tectonophysics, 637, 80-105.

Naydenov, K.V, Lehmann, J., Saalmann, K., Milani, L., Poterai, J., Kinnaird, J.A., Charlesworth, G. and Kramers, J.D. 2015. The geology of the Matala Dome: an important piece of the Pan African puzzle in Central Zambia. International Journal of Earth Sciences, 105,3, 695-712.

Oesterlen, P.M. and Blenkinsop, T.G. 1994. Extension directions and strain near the failed triple junction of the Zambezi and Luangwa Rift zones, southern Africa. Journal of African Earth Sciences, 18, 2, 175-180.

Pirajno, F. 1992. Hydrothermal mineral deposits: principles and fundamental concepts for the exploration geologist. Springer-Verlag, 247-277.

Plant, J.A., Kinniburgh, D.G., Smedley, P.L. Fordyce, F.M. and Klinck, B.A. 2007. Arsenic and selenium. In, (Ed.) Sherwood Lollar B., Environmental Geochemistry, Treatise on Geochemistry, 9, Elsevier Ltd, 17-66.

Porada, H. 1989. Pan-African rifting and orogenesis in southern to equatorial Africa and eastern Brazil. Precambrian Research, 44, 103-106.

Porada, H. and Berhorst, V. 2000. Towards a new understanding of the Neoproterozoic-Early Palaeozoic Lufilian and Northern Zambezi Belts in Zambia and the Democratic Republic of Congo. Journal of African Earth Science, 30, 3, 727-771.

Porter, S.J., Selby, D. and Vyllinniskii, C. 2014 Characterising the nickel isotopic composition of organic-rich marine sediments. Chemical Geology, 387, 12-21.

Reimann, K.U. 1986. Prospects for oil and gas in Zimbabwe, Zambia and Botswana. Episodes, 9, 2, 95-101.

Reinaud, C., Master, S., Armstrong, R.A., Phillips, D. and Robb, L.L. 2005. Monazite U-Pb dating and 40Ar-39 Ar thermochronology of metamorphic events in the Central African Copperbelt during the Pan-African Lufilian Orogeny. Journal of African Earth Sciences, 42, 183-199.

Rose, A.W. 1976. The effect of cuprous chloride complexes in the origin of red-bed copper and related deposits. Economic Geology, 71, 1036-1048.

Rose, A.W. 1986. Mobility of Cu and other chalcophile elements in low-temperature near-surface environments. Symposium on sediment-hosted stratiform copper deposits, Ottawa May 17 - 19 1986. Canadian Mineralogist, Vol. 24, 169-214.

Satish-Kumar, M. and Harley, S.L. 1998. Reaction textures in scapolite-wollastonite-grossular calc-silicate rock from the Kerala Khondalite Belt, southern India: evidence for high-temperature metamorphism and initial cooling. Lithos, 44, 83-99.

Schrijver, K., Chevé, S.R. and Tassé, N. 1986. Mineral Assemblages in fenestral structures in carbonate rocks: A possible aid in exploration for copper deposits. Symposium on sediment-hosted stratiform copper deposits, Ottawa May 17 - 19 1986. Canadian Mineralogist, Vol. 24, 169-214.

Seasor, R.W. and Brown, A.C. 1986. Syngenetic and diagenetic concepts at White Pine, Michigan. Symposium on sediment-hosted stratiform copper deposits, Ottawa May 17 - 19 1986. Canadian Mineralogist, Vol. 24, 169-214.

Selley, D., Broughton, D., Scott, R., Hitzman, M., Bull, S., Large, R., McGoldrick, P., Croaker, M., Pollington, N. and Barra, F. 2005. A new look at the geology of the Zambian Copperbelt. Society of Economic Geologists, Inc. Economic Geology 100th Anniversary Volume, 965-1000.

Shelton, K.L., Gregg, J.M. and Johnson, A.W. 2009. Replacement dolomites and ore sulphides as recorders of multiple fluids and fluid sources in the southeast Missouri Mississippi Valley-Type district: halogen- $^{87}Sr/^{86}Sr$-$\delta^{18}O$-$\delta^{34}S$ systematic in the Bonneterre Dolomite. Economic Geology, 104, 733-748.

Simpson, J.G., Drysdall, A.R. and Lambert, H.H. 1963. The geology and groundwater resources of the Lusaka area: explanation of degree sheet 1528, NW Quarter. Report Geological Survey North Rhodesia, 16, 59pp.

Smedley, P.L., Zhang, M., Zhang, G. and Luo, Z. 2003. Mobilisation of arsenic and other trace elements in fluviolacustrine aquifers of the Huhhot Basin, Inner Mongolia. Applied Geochemistry, 18, 1453-1477.

Smith, A.G. 1964. The Geology of the Country around Mazabuka and Kafue. Geol. Surv. Northern Rhodesia, Report 2, 32pp.

Smulikowski, W., Desmons, J., Fettes, D.J., Harte, B., Sassi, F.P. and Schmid, R. 2007. 2. Types, grades and facies of metamorphism. A proposal on behalf of the IUGS Subcommission on the Systematics of metamorphic Rocks (SCMR), recommendations, web version of 01.02.2007, 10pp.

Stillman, C.J. and De Swardt, A. M. J. 1965. The response to Lufilian folding of the Basement Complex around the northern edge of the Mpande Dome, Northern Rhodesia. The Journal of Geology, 73, 1, 131-141.

Sun, Y. and Püttmann, W. 1996. Relationship between metal enrichment and organic composition in Kupferschiefer hosting structure-controlled mineralisation from Oberkatz Schwelle, Germany. Applied Geochemistry, 11, 567-581.

Sverjensky, D.A. 1986. Chemical evolution of basinal brines that form sediment-hosted Cu-Pb-Zn deposits. Symposium on sediment-hosted stratiform copper deposits, Ottawa May 17 - 19 1986. Canadian Mineralogist, Vol. 24, 169-214.

Sweeney, M.A. and Binda, P.L. 1986. The role of diagenesis in the formation of the Konkola Cu-Co orebody of the Zambian Copperbelt. Symposium on sediment-hosted stratiform copper deposits, Ottawa May 17 - 19 1986. Canadian Mineralogist, Vol. 24, 169-214.

Theron, S.J. 2013. The origin of the Central African Copperbelt: in a nutshell. Base Metals Conference 2013, Southern African Institute of Mining and Metallurgy, 21-36.

Treloar, P.J. 1988. The geological evolution of the Magondi Mobile Belt, Zimbabwe. Precambrian Research, 38, 1, 55-73.

Tsikos, H. and Moore, J.M. 2005. Sodic metasomatism in the Paleoproterozoic Hotazel iron-formation, Transvaal Supergroup, South Africa: implications for fluid-rock interaction in the Kalahari manganese field. Geofluids, 5, 264-271.

Unrug, R. 1983. The Lufilian Arc: a microplate in the Pan-African collision zone of the Congo and the Kalahari cratons. Precambrian Research, 21, 181-196.

Vrána, S., Prasad, R. and Fediuková, E. 1975. Metamorphic Kyanite Eclogites in the Lufilian Arc of Zambia. Contrib. Mineral. Petrol., 51, 139-160.

Walker, E.C., Cuttitta, F. and Senftle, F.E. 1958. Some natural variations in the relative abundance of copper isotopes. Geochimica et Cosmochimica Acta, 15, 183-194.

Walker, T.R. 1986. Diagenetic alterations in red beds and their application to the origin of copper and other heavy metals in stratiform ore-deposits. Symposium on sediment-hosted stratiform copper deposits, Ottawa May 17 - 19 1986. Canadian Mineralogist, Vol. 24, 169-214.

Warren, J. 1999. Evaporites – their evolution and economics. Blackwell Science Pty Ltd.

Webster, J.D. 2004. The solubility of magmatic hydrosaline chloride liquids. Chemical Geology, 210, 33-48.

Woodhead, J.A. 2013. The Neoproterozoic Roan Group in the Zambian Copperbelt: sequence stratigraphy, alteration and mineralisation. Colorado School of Mines, PhD Thesis Geology, 260pp.

Yemane, K., Grujic, D. and Nyambe, I. 2002. Paleohydrological signatures and rift tectonics in the interior of Gondwana documented from Upper Permian Lake Deposits, the Mid-Zambezi Rift basin, Zambia. SEPM Special Publication 73, 143-162.

Zambezi Resources. 2004. Zambezi Resources Exploration Update Report, 23 November 2004. Press release, 7pp.

Zambezi Resources. 2004a. Zambezi Resources Press release corresponding to the AIM admission document, 1pp.

Zambezi Resources. 2005. Zambezi Resources Report on Mulofwe Dome, 7 March 2005. Press release, 3pp.

Zambezi Resources. 2005a. Zambezi Resources Summary of 2004 field season exploration programmes, 5 April 2005. Press release, 4pp.

Zambezi Resources. 2007. Zambezi Resources Prospectus, p66-69.

Zambezi Resources. 2008. Zambezi Resources copper gold projects update, 20 May 2008. Press release, 3pp.

Zientek, M.L., Bliss, J.D., Broughton, D.W., Christie, M., Denning, P.D., Hayes, T.S., Hitzman, M.W., Horton, J.D., Frost-Kilian, S., Jack, D.J., Master, S., Parks, H.L., Taylor, A.B., Wintzer, N.E., and Woodhead, J. 2014. Sediment-hosted stratabound copper assessment of the Neoproterozoic Roan Group, Central African Copperbelt, Katanga Basin, Democratic Republic of Congo. U.S. Geological Survey Scientific Investigations Report 2010–5090–T, 162pp.

APPENDICES

APPENDIX 1: Geological Logs of the Shantumbu diamond drill core, southern Zambia

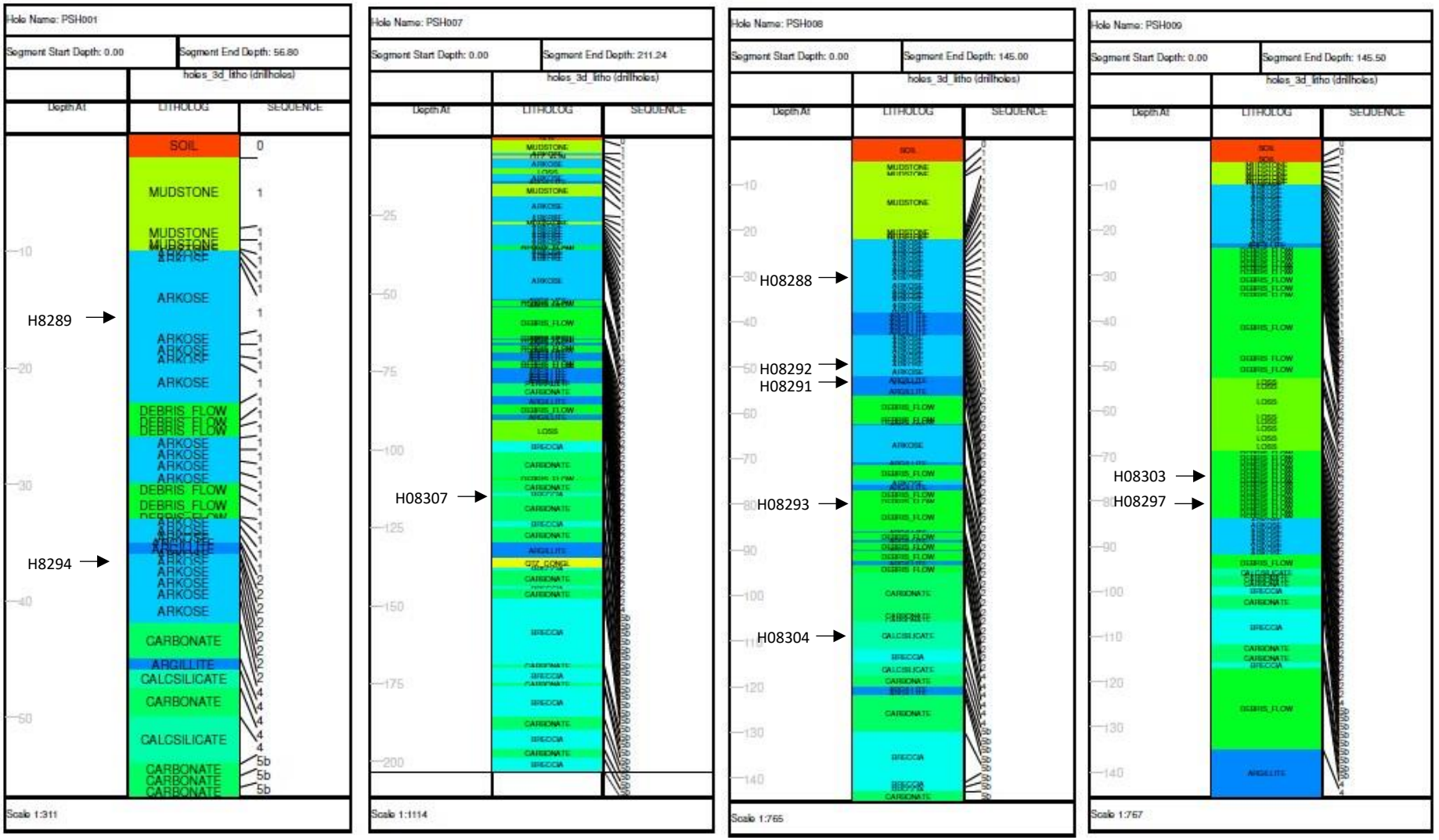
Hole Name: PSH001
Segment Start Depth: 0.00
Segment End Depth: 56.80
holes_3d_litho (drillholes)
Depth At
LITHOLOG
SEQUENCE
SOIL
MUDSTONE
ARKOSE
DEBRIS_FLOW
CARBONATE
ARGILLITE
CALCSILICATE
H8289
H8294
Scale 1:311
Hole Name: PSH007
Segment Start Depth: 0.00
Segment End Depth: 211.24
holes_3d_litho (drillholes)
Depth At
LITHOLOG
SEQUENCE
H08307
Scale 1:1114
Hole Name: PSH008
Segment Start Depth: 0.00
Segment End Depth: 145.00
holes_3d_litho (drillholes)
Depth At
LITHOLOG
SEQUENCE
H08288
H08292
H08291
H08293
H08304
Scale 1:765
Hole Name: PSH009
Segment Start Depth: 0.00
Segment End Depth: 145.50
holes_3d_litho (drillholes)
Depth At
LITHOLOG
SEQUENCE
H08303
H08297
Scale 1:767

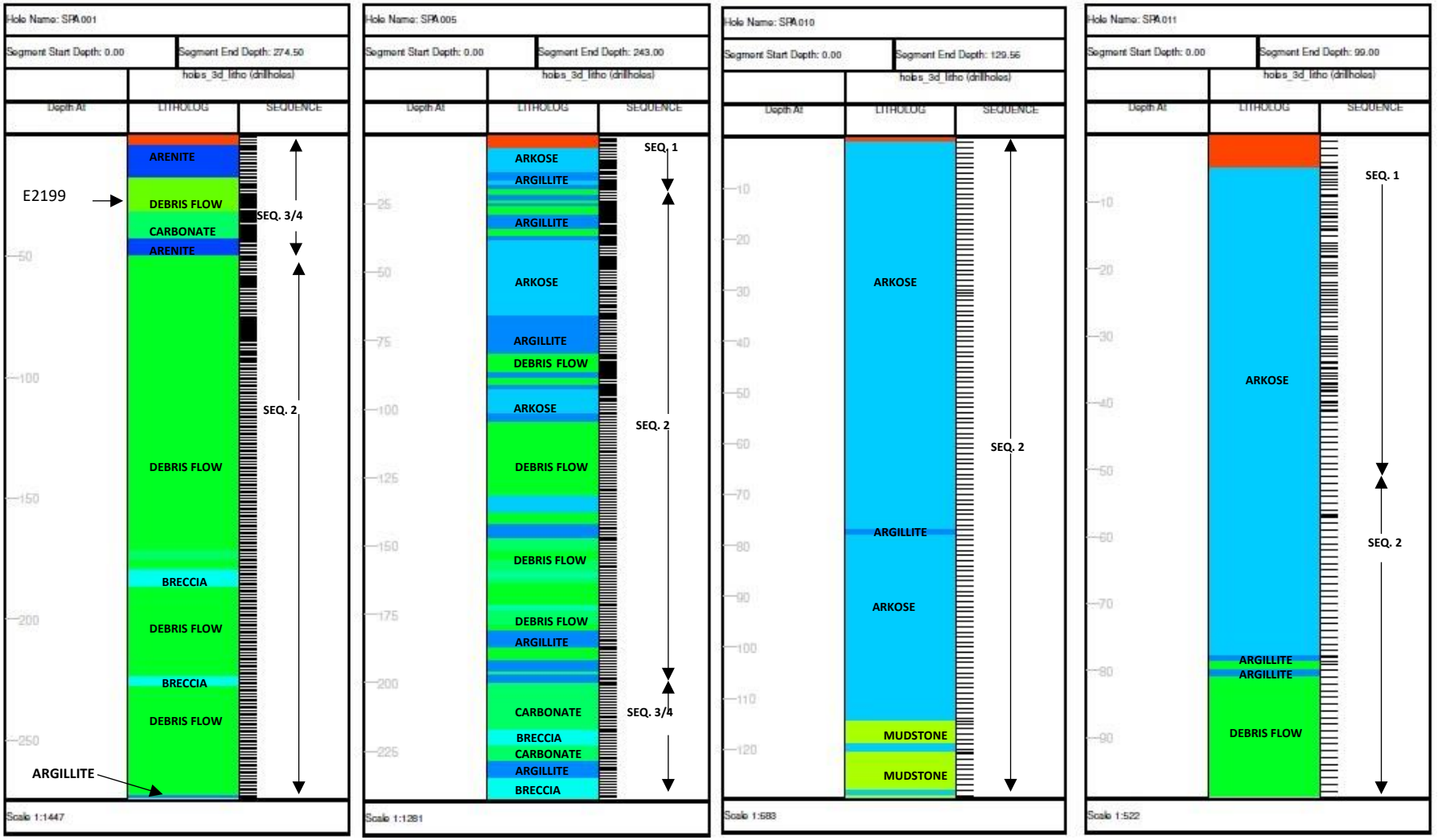
Hole Name: SPA001
Segment Start Depth: 0.00
Segment End Depth: 274.50
holes_3d_litho (drillholes)
Depth At
LITHOLOGY
SEQUENCE
E2199
ARENITE
DEBRIS FLOW
CARBONATE
ARENITE
DEBRIS FLOW
BRECCIA
DEBRIS FLOW
BRECCIA
DEBRIS FLOW
ARGILLITE
SEQ. 3/4
SEQ. 2
Scale 1:1447
Hole Name: SPA005
Segment Start Depth: 0.00
Segment End Depth: 243.00
holes_3d_litho (drillholes)
Depth At
LITHOLOGY
SEQUENCE
ARKOSE
ARGILLITE
ARGILLITE
ARKOSE
ARGILLITE
DEBRIS FLOW
ARKOSE
DEBRIS FLOW
DEBRIS FLOW
DEBRIS FLOW
ARGILLITE
CARBONATE
BRECCIA
CARBONATE
ARGILLITE
BRECCIA
SEQ. 1
SEQ. 2
SEQ. 3/4
Scale 1:1281
Hole Name: SPA010
Segment Start Depth: 0.00
Segment End Depth: 129.56
holes_3d_litho (drillholes)
Depth At
LITHOLOGY
SEQUENCE
ARKOSE
ARGILLITE
ARKOSE
MUDSTONE
MUDSTONE
SEQ. 2
Scale 1:683
Hole Name: SPA011
Segment Start Depth: 0.00
Segment End Depth: 99.00
holes_3d_litho (drillholes)
Depth At
LITHOLOGY
SEQUENCE
ARKOSE
ARGILLITE
ARGILLITE
DEBRIS FLOW
SEQ. 1
SEQ. 2
Scale 1:522

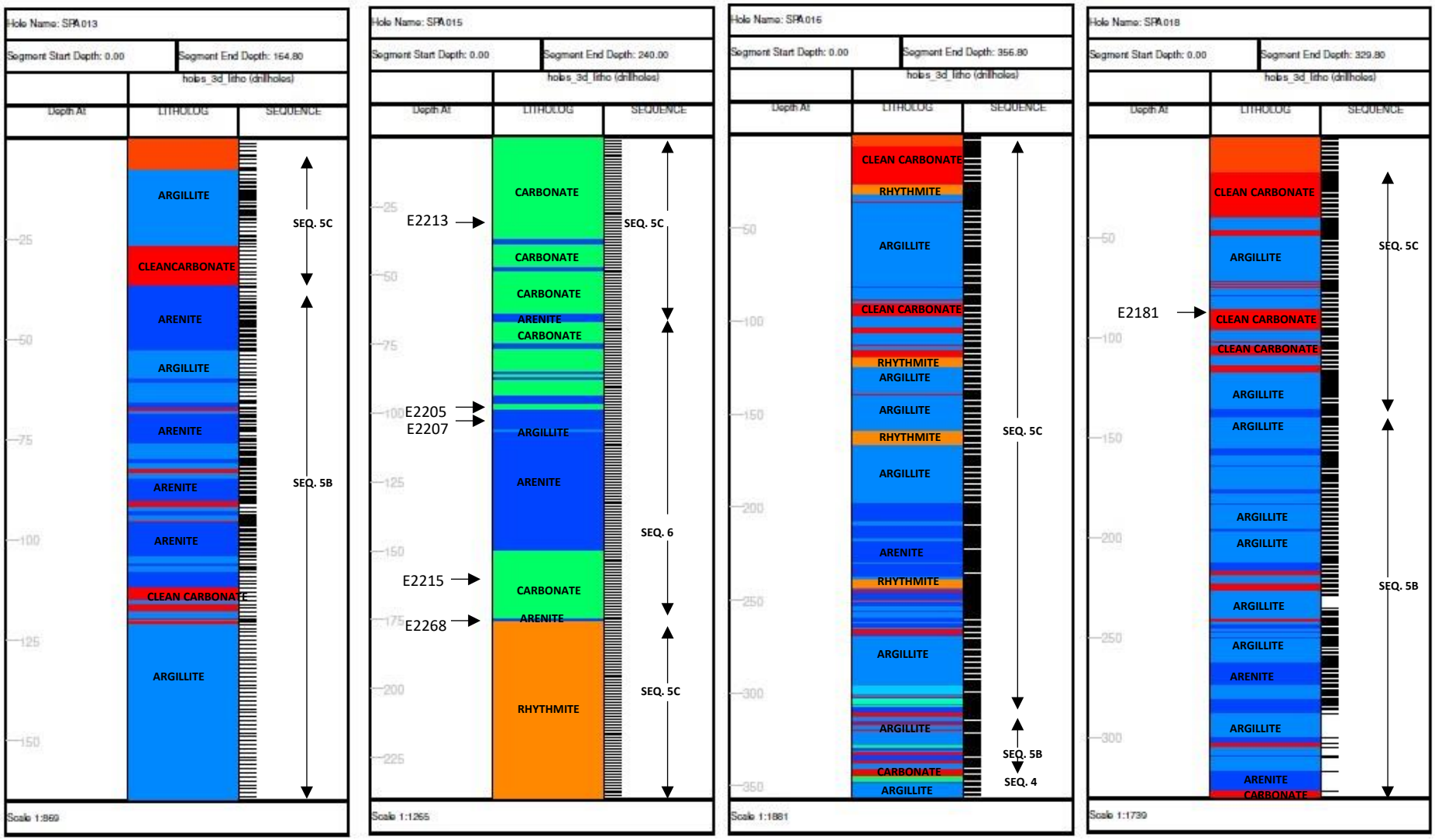
Hole Name: SPA013
Segment Start Depth: 0.00
Segment End Depth: 164.80
holes_3d_litho (drillholes)
Depth At
LITHOLOG
SEQUENCE
ARGILLITE
CLEANCARBONATE
ARENITE
ARGILLITE
ARENITE
ARENITE
ARENITE
CLEAN CARBONATE
ARGILLITE
SEQ. 5C
SEQ. 5B
Scale 1:869
Hole Name: SPA015
Segment Start Depth: 0.00
Segment End Depth: 240.00
holes_3d_litho (drillholes)
E2213
E2205
E2207
E2215
E2268
CARBONATE
CARBONATE
CARBONATE
ARENITE
CARBONATE
ARGILLITE
ARENITE
CARBONATE
ARENITE
RHYTHMITE
SEQ. 5C
SEQ. 6
SEQ. 5C
Scale 1:1265
Hole Name: SPA016
Segment Start Depth: 0.00
Segment End Depth: 356.80
holes_3d_litho (drillholes)
CLEAN CARBONATE
RHYTHMITE
ARGILLITE
CLEAN CARBONATE
RHYTHMITE
ARGILLITE
ARGILLITE
RHYTHMITE
ARGILLITE
ARENITE
RHYTHMITE
ARGILLITE
ARGILLITE
CARBONATE
ARGILLITE
SEQ. 5C
SEQ. 5B
SEQ. 4
Scale 1:1881
Hole Name: SPA018
Segment Start Depth: 0.00
Segment End Depth: 329.80
holes_3d_litho (drillholes)
E2181
CLEAN CARBONATE
ARGILLITE
CLEAN CARBONATE
CLEAN CARBONATE
ARGILLITE
ARGILLITE
ARGILLITE
ARGILLITE
ARGILLITE
ARENITE
ARGILLITE
ARENITE
CARBONATE
SEQ. 5C
SEQ. 5B
Scale 1:1739

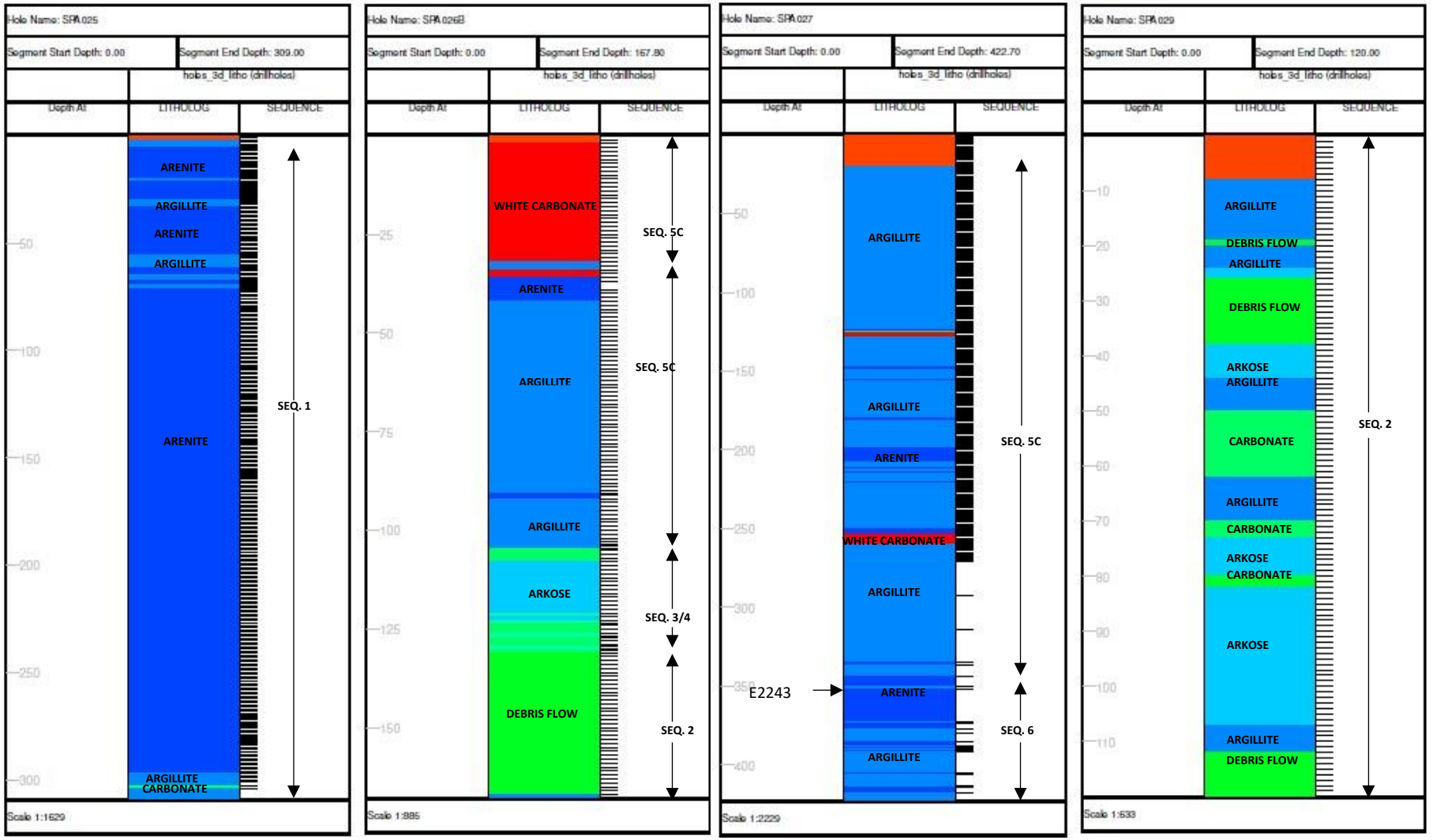
Hole Name: SPA025
Segment Start Depth: 0.00
Segment End Depth: 309.00
holes_3d_litho (drillholes)
Depth At
LITHOLOG
SEQUENCE
ARENITE
ARGILLITE
ARENITE
ARGILLITE
ARENITE
ARGILLITE
CARBONATE
SEQ. 1
Scale 1:1629
Hole Name: SPA026B
Segment Start Depth: 0.00
Segment End Depth: 167.80
holes_3d_litho (drillholes)
Depth At
LITHOLOG
SEQUENCE
WHITE CARBONATE
ARENITE
ARGILLITE
ARGILLITE
ARKOSE
DEBRIS FLOW
SEQ. 5C
SEQ. 5C
SEQ. 3/4
SEQ. 2
Scale 1:885
Hole Name: SPA027
Segment Start Depth: 0.00
Segment End Depth: 422.70
holes_3d_litho (drillholes)
Depth At
LITHOLOG
SEQUENCE
ARGILLITE
ARGILLITE
ARENITE
WHITE CARBONATE
ARGILLITE
E2243
ARENITE
ARGILLITE
SEQ. 5C
SEQ. 6
Scale 1:2229
Hole Name: SPA029
Segment Start Depth: 0.00
Segment End Depth: 120.00
holes_3d_litho (drillholes)
Depth At
LITHOLOG
SEQUENCE
ARGILLITE
DEBRIS FLOW
ARGILLITE
DEBRIS FLOW
ARKOSE
ARGILLITE
CARBONATE
ARGILLITE
CARBONATE
ARKOSE
CARBONATE
ARKOSE
ARGILLITE
DEBRIS FLOW
SEQ. 2
Scale 1:533

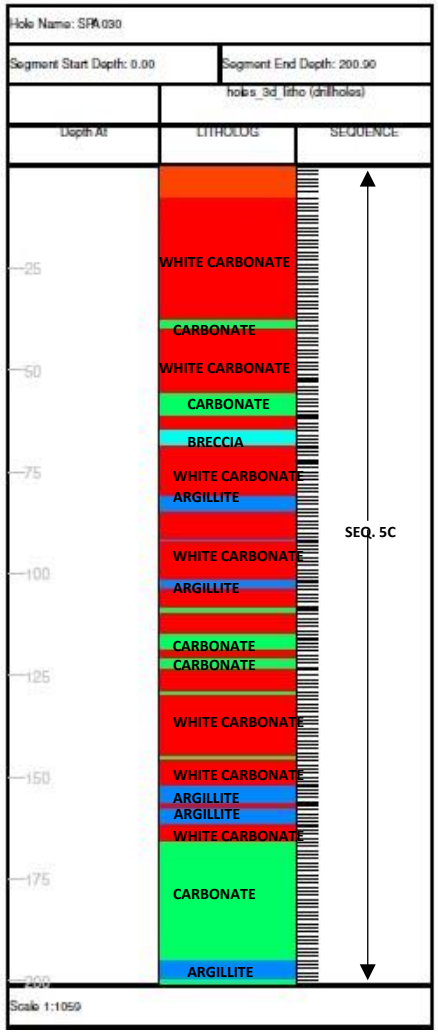

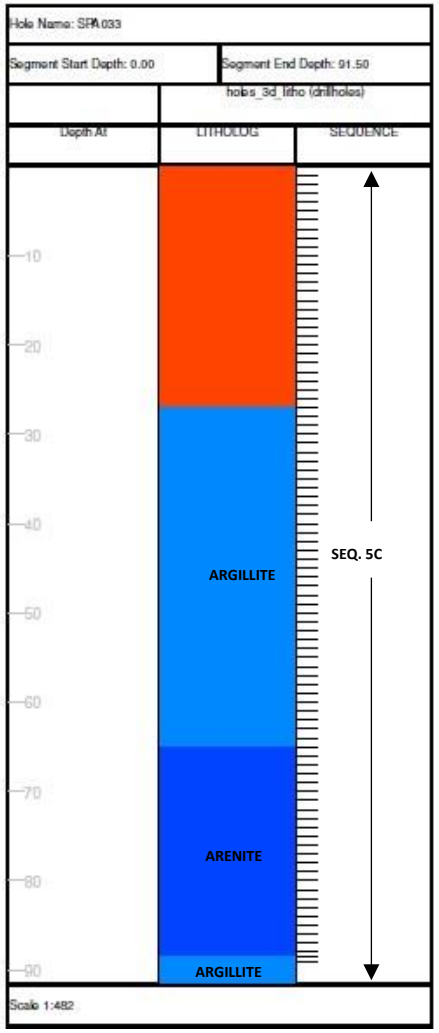

LEGEND

- [ARENITE]
- [ARGILLITE]
- [ARKOSE]
- [BRECCIA]
- [CALCSILICATE]
- [CARBONATE]
- [DEBRIS_FLOW]
- [GREY-GREEN]
- [LOSS]
- [MUDSTONE]
- [QTZ_CONGL]
- [QTZ_VEIN]
- [RHYTHMITE]
- [SOIL]
- [WHITE CLEAN CARB]

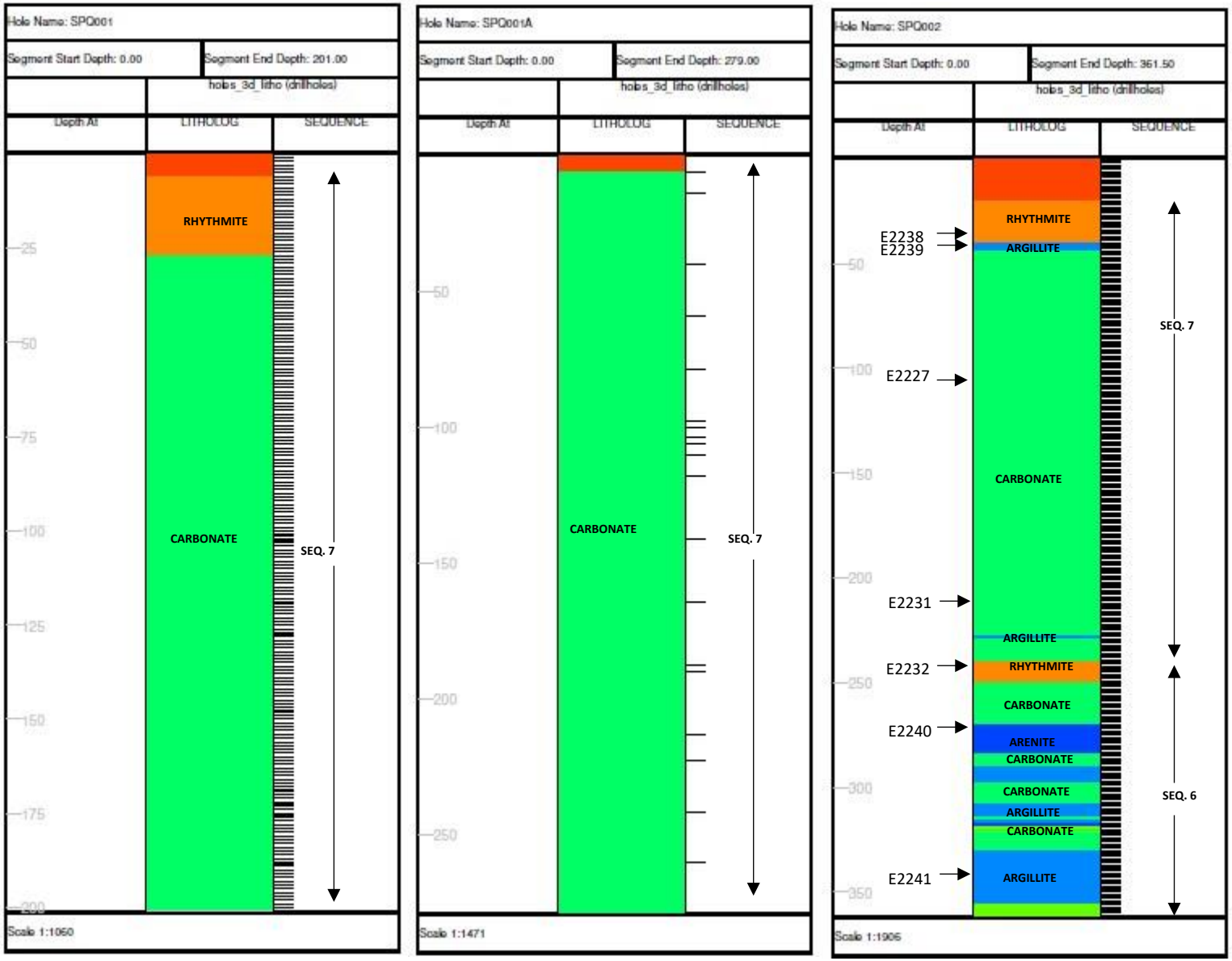
Hole Name: SPC001
Segment Start Depth: 0.00
Segment End Depth: 201.00
holes_3d_litho (drillholes)
Depth At
LITHOLOG
SEQUENCE
RHYTHMITE
CARBONATE
SEQ. 7
Scale 1:1060
Hole Name: SPC001A
Segment Start Depth: 0.00
Segment End Depth: 279.00
holes_3d_litho (drillholes)
Depth At
LITHOLOG
SEQUENCE
CARBONATE
SEQ. 7
Scale 1:1471
Hole Name: SPC002
Segment Start Depth: 0.00
Segment End Depth: 361.50
holes_3d_litho (drillholes)
Depth At
LITHOLOG
SEQUENCE
E2238
E2239
E2227
E2231
E2232
E2240
E2241
RHYTHMITE
ARGILLITE
CARBONATE
ARENITE
SEQ. 7
SEQ. 6
Scale 1:1906

APPENDIX 2: PORTABLE XRF VALUES OF THE SHANTUMBU DIAMOND DRILL CORE, SOUTHERN ZAMBIA

APPENDIX 3: ICP-OES VALUES OF THE SHANTUMBU DIAMOND DRILL CORE, SOUTHERN ZAMBIA